Directionality and soils' effects on the seismic hazard and risk. Applications to ground motion big data sets and to urban environments

Author: Luis Alejandro Pinzón Ureña

A thesis submitted in partial fulfillment of the
requirements for the degree of
Doctor of Philosophy

Supervisor: Dr. Luís G. Pujades
Co-Supervisor: Dr. Albert Macau

Ph.D. program on Earthquake Engineering and Structural Dynamics
Department of Civil and Environmental Engineering
Universitat Politècnica de Catalunya

To *my wife and family*

"It's your world...pay attention"

H.S. Thompson (1937-2005)

Acknowledgements

In the following lines, I would like to express a deep and sincere thanks to all those people and institutions that with their help have collaborated in the development of this PhD thesis.

To Professor Luís G. Pujades, supervisor of this work, for his patience, orientation, continuous supervision, knowledge, experience and motivation provided throughout the development of this thesis. I will always be grateful for your trust and support during these last four years.

To Dr. Albert Macau, co-supervisor of this thesis, for all the help and support provided during the development of this work.

To the Universitat Politècnica de Catalunya (UPC) for being my house of study and for providing me with its facilities for the development of this project.

UNIVERSITAT POLITÈCNICA DE CATALUNYA BARCELONATECH

To the Cartographic and Geological Institute of Catalonia (ICGC), the Spanish National Geographic Institute (IGN) and the Earthquake Engineering Laboratory of the University of Costa Rica (LIS-UCR) for providing me with data and resources for the preparation of this thesis.

ICGC Institut Cartogràfic i Geològic de Catalunya

INSTITUTO GEOGRÁFICO NACIONAL

LIS Laboratorio de Ingeniería Sísmica

To all those who have collaborated in the development of this work, specially to Dr. Yeudy Vargas (UPC), Rodrigo Alva (UPC), Dr. Miguel Mánica (National Autonomous University of Mexico, UNAM), Dr. Diego Hidalgo (LIS-UCR), Dr. Sergio Díaz (Autonomous Juarez University of Tabasco, UJAT) and Dr. Sara Figueras (ICGC).

All this would not have been possible without the unconditional support of my family, especially of my wife Lis, my parents, Luis and Viola, my grandmother, Nella, and my siblings, Fani and José.

Finally, to thank all my friends and work colleagues who supported and accompanied me these last four years in Barcelona.

Luis Alejandro Pinzón Ureña

Barcelona, 2020

Funding

This research has been partially funded by the Spanish Government's Ministry of Economy and Competitiveness (MINECO) and by the European Regional Development Fund (ERDF) of the European Union (EU) through projects referenced as CGL2015-65913-P (MINECO/ERDF, EU) and EFA158/16/POCRISC (INTERREG/POCTEFA, EU). The author of this thesis has been supported by a PhD scholarship grant from the Institute for the Training and Development of Human Resources (IFARHU) and the Government of Panama's National Secretariat of Science, Technology, and Innovation (SENACYT). The support of these institutions is highly recognized and acknowledged.

Abstract

Earthquakes are defined as a *"violent shaking of the Earth's crust and mantle, caused by forces acting inside the Earth"*. In most cases, these forces are caused by an energy release process generated from the contact of the Earth's tectonic plates. Other less common causes are the human-induced earthquakes or those generated through volcanic activity. In either case, the energy is released in the form of multi-directional waves, which reach the surface, causing different effects. However, the intensity of an earthquake is not uniform in all its propagating directions. Many times, the motion is polarized due to the type of fault and/or the proximity to it, causing higher intensities in specific directions, depending on the dynamics and geometry of the rupture. This is what is known as the directivity effect. Furthermore, both the intensity and the shape of the wave vary depending on the propagation medium. Ground motion prediction models deal with the spread of the released energy from source to site. Local site effects, both soil effects and topographical effects, are also important. Rigid media, such as rocky and stiff soils, do not tend to amplify the seismic motion, while soft soils amplify specific frequencies depending on local sub-soil geology and on the motion characteristics. Directionality effects refer to the strong motion in a specific site. This thesis deals with two important issues related to directionality. The first one refers to the orientation of the sensors recording the seismic actions; the second one refers to the expected damage in buildings depending on the directions of their strong and weak main axes. It is worth to mention that nowadays, directionality effects are not considered in most structural regulations. In this thesis, special attention is paid to the directionality and soil effects. Since 2008, around 360,000 earthquake fatalities have been reported. This evidence demonstrates the need to develop more and better ways to assess and to prevent seismic risk. Therefore, the main objective of this thesis is to identify and evaluate the strong-motion directionality and the soils' effects on the seismic hazard and risk, with applications to strong-motion data sets and soils' in urban environments. This thesis is divided into three principal blocks: I) directionality effects, II) Soils effects, site classification and other seismic risk-related issues and, III) relevant case studies related to the previous two blocks. In the first block, directionality effects have been considered in the expected strong seismic actions, through the estimation of intensity measures using databases from Italy and Costa Rica. Also, in the assessment of the expected damage of buildings through non-linear dynamic analyses, a simplified approach has been proposed to consider directionality effects. In the second block, microzonation and soil-building resonance effects in the city of Barcelona are studied. In addition, a seismic site classification is defined for the Spanish strong-motion network. The dynamic soil-structure interaction, considering directionality effects and, the proposal of a new drift-correlated intensity measure, appeared as supplementary subjects in this block. Finally, in the third block, other relevant contributions were included to complement this dissertation. The results demonstrate 1) that directionality effects in expected seismic actions are significant and should be considered in Probabilistic Seismic Hazard Analysis (PSHA) and in seismic risk assessments; and 2) they confirm the relevance that site effects (soil effects), has both in seismic hazard studies and in the assessment of the expected damage. This PhD thesis wants to be an additional step towards the assessment, prevention, and reduction of the risk due to earthquakes.

Keywords: earthquake engineering; engineering seismology; directionality effects; site effects; damage assessment; site classification; ground-motions; intensity measures; soil-structure interaction; microzonation; seismic hazard; seismic risk; horizontal-to-vertical spectral ratios; fundamental periods; inter-story drift; soils' effects; strong motion site characterization

UNESCO codes: 2507.05; 3305.32

Resum

Els terratrèmols es defineixen com una *"sacsejada violenta de l'escorça i el mantell, produïda per forces que actuen a l'interior de la Terra"*. En la majoria dels casos, aquestes forces són causades per processos relacionats amb l'alliberament d'energia, produït pel contacte entre plaques tectòniques. Altres terratrèmols menys freqüents, són els induïts per activitats antròpiques o els d'origen volcànic. En qualsevol cas, l'energia s'allibera en forma d'ones multidireccionals, que arriben a la superfície, causant efectes diversos. Les intensitats causades per un terratrèmol però, no són uniformes en totes les direccions de la seva propagació. Tot sovint, el moviment fort està polaritzat, degut al tipus de falla i/o a la proximitat a l'hipocentre, de forma que, depenent de la geometria i dinàmica de la ruptura, les acceleracions són més intenses en determinades direccions. Aquest fenomen es coneix com l' efecte de directivitat. D'altra banda, la intensitat i la forma de l'ona varien depenent del medi de propagació. En aquest sentit, els models predictius del moviment fort del sòl tenen en compte, també, el efectes deguts a la propagació, des de la font al lloc d'interès, de l'energia alliberada. Els efectes locals, principalment els deguts a la topografia i a la geologia locals, també són importants. Els medis rígids, com els sòls rocosos i compactes, no tendeixen a amplificar el moviment sísmic, mentre que els sòls tous sí que amplifiquen freqüències específiques, depenent de les propietats del subsol i de les característiques del moviment. Els efectes de direccionalitat fan referència al moviment fort en un lloc específic. Aquesta tesis aborda dos temes importants en relació a aquests efectes. El primer es refereix a l'orientació dels sensors que enregistren les accions sísmiques; el segon està relacionat amb el dany esperat en edificis concrets, depenent de l'orientació dels seus eixos principals. Val a dir que, avui en dia, la major part de les normatives sísmiques encara no consideren els efectes de direccionalitat. En aquesta tesis, es fa especial atenció a la direccionalitat i als efectes de sòl. Des de l'any 2008, s'ha informat de 360,000 morts, aproximadament, per causa de terratrèmols. Aquest fet evidencia la necessitat de desenvolupar més i millors maneres d'avaluar i prevenir el risc sísmic. Així doncs, l'objectiu principal d'aquesta tesis ha estat identificar i avaluar com la direccionalitat del moviment fort i els efectes de sòl influeixen en la perillositat i el risc sísmic, amb aplicacions a la zonificació sísmica de sòls en entorns urbans i a grans bases de dades d'accelerogrames. La tesis es divideix en tres blocs: I) els efectes de direccionalitat, II) els efectes de sòl, classificació de llocs i altres temes relacionats amb el risc sísmic, i III) estudis de cas rellevants relacionats amb els dos blocs anteriors. En el primer bloc, s'han considerat els efectes de direccionalitat en les accions esperades; per la qual cosa, s'han estimat mesures d'intensitat utilitzant les bases de dades d'Itàlia i Costa Rica. A més, en l'avaluació del dany previsible en edificis, emprant anàlisis dinàmiques no lineals, s'ha proposat un nou plantejament que permet considerar els efectes de direccionalitat de forma simplificada. En el segon bloc, es realitzen estudis de micro-zonació i de ressonància (sòl-edifici) a la ciutat de Barcelona; tanmateix, es realitza una classificació sísmica dels emplaçaments de les estacions acceleromètriques de la xarxa espanyola; l'anàlisi d'interacció sòl-estructura, considerant els efectes de direccionalitat, i la proposta d'una nova mesura d'intensitat, molt correlacionada amb la deriva (drift), apareixen com a temes complementaris en aquest bloc. Finalment, en el tercer bloc, s'inclouen altres contribucions rellevants que completen aquesta dissertació. Els resultats demostren, 1), que els efectes de direccionalitat en les accions sísmiques esperades són significatius i cal considerar-los en els estudis probabilístics d'amenaça sísmica, així com en les avaluacions de risc sísmic i confirmen, 2), la rellevància que els efectes de lloc tenen, tant en els estudis del perill sísmic com en l'avaluació del dany esperat en estructures. Aquesta tesis doctoral vol ser un pas endavant vers l'avaluació, prevenció i reducció del risc sísmic.

Codis UNESCO: 2507.05; 3305.32

Contents

1 Introduction **1**
1.1 Background . . . 1
1.2 Objectives . . . 4
1.2.1 Block I. Directionality effects . . . 4
1.2.2 Block II. Soils' effects, site classification and other seismic risk related issues . . 5
1.2.3 Block III. Other relevant contribution . . . 6
1.3 Methdology . . . 6
1.3.1 Block I. Directionality effects . . . 6
1.3.2 Block II. Soils effects, site classification and other seismic risk related issues . . 7
1.3.3 Block III. other relevant contributions . . . 8
1.4 Thesis layout . . . 9
1.5 Brief summary of chapters . . . 12

2 Directionality models from ground motions of Italy **15**
2.1 Abstract . . . 15
2.2 Introduction . . . 15
2.3 Time histories . . . 16
2.3.1 As-recorded time histories . . . 16
2.3.2 Response time histories . . . 16
2.4 Directionality analysis . . . 18
2.4.1 Rotated (Rot) time histories . . . 18
2.4.2 Peak values and IMs . . . 18
2.4.3 Rotation dependent (RotD) and independent (RotI) . . . 20
2.4.4 Main IMs . . . 21
2.4.5 IMs comparison . . . 24
2.5 Directionality in Italy . . . 24
2.5.1 Data . . . 25
2.5.2 Results . . . 26
2.5.3 Model . . . 29
2.6 Summary, discussion and conclusions . . . 31

3 A Strong-Motion Database of Costa Rica: 20 Years of Digital Records **33**
3.1 Abstract . . . 33
3.2 Introduction . . . 33
3.3 Strong-Motion Network . . . 34
3.4 Strong-Motion Database . . . 35
3.5 Data processing . . . 36
3.6 Intensity measures . . . 38
3.7 Conclusions . . . 41

4 An efficient method for considering the directionality effect of earthquakes on structures **43**
4.1 Abstract . . . 43
4.2 Introduction . . . 43
4.3 Methodology . . . 44

4.3.1 Complete rotational method . . . 44
4.3.2 Predictive percentile method . . . 45
4.3.3 Spectral matching technique . . . 47
4.4 Building's application model . . . 48
4.5 Ground motions selection . . . 50
4.6 Results . . . 50
4.6.1 Regular building . . . 50
4.6.2 Irregular building . . . 54
4.6.3 Performance in the non-linear range . . . 60
4.6.4 Near- and far-fault earthquakes . . . 60
4.7 Discussion and conclusions . . . 64

5 Increased seismic hazard in Barcelona (Spain) due to soil-building resonance effects 67
5.1 Abstract . . . 67
5.2 Introduction . . . 67
5.3 Building period map . . . 69
5.4 Soil period map . . . 71
5.5 Crossing period maps . . . 71
5.6 Discussion and Conclusions . . . 75

6 Seismic site classification from the horizontal-to-vertical response spectral ratios: use of the Spanish strong motion database 79
6.1 Abstract . . . 79
6.2 Introduction . . . 79
6.3 Methodology . . . 83
6.4 Data . . . 83
6.5 Results . . . 85
6.6 Conclusions . . . 90

7 Dynamic soil-structure interaction analyses considering directionality effects 93
7.1 Abstract . . . 93
7.2 Introduction . . . 93
7.3 Case study . . . 94
7.3.1 Input motions . . . 95
7.3.2 Surface structure . . . 97
7.3.3 Main features of the finite element model . . . 98
7.4 Complete rotational approach - CRA . . . 100
7.5 Simplified rotational approach - SRA . . . 102
7.5.1 Free-field seismic actions computations . . . 102
7.5.2 Intensity measures . . . 103
7.5.3 Peak ground acceleration, peak ground velocity, and PGV/PGA ratio . . . 105
7.5.4 Arias intensity - AI . . . 106
7.5.5 Specific energy density - SED . . . 106
7.5.6 Cumulative absolute velocity - CAV . . . 108
7.5.7 Maximum spectral response . . . 108
7.5.8 Spectral response for the fundamental period of the building - SA_{Tf} . . . 109

7.6 CRA and SRA comparison . . . 110
7.7 Conclusions . . . 114

8 A drift-correlated ground motion intensity measure: application to steel frame buildings 117
8.1 Abstract . . . 117
8.2 Introduction . . . 117
8.3 Intensity measures . . . 118
8.3.1 Intensity measures based on ground motion time histories . . . 119
8.3.2 Intensity measures based on peak responses . . . 120
8.4 Structural models . . . 120
8.5 Ground motion records . . . 122
8.6 Correlation between the IMs and the MIDR . . . 124
8.7 New IM . . . 124
8.8 Correlation between IMs . . . 128
8.9 Validation through probabilistic NLDA . . . 128
8.10 Conclusions . . . 134

9 Discussion and conclusions 135
9.1 Main results and discussion . . . 135
9.2 Recommendations and future trends . . . 139
9.3 Conclusions and final remarks . . . 142

Bibliography 143

A Appendix. Chapter 4 tables. 161

B Appendix. A simplified approach to account for directionality effects on 2D dynamic soil-structure interaction analysis 167
B.1 Abstract . . . 167
B.2 Introduction . . . 167
B.3 Methodology . . . 169
B.3.1 Complete rotational approach (CRA) . . . 169
B.3.2 Simplified rotational approach (SRA) . . . 169
B.4 Finite element model . . . 171
B.5 Results . . . 172
B.6 Conclusions . . . 173

C Appendix. Case study of a heavily-damaged building during the 2016 M_W 7.8 Ecuador earthquake: Directionality effects in seismic actions and damage assessment 175
C.1 Abstract . . . 175
C.2 Introduction . . . 175
C.3 Directionality in ground motions . . . 176
C.4 Directionality in the spectral response . . . 182
C.5 Damage assessment of a heavily-damage building . . . 183
C.5.1 Studied building . . . 183
C.5.2 Parametric model . . . 186

C.5.3 Park and Ang based damage index . . . 188
C.5.4 Fragility curves and mean damage state . . . 188
C.5.5 Seismic actions . . . 191
C.5.6 Building-seismic action interaction . . . 192
C.6 Conclusions . . . 196

D Appendix. Seismic site classification of the Costa Rican Strong-Motion Network based on V_{S30} measurements and site fundamental period 199
D.1 Abstract . . . 199
D.2 Introduction . . . 199
D.3 Average shear-wave velocity of the top 30 m (V_{S30}) . . . 200
D.4 Fundamental period through HVSR . . . 201
D.5 V_{S30} and site fundamental period relation . . . 201
D.6 CRSM site characterization . . . 203
D.7 Conclusions . . . 205

E Appendix. Do Directionality Effects Influence Expected Damage? A Case Study of the 2017 Central Mexico Earthquake 207
E.1 Abstract . . . 207
E.2 Introduction . . . 207
E.3 Mexico City and the 2017 Central earthquake . . . 208
E.3.1 Seismic hazard in Mexico City . . . 208
E.3.2 The 2017 Central Mexico earthquake . . . 208
E.4 The case of the Tlalpan 1C building . . . 208
E.4.1 Structural analysis . . . 210
E.5 Phenomena related to anomalous performance of buildings . . . 212
E.5.1 Geological soft soil (GSS) effects . . . 212
E.5.2 Soil-structure interaction (SSI) . . . 213
E.5.3 Site-city interaction (SCI) . . . 214
E.6 Directionality effects . . . 214
E.6.1 Effects on the 1C building . . . 215
E.6.2 Ground motions and design spectra . . . 216
E.6.3 Overall directionality effects . . . 218
E.7 Conclusions . . . 220
E.8 Data and Resources . . . 221

F Appendix. Reply to "Comment on 'Do Directionality Effects Influence Expected Damage? A Case Study of the 2017 Central Mexico Earthquake' by Luis A. Pinzón, Luis G. Pujades, Sergio A. Diaz, and Rodrigo E. Alva" by Eduardo Reinoso, Pablo Quinde, Danny Arroyo, Mario Ordaz, and Amador Terán-Gilmore 223
F.1 Introduction . . . 223
F.2 Collapse of a building in the ISSSTE multifamily complex . . . 223
F.3 Directionality effects and earthquake-resistant design . . . 226
F.4 Closure . . . 226

List of Publications

List of work published related to this PhD thesis.

Indexed journals

Pinzón, L. A., Pujades, L. G., Diaz, S. A., & Alva, R. E. (2018). Do Directionality Effects Influence Expected Damage? A Case Study of the 2017 Central Mexico Earthquake. *Bulletin of the Seismological Society of America, 108*(5A), 2543–2555. doi: 10.1785/0120180049

Pinzón, L. A., Pujades, L. G, Hidalgo-Leiva, D. A., & Díaz, S. A. (2018). Directionality models from ground motions of Italy. *Ingegneria Sismica, 35*(3), 43–63.

Díaz, S. A., Pujades, L. G., Pinzón, L. A., & Vargas-Alzate, Y. F. (2018). An alternative approach to consider the effect of seismic directionality. *Revista Ingeniería de Construcción, 33*(3), 279–290. doi: 10.4067/S0718-50732018000300279

Pinzón, L. A., Pujades, L. G, Macau, A., & Figueras, S. (2019). Increased seismic hazard in Barcelona (Spain) due to soil-building resonance effects. *Soil Dynamics and Earthquake Engineering, 117*, 245–250. doi: 10.1016/j.soildyn.2018.11.022

Pinzón, L. A., Diaz, S. A., Pujades, L. G., & Vargas-Alzate, Y. F. (2019). An efficient method for considering the directionality effect of earthquakes on structures. *Journal of Earthquake Engineering*, in-press, 1–30. doi: 10.1080/13632469.2019.1597783

Pinzón, L. A., Pujades, L. G, Macau, A., Carreño, E. & Alcalde, J. M. (2019). Seismic Site Classification from the Horizontal-to-Vertical Response Spectral Ratios: Use of the Spanish Strong-Motion Database. *Geosciences, 9*(7), 294. doi: 10.3390/geosciences9070294

Pinzón, L. A., Pujades, L. G., Diaz, S. A., & Alva, R. E. (2018). Reply to "Comment on 'Do Directionality Effects Influence Expected Damage? A Case Study of the 2017 Central Mexico Earthquake' by Luis A. Pinzón, Luis G. Pujades, Sergio A. Diaz, and Rodrigo E. Alva" by Eduardo Reinoso, Pablo Quinde, Danny Arroyo, Mario Ordaz, and Amador Terán-Gilmore. *Bulletin of the Seismological Society of America, 110*(1), 393–396. doi: 10.1785/0120190168

Pinzón, L. A., Mánica, M. A., Pujades, L. G & Alva, R. E. (2020). Dynamic soil-structure interaction analyses considering directionality effects. *Soil Dynamics and Earthquake Engineering, 130*, 106009. doi: 10.1016/j.soildyn.2019.106009

Pinzón, L. A., Vargas-Alzate, Y. F., Pujades, L. G & Diaz, S. A. (2020). A drift-correlated ground motion intensity measure: application to steel frame buildings. *Soil Dynamics and Earthquake Engineering, 132*, 106096. doi: 10.1016/j.soildyn.2020.106096

Moya-Fernández, A., Pinzón, L. A., Schmidt-Díaz, V., Hidalgo-Leiva, D. & Pujades, L. G (2020). A Strong-Motion Database of Costa Rica: 20 Years of Digital Records. *Seismological Research Letters*, under-review.

Conferences and Workshops

Pinzón, L. A., Pujades, L. G., & Hidalgo-Leiva, D. A. (2018). Geometric- and Non-geometric-mean Sensor-orientation-independent Seismic Intensities. Application to the Italian Strong Motion

Database. In *16th European Conference on Earthquake Engineering (16ECEE)*, Thessaloniki, Greece.

Pinzón, L. A., Pujades, L. G., Macau, A., Figueras, S., & Alva, R. E. (2018). Microzonation and zones of increased Hazard due to resonance effects in Barcelona. In *12th International Workshop on Seismic Microzoning and Risk Reduction*, Yokohama, Japan.

Pinzón, L. A. (2018). Directionality in seismic actions: the case of Italy. In *Workshop on advanced tools for seismic risk assessment and management*, Granada, Spain.

Pinzón, L. A. (2018). Directionality in expected damage in buildings. In *Workshop on advanced tools for seismic risk assessment and management*, Granada, Spain.

Pinzón, L. A. (2018). Likely soil-buildings resonant effects in Barcelona. Soil's and building's periods' maps. In *Workshop on advanced tools for seismic risk assessment and management*, Granada, Spain.

Pinzón, L. A. (2018). Directionality in seismic actions and expected damage in buildings. In *KaIROS Initial Meeting*, Barcelona, Spain.

Pinzón, L. A., Mánica, M. A., Pujades, L. G., & Alva, R. E. (2019). A simplified approach to account for directionality effects on 2D dynamic soil-structure interaction analysis. In *7th International Conference on Earthquake Geotechnical Engineering*, Rome, Italy.

List of work published during the PhD related to other research projects.

Indexed journals

Alva, R. E., Pujades, L. G., González-Drigo, J. R., Luzi, G., Caselles, O. & Pinzón, L. A. (2020). Dynamic Monitoring of a Mid-Rise Building by Real-Aperture Radar Interferometer: Advantages and Limitations. *Remote Sensing, 12*(6), 1025. doi: 10.3390/rs12061025

Conferences and Workshops

Hidalgo-Leiva, D. A., Pujades, L. G., Barbat, A. H., Díaz, S. A., Vargas-Alzate, Y. F., & Pinzón, L. A. (2018). Damage Index for structures with elements of high flexural stiffness and/or brittle behavior. In *16th European Conference on Earthquake Engineering (16ECEE)*, Thessaloniki, Greece.

Alva, R. E., Pujades, L. G., González-Drigo, J. R., & Pinzón, L. A. (2018). Acquisition and processing of buildings' vibrations using Real-Aperture Radar, a non-invasive method. In *12th International Workshop on Seismic Microzoning and Risk Reduction*, Yokohama, Japan.

Alva, R. E., González-Drigo, J. R., Luzi, G., Caselles, O., Pujades, L. G., Vargas-Alzate, Y. F., & Pinzón, L. A. (2019). Remote ambient vibration measurements with Real-Aperture Radar to estimate buildings dynamic properties. In *7th International Conference on Computational Methods in Structural Dynamics and Earthquake Engineering*, Crete, Greece.

Vargas-Alzate, Y. F., Pujades, L. G., González-Drigo, J. R., Alva, R. E., & Pinzón, L. A. (2019). On the equal displacement approximation for mid-rise reinforced concrete buildings. In *7th International Conference on Computational Methods in Structural Dynamics and Earthquake Engineering*, Crete, Greece.

List of Figures

1 On the left a diagram showing an explosive source (star) with spherical radiation in a homogeneous and isotropic medium. Eight sensors are located at the same radial distance. On the right, the motion records in the two horizontal-orthogonal components of each sensor are shown. 2

2 Scheme similar to Figure 1. Sensors are substituted by buildings facing the same direction and located at the same radial distance. Buildings have a strong axis ($2k$-EW) and a weak axis ($1k$-NS).The two buildings most likely to be damaged are marked with a red circle. In these cases the strongest action hits the weak axis of the building. . . 3

3 PhD dissertation layout. See also Table 2 11

4 As-recorded EW (a) and NS (c) accelerograms in the time and frequency domains. 5% damped acceleration responses for T=0.17 and 5% damped acceleration response spectra, Sa (T), for the EW (b) and NS (d) registers. The 0.17 s period is marked in the Fourier and response spectra, and maximum values are marked in the time histories. 17

5 (a) Maximum values of the rotated accelerograms; the corresponding time arrivals (middle) and time lags (down) are also depicted. (b) Same as (a) for the responses of the rotated accelerograms for a 5% damped SDOF system with T=0.17 s. See also Figure 4. 19

6 (a) As-recorded accelerograms, pGM and pVC compositions; maximum values, PGA, mpGM and mpVC are marked. GM and VC are also shown. (b) Same as (a) but for the acceleration responses of a 5% damped SDOF system with a period of 0.17 s. . . . 20

7 (a) mpGM, mpVC, GM, and VC as functions of the rotation angle, θ, for the as-recorded rotated signals. (b) Same as (a) for the acceleration responses of the as-recorded rotated signals. 21

8 (a) 5% damped response spectra of the rotated accelerograms according to Equations 5 and 6. (b) 3D plots of the response spectra as functions of the period, T, and of the rotation angle, θ. The RotD50 and the RotI50 are also plotted in these figures. c) Angle $\theta(t)$ at which the RotD50 (black dots) and the RotI50 (black line) are achieved. 22

9 (a) 5% damped response spectra calculated with mpVC, Larger, mpGM, GM, NS, and EW as-recorded IMs from the Umbria earthquake and (b) zoom-in range of periods [0.045 0.065]s. Data corresponds to the Central Italy, M_W=6.5, Umbria earthquake, recorded at station T1213, which occurred on 30 October 2016 at 06:40:18. 24

10 Comparison among several IMs for the 5% damped response spectra. Note that LRotD100, RotD100, and mpVC are equivalent IMs. 25

11 Epicenters and magnitudes of the earthquakes used in this study. 26

12 Ratios for IMs. (a) mpGM/GM, mpGMRotD50/GM, and pmGMRotI50/GM; (b) GMRotD50/GM, GMRotI50/GM, and RotD50/GM; (c) Larger/GM, LRotD50/GM, and mpVC/GM. The 95% confidence intervals are also shown. 27

13 Geometric mean value of the ratio mpVC/GMRotI50 found in this study and comparison with ratios obtained by others. 28

14 Geometric mean of the ratio mpVC/GMRotI50 and 95% confidence intervals for different magnitude ranges. 28

15 Geometric mean of the ratio mpVC/GMRotI50 for close and distant (Type 1 and Type 2). 29

16 SampGM/SaGM, SampGMRotD50/SaGM, and SaGMRotI50/SaGM compared to the proposed model for (a) EC-8 Type 1 earthquakes; (b) EC-8 Type 2 earthquakes. SaRotD50/SaGM compared to the proposed model for (c) EC-8 Type 1 earthquakes; (d) EC-8 Type 2 earthquakes. Ratios SaLarger/SaGM, SaLRotD50/SaGM and (SaLRotD100 or SaRotD100 or SampVC/SaGM compared to the proposed model for (e) EC-8 Type 1 earthquakes; (f) EC-8 Type 2 earthquakes. 30
17 Station distribution for the LIS-UCR strong-motion network. White lines correspond to administrative divisions by provinces and gray lines to major roads. 34
18 Station distribution and soil classification. 35
19 Number of ground motions recorded per year. 36
20 (a) Magnitude as a function of the hypocentral distance for the 2471 records and (b) magnitude distribution. 37
21 Epicenter location for the earthquakes recorded between 1998 and 2019. 37
22 Peak ground acceleration as a function of the hypocentral distance for the three as-recorded components. 39
23 Several intensity measures as a function of the hypocentral distance: (a) PGV, (b) PGV/PGA, (c) Arias intensity, (d) acc_{RMS}, (e) vel_{RMS}, (f) Specific Energy Density, (g) Characteristic intensity, (h) Cumulative Absolute Velocity and (i) Significant duration. 40
24 Comparison of the 5% damped response spectra estimated with RotD100, GM, horizontal acceleration components (N00E and N90E) and the rotated components (θ^o rot) from the 7.6 M_W Nicoya earthquake recorded at station GNSR, which occurred on 5 September 2012. 41
25 Comparison of the 5% damped response spectra estimated with RotD100, Larger, RotD50, GMRotI50, GMRotD50 and the GM using the 7.6 M_W Nicoya earthquake recorded at station GNSR, which occurred on 5 September 2012. 41
26 180 rotated response spectra from Umbria, Italy earthquake (October 30, 2016). In blue the spectrum corresponding to de maximum demand (RotD100), in black the median (RotD50) and the as-recorded components, N-S and E-W, in red and green respectively. 45
27 Main screen of the MatchPercentile application. 47
28 Regular steel frame model dimensions used to study the directionality effect. 48
29 Irregular steel frame model dimensions used to study the directionality effect. 49
30 Particle acceleration motions of the 20 selected accelerograms. 51
31 Accelerograms of the as-recorded N-S and E-W horizontal components from Umbria, Italy earthquake (October 30, 2016) recorded in T1220 station. 53
32 Influence of the angle of incidence on (a) roof displacement in X-Direction and (b) roof displacement in Y-Direction of the regular building. 54
33 Influence of the angle of incidence on (a) base shear in X-Direction and (b) base shear in Y-Direction of the regular building. 54
34 Regular building principal axes fundamental period (T X-Direction and Y-Direction), 2% damped response spectra corresponding to the maximum demand ($\text{Max}_{RotD100}$), median demand (Median_{RotD50}), and the as-recorded N-S and E-W horizontal components from Umbria, Italy earthquake (October 30, 2016) recorded in T1220 station. . . 55
35 Matched accelerograms spectra corresponding to the maximum demand ($\text{Max}_{RotD100}$), median demand (Median_{RotD50}) and the as-recorded N-S and E-W horizontal components from Umbria, Italy earthquake (October 30, 2016) recorded in T1220 station. . . 55

36 Comparison between the roof displacement results from both CRM and PPM method for the regular building. Values of the median and maximum response in (a) roof displacement as a function of the rotation angle in X-Direction; (b) histogram of roof displacement values in X-Direction; (c) roof displacement as a function of the rotation angle in Y-Direction; (d) histogram of roof displacement values in Y-Direction. 56
37 Comparison between the base shear results from both CRM and PPM method for the regular building. Values of the median and maximum response in (a) base shear as a function of the rotation angle in X-Direction; (b) histogram of base shear values in X-Direction; (c) base shear as a function of the rotation angle in Y-Direction; (d) histogram of base shear values in Y-Direction. 57
38 Bar graphics comparing the CRM and the PPM for the regular building. Values of the as-recorded, median and maximum response of (a) roof displacement in X-Direction and (b) roof displacement in Y-Direction (c) base shear in X-Direction and (d) base shear in Y-Direction. 58
39 Comparison between the base shear results from both CRM and PPM method for the irregular building. Values of the median and maximum response in (a) base shear as a function of the rotation angle in X-Direction; (b) same in Y-Direction; (c) base shear as a function of the rotation angle in X-Direction; (d) same in Y-Direction. 59
40 (a) E-W and (b) N-S as-recorded components of ground motions recorded at MSCT station, 2017 Abruzzo earthquake. 63
41 Response spectra for as-recorded ground motions components of MSCT station, 2017 Abruzzo earthquake; damping ratio = 5%. 63
42 The geometric mean of RotD100/Larger ratio from 949 ground motion pairs of ITACA database. 66
43 (a) Microzonation map of Barcelona city and (b) topography of the city. 69
44 Example of building database for Barcelona City. 70
45 Example of building database map with the respective (a) structural typology and (b) construction year (zoom-in of Gracia district). 70
46 (a) Map with the estimated fundamental period of the building database of Barcelona, (b) zoom-in the cross between Diagonal Ave. and Passeig de Gracia street and (c) 3D view of (b). 72
47 Microzonation map of Barcelona based on soil periods. The points represent the available experimental data. 74
48 Microzonation map of Barcelona based on soil periods compared with (a) elevations of the city and (b) Cid *et al.* (2001) microzonation zones. 75
49 (a) Resonance zones in Barcelona and (b) zoom-in of Gracia district. 76
50 The 11 May 2011 Lorca (Spain) earthquake, 5.1 M_W at 18:47:00 local time. (a) Response spectra comparison and (b) 3D particle motion for the ground-motion record registered in LOR station. E30°N and N30°W correspond to the as-recorded accelerograms. 81
51 Horizontal-to-vertical (H/V) 5% damped response spectral ratio comparison for (a) the 11 May 2011 Lorca (Spain) earthquake recorded in the LOR station (5.1 M_W at 18:47:00 local time) and (b) the 24 February 2004 Alhucemas (Morocco) earthquake recorded in the ALG station (6.3 M_W at 02:27:47 local time). 82
52 Magnitudes and hypocentral distances for selected earthquakes and stations. 84
53 Location of the earthquakes used in the analysis. 84

54 H/V response spectral ratios for the LOR station. Gray lines are the H/V ratios of all the ground motions recorded in LOR station and in black the 50th percentile. The predominant period found is 0.46 s. 85
55 Location of accelerometric stations. 86
56 (a) Geometric means (GM) of the H/V ratios of the 5% damped response spectra for each site class. (b) The corresponding standard deviations. 86
57 Comparison between the EC-8 Type 2 design spectra and the mean spectral shapes obtained for the site classes: (a) CL-I, (b) CL-II, (c) CL-III, (d) CL-IV, (e) CL-V, (f) CL-VI, and (g) CL-VII. 90
58 Input motion for DSSI analyses from an acceleration history recorded at a rock outcrop. 95
59 As recorded ground motion horizontal components of the earthquakes considered: (a) Friuli in 1976, (b) Campania in 1980, and (c) Umbria in 1997. 96
60 Particle acceleration motion of the accelerograms of the Friuli earthquake. 97
61 (a) Building geometry and (b) soil-building FE model employed. 99
62 Maximum relative roof displacement as a function of the rotation angle obtained from the CRA for groups 1 (a), 2 (b) and 3 (c). 101
63 Geometry, mesh, and boundary conditions of the free-field FE simulation. 103
64 Time histories from the recorded motion and the free-field motion at the Surface for the accelerograms of the Friuli earthquake. Rotation angles of (a) $\theta = 0^{o}$, (b) $\theta = 50^{o}$, and (c) $\theta = 90^{o}$. 104
65 Response spectra from the rotated histories and their envelope (RotD100) for the (a) recorded motion and (b) the free-field motion at the surface. 104
66 Normalised (a) peak ground acceleration and (b) peak ground velocity as a function of the rotation angle for the Friuli, Campania, and Umbria seismic actions (group 1). . . 105
67 Normalised PGV/PGA ratio as a function of the rotation angle for the Friuli, Campania, and Umbria seismic actions (group 1). 106
68 Normalised Arias intensity as a function of the rotation angle for the Friuli, Campania, and Umbria seismic actions (group 1). 107
69 Normalised specific energy density as a function of the rotation angle for the Friuli, Campania, and Umbria seismic actions (group 1). 107
70 Normalised cumulative absolute velocity as a function of the rotation angle for the Friuli, Campania, and Umbria seismic actions (group 1). 108
71 $SA_{rot}/SA_{RotD100}$ spectral ratio as a function of the rotation angle for the Friuli earthquake for vibration periods (a) between 0.0 and 2.0 s and (c) between 0.9 and 1.0 s. Response spectra from the rotated motions, the RotD100 spectrum, and the RotI100T_1T_2 spectrum for the Friuli seismic actions for vibration periods (b) between 0.0 and 2.0 s and (d) between 0.9 and 1.0 s. 109
72 Normalised spectral response for the fundamental period of the building ($T_f = 0.95s$) as a function of the rotation angle for the Friuli, Campania, and Umbria seismic actions (group 1). 110
73 Comparison between the relative roof displacements obtained from the CRA and SRA for the (a) Friuli, (b) Campania, and (c) Umbria seismic actions (group 1). 111
74 Definition of the significant duration of a single accelerograms using the Husid plot (Husid, 1969) [accumulative energy (%) in terms of Arias intensity vs. time (s)]. . . . 119
75 Steel moment frame model dimensions for (a) 3-story, (b) 7-story and (c) 13-story buildings. 121

76 Five per cent damped response spectra, corresponding to the 80 selected accelerograms, matched to the design spectrum of Eurocode 8 for earthquakes with M > 5.5 (type I) located in rock. 122
77 Correlation between the maximum drift and several intensity measures: (a) PGA, (b) PGV, (c) SA_{T1}, (d) acc_{RMS}, (e) vel_{RMS}, (f) Arias intensity, (g) Characteristic intensity, (h) Specific Energy Density and (i) Cumulative Absolute Velocity. 125
78 Influence of duration on the maximum drift for scaled accelerograms and ranges of PGV: (a) 25<PGV<40 cm/s and (b) 40<PGV<60 cm/s. 126
79 (a) Comparison between the maximum drift and the proposed intensity measure $I_{\Delta-PGV}$. (b) In red, damaged buildings (with DI > 0.1) and in black, buildings that did not suffer damage. 127
80 Coefficient of determination (R^2) for the comparison of different IMs with the MIDR drift corresponding to the results obtained by performing the NLDAs for the 3-story building, 7-story building, 13-story building and all the buildings. 127
81 Matrices of R^2 from the correlation between the IMs used in this study for the (a) original records, (b) scaled records and (c) the matched records. 129
82 Twenty 2-D steel-frame building models. 131
83 Response spectra of the selected ground motion records for the probabilistic analysis. . 132
84 Results after performing the 500 NLDA. Relation between the MIDR and the proposed intensity measure $I_{\Delta-PGV}$. 133
B1 Friuli earthquake with moment magnitude (M_W) = 6.5, recorded at TLM1 station on May 6, 1976. (a) Ground motion horizontal components from Ambraseys *et al.* (2000) database, (b) response spectra from the as-recorded and rotated histories and the RotD100 response spectrum, and (c) acceleration hodogram. 168
B2 Response spectra from the rotated motions, the RotD100 spectrum, and the RotI100T_1T_2 spectrum [with (a) T_1 = 0.01 s and T_2 = 1.6 s and (b) T_1 = 0.8 s and T_2 = 1.2 s] from 1976 Friuli earthquake. 170
B3 (a) Building and (b) soil-building finite element models. 171
B4 (a) Arias intensity, (b) peak ground acceleration, and (c) $SA_{rot}/SA_{RotD100}$ spectral ratios as a function of the rotation angle for the 1976 Friuli earthquake. 172
B5 Comparison of the maximum roof displacements obtained for the (a) building and (b) soil-building models using the CRA (continuous line) and the SRA. 173
B6 (a) Arias intensity, (b) peak ground acceleration, and (c) $SA_{rot}/SA_{RotD100}$ spectral ratios as a function of the rotation angle for the 1976 Friuli earthquake derived from the time histories computed on the top of the free-field analyses. 174
B7 Comparison of the maximum roof displacements obtained for the soil-building model using the CRA (continuous line) and the SRA combined with free-field calculations. . 174
C1 Strong-motion station from the National Accelerographic Network of Ecuador (RENAC). 178
C2 Peak ground acceleration maps from the as-recorded components (a) N-S and (b) E-W, (c) the larger value of the as-recorded components and (d) the true peak acceleration ($PGA_{RotD100}$). 180
C3 $PGA_{RotD100}$ flow direction in the horizontal plane during the 2016 Ecuador earthquake. 181
C4 Response spectra from the as-recorded and rotated histories, and the RotD100 response spectrum from the 2016 Ecuador earthquake ground motion recorded in AMNT station. 182
C5 Comparison of the ratios RotD100/GM and RotD100/Larger with ratios proposed by other researchers. 183

C6 (a) Studied building. (b) In green, the main-building used to generate the structural model and in red, the annex that was not considered in the structural model. Images taken from Google Maps street view. 184
C7 Distribution and geometry of the beams and columns. 185
C8 Capacity curve and spectra in the X and Y directions. The points resulting from the pushover analysis, the interpolated curves (int) at a fixed pitch and the bilinear forms (Bilinear) are shown. 186
C9 Parametric model adjustment in the X-direction. 187
C10 Parametric model adjustment in the Y-direction. 187
C11 Capacity spectra (left) and damage functions (right) for: a) X direction and b) Y direction. Bilinear forms of capacity spectra and thresholds of damage states based on the Risk-UE project (Ds_{TrhRUE}) and those based on the Park and Ang damage index (Ds_{TrhIPA}) are shown. See also explanations in the text. 189
C12 Fragility curves: a) X-direction, Risk-UE thresholds, b) X-direction, Park and Ang index thresholds. c) Y-direction, Risk-UE thresholds, d) Y-direction, Park and Ang index thresholds. 191
C13 Mean damage state curves based on Risk-UE and Park and Ang damage index. 192
C14 Location and distance between the studied building and the closest accelerometric station, AMNT. The orientation of the building respect to the north is also depicted. . . 193
C15 2016 M_W 7.8 Ecuador earthquake, recorded at AMNT station. (a) As-recorded E-W and N-S accelerograms, and (b) acceleration hodogram. 194
C16 5% damped response spectra for the accelerograms obtained in the direction defined by the angle θ, from the projection of the as-recorded components EW and NS recorded at AMNT station. Figure is given in spectral acceleration-period ($Sa-T$) and in spectral acceleration-spectral displacement ($Sa-Sd$) formats. The fundamental periods of the principal axes of the building ($X_{Trans.}$ and $Y_{Long.}$) are also indicated. 194
C17 Linear equivalent approximation to estimate the performance point of the $X_{Trans.}$ (144° case) and $Y_{Long.}$ (54° case) axes. 195
C18 Mean damage state and Complete damage probability as a function of the rotation angle of the seismic action. The orientation of the principal axes of the building (54° and 144°) are shown. 195
C19 Damage probability matrices for the two main axes of the building (54° and 144° approximately) and for the two hypotheses used to define the damage states thresholds. 196
D1 Shear-wave velocity profiles from stations (a) PCOB and (b) PPQR. 201
D2 Horizontal-to-vertical spectral ratios normalized by the maximum amplitude value and the site fundamental period from stations (a) PCOB and (b) PPQR. 202
D3 Comparison between the site fundamental periods obtained through $\text{HVSR}_{SA(5\%)}$ and $\text{HVSR}_{Fourier}$. 202
D4 Measured V_{S30} values at the stations of the Costa Rican Strong-Motion Network plotted against the site fundamental period values (T_f) obtained from HVSR. The bilinear model (continuous line) and the proposed model based on the Costa Rican Seismic Code (dashed line) are depicted. 202
D5 Site classification proposal based on V_{S30} and site fundamental period values. 203
D6 Map with the geographical distribution of the accelerometric stations with the assigned soil class. 204

D7 (a) Number of stations per site class and (b) mean HVSR from all the stations per site class. 204
E1 Comparison between the response spectra (5% damped) of the horizontal as-recorded components from the 1985 Mexico City earthquake (SXVI station – seismic zone II) and the 2017 Central Mexico earthquake (CO47 station – seismic zone II). 209
E2 Comparison between the response spectra (5% damped) of the horizontal as-recorded components from the 1985 Mexico City earthquake (SCT station – seismic zone III C) and the 2017 Central Mexico earthquake (BA49 station – seismic zone III C). 209
E3 (a) ISSSTE multifamily complex development, Tlalpan, Mexico City, 1957 (see Data and Resources). (b) Plan view of the complex. Damage levels in the complex are shown. 210
E4 3D building model. 211
E5 (a) Shear and (b) inter-story drift comparison between the 1C and 4A, B and C buildings obtained through the time-history analysis with the ground motion of the DX37 station. 211
E6 H/V response spectral ratios for the strong-motion stations (a) DX37, (b) CH84, and (c) AO24. 213
E7 (a) Strong and weak axes of a building and (b) effective seismic forces affecting the strong and weak axes, as a function of the rotation angle. 215
E8 The azimuth of the 1C building measured from the south. 216
E9 (a) Epicentral distance from the 2017 Central Mexico earthquake to the 1C building. (b) The three accelerographic stations closest to the 1C building site. 216
E10 Particle acceleration motions at the four accelerometric stations closest to the 1C building site: DX37 station, CH84 station, IB22 station and AO24 station. The weak direction of the building (dashed blue line) is depicted. 217
E11 Variation of PGA and spectral acceleration, Sa, of a single-degree-of-freedom 5% damped oscillator with T=0.3 s as a function of the orientation angle, at DX37 accelerographic station. Vertical lines indicate the azimuths, measured from the south, to the weak axis of the 1 (C), 2 (A, B and C), and 4 (A, B and C) buildings. 218
E12 Comparison of response spectra of records at different accelerometric stations in Mexico City, during the 2017 Central Mexico earthquake: (a) CP28 station [zone I], (b) PA34 station [zone I], (c) DX37 station [zone II], (d) EO30 station [zone II], (e) CH84 station [zone IIIA], and (f) JC54 station [zone IIIA]. 219
E13 Comparison of the ratios RotD100/N-S, RotD100/E-W, RotD100/GM, and RotD100/Larger with ratios proposed by other researchers. 220
F1 Hodograms at stations AO24, IB22, DX37 and CH84 close to the building site. The weak direction of the building (dashed blue line) is depicted. 225

List of Tables

1 Top five major earthquakes by $US dollar value of property losses in the last twelve years. . . . 1
2 PhD dissertation layout. . . . 10
3 Maximum values and times at which they are attained for the EW and NS as-recorded accelerograms and acceleration responses of a 5% damped SDOF system with a period of 0.17 s. (See Figure 4). . . . 18
4 Summary of the main ground-motion IMs. The name, description and computation method are in the first, second, and third columns respectively. . . . 23
5 Ground motions records (NS and EW components) for type 1 and type 2 events. . . . 29
6 Coefficients for the ratio model for Type 1 earthquakes. . . . 31
7 Coefficients for the ratio model for Type 2 earthquakes. . . . 31
8 Magnitude, depth and epicentral distance statistics for the entire database. Number and percentage of three-components records per interval. . . . 36
9 List of intensity measures based on ground motion time histories. . . . 38
10 List of intensity measures based on peak responses. . . . 39
11 Values of T_1, W, PF_1 and α_1 of the regular building. . . . 49
12 Values of T, PF, α_x and α_y of the irregular building. . . . 50
13 Ground motions selection from ITACA database. . . . 52
14 Regular building results; roof displacement and base shear in X-Direction for the 20 scaled ground motion pairs selected from the ITACA database. . . . 61
15 Regular building results; roof displacement and base shear in Y-Direction for the 20 scaled ground motion pairs selected from the ITACA database. . . . 61
16 Irregular building results; roof displacement and base shear in X-Direction for the 20 scaled ground motion pairs selected from the ITACA database. . . . 62
17 Irregular building results; roof displacement and base shear in Y-Direction for the 20 scaled ground motion pairs selected from the ITACA database. . . . 62
18 Hypocentral distance, PGA, PGV, PGD and source-type of the selected ground motions. 65
19 Average error in percentage for near-fault and far-fault events comparing maximum values of the CRM and PPM. . . . 66
20 Structural typologies and coefficient, C_t, used in this study. (URM: unreinforced masonry; RC: reinforced concrete) . . . 69
21 Available soil data from Barcelona used in this study. . . . 73
22 Summary of parameters of interest: microzonation zones, topography, geomorphology, Vs_{30}, predominant frequency and fundamental period obtained in this study.) . . . 74
23 Classification based on Vs30 for seismic codes and standard regulations from Europe, Spain, and the United States. . . . 80
24 Comparison of the site classification definition based on the predominant period (T_g) proposed by Zhao *et al.* (2006), Fukushima *et al.* (2007), and di Alessandro *et al.* (2012). 83
25 Number of accelerometric stations and ground-motion records for each site class according to the di Alessandro *et al.* (2012) classification. . . . 85
26 Site classification of the Spanish strong-motion stations. . . . 87
27 Numerical values of the GM of the H/V ratios of the 5% damped response spectra for the site classes of the accelerometric stations based on the Spanish ground-motion database. . . . 88

28 Standard deviation of the GM of H/V ratios of the 5% damped response spectra for the site classes of accelerometric stations based on the Spanish ground-motion database. 89
29 Main similarities among the classification obtained in this study for the Spanish strong motion database and the soil classification of the Eurocode 8. 89
30 Cases studied. 95
31 Soil parameters 100
32 Critical incidence angles where the maximum relative roof displacement occurred with the CRA and the SRA. 112
33 Comparison between the relative roof displacements obtained through the CRA and SRA. 113
34 Comparison between the relative roof displacements obtained through the CRA and the as-recorded components. 115
35 List of intensity measures used in this study (see also explanation in the text). 118
36 Ground motions selection from the ITACA database. 123
37 R^2 value obtained from the correlation of each IM with the MIDR. 124
38 Equation and coefficients used in the minimization (720 NLDA). 126
39 R^2 values obtained from the correlation of $I_{\Delta-PGV}$ IM and MIDR. 128
40 Linear correlation of the IMs used in this study for all the available records (original + scaled + matched). 128
41 IMs with correlations values > 0.80. 130
42 Beam and column sections of the first floor per number of stories. American wide flanges steel sections - ASTM A992. 131
43 Properties of the variables considered in the probabilistic NLDA. 131
44 Comparison of R^2 values from the correlation of the studied IMs and MIDR obtained through the first approach and probabilistic NLDA. 133
A1 Regular building results; roof displacements (δ) in X-Direction summary results for the 20 ground motion pairs selected from the ITACA database. 161
A2 Regular building results; roof displacements (δ) in Y-Direction summary results for the 20 ground motion pairs selected from the ITACA database. 162
A3 Regular building results; base shear (V_B) in X-Direction summary results for the 20 ground motion pairs selected from the ITACA database. 162
A4 Regular building results; base shear (V_B) in Y-Direction summary results for the 20 ground motion pairs selected from the ITACA database. 163
A5 Irregular building results; roof displacements (δ) in X-Direction summary results for the 20 ground motion pairs selected from the ITACA database. 163
A6 Irregular building results; roof displacements (δ) in Y-Direction summary results for the 20 ground motion pairs selected from the ITACA database. 164
A7 Irregular building results; base shear (V_B) in X-Direction summary results for the 20 ground motion pairs selected from the ITACA database. 164
A8 Irregular building results; base shear (V_B) in Y-Direction summary results for the 20 ground motion pairs selected from the ITACA database. 165
C1 Values of PGA_{EW}, PGA_{NS}, $PGA_{RotD100}$, $PGA_{RotD100}/PGA_{Larger}$ ratio and $\theta_{PGA(RotD100)}$ from the 21 ground motions recorded by the National Accelerographic Network of Ecuador. 179
C2 Geometry of the sections and specifications of the materials of the beams and columns of the building studied. 184

C3 Parameters of the parametric model for the capacity spectra (CS) in the X and Y axes. 187
C4 Performance point values from the principal axes of the studied building. 192
C5 Mean damage state and Complete damage probability in the main axes of the building based on the proposal of the Risk- UE project and, the Park and Ang damage index. . 193
D1 Site classification of the Costa Rican Seismic Code, NEHRP equivalence, V_{S30} ranges and site fundamental periods proposed. 203
E1 Modal properties, period (T), and mass participation factors (W) of the studied building. 210
E2 Maximum base shear (F in kN) and maximum roof displacements (δ in cm) generated in each building through the time-history analysis. 211
E3 Site fundamental periods obtained through SASID Software and Horizontal-to-Vertical (H/V) Response Spectral Ratio. 213
E4 Summary of ground motion IMs considered in this study. 217

1 Introduction

1.1 Background

Over the last twelve years, a significant number of high-magnitude earthquakes have happened, causing significant property damage and fatalities. Earthquakes such as those in Sichuan (China, 2008), Maule (Chile, 2010), Tohoku (Japan, 2011), Christchurch (New Zealand, 2011), Emilia (Italy, 2012), Umbria (Italy, 2016), Ecuador (Ecuador, 2016) and Mexico City (Mexico, 2017) have generated almost $400 billion losses in damages (National Geophysical Data Center / World Data Service (NGDC/WDS), 2018) (see Table 1). Remarkably, the 2010 Haiti earthquake caused 222,570 fatalities (National Geophysical Data Center / World Data Service (NGDC/WDS), 2018).

Table 1: Top five major earthquakes by $US dollar value of property losses in the last twelve years.

Rank	Event	Country	Year	Magnitude	Damage ($ billion)
1	Tohoku	Japan	2011	9.1	220.0
2	Sichuan	China	2008	8.0	86.0
3	Maule	Chile	2010	8.8	30.0
4	Emilia	Italy	2012	6.1	15.8
5	Christchurch	New Zealand	2011	6.3	15.0

Earthquakes such as those in Sicily (Italy) in 1693 (Bianca et al., 1999), Lisbon (Portugal) in 1755 (Baptista et al., 2010), and Messina (Italy) in 1908 (Amoruso et al., 2002) were highly destructive events that left their mark on the European continent in the past. In the last decade, in Italy, the earthquakes of L'Aquila (Italy) in 2009 (Çelebi et al., 2010) and the Central Italian events of 2016 (Fiorentino et al., 2018) caused around 600 fatalities and thousands lost their homes. In Spain, the Lorca 2011 earthquake is an example of how a moderate earthquake ($M_W = 5.1$) can produce significant damage with considerable economic loss, homeless people, and fatalities (De Luca et al., 2014; Alfaro et al., 2012). This confirms the need to increase knowledge of earthquakes and provide advanced tools to improve the assessment and management of seismic hazard and risk (Pinzón et al., 2019d).

Seismic risk is defined as the probability, or rate, of the expected cost due to earthquakes in a specific period of time. Three aspects must be considered to assess the expected seismic risk in a specific area: hazard, exposure/vulnerability, and the value of the exposed goods. The Probabilistic Seismic Hazard Analysis (PSHA) defines the annual probability, or rate, of earthquake occurrence which is determined by: 1) seismic source studies including the geometric distribution of faults, the focal mechanism, and earthquake recurrence models, 2) calculation of Ground Motion Prediction Equations (GMPE), and 3) characterization of local effects, including soil, topographic, and other induced effects, such as landslides and soil liquefaction (Franke et al., 2016; Li et al., 2018). The results of a hazard study allow us to determine the probability of exceedance of a given threshold of ground motions and other intensity related parameters, also known as Intensity Measures (IM), during a specific time period. Several examples of intensity measures are macroseismic intensity, peak ground acceleration, spectral values of the structural response, among many other parameters.

An important topic in PSHA is to know how seismic waves propagate and attenuate from the hypocentre to a specific site. GMPEs help to solve this issue. The basic information for the GMPEs (attenuation laws) comes from maximum parameters of ground motions. Along the former 20th century, most of these studies were based on macroseismic intensity, as data of this parameter is available for very long time periods. Recall that seismological instrumentation dates from the beginning of the twentieth century and that the first strong motion accelerogram in United States was recorded during

the 1933 Long Beach earthquake in California (Brady, 2009). Nowadays, peak ground acceleration and response spectra, estimated from accelerograms recorded at different distances, are used.

Modern accelerometers record strong motion with three orthogonal components, two horizontal (usually for free field stations, N-S and E-W) and one vertical. A controversial point in handling acceleration data is how these two horizontal orthogonal components are combined. The geometric mean (GM) of the maximum values is usually used; the main reason is that GM produces less dispersion in the GMPEs. However, the orientation of recording accelerometers rarely captures the maximum intensities, which generally take place at an intermediate unknown orientation. This phenomenon is what we call *earthquake directionality effects*.

The directionality effect is related to the propagation direction of the earthquake energy. Imagine the following situation: an explosive source with radiation of totally spherical geometry, assuming a homogeneous and isotropic medium, and eight sensors located at the same radial distance (Figure 1). The sensors are oriented to the north. Although they are located at the same distance, they do not register the same accelerograms in their horizontal components (N-S and E-W). The sensors with their horizontal components in the radial direction and tangential to the circle with the centre at the location of the explosion would record all the ground motion in the radial component and none in the tangential (A, B, C and D). Instead, the sensors located at 45° from the source (E, F, G and H) register the same values in their two horizontal components (only varying the signs). This fact demonstrates the difficulty of defining an intensity measure directly from the as-recorded components. For this reason, Boore et al. (2006) analysed the dependence of the geometric mean with the orientation angle of the recording sensor, concluding that it is necessary to analyse large databases to establish orientation independent measures and recalculate the GMPEs with these new intensity measures. Thus, Figure 1 illustrates the directionality effect in the as-recorded seismic actions, mainly

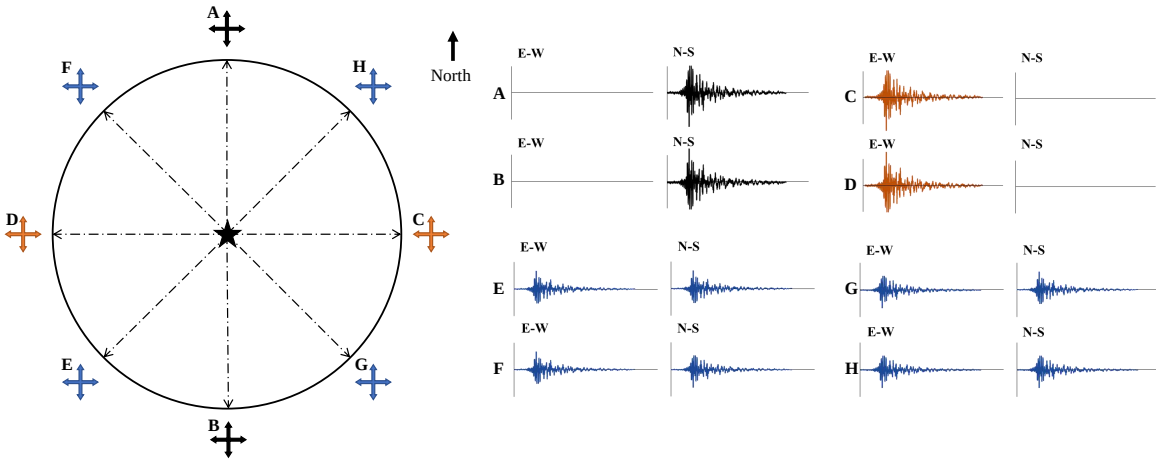

Figure 1: On the left a diagram showing an explosive source (star) with spherical radiation in a homogeneous and isotropic medium. Eight sensors are located at the same radial distance. On the right, the motion records in the two horizontal-orthogonal components of each sensor are shown.

A second important concern related to directionality effects is how those effects may influence the expected damage in a specific building, located at a precise site and, with definite azimuths of their two main geometrical axes. In this regard, former directionality studies in Spain were developed by Vargas-Alzate et al. (2018), who analysed ground motion records of the Lorca earthquake and detected the sensitivity of the expected damage in a building with respect to its spatial orientation.

They observed how buildings with similar characteristics, in the San Fernando neighbourhood, suffered different degrees of damage during the Lorca earthquake. This fact was attributed to the influence of the orientation of the buildings with respect to a near-source, highly polarized accelerogram. As an example, let us take again the case of Figure 1 and substitute the sensors with rectangular-shaped buildings, located at the same distance and facing the same direction (see Figure 2). Let us assume that these buildings have a strong axis with twice the stiffness of the weak axis. Surely, the buildings located to the north and south of the event (black buildings) will be more likely to suffer damage than the rest, because the component with the highest intensity hits the weak axis of the structure. For buildings located West and East, the strongest seismic action hits the strong axis, thus leading to a lesser expected damage grade.

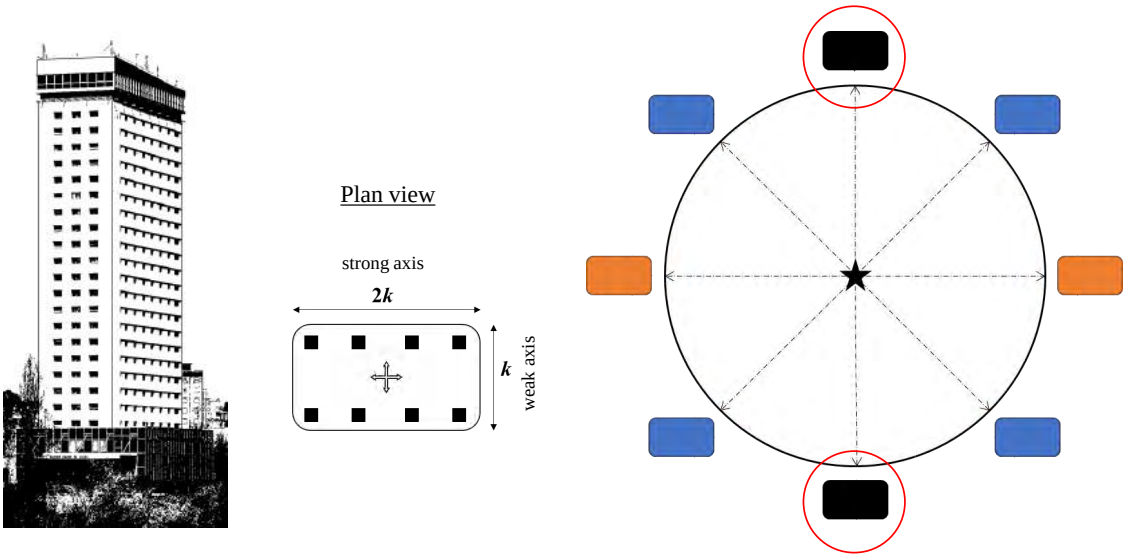

Figure 2: Scheme similar to Figure 1. Sensors are substituted by buildings facing the same direction and located at the same radial distance. Buildings have a strong axis ($2k$-EW) and a weak axis ($1k$-NS).The two buildings most likely to be damaged are marked with a red circle. In these cases the strongest action hits the weak axis of the building.

Local/site effects are other factors affecting the behaviour of building subjected to specific seismic actions. Resonance is an important factor to consider among the effects of local geology on the amplification of seismic action. Regarding local effects, specifically on-site effects due to local geology (Fatahi et al., 2014), soil response maps, particularly in urban environments, usually have low resolution and they may be biased because of limitations in the quantity and geometrical distribution of sampling points, for which reliable information is available. It is known that anomalies can occur due to underground aquifers and/or ravines and streams responsible for draining rainwater from the highlands to the plains in large cities, among other factors. These underground anomalies are very common in most modern cities, particularly in those with rivers that cross them, those that are built on coasts, or those that have both characteristics. Several examples of such cities in Spain, where seismic microzonation studies to evaluate site effects have been performed, are Malaga, Lorca, and Valencia (Goded et al., 2012; Navarro et al., 2014; Caselles et al., 2010), among others.

In Barcelona, seismic microzonation studies first began at the end of the 1990s and early 2000s. Initial research took advantage of existing geological maps and geotechnical soundings (Cid et al., 2001; Jiménez et al., 2000; Figueras et al., 1995). Data concerning H/V spectral ratios (Alfaro et al., 2001) were also used. As a result of a soil response modelling process, four homogeneous and regular soil zones

were defined in lines approximately parallel to the coast-line (Cid et al., 2001). Afterwards, Cadet et al. (2011) used all the available information and complemented it with new array measurements to characterize each zone by means of fundamental frequencies of soil layers and shear-wave velocity profiles. These authors proposed an average soil for each zone and a standard reference rock site.

1.2 Objectives

The initial main purpose of this PhD thesis concerned to directionality and soils effects, with relevant impacts on probabilistic seismic hazard analysis and seismic risk assessments. Along three years of intense research and study, appeared other seismic risk related issues that were considered worth of being analysed in some detail. This way, two other objectives were adopted: the first one is related to the soil-structure-interaction, while the second one is to propose a new intensity measure, which is related to the maximum inter-storey drift. Thus, accordingly, this dissertation has been divided in three main blocks: I) directionality effects, II) Soils effects, site classification and other seismic risk related issues and, III) other relevant contributions. Moreover, an important part of this research has been tackled by means of specific case-studies, which has allowed us to develop ad-hoc methods but, also to apply them. In the following, the general and specific objectives of each block are described.

1.2.1 Block I. Directionality effects

The chief purpose of this block has been to analyze and to assess directionality effects, such as they have been described above (section 1.1). Two related, but different, problems are included in this block: directionality in the expected seismic actions (see Figure 1) and expected seismic damage of a specific building hit by a concrete strong motion (see Figure 2). Let's refer to these two gross objectives as Block I.1 and Block I.2.

Concerning directionality in expected strong seismic actions (Block I.1), specific objectives have been the following:

1. Theoretical analysis of the problem.
2. Development of specific software and numerical tools to deal with the complexities of the massive analysis of strong motion databases.
3. Application to selected case studies. Namely, the Italian Accelerometric Archive (ITACA) and the Costa Rican Strong-Motion Database have been selected.

In relation to the expected seismic damage and risk for specific structures and buildings hit by a strong motion, (Block I.2), specific objectives have been as follows:

1. To analyze the problem from a theoretical and practical point of view.
2. To select and learn proper software packages for structural analyses.
3. Development of numerical tools and specific software to deal with the complexities of the problem; this is: structural modelling, non-linear static and dynamic analysis, selection and implementation of procedures to study the structural response, and so on.
4. Development of a predictive and expedite simplified method, allowing us to know the rotated ground motion, which will produce the maximum response of the structure.
5. Detailed analysis of selected case studies.

The methodological aspects to achieve those objectives are shown below, in the section devoted to methodology.

1.2.2 Block II. Soils' effects, site classification and other seismic risk related issues

Important challenges of this block have been, to improve the microzonation studies in Barcelona city and to apply horizontal-to-vertical spectral-ratios based methods to site classification of accelerometric stations (Block II.1). Moreover, as pointed out before, the dynamic soil-structure interaction, considering directionality effects and, the proposal of a new drift-correlated intensity measure, appeared as supplementary subjects deserving to be analyzed; These two new targets will be included in Block II.2.

Regarding microzonation studies in Barcelona city (Block II.1a), specific objectives have been:

1. To review previous studies and to collect existing information and data to set up a unified and georeferenced database concerning soils and residential buildings in Barcelona city.
2. To develop an improved microzonation map of soils, based on the compiled information and data.
3. To obtain a map with the fundamental periods of the buildings' stock.
4. To find zones of likely-increased seismic amplifications due to soil-structure resonance effects.

With respect to site classification of accelerometric stations (Block II.1b), particular objectives have been:

1. Revision of Horizontal-to-Vertical Spectral Ratio (HVSR) methods.
2. To analyze the influence of directionality effects in HVSR based methods.
3. Case studies. Accelerometric networks will be studied in detail.

With regard to Block II.2, specific goals of the analysis of the dynamic soil-structure interaction, considering directionality effects (Block II.2a) have been:

1. To search for simplified alternatives allowing to incorporate directionality effects in dynamic-soil-structure-interaction analyses (DSSI) by means of finite element (FE) methods.
2. The main goal is to identify, in advance, the angle that produces the maximum response of the soil structure system, for a given seismic action.
3. The assumption explored is that the incidence angle that generates the maximum value of an intensity measure (IM), at the top of the soil deposit (free-field), also would be the responsible one for the maximum response of the structure.
4. To use specific case studies to illustrate the advantages of the new method.

And, specific aims of search for a new, better drift-correlated, intensity measure (Block II.2b) have been:

1. To analyze the correlation between well-stablished, and often used, IMs with the maximum inter-story-drifts (MIDR).

2. To analyze the correlation between existing IMs and expected damage and, to search for new IMs with higher correlations.

3. To propose a new IM, which is highly correlated with MIDR and with expected damage.

1.2.3 Block III. Other relevant contribution

Only because of completeness and thoroughness, it has been considered appropriate to include, in this dissertation, other relevant contributions related to: i) simplified approaches to account for directionality effects on SSI analyses, ii) the case studies of two buildings severely damaged during the 2016 Ecuador and 2017 Mexico earthquakes and, iii) seismic site classification of the accelerometric stations of the Costa Rica strong motion network. The objectives of these three contributions are the same as the ones of Block II.2a, Block I.2, and Block II.1b, respectively. These contributions are included as appendixes in the document.

1.3 Methdology

In this section, the main methods and tools used in the research are described. The same scheme used for objectives is used for the methodological aspects; that is, methods referred to the three blocks in which this dissertation has been structured.

1.3.1 Block I. Directionality effects

Concerning directionality in expected strong seismic actions (Block I.1), the main methods, tools and tasks have been:

- Construction and preliminary statistical analysis of a unified database, for the study regions.
- Massive analysis of the strong-motion databases and detailed analysis of the as-recorded and rotated acceleration time histories. To do that, existing software has been adapted and a thorough program, in MATLAB platform, has been written.
- Development of a catalogue with metadata from the ground-motion records.
- Assessment, analysis and discussion of existing -dependent and orientation-independent intensity measures (Boore et al., 2006; Boore, 2010).
- Analysis and proposal of new orientation-independent intensity measures. These new measures are based on prior combination of acceleration time-histories.
- Comparison and discussion of the old and new IMs.
- Proposal of models for IMs ratios. To provide adequate corrections for former IMs, which were obtained without considering directionality effects, IM ratios have been obtained and modelled. These ratios allow us to update previous GMPEs in an easy and straightforward way.
- To publish and to give easy access to the Costa Rican strong-motion database. This database includes accelerograms from events recorded by the Earthquake Engineering Laboratory at the University of Costa Rica. The database consists of 2471 three-component accelerograms of 155 digitally recorded events and, it covers the last 20 years of measurements. New records are being incorporated to it.

In relation to the expected seismic damage and risk for specific structures (Block I.2), methods and tools have been:

- Building's selection.
- Search of existing software packages for structural analysis and choice of the most appropriate for the objectives of the study. The building is then modelled and analyzed.
- Selection and analysis of the seismic actions.
- Nonlinear dynamic analysis (NLDA). The orientation of the building is rotated with respect to the seismic action. Peak response parameters, base shear and roof displacement are carefully analyzed as functions of the orientation angle.
- Proposal of a simplified rotational approach to incorporate directionality effects in the analyses.
- Comparison of the results coming from the simplified approach with the ones of the complete rotational procedure.
- Moreover, in several cases, the influence of the significant duration on the expected damage of buildings, has been also investigated through time-history analyses.

1.3.2 Block II. Soils effects, site classification and other seismic risk related issues

Regarding microzonation studies in Barcelona city (Block II.1a), methods and tools have been:

Concerning soils.

- To collect as much as available information and data on the soils of the city.
- To set up a GIS system to manage the information concerning soils.
- To set up and improves microzonation map for soils in Barcelona city.

Concerning buildings.

- To collect as much as available information and data on residential buildings of the city.
- To set up a GIS system to manage the information concerning buildings.
- To review empirical equations and formulae allowing to estimate, in an expedite and simplified way, the fundamental periods of the building's response. The equation provided by the Eurocode 8, has been the preferred one.
- To set up a new map with the geographical distribution of periods.

Concerning soil-building resonance.

- To cross microzonation amplification periods and buildings response fundamental periods.
- To depict a map with likely increased amplification, due to resonance effect.

With respect to site classification of accelerometric stations (Block II.1b), the methodology to achieve the specific objectives has been as follows:

- Massive analyses of the strong motion databases.
- Detailed analyses of the spectral ratio HVSR of the 5% damped response spectra.

- Analysis of the likely directionality effects on the HVSR.
- Comparison of spectral amplification shapes with the ones obtained by other researchers and with design spectra provided in the Eurocode 8 for different soil types.
- Allocation of a site class to each accelerometric station, based on the HVSR shape and according to a classification pattern.

Methodological issues regarding to analysis of the dynamic soil-structure interaction, considering directionality effects (Block II.2a) have been:

- To search for an adequate and simplified soil-building models.
- Development of soil-structure 2D models.
- Simplified structural models have been developed for the building.
- Soils and foundations of the buildings have been modelled by means of finite elements (FE) based methods.
- The Plaxis 2D software (Brinkgreve et al., 2017), has been preferred for the SSI analysis.
- Selection of proper seismic actions.
- Directionality effects have been investigated by means of completed (CRA) and simplified rotational approaches (SRA), thus allowing to establish the advantages of the simplified approach.

Finally, the main methods and tools for the search of a new and better-drift-correlated intensity measure (Block II.2b) are described.

- Review of the often-used ground motion intensity measures.
- Selection of low- mid- and high-rise steel buildings, having 3, 7 and 13 stories respectively.
- These 3 steel buildings were modelled as 2D framed structures. Available structural analysis software was used.
- Forty accelerograms (two horizontal components each) were selected from the Italian database (ITACA).
- Then, a suite of 720 nonlinear dynamic analyses were performed. This number of NLDA correspond to 3 buildings (80 as recorded accelerograms + 80 scaled accelerograms + 80 matched acceleration time histories). The as recorded accelerograms were scaled to 700 cm/s^2. The target spectrum for matching was the EC-08 design spectrum for soil type A (rock site) and great earthquakes (type I, $M > 5.5$).
- Proposal of the new intensity measure. Computation of the IMs tested and of the new proposed one.
- Correlation analysis and discussion of the obtained results.
- Probabilistic validation of the robustness and appropriateness of the new intensity measure.

1.3.3 Block III. other relevant contributions

Concerning the contributions included in this block recall that they are linked to Block II.2a, Block I.2, and Block II.1b, therefore the methods and tools used are the ones listed and described in sections 1.3.1 and 1.3.2.

1.4 Thesis layout

This research has produced a number of relevant scientific contributions and papers. In addition to several research reports and contributions to relevant scientific and/or technical meetings and conferences, a total of eight, peer reviewed articles, have been published in high impact journals, indexed in the expanded science citation indexes (SCI) [see also the master journal list (MJL) in the web of science group[1]]. To take advantage of these contributions, the format of article-based-thesis[2] has been chosen.

Main subjects have been: i) directionality effects, both in the seismic actions and in the expected damage of buildings, ii) soils' effects in urban areas and site classification of accelerometric stations and iii) other seismic-risk-related relevant contributions. The document has nine chapters and six appendixes. Table 2 and Figure 3 summarize the structure of the PhD dissertation; for easy reading and clarity a colour key is used to identify these main issues.

After this introduction (Chapter 1), Chapter 2 is an accurate study of directionality in Italy (Pinzón et al., 2018b), concerning the expected seismic actions. Chapter 3 (Moya-Fernández et al., 2020) describes a research, done during a recent stay of the author of this PhD thesis, in the Earthquake Engineering Laboratory (Laboratorio de Ingeniería Sismica, LIS) of the University of Costa Rica (UCR), concerning to the strong motion database of this country. Chapter 4 introduces the directionality effects in the expected damage in structures and buildings (Pinzón et al., 2019a); note that in Appendix A several tables which supplement Chapter 4 are included. Two interesting case studies related to the anomalous damage observed in specific buildings during earthquakes are shown in Appendixes C , E (Pinzón et al., 2018a) and F (Pinzón et al., 2020b). Chapter 5 and Chapter 6 are devoted, respectively, to soils' effects in Barcelona (Pinzón et al., 2019d) and to site classifications for accelerometric stations (Pinzón et al., 2019c); note that the site classification for accelerometric stations in Costa Rica is included in Appendix D. Chapter 7 (Pinzón et al., 2020a) and Appendix B (Pinzón et al., 2019b) are devoted to analyze directionality effects in the dynamic soil-structure interactions. Moreover, a very interesting finding, in our view, along the development of this work, concerning to a new drift-correlated ground motion intensity measure (Pinzón et al., 2020c) has been included in Chapter 8. The last chapter (Chapter 9) is devoted to discussion, conclusions and suggestions for forward research and developments.

[1]WOSG (2020) mjl.clarivate.com/ (last accessed June 4, 2020)
[2]UPC (2020) doctorat.upc.edu/en/thesis/the-doctoral-thesis (last accessed June 4, 2020).

Table 2: PhD dissertation layout.

PhD Thesis Scheme

	Chap. 1	Introduction	
Block I	**Chap. 2**	Directionality models from ground motions of Italy	Pinzón et al. (2018). Ingegneria Sismica, 35(3), 43-63.
Block I	**Chap. 3**	A strong-motion database of Costa Rica: 20 years of digital records	Moya-Fernández, Pinzón et al. (2020). SRL (under-review).
Block I	**Chap. 4**	An efficient method for considering the directionality effect of earthquakes on structures	Pinzón et al. (2019). JEE, (online first).
Block II	**Chap. 5**	Increased seismic hazard in Barcelona (Spain) due to soil-building resonance effects	Pinzón et al. (2019). SDEE, 117, 245–250.
Block II	**Chap. 6**	Seismic site classification from the horizontal-to-vertical response spectral ratios: use of the Spanish strong motion database	Pinzón et al. (2019). Geosciences, 9(7), 294.
Block II	**Chap. 7**	Dynamic soil-structure interaction analyses considering directionality effects	Pinzón et al. (2020). SDEE 130, 106009.
Block II	**Chap. 8**	A drift-correlated ground motion intensity measure: application to steel frame buildings	Pinzón et al. (2020). SDEE 132, 106096.
	Chap. 9	Discussion and conclusions	
	App. A	Chapter 4 Tables	
Block III	**App. B**	A simplified approach to account for directionality effects on 2D dynamic soil-structure interaction analysis	7th Int. Conf. on Earthquake Geotechnical Engineering, Rome, Italy.
Block III	**App. C**	Case study of a heavily-damaged building during the 2016 Mw 7.8 Ecuador earthquake: Directionality effects in seismic actions and damage assessment	To be submitted.
Block III	**App. D**	Seismic site classification of the Costa Rican Strong-Motion Network based on V_{S30} measurements and site fundamental period	Internal report. Earthquake Engineering Laboratory, University of Costa Rica.
Block III	**App. E**	Do Directionality Effects Influence Expected Damage? A Case Study of the 2017 Central Mexico Earthquake	Pinzón et al. (2018). BSSA, 108(5A), 2543-2555.
Block III	**App. F**	Reply to "Comment on 'Do Directionality Effects Influence Expected Damage? A Case Study of the 2017 Central Mexico Earthquake' by Luis A. Pinzón, Luis G. Pujades, Sergio A. Diaz, and Rodrigo E. Alva" by Eduardo Reinoso, Pablo Quinde, Danny Arroyo, Mario Ordaz, and Amador Terán-Gilmore	Pinzón et al. (2018). BSSA, 110(1), 393-396.

Colors' key

- Directionality effects in seismic actions and in PSHA
- Directionality effects in the damage expected on buildings
- Local soils' and sites' response
- Soil-Structure interaction and other risk related issues

PhD Thesis Scheme

Block I. Directionality effects

In expected seismic actions		In damaged buildings
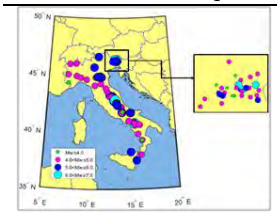	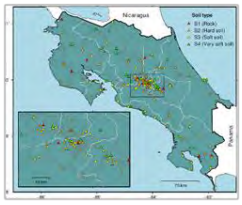	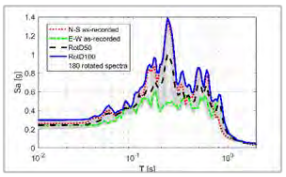
Chapter 2	**Chapter 3**	**Chapter 4**
Directionality in Italy	Str. Mot. in Costa Rica	Effects on structures
Pinzón et al. (2018b)	Moya, Pinzón et al. (2020)	Pinzón et al. (2019a)
Ingeg. sismica, 35(3)	*SRL (under rev.)*	*JEE (online first)*

Block II. Soils, site and other seismic risk related issues

Soil's and site effects		Other risk related issues	
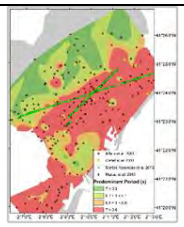	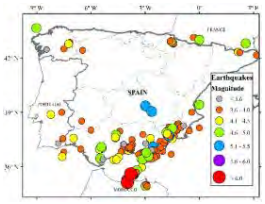	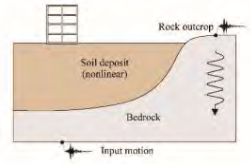	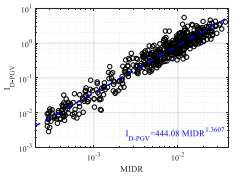
Chapter 5	**Chapter 6**	**Chapter 7**	**Chapter 8**
Resonance in Barcelona	Sites classific. (Spain)	Soil-struct. interaction	Drift-correlated GMIM
Pinzón et al. (2019d)	Pinzón et al. (2019c)	Pinzón, Mánica et al. (2020)	Pinzón, Vargas et al. (2020)
SDEE 117	*Geosciences 9(7)*	*SDEE 130*	*SDEE 132*

Block III. Other relevant contributions. (Suppl. material)

Soil-structure int.	Directionality	Site classification	Directionality
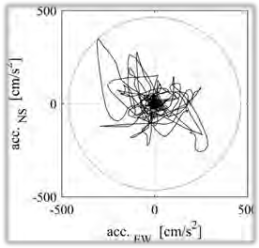	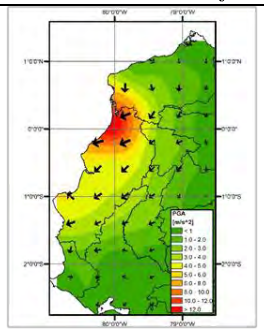	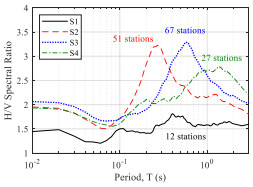	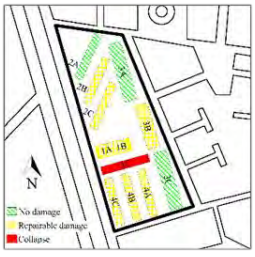
Appendix B	**Appendix C**	**Appendix D**	**Appendices E & F**
A simpl. App. for SSI	2016 Ecuador earthquake	Sites class. (Costa Rica)	2017 Mex. Earthquake
Pinzón et al. (2019b)	Pinzón, Pujades et al. (2020)	Pinzón, Hidalgo et al. (2020)	Pinzón et al. (2018a)
17th ICEGE- Rome	*To be submitted*	*LIS-UCR report*	*BSSA 108(5A) & 110(1)*

Figure 3: PhD dissertation layout. See also Table 2

1.5 Brief summary of chapters

With the aim of providing the reader with a quick screening of the main contents of this PhD dissertation, a brief summary of each chapter is provided.

Chapter 1

Introduction

The backgrounds, objectives and methods are described in this chapter. Also, a detailed view of the dissertation layout is given, so that the reader may have a rapid screening of the PhD thesis.

Chapter 2

Directionality models from ground motions of Italy (Pinzón et al., 2018b).

In this chapter, the directionality effects on the expected strong ground motion in Italy are investigated. After a brief description of the directionality effect and the intensity measures involved, a wide Italian database of strong ground motion records is used. 949 horizontal accelerograms (two components) are used in the analyses, which are performed for 5% damped response spectra in the 0.01–4 s period range. Rotation-independent intensity measures, resulting from combining maximum values of the as-recorded accelerograms, are investigated. An interesting novelty is that the study has also been performed using maximum values of the time histories resulting from the previous combination of the as-recorded time histories. Ratios between these rotation-independent intensity measures and those formerly used in ground motion predictive equations have been computed and modelled by means of a simple theoretical model. Thus, the results are useful for updating former strong ground motion predictive equations in a simple and straightforward way.

Chapter 3

A strong-motion database of Costa Rica: 20 years of digital records (Moya-Fernández et al., 2020).

In this chapter, a strong-motion database from earthquakes recorded by the Earthquake Engineering Laboratory at the University of Costa Rica is presented. The database consists of 2471 three-component accelerograms from 155 digitally recorded events. It covers the last 20 years of measurements, including records from the Nicoya earthquake of M_W 7.6 on 2012 September 5. The engineering and seismological communities can use this data either to conduct new research or to improve seismic or hazard studies in the region. A catalogue is also available with metadata of each record containing several intensity measures from the ground-motion time-histories.

Chapter 4

An efficient method for considering the directionality effects of earthquakes on structures (Pinzón et al., 2019a).

Recent research has proven the importance of considering the directionality effects on the expected seismic damage of structures. However, to analyse such effects in detail, usually demands a high computational effort, in particular when nonlinear dynamic analysis (NLDA) is used to estimate the seismic response. This section presents a simplified approach to obtain peak response parameters for a building subjected to ground motions considering the directionality effect. To do so, the maximum and median response spectra, considering all the non-redundant response spectra, of several ground motion pairs are calculated. Afterwards, a spectral matching technique is applied to these spectra and new acceleration components are obtained. A series of NLDA are performed with these new components and the roof displacement and base shear values are calculated. These results are compared with the maximum and median values, calculated by performing a series of NLDA, after rotating the earthquake records by considering increments of 1° in the interval 0°–180°. The results agree with both approaches validating the efficiency of the simplified proposed approach.

Chapter 5

Increased seismic hazard in Barcelona (Spain) due to soil-building resonance effects (Pinzón et al., 2019d).

In this section, previous microzonation studies in Barcelona (Spain) were revisited, and available data on the predominant periods of soils in the city were compiled to develop an updated microzonation map of the city. In addition, the buildings' database was updated and used to create a map of buildings' fundamental periods. The crossing of soil predominant period and buildings' fundamental period map led to the detection of areas in which resonance phenomena and, indeed, increased amplification of the structural response, is expected. Thus, zones of Barcelona were identified in which the seismic hazard would be greater due to resonance effects. The improved microzonation maps and the detection of soil-building resonance areas contribute significantly to enhanced precision and awareness of seismic hazard and risk in Barcelona.

Chapter 6

Seismic site classification from the horizontal-to-vertical response spectral ratios: use of the Spanish strong motion database (Pinzón et al., 2019c).

Normally, the average of the horizontal-to-vertical (H/V) ratios of the 5% damped response spectra of ground motions is used to classify the site of strong-motion stations. In these cases, only the three-orthogonal as-recorded acceleration components are used in the analysis, and all the vector compositions that can generate a different response for each period oscillator are excluded. In this study, the Spanish strong-motion database was used to classify the sites of accelerometric stations based on the predominant periods through the average horizontal-to-vertical spectral ratios (HVSR) of recorded ground motions. Moreover, the directionality effects, using the vector composition of the horizontal components of ground motions, were also considered in the estimations of H/V ratios. This consideration is a relevant novelty compared to the traditional H/V ratio-based methods. Only earthquakes with magnitudes above 3.5 and hypocentral distances below 200 km were selected, which resulted in 692 ground-motion records, corresponding to 86 stations, from events in the time period between 1993 and 2017. After the analysis, a predominant-period site classification was assigned to each station. On the whole, the obtained mean and standard deviation values of the spectral ratios are comparable to those shown by other researchers. Therefore, the advantages of the proposed procedure, which takes the directionality effects into account, can be summarized as follows: (a) The obtained information is richer and enables more sophisticated and realistic analyses on the basis of percentiles and (b) it is easier to detect anomalous stations, sites, and/or accelerograms. Moreover, the method eliminates the effect of directionality as a contributor to epistemic uncertainty.

Chapter 7

Dynamic soil-structure interaction analyses considering directionality effects (Pinzón et al., 2020a).

In this chapter the directionality effects of ground motions in the context of dynamic soil- structure interaction analyses are investigated. The problem addressed corresponds to a nonlinear soil deposit, overlaying firm ground, where the input motion was derived from acceleration time history recorded at a rock outcrop. A simplified procedure is proposed to incorporate directionality effects. The main objective is to identify beforehand the incidence angle producing the maximum response of a structure for a given earthquake. Results from the simplified procedure were evaluated by comparison with what is called here the complete rotational approach, where the behaviour of the structure, as a function of the incidence angle of the input motion, is derived through a large number of nonlinear dynamic soil-structure interaction analyses.

Chapter 8

A drift-correlated ground motion intensity measure: application to steel frame buildings (Pinzón et al., 2020c).

Estimations of seismic risk in urban areas should include quantification of the expected damage to civil structures subjected to earthquakes. In buildings, this quantification depends on the maximum inter-story drift (MIDR), among other aspects. In this chapter, the correlation between several intensity measures (IMs) and the maximum inter-story drift of steel structures was investigated. Three steel frame buildings of 3, 7 and 13 stories were used as a testbed. These buildings were modelled as 2D framed structures. For the seismic hazard, forty strong ground motion pairs were selected (80 individual horizontal components) from the Italian database. These records were scaled to a specific peak ground acceleration (PGA) and matched to a design spectrum from Eurocode 8. Nonlinear dynamic analysis was used to estimate the seismic response of the structures. Thus, 720 nonlinear dynamic analyses (NLDA) were performed [3 structures (80 as recorded accelerograms + 80 scaled records + 80 matched records)]. Preliminary results indicate that PGA show the worst correlation with MIDR. A higher correlation was observed for peak ground velocity, root-mean-square velocity and specific energy density intensity-based measures. Finally, a new IM, which is highly correlated with MIDR, is proposed. This IM is called $I_{\Delta-PGV}$ and considers both the PGV and the significant duration.

Chapter 9

Discussion and conclusions.

In this last chapter the results got in the researches shown are discussed and the main conclusions, coming from these results, are outlined and highlighted. Also several recommendations for ongoing and future research are provided. These recommendations come from the learned lessons and from the what the author believes may be promising and fruitful research lines.

Appendixes

Six appendixes close the document (see also Table 2 and Figure 3). **Appendix A** collects supplementary material for Chapter 4, mainly tables. **Appendix B** describes a simplified procedure to account for directionality effects on soil-structure interaction analysis (Pinzón et al., 2019b); **Appendixes C**, **E** (Pinzón et al., 2018a) and **F** (Pinzón et al., 2020b), respectively, are case studies corresponding to damaged buildings during the 2016 Ecuador and 2017 Mexico earthquakes; those anomalous damages were attributed to the azimuthal orientation of buildings with respect to the strong motions in the site. **Appendix D** describes a recent work related to the seismic site classification of the accelerometric stations of the Costa Rica strong motion network.

2 Directionality models from ground motions of Italy

Based on the published article: Pinzón, L. A., Pujades, L. G, Hidalgo-Leiva, D. A., & Díaz, S. A. (2018). Directionality models from ground motions of Italy. *Ingegneria Sismica, 35*(3), 43–63.
Journal URL: ingegneriasismica.org/directionality-models-from-ground-motions-of-italy
FUTUR UPC URL: futur.upc.edu/23504584

2.1 Abstract

Directionality effects on the expected strong ground motion in Italy are investigated. After a brief description of the directionality effect and the intensity measures involved, a wide Italian database[3] of strong ground motion records is used, with a total of 949 horizontal accelerograms (two components). The analysis is performed for 5% damped response spectra in the 0.01–4 s period range. Rotation-independent intensity measures, resulting from combining maximum values of the as-recorded accelerograms, are investigated. The study has also been performed using maximum values of the time histories resulting from the previous combination of as-recorded time histories. Ratios between these rotation-independent intensity measures and those formerly used in ground motion predictive equations have been computed and modelled by means of a simple theoretical model. Thus, the results are useful for updating former strong ground motion predictive equations in a simple and straightforward way.

2.2 Introduction

Most ground motion prediction equations (GMPE) use as intensity measures (IMs) the peak ground acceleration and the 5% damped spectral response of a single degree of freedom (SDOF) system corresponding to the as-recorded horizontal ground motions (Beyer and Bommer, 2006; Douglas, 2017). Moreover, there are many ways to combine the peak values of these two as-recorded horizontal components in the GMPEs (Douglas, 2003): the arithmetic mean (AM), the geometric mean (GM), or the largest value of both components (Largest) are three of them. The GM of the response spectra is the most commonly used IM. An advantage of the GM is that the variability of the results of regressions used in the GMPEs is lower than with other measures (Beyer and Bommer, 2006). However, the GM of the response spectra have a potentially significant drawback: they are not invariant to sensor orientation. Therefore, these measures differ for the same ground strong motion depending on the orientation of the recording instrument.

As an extreme case, let us consider a noise-free, polarized signal. If one of the sensors is aligned with the direction of polarization, the GM of the response spectra of the as-recorded ground motion would be zero (Boore et al., 2006). This is an essential consideration for near-fault records. In these cases, the rupture orientation and the radiation pattern, including directivity effects, can produce strong motions correlated for 1 s or for longer periods (Spudich et al., 2004). The directionality effects are present, more or less significantly, in any pair of strong ground motion records (Pinzón et al., 2018a).

For these reasons, various sensor orientation-independent measures have been proposed, including: GMRotDpp, GMRotIpp, RotDpp, and RotIpp (Boore et al., 2006; Boore, 2010). In these measures "GM" means geometric mean, "Rot" means rotation, letters D and I indicate dependent and independent of the period, and "pp" represents the percentile. Generally, the 50th percentile is used in GMPEs. By using these new measures, the sensor orientation effect is eliminated as a component of epistemic uncertainty. This correction may be important in assessments of the probabilistic seismic

[3]Italian Accelerometric Archive (ITACA): http://itaca.mi.ingv.it/ItacaNet/ (last accessed 26 May 2017)

risk due to ground motions with long return periods (Bommer et al., 2004). Moreover, in determinations of IMs, the maximum values of two time histories are usually combined, thus mixing up peak values that normally occur at different time instants, leading to meaningless and biased results.

The main purpose of this study is to assess ground-motion directionality effects in Italy. To this end, the Italian Accelerometric Archive (ITACA) will be used. Another goal is to propose new sensor orientation-independent IMs, which are based on the maximum values of the time history obtained by combining the two horizontal components, rather than on the combination of the two maximum values of each component. These new IMs will be called LRotDpp for the Larger measure, and mpGM, mpGMRotDpp, and mpGMRotIpp for the IMs involving geometric mean values as defined above. Finally, to provide adequate corrections for former IMs, which were obtained without considering directionality effects, IM ratios will be obtained and modelled. These ratios will allow us to update previous GMPEs in an easy and straightforward way.

However, because of the number and involvedness of the IMs in this study, first a specific section is devoted to clearly describing these quantities and explaining how they are computed for a single time histories pair.

2.3 Time histories

In this section, the main ways of considering time histories in directionality analyses are summarized and briefly described.

2.3.1 As-recorded time histories

Usually, accelerometric stations are equipped with three orthogonal sensors, EW, NS and Z. Generally, only the two horizontal components are used in probabilistic seismic hazard analysis (PSHA), seismic design, and seismic risk assessment. These time histories can come also from instrumented buildings or civil facilities such as bridges or nuclear power plants. In these cases, the orientation of the sensors is often linked to the geometry of the instrumented structure, and transversal and longitudinal sensors are frequently used. Two horizontal accelerograms, EW and NS components, recorded at the station T1213 are used as examples of acceleration time histories. The records correspond to the Central Italy, M_W=6.5, Umbria earthquake, which occurred on 30 October 2016 at 06:40:18 (INGV 2016). Data have been downloaded from the ITACA strong motion database and are provided with the baseline removed (Pacor et al., 2011). These EW and NS as-recorded time histories and their amplitude Fourier spectra are shown in Figure 4.

2.3.2 Response time histories

Many seismic design and seismic risk assessment methodologies are based on the response of single degree of freedom (SDOF) systems. Maximum values of the responses lead to response spectra. The equation of motion of an SDOF system, with a mass m, moving on a frictionless surface, driven by horizontal ground motion with acceleration $\ddot{U}(t)$, with a spring with stiffness k, and a dashpot with a coefficient of viscous damping c is (Chopra, 2017; Douglas, 2003):

$$\ddot{u}(t) + 2\xi\omega\dot{u}(t) + \omega^2 u(t) = -\ddot{U}(t) \tag{1}$$

In this equation, ξ is the fraction of critical damping of the system, ξ=$c/(2\omega \mathrm{m})$, and T is the period of the SDOF vibrating system, T=$2\pi/\omega$. $acc(t)$=$\ddot{u}(t)$+$\ddot{U}(t)$ is the absolute acceleration response, $\ddot{u}$(t), $\dot{u}(t)$ and $u(t)$ are the relative acceleration, velocity and displacement responses, respectively. Typical

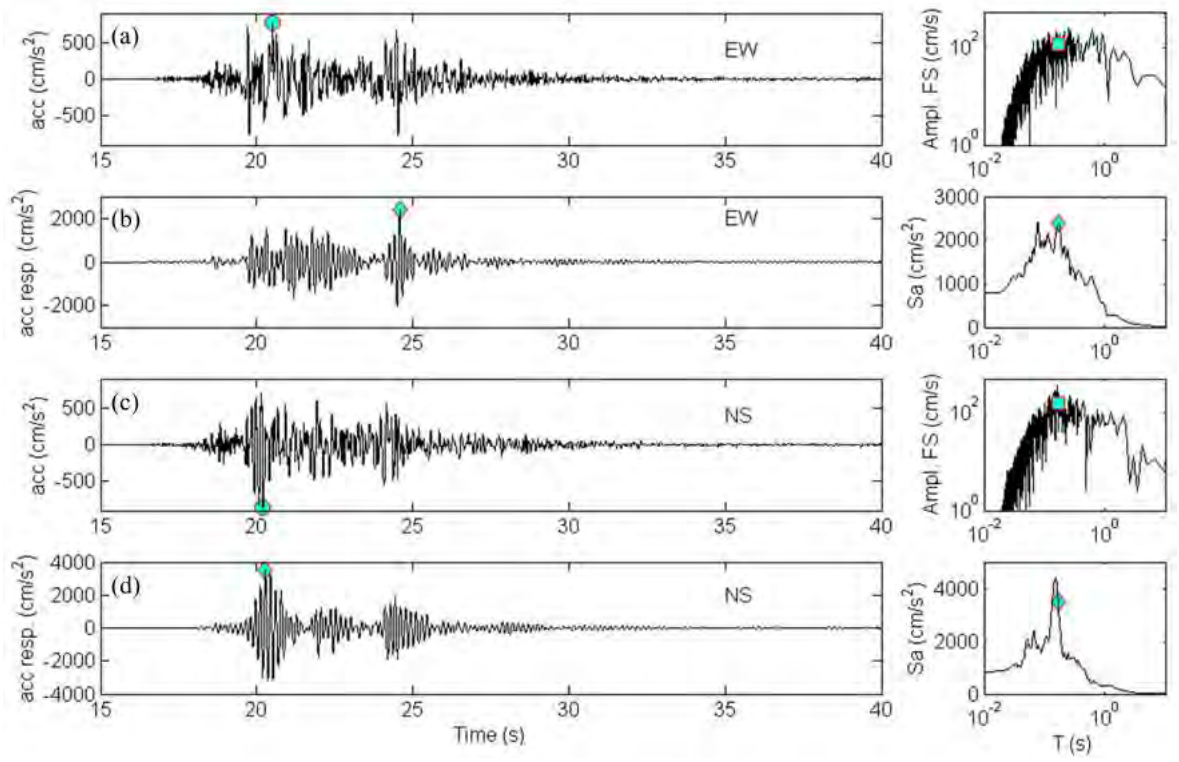

Figure 4: As-recorded EW (a) and NS (c) accelerograms in the time and frequency domains. 5% damped acceleration responses for T=0.17 and 5% damped acceleration response spectra, Sa (T), for the EW (b) and NS (d) registers. The 0.17 s period is marked in the Fourier and response spectra, and maximum values are marked in the time histories.

ξ values for buildings are in the range of [0.01 0.2] and typical periods are in the range of [0.1 10]s. Because different periods and damping values are involved in seismic design and in damage and risk assessments, $\ddot{u}(t)$ and, therefore, $acc(t)$, $\dot{u}(t)$ and $u(t)$ really depend on the damping ratio, ξ, and the period, T. Maximum values of these responses define the well-known acceleration, velocity, and displacement response spectra; that is:

$$Sa(T,\xi) = max\left|\ddot{u}(t,T,\xi) + \ddot{U}(t)\right|_{for\ t} = max\left|acc(t,T,\xi)\right|_{for\ t} \tag{2}$$

$$Sv(T,\xi) = max\left|\dot{u}(t,T,\xi)\right|_{for\ t} \tag{3}$$

$$Sd(T,\xi) = max\left|u(t,T,\xi)\right|_{for\ t} \tag{4}$$

For T=0, these values are known as peak ground acceleration (PGA), peak ground velocity (PGV), and peak ground displacement (PGD). PGA, PGV and PGD are ξ-independent. The 5% damped acceleration response spectra have been computed for the accelerograms shown in Figure 4. In addition, the acceleration responses of an SDOF system with ξ=0.05, 5% of critical damping, and ξ=0.17 s, have also been computed. The Nigam and Jennings method (Nigam and Jennings, 1969) has been used to compute responses and response spectra. For this case study, Figure 4 also displays the acceleration response time histories for a 5% damped SDOF system with a period T=0.17 s. The 0.17 s period is marked in the amplitude Fourier spectra and in the response spectra. Peak values are also marked

in the corresponding time histories. Table 3 shows these peak values and the time instants at which they are attained.

Table 3: Maximum values and times at which they are attained for the EW and NS as-recorded accelerograms and acceleration responses of a 5% damped SDOF system with a period of 0.17 s. (See Figure 4).

Period	EW as-recorded component		NS as-recorded component	
	max (cm/s^2)	t$_{max}$ (s)	max (cm/s^2)	t$_{max}$ (s)
T=0.00 s	760	20.51	-850	20.21
T=0.17 s	2254	24.58	3452	20.27

2.4 Directionality analysis

In engineering seismology and earthquake engineering, GMPE and design specifications have been based on maximum or peak values of as-recorded strong motion. The point is how the two peak values, coming from two orthogonal accelerograms, are obtained and, mainly, how they are combined in a rational way. Clearly, strong dependence on the azimuth of the recording sensors is expected, and it is convenient to define rotation-independent measures. In this section these issues are tackled. The most common ways of quantifying peak values and response spectra are described and new ways of dealing with peak values with more physical sense are investigated.

2.4.1 Rotated (Rot) time histories

It is well-known that as-recoded time histories strongly depend on the orientation of the sensor. This may be critical for polarized strong motions. Rotated time histories corresponding to the combination of two as-recorded time histories are the time histories that would have been recorded by seismic sensors rotated by an angle, θ. Rotated time histories, $acc_1(t,\theta,T,\xi)$ and $acc_2(t,\theta,T,\xi)$ of the acceleration responses $acc_1(t,0,T,\xi)$ and acc_2 $(t,0,T,\xi)$ of the as-recorded time histories are obtained according to the following equations:

$$acc_1(t,\theta,T,\xi) = acc_1(t,0,T,\xi)\cdot cos\theta + acc_2(,t,0,T,\xi)\cdot sin\theta \tag{5}$$

$$acc_2(t,\theta,T,\xi) = -acc_1(t,0,T,\xi)\cdot sin\theta + acc_2(,t,0,T,\xi)\cdot cos\theta \tag{6}$$

Usually, $acc_1(t,0,0,0)$ and $acc_2(t,0,0,0)$ are the as-recorded EW and NS accelerograms. Rot-time-histories of responses may be obtained in the same way. In some cases, it may be useful to analyze only one of the two Rot orthogonal time histories, that is $acc_1(t,0,T,\xi)$ or $acc_2(t,0,T,\xi)$. For reasons of symmetry, in these cases, θ-angles are considered in the range between 0 and 180^o. When the two components are analyzed, the angle range between 0 and 90^o is sufficient.

2.4.2 Peak values and IMs

To see how maximum values vary with the orientation of the recording accelerographs, Figure 5a shows the peak values, PGAs, and the time instants at which they are achieved as functions of the angle, θ. Figure 5b shows the maximum values (Sa) of the responses of a 5% damped SDOF system with period T=0.17 s. Maximum values of the two orthogonal components are attained at different time instants. Differences in the order of 5 s may occur in this case.

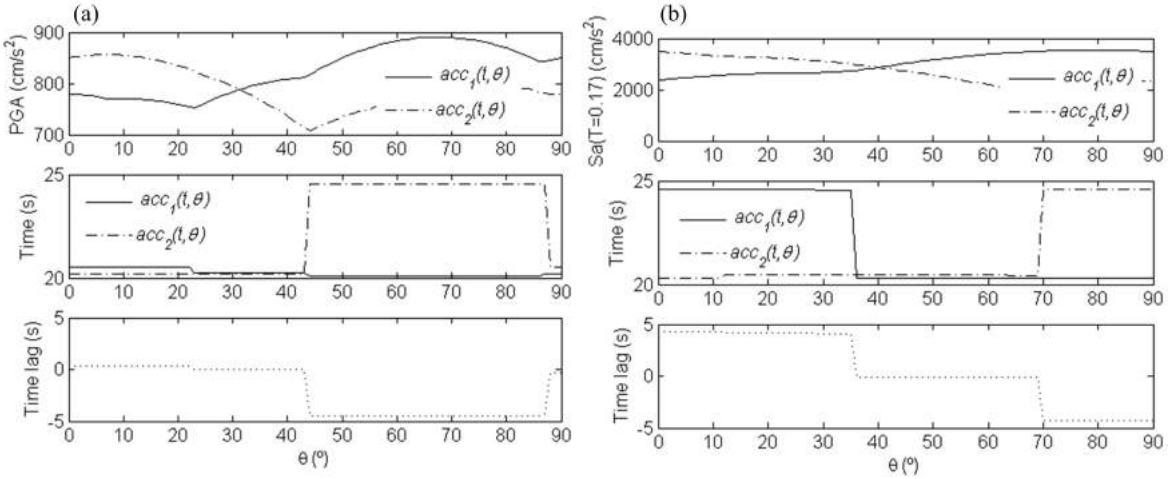

Figure 5: (a) Maximum values of the rotated accelerograms; the corresponding time arrivals (middle) and time lags (down) are also depicted. (b) Same as (a) for the responses of the rotated accelerograms for a 5% damped SDOF system with T=0.17 s. See also Figure 4.

There are several ways of combining peak values to obtain two component based intensity measures. The main IMs involved in the assessment of seismic directionality effects are described in this section. The geometric mean (GM) and the vector composition (VC) of the maximum values are discussed below. Note that, often these IMs could not be attained in real cases, because the maximum quantities involved are not concurrent, so their physical meaning is poor. However, it is also true that statistically average or median values of GM and VC may be adequate for representing expected IMs. In this study, an alternative way of obtaining maximum values is also considered. The idea is to combine the time histories and then determine the maximum values of the resulting time histories. This way, maximum values would correspond to a specific time instant. The following equations are used for pGM and pVC combinations:

$$pGM(t,\theta,T,\xi) = |acc_1(t,\theta,T,\xi) \cdot acc_2(t,\theta,T,\xi)|^{1/2} \tag{7}$$

$$pVC(t,\theta,T,\xi) = \left[acc_1^2(t,\theta,T,\xi) + acc_2^2(t,\theta,T,\xi)\right]^{1/2} \tag{8}$$

p means prior combination of the time histories. Figure 6a shows the case of the two as-recorded signals presented in Figure 4. The third and fourth graphs show pGM and pVC respectively. The acceleration responses of the 5% damped SDOF system with a period of 0.17 s are combined in the same way in Figure 6b. In these figures, the maximum values, now called mpGM and mpVC, are also displayed. In the cases of pGM and pVC, GM and VC are displayed (blue squared markers) in the time histories.

Now the two as-recorded signals are rotated, and the maximum values described above are computed. These four peak values, mpGM, mpVC, GM, and VC, are shown in Figure 7 as functions of the rotation angle. Because of the symmetry of the rotated components, only the θ-range between 0 and 90º is shown. It can be observed how mpVC is θ-invariant; GM and VC are greater than mpGM and mpVC respectively. However, GM has been widely used to develop strong ground motion predictive equations (Douglas, 2017) in PSHA, because less dispersion is obtained and, of course, they may lead to good average estimates. However, it is important to consider that, in deterministic studies, both GM and VC have little physical sense. Hence, the new quantities mpGM and mpVC will be analysed in this study.

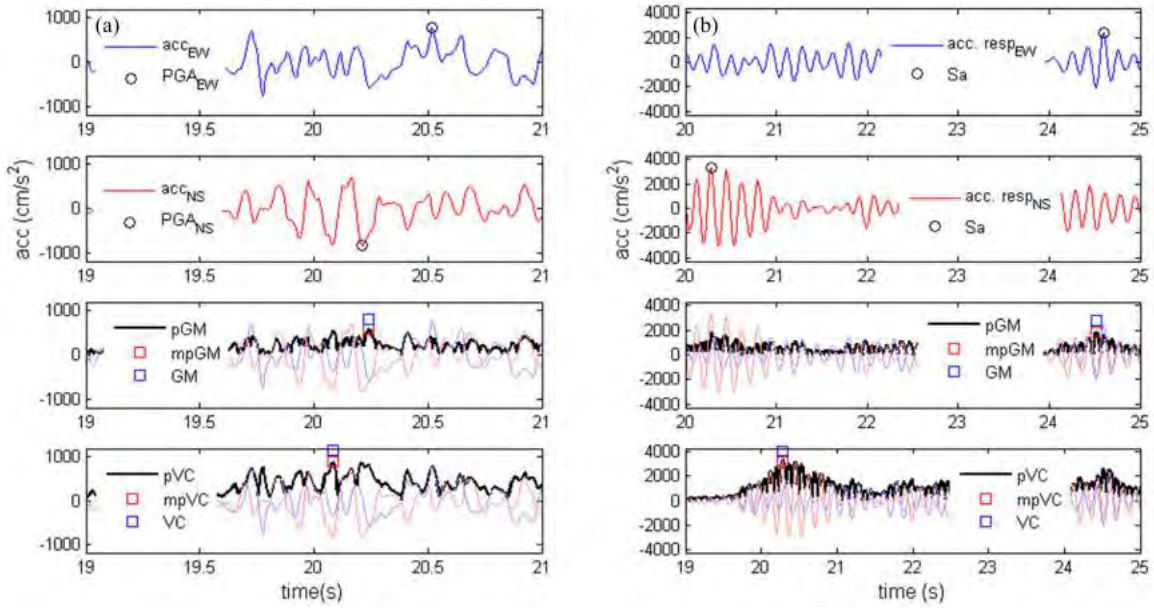

Figure 6: (a) As-recorded accelerograms, pGM and pVC compositions; maximum values, PGA, mpGM and mpVC are marked. GM and VC are also shown. (b) Same as (a) but for the acceleration responses of a 5% damped SDOF system with a period of 0.17 s.

2.4.3 Rotation dependent (RotD) and independent (RotI)

To introduce rotation-dependent (RotD) and rotation-independent (RotI) IMs, Figure 8 shows the response spectra of the as-recorded-rotated signals for angles in the range 0°–90°. In this case, a range between 0° and 90° was used as an example. Normally, these two measures are defined with a span of 180° using one of the linear combination $acc_1(t,\theta,T,\xi)$ or $acc_2(t,\theta,T,\xi)$ (see Equations 5 and 6). Rotated acceleration time histories, $acc_1(t,\theta,T,\xi)$ and $acc_2(t,\theta,T,\xi)$ are obtained for ξ=0.05 and periods in the range 0.01–1 s and the corresponding response spectra $Sa_{acc1}(T,\theta)$ and $Sa_{acc2}(T,\theta)$ are computed. For each period, T, response spectra values are sorted. Then, the 50th percentile spectrum is obtained, together with the angles at which the 50th percentile spectrum values are attained. Figure 8a shows the response spectra $Sa_{acc1}(T,\theta)$ and $Sa_{acc2}(T,\theta)$. The 50th percentile response spectra are also shown. Figure 8b is a 3D plot showing the angles at which the 50th percentile values are achieved. Figure 8c plots these angles, θ, as functions of the period.

This kind of spectra are called RotDpp. Rot means rotated, D means dependent on the period, and pp means percentile, which is the 50th in this case. Boore et al. (2006) and Boore (2010) proposed the following penalty function that allows us to find the individual response spectrum closest to RotDpp.

$$penalty(\theta) = \frac{1}{N_{per}} \sum_{i=1}^{h} \left[\frac{Sa(T_i,\xi,\theta)}{Sa_{RotDpp}(T_i,\xi)} - 1 \right]^2 \tag{9}$$

Recall that, in this equation, ξ is the fraction of critical damping. Then, SaRotIpp, is the response spectrum, $Sa(T,\xi,\theta_k)$, and θ_k is the angle that minimizes the Penalty function. Note that I means period-independent. Equation 9 has been applied to the response spectra of Figure 8a and Figure 8b, using RotD50 as a target spectrum. The obtained SaRotI50 spectra (green colour lines) are also plotted. The θ_k values are 45° and 48° for acc_1 and acc_2 cases respectively. This technique can be used to find RotDpp and RotIpp for any IM coming from rotated time histories or from their combinations.

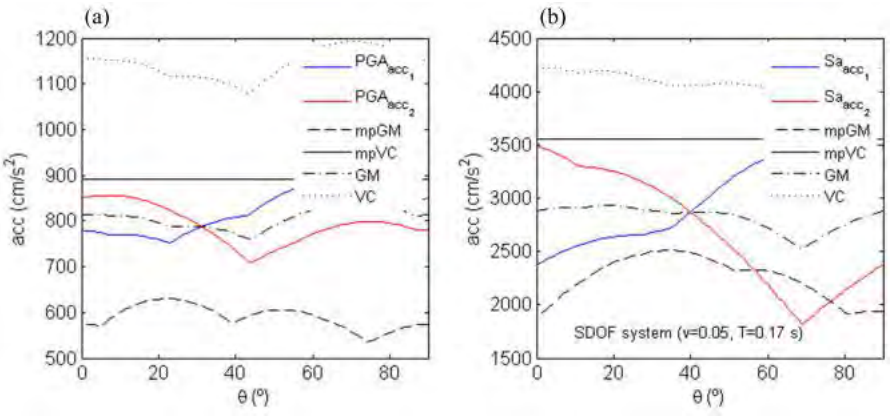

Figure 7: (a) mpGM, mpVC, GM, and VC as functions of the rotation angle, θ, for the as-recorded rotated signals. (b) Same as (a) for the acceleration responses of the as-recorded rotated signals.

2.4.4 Main IMs

PGA and $Sa(T,\xi)$ are the main intensity measures used in PSHA, design, and assessments. The concern originates when a single measure is needed that comes from mixing up IMs corresponding to two orthogonal components. The main IMs used in PSHA are well-described in Douglas (2003). Two important ways of combining these measures are the GM and the VC, as described above. Thus, in Figure 7, the mpGM, mpVC, GM, and VC are shown for the as-recorded rotated accelerograms and for their responses in a SDOF system with ξ=0.05 and T=0.17 s. GM is greater than mpGM and VC is greater than mpVC. The physical meaning of GM and VC is uncertain because of the non-simultaneity of the composed quantities, although GM is used in PSHA as a good statistical estimator of the expected IMs. Note that the mpVC is θ-invariant. In fact, mpVC is equal to the resultant, which is defined in Douglas (2003) as a_r, according to the second line of the following equation.

$$\begin{aligned} mpVC(\theta) = max\left[acc_1^2(t,\theta) + acc_2^2(t,\theta)\right]_{for\ t}^{1/2} = a_r = \\ = max\left[max\left|acc_1(t,0)\cdot cos\theta + acc_2(t,0)\cdot sin\theta\right|_{for\ t}\right]_{for\ \theta} \end{aligned} \tag{10}$$

Table 4 summarizes the main IMs used to deal with directionality effects. The first column of this table gives the names of the IMs, the second column provides a brief description, and the third column contains a summary of the computation method. RotDpp and RotIpp can be used for any of the IMs in the table. Thus, GMRotD50 and GMRotI50 were used by Boore et al. (2006), RotD50 and RotD100 were introduced by Boore (2010), and they are the 50th and 100th percentiles of the response spectra of the two horizontal orthogonal components rotated onto all non-redundant angles. Concerning the maximum values of the combined time histories, the following IMs are analysed: mpGMRotDpp, mpGMRotIpp, and mpVC. The mpVC(θ), that is, the *Resultant* as defined in Douglas (2003) [see also Equation 10, was also identified as the maximum response by Hidalgo-Leiva et al. (2017)]. mpGMRotD50 and mpGMRotI50 correspond to the 50th percentile, period-dependent and period-independent respectively, of the mpGM (T,ξ,θ) computed for all non-redundant θ angles. The *Larger* has been used in several directionality studies (Beyer and Bommer, 2006; Bradley and Baker, 2015; Boore and Kishida, 2016). This measure was one of the most frequently used in the development of GMPEs before it was realised that the use of geometric mean-based IMs leads to better results in the regressions used in the GMPE calculations. To reduce the epistemic uncertainty of this IM, LRotD50 and LRotD100 sensor orientation-independent IMs are proposed.

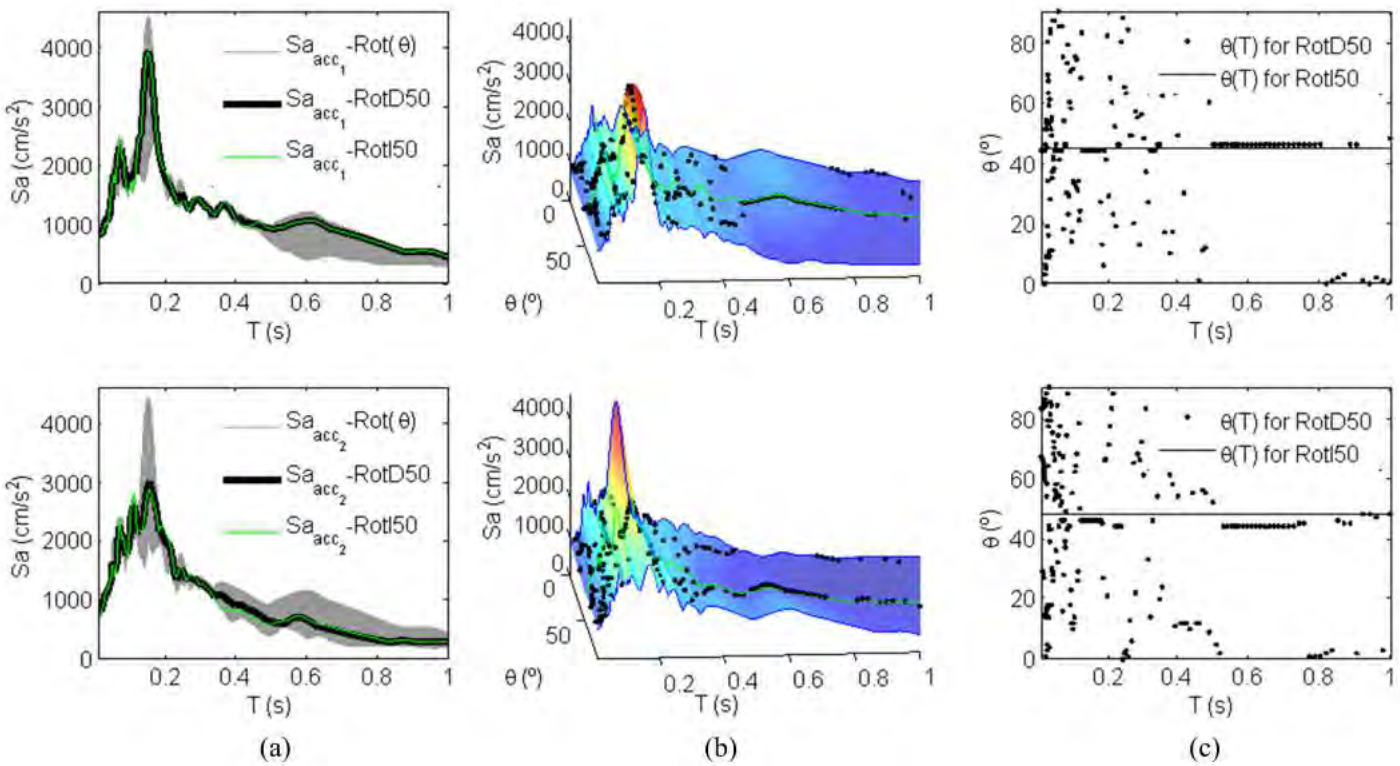

Figure 8: (a) 5% damped response spectra of the rotated accelerograms according to Equations 5 and 6. (b) 3D plots of the response spectra as functions of the period, T, and of the rotation angle, θ. The RotD50 and the RotI50 are also plotted in these figures. c) Angle $\theta(t)$ at which the RotD50 (black dots) and the RotI50 (black line) are achieved.

Table 4: Summary of the main ground-motion IMs. The name, description and computation method are in the first, second, and third columns respectively.

Individual time histories		
$acc(t,\theta,T,\xi)$	Absolute acceleration response time history. θ is the axes-rotation-angle. As-recorded accelerograms, acc_1 and acc_2correspond to $T=0$ and $\theta=0$.	Solving equation of motion (Nigam and Jennings, 1969)
$\mathrm{Rot}(T,\theta,T,\xi)$	Maximum value of $acc(t,\theta,T,\xi)$, for t. $T=0$ and $\theta=0$ corresponds to PGA.	$max\|acc(t,T,\xi,\theta)\|_{for\,t}$
Combined two orthogonal time histories		
$pGM(t,T,\xi,\theta)$	Prior combination of the time histories through the geometric mean.	$\|acc_1(t,T,\xi,\theta)\cdot acc_2(t,T,\xi,\theta)\|^{1/2}$
$pVC(t,T,\xi,\theta)$	Prior combination of the time histories through vector composition.	$[acc_1^2(t,T,\xi,\theta)+acc_2^2(t,T,\xi,\theta)]^{1/2}$
$mpGM(T,\xi,\theta)$	Maximum value of $pGM(t,T,\xi,\theta)$ for t	$max[pGM(t,T,\xi,\theta)]_{for\,t}$
$mpVC(T,\xi,\theta)$	Maximum value of $pVC(t,T,\xi,\theta)$ for t	$max[pVC(t,T,\xi,\theta)]_{for\,t}$
$GM(T,\xi,\theta)$	Geometric mean of two $Sa(T,\xi,\theta)$ corresponding to two orthogonal time histories. Used in GMPE and in PSHA.	$[Sa_1(T,\xi,\theta)\cdot Sa_2(T,\xi,\theta)]^{1/2}$
VC	Vector composition of two $Sa(T,\xi,\theta)$ corresponding to two orthogonal time histories (rarely used).	$[Sa_1^2(T,\xi,\theta)+Sa_2^2(T,\xi,\theta)]^{1/2}$
$Larger(T,\xi,\theta)$	Maximum value of the maximum values, for t, of the two time histories. Also called *Largest*.	$max\begin{bmatrix}\max\|\mathrm{acc}_1(t,T,\xi,\theta)\|_{for\,t}\\ \max\|\mathrm{acc}_2(t,T,\xi,\theta)\|_{for\,t}\end{bmatrix}$
Time histories resulting from rotating two orthogonal components		
$RotDpp(T,\xi,\theta)$*	pp percentile of the IMs of the combined θ-rotated time histories. Values at different periods may correspond to different θ-rotated $Sa(T,\xi,\theta)$.	Standard percentile computation methods
$RotIpp(T,\xi,\theta)$*	$Sa(T,\xi,\theta_{min})$ that minimizes the Penalty function of Equation 9, for θ.	Minimizing the Penalty function for θ. (See Equation 9)

* $\mathrm{RotDpp}(T,\xi,\theta)$ and $\mathrm{RotIpp}(T,\xi,\theta)$ can be used for any of the individual and combined IMs.

2.4.5 IMs comparison

The accelerograms recorded at station T1213 on 30 October 2016 in the Central Italy, M_W=6.5, Umbria earthquake, have been used to illustrate these IMs. Figure 9a shows the response spectra of the as-recorded signals for the mpVC, Larger, mpGM, and GM. Figure 9b shows a narrower band of periods. This figure also includes the Sa_{NS} and Sa_{EW} acceleration spectra.

NS is higher than EW for almost all the periods. Note that, Larger is practically the same as NS. Clearly, mpVC shows the maximum value in each period followed by Larger. The comparison of mpGM and GM confirms that GM is conservative (see also Figure 7).

Independent-orientation IMs were evaluated and compared with those obtained by combining the as-recorded accelerograms. In Figure 10, the following three distinct groups of IMs can be seen: i) mpGM, mpGMRotD50, and mpGMRotI50 corresponding to the maximum values of the combination of time histories (black), ii) GM, GMRotD50, and GMRotI50 corresponding to maximum values of the time histories (red), and iii) Larger, LRotD50, and LRotD100 (blue). In this case, mpGM, mpGMRotD50, and mpGMRotI50 are similar. Also similar are GM, GMRotD50 and GMRotI50, and RotD50. Finally, Larger and LRotD50 are very close. mpVC has the same values as RotD100 for every period. However, LRotD100, presented in this paper, also has the same values, which indicates a new way to obtain the maximum spectral response.

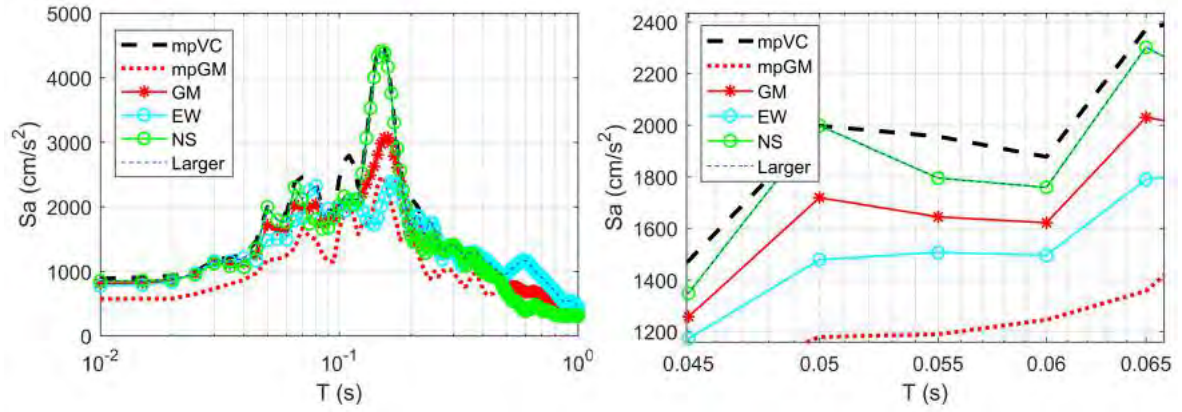

Figure 9: (a) 5% damped response spectra calculated with mpVC, Larger, mpGM, GM, NS, and EW as-recorded IMs from the Umbria earthquake and (b) zoom-in range of periods [0.045 0.065]s. Data corresponds to the Central Italy, M_W=6.5, Umbria earthquake, recorded at station T1213, which occurred on 30 October 2016 at 06:40:18.

2.5 Directionality in Italy

A principal aim of this study is to dimension the impact of the directionality effects on the strong ground motion predictive equations, which have usually been obtained without considering directionality effects. To this end, the geometric mean of the response spectra of the as-recorded acceleration time histories, that is $GM(T,\xi,\theta)$ for θ=0º and ξ=0.05 in Table 4, will be used as a reference because this is the main IM used in PSHA and in GMPE. Ratios between directionality-affected IMs and this reference IM will provide factors, such as functions of the period, indicating the influence of directionality effects and how close to or far from the reference IM are the directionality-affected IMs. As this study is performed for a wide, comprehensive database of strong ground motions in Italy, the results will also be useful for considering, in an easy and straightforward way, the directionality effects in existing PSHA and GMPE in Italy.

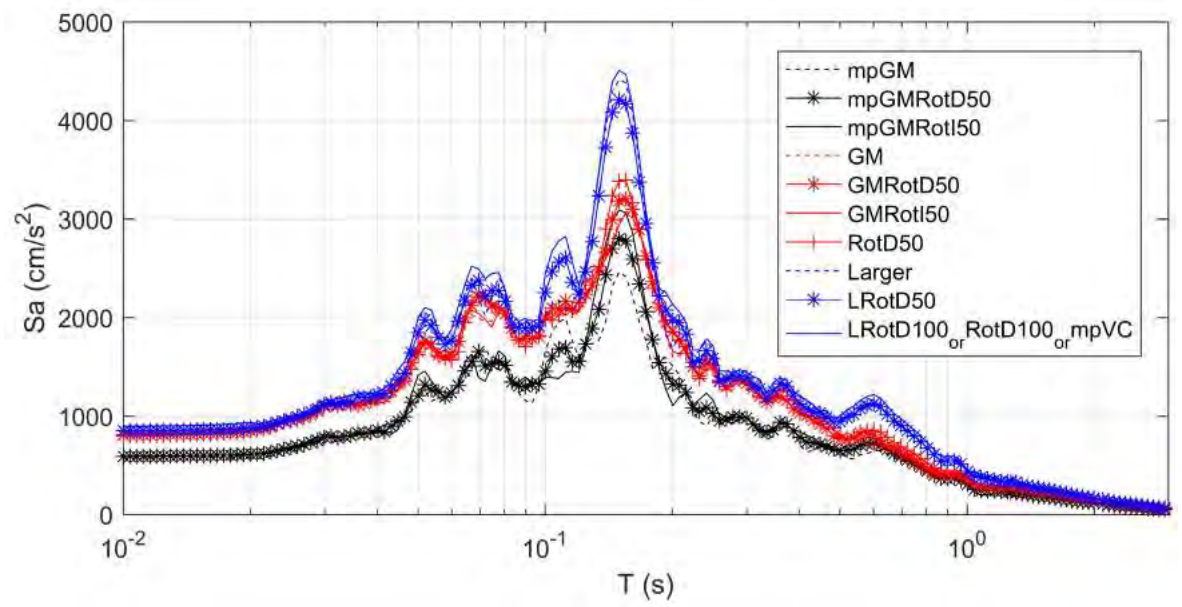

Figure 10: Comparison among several IMs for the 5% damped response spectra. Note that LRotD100, RotD100, and mpVC are equivalent IMs.

The directionality-affected IMs analysed herein are: SaGMRotD50, SaGMRotI50, and SaRotD50. For definitions of the IMs GM, RotDpp, RotIpp, GMRotDpp, and GMRotIpp, see the explanations in Table 4. Sa before these quantities means that 5% damped acceleration response spectra are considered. In addition, ratios for SaLarger, SaLRotD50, and SaLRotD100 will be investigated. Note that SaLRotD100 and SaRotD100 are equivalent IMs. Moreover, other IMs computed after combining the time histories will be studied too, namely: SampVC, SampGM, SampGMRotD50, and SampGMRotI50. Recall that RotDpp measures are period-dependent in the sense that the pp percentile for each period is attained for different rotation angles. In contrast, RotIpp measures are period-independent in the sense that RotIpp correspond to the same rotation angle for all the periods (see Figure 8).

2.5.1 Data

The database used for this research consists of accelerograms from earthquakes that occurred and were recorded in Italy between 1974 and 2017. This database was collected and standardized first using the records of the Italian Accelerometric Archive [ITACA, (Luzi et al., 2016a)]. Then, records of events after 31 December 2015 were downloaded from the Engineering Strong-Motion Database [ESM, (Luzi et al., 2016b)]. The complete database has 1583 three-component acceleration records, which correspond to 405 stations and 222 earthquakes. For each record, information about the event (for example, the magnitude, location, and fault mechanism) and about the accelerometric station (epicentral distance, site condition, and location) is available in the header of each file.

The processed accelerograms (corrected data) were used to estimate the response spectra and to obtain the IMs described above. A rigorous selection procedure was applied to the strong ground motion recordings. The following criteria were applied for the selection: depth (h $\leq$ 30 km), moment magnitude ($M_W \geq 4$), and epicentral distance ($\Delta \leq 50$ km). After this screening, 949 records corresponding to 249 stations and 131 earthquakes (Figure 11) were available.

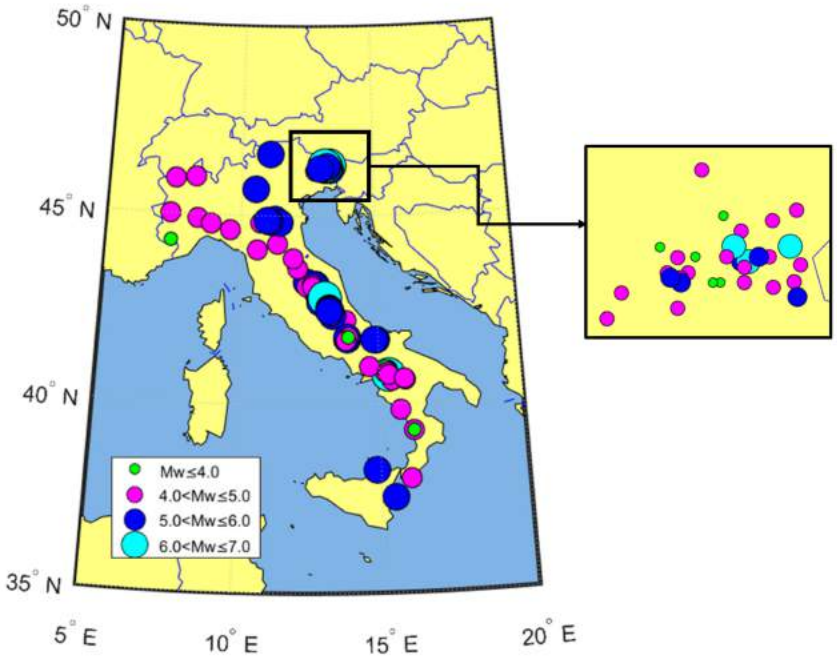

Figure 11: Epicenters and magnitudes of the earthquakes used in this study.

2.5.2 Results

To compare the IMs, we used a MATLAB script developed by Pinzón (2014) to perform a massive calculation of the two horizontal orthogonal components of the 949 selected records. First, the 5% damped acceleration response spectra were obtained for all the as-recorded signals and for all the linear combinations considered with the rotation angle variation (range 1°–180° with increments of 1°) (see Equations 5 and 6). Subsequently, the methods described in Section 2.4.3 were used to obtain sensor orientation-independent measures. Finally, three groups of ratios were computed. mpGM/GM, mpGMRotD50/GM, and pmGMRotI50/GM are the first group of ratios analysed. Note that Sa before these names has been removed for simplicity in the notation. As pointed out above, ratios were computed with GM=SaGM(T, ξ=0.05, θ=0) as the divisor. GM was chosen because this is the most common IM used in PSHA and in GMPE. The second group of ratios is: GMRotD50/GM, GMRotI50/GM, and RotD50/GM and, the third group is Larger/GM, LRotD50/GM, and mpVC/GM. All these quantities are functions of the period in the range 0.01–4 s. Note that most of the records supply information on the range of all the periods. However, the period range is lower for the analogic recordings. Mean values and 95% confidence intervals have been computed for these 9 ratios. For the calculation of the mean values, the antilogarithm of the average of the natural logarithms of the ratios was used, thus representing the GM of the ratios (Shahi and Baker, 2014).

Figure 12a illustrates the first group of ratios. As pointed out above, GM is conservative when compared with mpGM. Moreover, mpGMRotD50/GM and mpGM/GM are in the ranges 0.78–0.82 and 0.76–0.80 respectively, which again indicates that GM is conservative. Because of the nature of RotD and RotI, both are close to each other. The second group of ratios is shown in Figure 12b. Ratios are close to 1% for GMRotD50 and they are in the range of 1.5–4.5% for RotD50. Again, because of the nature of GMRotI50, in this case, ratios are similar to those of GMRotD50 but a little greater, in the range of 1–2%. The differences increase with increasing periods. These three ratios show good agreement with the results of similar studies in other regions (Boore et al., 2006; Boore,

2010; Shahi and Baker, 2014; Bradley and Baker, 2015). Finally, Figure 12c displays the third group of ratios. For Larger, the ratio varies between 14% and 20%. Similar results were reported by Bradley and Baker (2015). For LRotD50, the ratio is in the range of 15–22%, and varies about 1% compared to Larger. No previous information is available on LRotD50. We confirm that the maximum value of the vector compositions, mpVC, of the two orthogonal components is angle- and period-independent. Our results also confirm that mpVC is equal to RotD100 and LRotD100. In this case, the ratios are in the range of 23–31%.

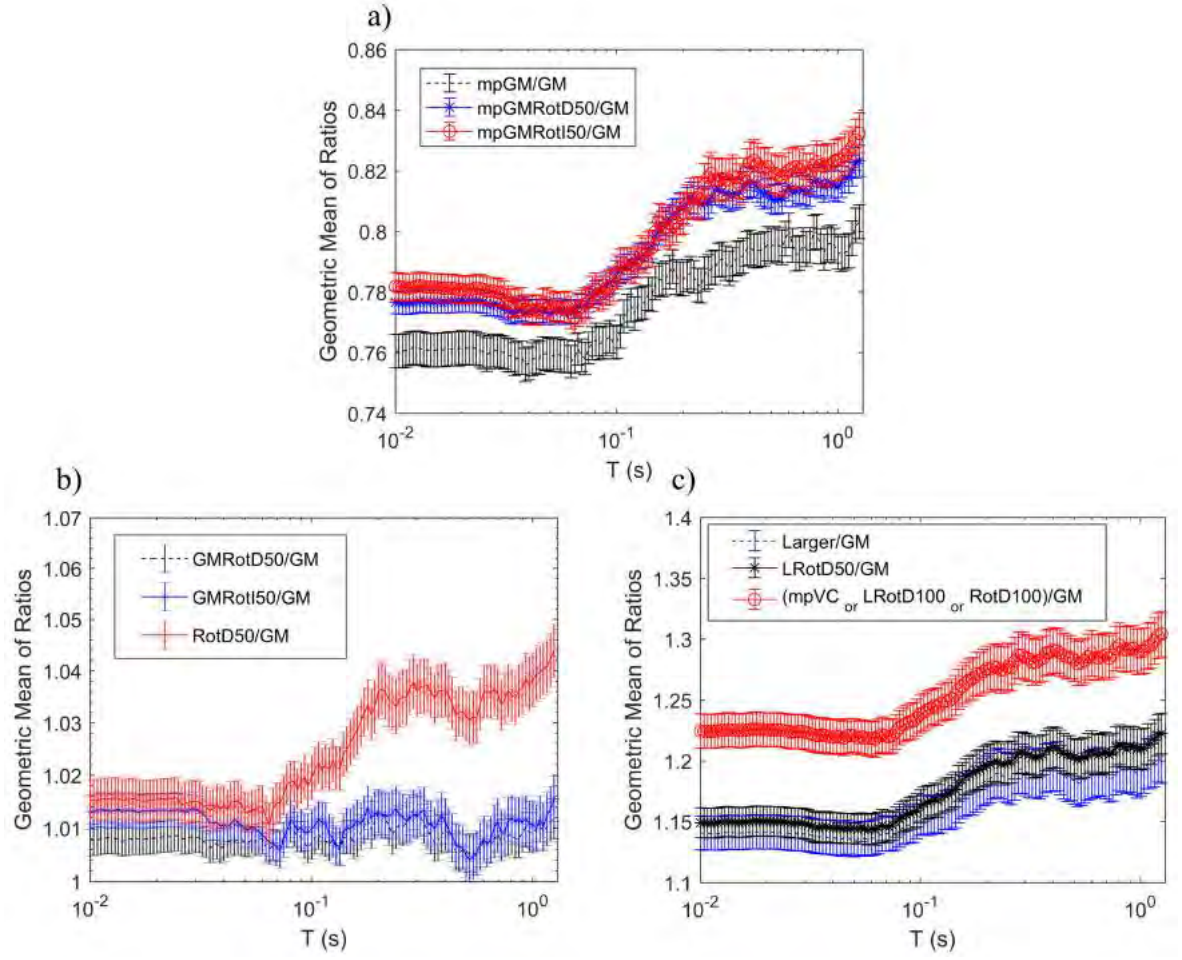

Figure 12: Ratios for IMs. (a) mpGM/GM, mpGMRotD50/GM, and pmGMRotI50/GM; (b) GMRotD50/GM, GMRotI50/GM, and RotD50/GM; (c) Larger/GM, LRotD50/GM, and mpVC/GM. The 95% confidence intervals are also shown.

Moreover, the mpVC/GMRotI50 was computed, because this ratio has been evaluated in other studies (Beyer and Bommer, 2006; BSSC, 2009; Campbell and Bozorgnia, 2007; Huang et al., 2010; Watson-Lamprey and Boore, 2007). Figure 13 compares our results and those obtained by these authors. They are in good agreement. The first part of the curve is flat around a value of 1.20 and increases to 1.32 at the 4.0 s period. Finally, the influence of magnitude on this last ratio was also investigated. The database was disaggregated into the following magnitude intervals: $4 \leq M_W < 5$, $5 \leq M_W < 6$, and $M_W \geq 6$. An interesting result was obtained: the ratios mpVC/GMRotI50 are in the ranges of 1.24-1.30, 1.20–1.27, and 1.17–1.25 respectively for low, mid and high magnitudes. In the three cases, these ratios increase with increasing periods and differences are greater for low periods. Dispersion is greater for low magnitude events (Figure 14).

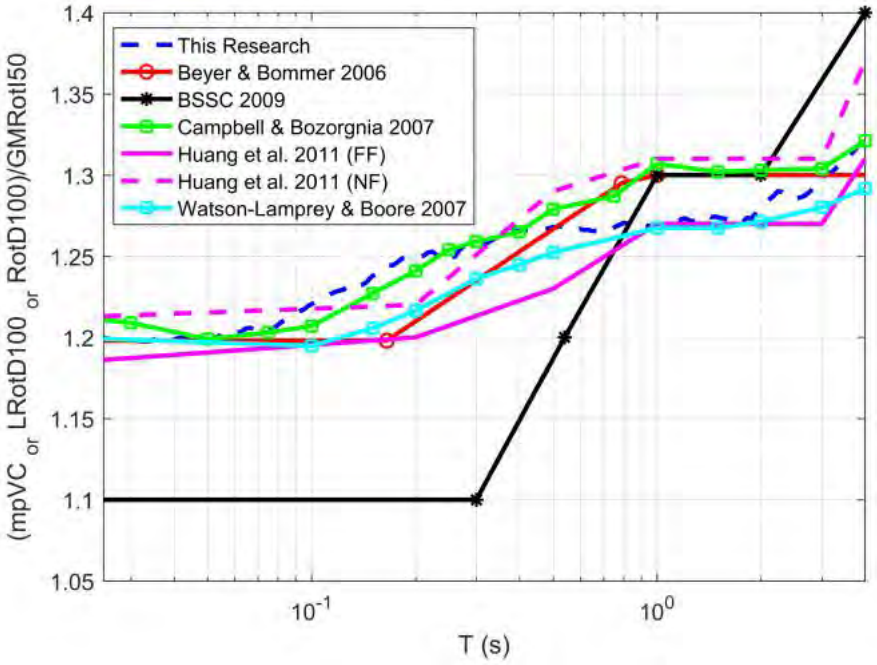

Figure 13: Geometric mean value of the ratio mpVC/GMRotI50 found in this study and comparison with ratios obtained by others.

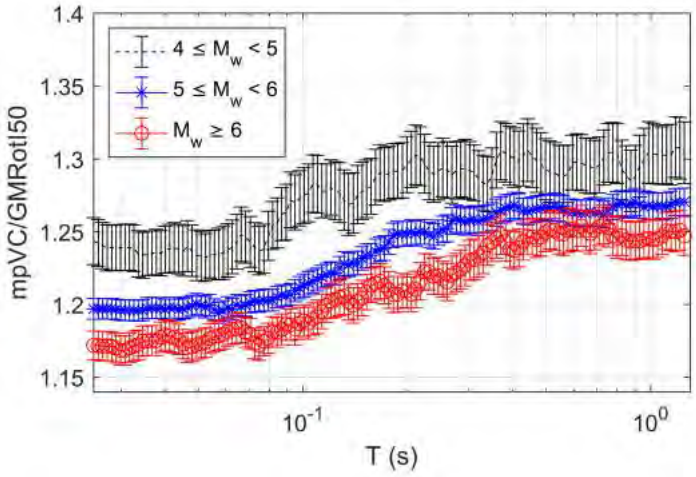

Figure 14: Geometric mean of the ratio mpVC/GMRotI50 and 95% confidence intervals for different magnitude ranges.

Finally, the ratio mpVC/GMRotI50 was also investigated for two ranges of epicentral distances (Epi); namely, Epi<15 km and Epi in the range 30–50 km. For this analysis, the events were also separated, according to great (M_W>5.5) and small (M_W≤5.5) magnitudes. Recall that these two groups of events are known as Type 1 and Type 2 earthquakes in Eurocode-8 (EC-8, (CEN, 2004)). The range of investigated periods was [0.01 4] s. Figure 15 shows the results. Distance influences the directionality effects. Ratios are greater for short distance earthquakes. Ratios are in the following ranges: 18–37%, 17–32%, 23–35% and 20–29% respectively for Type 1 near and distant events and

Table 5: Ground motions records (NS and EW components) for type 1 and type 2 events.

EC-8	Number of records
Type 1 ($M_W > 5$)	281
Type 2 ($M_W \leq 5$)	668
Total	949

Type 2 near and distant events, respectively.

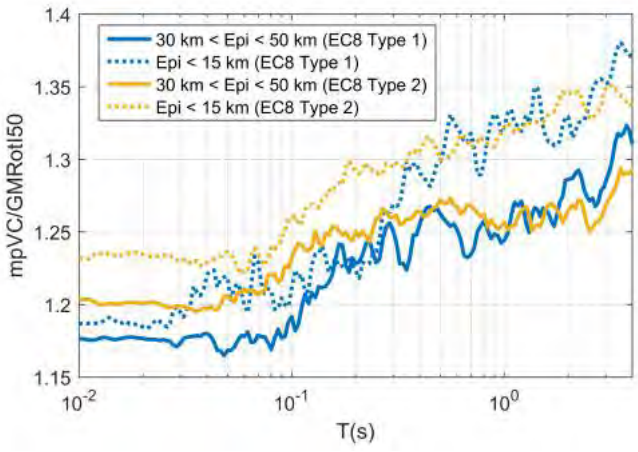

Figure 15: Geometric mean of the ratio mpVC/GMRotI50 for close and distant (Type 1 and Type 2).

2.5.3 Model

As can be seen in Figures 12 to 15, the ratios show a typical trend that has been exploited to model the results in a compact way, allowing easy conversion between available IMs that have not considered directionality and Rot-modified IMs. The model is a combination of log-linear functions tuning the obtained ratios. GMRotD50/GM and GMRotI50/GM are very similar, almost constant, in the entire period range (see Figure 12b) and were excluded from this fit. The model is defined as follows:

$$\begin{aligned} \rho = ratio = Y_1 \qquad & for\ T < T_1 \\ \rho = Y_1 + (Y_2 - Y_1)\left[\frac{ln(T/T_1)}{ln(T_2/T_1)}\right] \qquad & for\ T_1 \leq T < T_2 \\ \rho = Y_2 \qquad & for\ T_2 \leq T < T_3 \\ \rho = Y_2 + (Y_3 - Y_2)\left[\frac{ln(T/T_3)}{ln(T_4/T_3)}\right] \qquad & for\ T_3 \leq T < T_4 \end{aligned} \tag{11}$$

This is a piecewise model that depends on 7 parameters: Yi(i=1···3) and Tj (j=1···4). Median values (50 percentiles) have been used in the fit. The model was used to fit the ratios obtained for type 1 and type 2 events (CEN, 2004). Table 5 shows the number of records for each group.

Table 6 and Table 7 show the coefficients of the model of Equation 11 for type 1 and type 2 events, respectively. For comparison purposes, Figure 16 shows the ratio results, which are well-fitted by the model. This model can be used in GMPEs developed in Italy to convert the available IMs to Rot-modified ones.

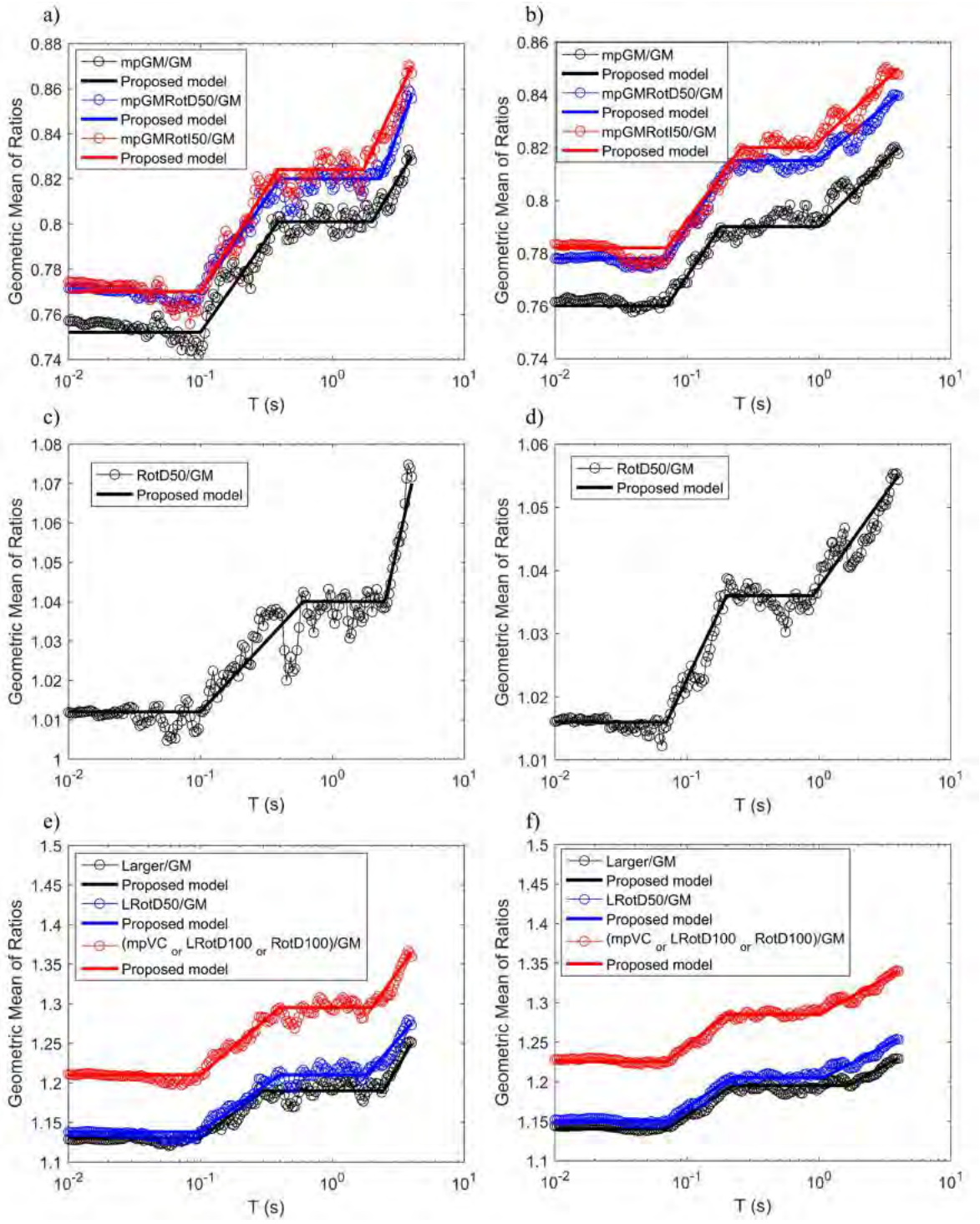

Figure 16: SampGM/SaGM, SampGMRotD50/SaGM, and SaGMRotI50/SaGM compared to the proposed model for (a) EC-8 Type 1 earthquakes; (b) EC-8 Type 2 earthquakes. SaRotD50/SaGM compared to the proposed model for (c) EC-8 Type 1 earthquakes; (d) EC-8 Type 2 earthquakes. Ratios SaLarger/SaGM, SaLRotD50/SaGM and (SaLRotD100 or SaRotD100 or SampVC/SaGM compared to the proposed model for (e) EC-8 Type 1 earthquakes; (f) EC-8 Type 2 earthquakes.

Table 6: Coefficients for the ratio model for Type 1 earthquakes.

Ratio	T1	T2	T3	T4	Y1	Y2	Y3
RotD50/GM		0.60	2.50		1.01	1.04	1.07
mpGM/GM		0.39	2.00		0.75	0.80	0.83
mpGMRotD50/GM		0.40	2.30		0.77	0.82	0.86
mpGMRotI50/GM	0.10*	0.39	1.72	4.00*	0.77	0.82	0.87
Larger/GM		0.30	2.45		1.13	1.19	1.25
LRotD50/GM		0.40	1.83		1.14	1.21	1.28
mpVC/GM		0.40	2.00		1.21	1.30	1.37

Table 7: Coefficients for the ratio model for Type 2 earthquakes.

Ratio	T1	T2	T3	T4	Y1	Y2	Y3
RotD50/GM		0.20	0.90		1.02	1.04	1.06
mpGM/GM		0.18	1.00		0.76	0.79	0.82
mpGMRotD50/GM		0.22	1.00		0.78	0.82	0.84
mpGMRotI50/GM	0.07*	0.26	0.90	4.00*	0.78	0.82	0.85
Larger/GM		0.22	1.67		1.14	1.20	1.23
LRotD50/GM		0.22	1.08		1.15	1.21	1.25
mpVC/GM		0.20	1.00		1.23	1.29	1.34

2.6 Summary, discussion and conclusions

Directionality effects in Italy have been analysed using a large, wide strong ground motion database. As the study involves massive calculations of the responses of 5% critically damped linear SDOF systems, the computing time is considerable. Among other factors, computation time depends on the computer components (hardware), software, and numerical algorithms used in the analysis. In this study, the numerical method proposed by Nigam and Jennings (1969) was implemented. Noticeably, this method produced the same accuracy of results and reduced the computing time around 10 fold compared to the step-by-step numerical integrations of the equation of motion via Duhamel's integral (Pinzón, 2014).

After a discussion and summary of the main IMs involved in directionality analysis, several ratios, related to the most frequently used IMs in PSHA and in GMPE, were debated, computed, and analysed. The main IM used in GMPE is the geometric mean of the peak values, Sa(T), of the two acceleration response time histories, which, for simplicity, has been called GM here. This IM is conservative in comparison to what is known as mpGM, that is, the maximum value of the geometric mean of the time histories.

Special attention has been devoted to the ratio mpVC/GMRotI50, and the results are in good agreement with previous directionality studies in other regions. Data have been disaggregated for magnitudes and distances. Directionality effects are more important for low magnitude ($4 \leq M_W < 5.5$) near (dist<15 km) events. Ratios increase with increasing periods. However, differences among ratios are greater for short periods, and smaller for long periods. Finally, to provide an easy tool to incorporate directionality effects in Italy in existing GMPE, a four-linear model was used to fit most of the ratios obtained.

A theoretical advantage of orientation-independent IMs is that they eliminate the sensor orientation effect as a contributor to the epistemic uncertainty. GMRotD50, GMRotI50, and RotD50 IMs are generally larger than the as-recorded GM. Although the difference between GMRotD50, GMRotI50, RotD50, and GM is small, orientation-independent measures should be used as they decrease epistemic uncertainty in the GMPEs (Beyer and Bommer, 2006). Notably, both GMRotI50 and RotD50 have

been used by the Pacific Earthquake Engineering Research Center (PEER) NGA GMPEs as new IMs. Similar results to those of Boore et al. (2006) and Boore (2010) were obtained.

In this paper, the vector composition of the time histories, mpVC, was analysed. It was found that mpVC is identical to RotD100 and LRotD100. The mpVC/GMRotI50 ratios obtained are very similar to those calculated in the studies cited above. For all cases, except for the expression proposed by the NEHRP (BSSC, 2009), the mpVC/GMRotI50 ratio is constant in low periods, with an approximate value of 1.20, increasing until 1.32 in the long period range. In fact, mpVC, RotD100, and LRotD100 can be considered the maximum response, corresponding to the most unfavourable case. Consequently, these values could be useful for the design or risk assessment of structures of special importance such as historical-cultural heritage buildings (Casapulla et al., 2017) or other high-risk constructions (Wu et al., 2017), since they are the maximum values for the available database.

Overall, the results obtained in this study are of significant interest in the improvement of the GMPEs in PSHA and in seismic design and risk assessments. In this respect, a simple theoretical model has been developed. This directionality model for Italy can be used to improve existing GMPE as it allows us to include directionality effects, by means of simple ratios, into equations obtained without any consideration of directionality.

3 A Strong-Motion Database of Costa Rica: 20 Years of Digital Records

Based on the published article: Moya-Fernández, A., Pinzón, L. A., Schmidt-Díaz, V., Hidalgo-Leiva, D. & Pujades, L. G (2020). A strong-motion database of Costa Rica: 20 years of digital records. *Seismological Research Letters*, under-review

3.1 Abstract

In this paper, we present a strong-motion database from earthquakes recorded by the Earthquake Engineering Laboratory at the University of Costa Rica. The database consists of 2471 three-component accelerograms from 155 digitally recorded events. It covers the last 20 years of measurements, including records from the Nicoya earthquake of M_w 7.6 on 2012 September 5. The engineering and seismological communities can use this data either to conduct new research or to improve seismic or hazard studies in the region. A catalog is also available with metadata of each record containing several intensity measures from the ground-motion time-histories.

3.2 Introduction

The convergence of the Cocos and Caribbean plates along the Pacific coast of Costa Rica is the major source of seismic activity for the country (Alvarado et al., 2017; Arroyo et al., 2017). As a result, many earthquakes occur along the subduction zone as well as active volcanism in the continental part. The outer slope side of the place generates normal faulting while reverse faulting takes place at depths between 15 and 50 km (Quintero and Güendel, 2000; DeShon et al., 2003; Norabuena et al., 2004). At depths between 50 and 280 km, intraplate or intra-slab earthquakes (deep subduction) occur and in general normal type mechanisms predominate (Guendel and Protti, 1998).

The Benioff zone gets shallower in the southern part of Costa Rica, where the Cocos mountain range subducts. The Panama Fracture Zone is a dextral fault system that separates the Cocos plate from the Nazca plate (Schmidt-Díaz, 2014). At the southern end of the Burica Peninsula lies the triple where the Cocos, Caribbean and Panama block meet. There is also a high number of seismic events that take place along the Northern Panama Deformed Belt (NPDB) and Central Costa Rica Deformed Belt (CRDB). These are a series of cortical deformation zones with a high density of active faults (Goes et al., 1993; Fan et al., 1993; Montero, 2001). This complex tectonic framework has resulted in numerous destructive earthquakes (i.e., 1991 Limon M_w 7.7; 2012 Nicoya M_w 7.6), and, consequently, a concern to develop and improve the seismic hazard and risk studies of the country.

The Earthquake Engineering Laboratory at the University of Costa Rica (LIS-UCR for its acronym in Spanish) started operations in 1983. That year, the United States Agency for International Development (USAID), donated several SMA-1 Kinemetrics strong-motion accelerographs to Costa Rica. They were located along the Pacific coast and the highly populated Central Valley. That was known as the Faculty of Engineering's Accelerographic Network. It was an analog network, which meant that after a strong earthquake took place, the collection and processing of the information took several days to weeks to get ready for analysis.

In 1989 the name was changed to LIS-UCR. New digital instruments were acquired and the geographic coverage of the stations increased. At the time of writing this document, the LIS-UCR has more than 160 digital, 24-bit strong-motion units located in free-field conditions, boreholes, and inside buildings. The LIS-UCR is in charge of recording, processing and storing all acceleration records for academic and research purposes.

The time span for the database provided in this paper ranges from 1998 to the present. The objective of this article is to give an overview and provide easy access to this database, and therefore, expanding its use on research.

3.3 Strong-Motion Network

The strong-motion network of the LIS-UCR began operating in 1983 with the installation of SMA-1 Kinemetrics analog sensors. In June 1991, digital processing started with the installation of several SSA-2 Kinemetrics type sensors. In 2010 many analog instruments were replaced by Ref Tek technology, and in 2012 Güralp and Nanometrics sensors were also added to the network. Nowadays, there are a total of 130 free-field stations (most of them with FBA sensors, but MEMS as well) as shown in Figure 17.

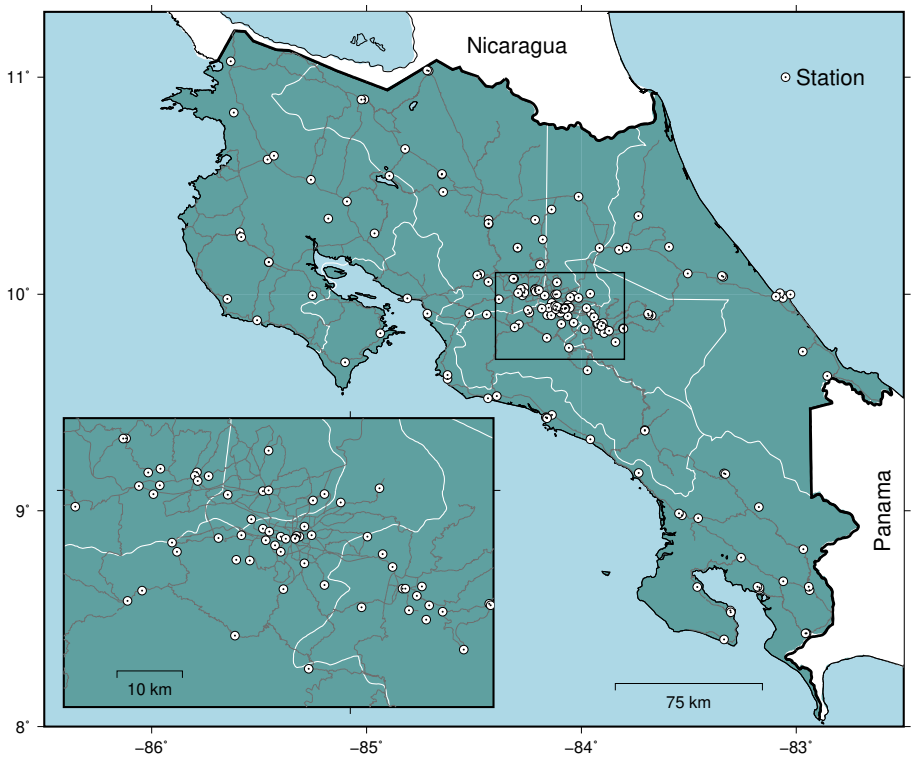

Figure 17: Station distribution for the LIS-UCR strong-motion network. White lines correspond to administrative divisions by provinces and gray lines to major roads.

There are four soil types according to the Costa Rican Seismic Code (CRSC) (CFIA, 2016). The site classification assigned to each station comes from the dynamic properties of the upper soil layers. This classification is similar to that proposed in the ASCE 7-16 (ASCE, 2017) with some differences. Soil types A and B are called S1 (rock). Soil types B, C, and D of ASCE 7-16 are equivalent to S2 (hard soil), S3 (soft soil) and S4 (very soft soil). There is no F type of soil in the CRCS classification.

Due to the complexity of data acquisition and the cost of the geotechnical studies, we used the classification method proposed by Zhao et al. (2006). The results can be found in Schmidt-Díaz (2011). The method is based on the horizontal-to-vertical (H/V) 5% damped response spectral ratio. From that, the fundamental period can also be obtained. We then used a classification index for each station. When available, geological and geotechnical information was also used as a reference.

A total of 42.0% stations are classified as soft soil (S3), 33.1% as hard soil (S2), 17.2% are classified as very soft soil (S4), and 7.7% as rock sites (S1). In order to get a better site characterization, we are also conducting MASW measurements to define the V_{S30} parameter. Figure 18 shows the site classification described above. There is also a table with a summary of the site conditions available at the LIS-UCR website (http://www.crsmd.lis.ucr.ac.cr/?id=Estaciones).

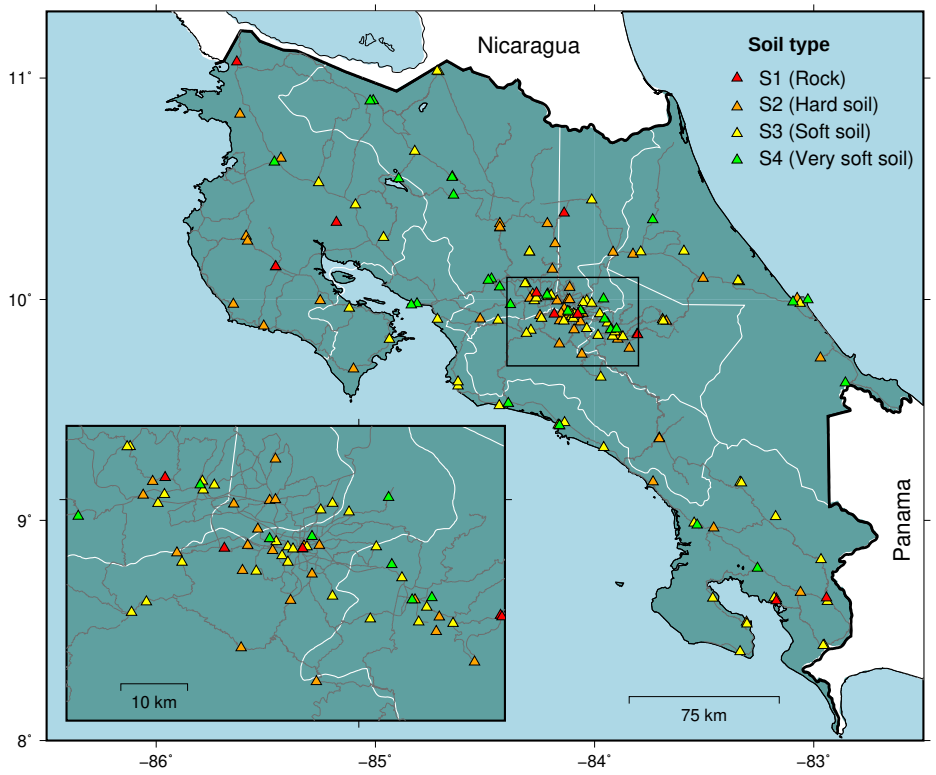

Figure 18: Station distribution and soil classification.

3.4 Strong-Motion Database

The strong-motion database we present here has a total of 2471 three-component accelerograms. They correspond to 155 earthquakes recorded from 1998 to the present. The database is being updated automatically with new events as they trigger the Accelerographic Monitoring System (SMA in Spanish) (Moya Fernández, 2018). Figure 19 shows the distribution of ground motion recordings per year. The number has increased in recent years because at present there are more stations. The earthquake's location (coordinates in WGS84 system), depth, and magnitude are calculated automatically by the SMA (Moya Fernández, 2018). The magnitude used to characterize the database is the moment magnitude (M_w). Table 8 shows a statistical summary of the number of records per different ranges of magnitude, depth, and epicentral distance. Figure 20a shows the relation magnitude vs hypocentral distance. The hypocentral distance for the events in the database ranges from 5 to 400 km. There are 1509 records from earthquakes with $M_w \geq 5$ (61.1%) (see Figure 20b). Figure 21 shows the location of the events in the database. Only one of the recorded earthquakes has an $M_w > 7$, the 7.6 M_w Nicoya earthquake of 2012. A total of 71 stations recorded that event which shook the whole country.

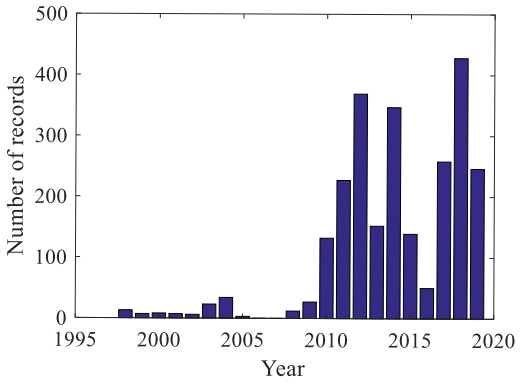

Figure 19: Number of ground motions recorded per year.

Table 8: Magnitude, depth and epicentral distance statistics for the entire database. Number and percentage of three-components records per interval.

Magnitude (M_W)	Depth (km)					
	<10	10—25	25—50	50—100	100—150	150
3.0 - 4.0	38 (1.5%)	27 (1.1%)	-	-	-	-
4.0 - 5.0	76 (3.1%)	348 (14.1%)	365 (14.8%)	108 (4.4%)	-	-
5.0 - 6.0	57 (2.3%)	472 (19.1%)	229 (9.3%)	144 (5.8)	-	28 (1.1%)
6.0 - 7.0	12 (0.5%)	232 (9.4%)	227 (9.2%)	7 (0.2%)	30 (1.2%)	-
7.0	-	71 (2.9%)	-	-	-	-
Magnitude (M_W)	Epicentral distance (km)					
	<10	10—25	25—50	50—100	100—150	150
3.0 - 4.0	17 (0.7%)	31 (1.3%)	5 (0.2%)	8 (0.3%)	4 (0.2%)	-
4.0 - 5.0	30 (1.2%)	130 (5.3%)	325 (13.1%)	326 (13.2%)	53 (2.1%)	33 (1.3%)
5.0 - 6.0	18 (0.7%)	58 (2.3%)	170 (6.9%)	316 (12.8%)	182 (7.4%)	186 (7.5%)
6.0 - 7.0	3 (0.1%)	12 (0.5%)	26 (1.0%)	104 (4.2%)	75 (3.0%)	288 (11.7%)
7.0	-	1 (0.1%)	1 (0.1%)	8 (0.3%)	13 (0.5%)	48 (2.0%)

The LIS-UCR stores strong-motion data in an ASCII format called "lis-format" (Moya Fernández, 2006). This is a special type of format developed for researchers and students to have access to time-series data. The files contain a header of 34 lines with relevant station and earthquake information of each record, after which there are the three independent columns corresponding to the north-south (N00E), vertical (UPDO), and east-west (N90E) component. This information is also available on the LIS-UCR website (http://crsmd.lis.ucr.ac.cr/).

3.5 Data processing

Each station transmits real-time data to the LIS-UCR servers in miniSEED format. When an earthquake is strong enough to trigger a given number of stations, the SMA extracts a predefined time-window and converts waveform data to SAC format (Goldstein et al., 2003) in cm/s^2. A baseline correction is applied by removing the mean value. After tapering on both ends, a second-order Butterworth bandpass filter is used. The SMA then processes the source parameters, calculate peak values, and gathers station information and soil type to save data into lis-format. Notice that the entire process is automatic, for that reason, the date is later inspected by eye in order to identify events with a low signal-to-noise ratio or with processing issues.

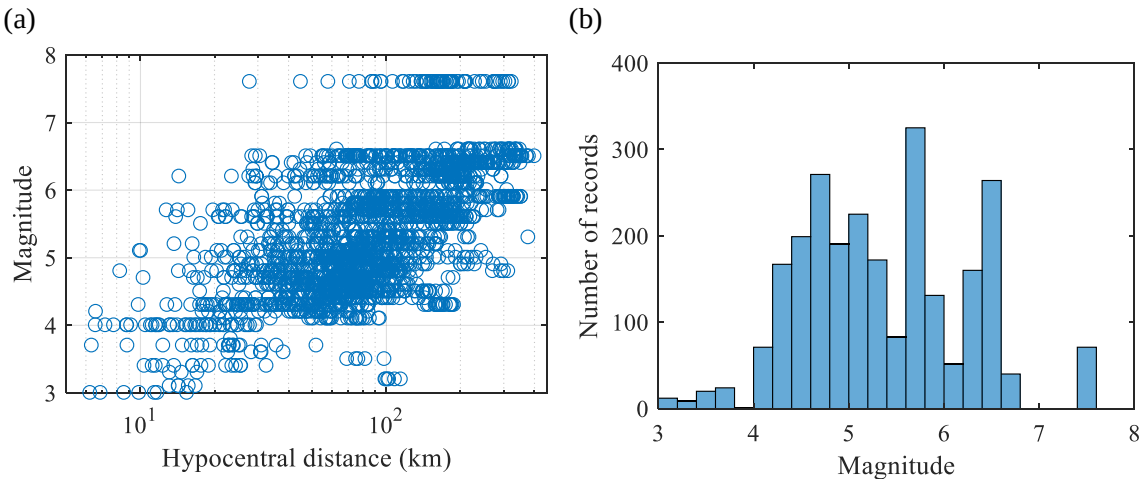

Figure 20: (a) Magnitude as a function of the hypocentral distance for the 2471 records and (b) magnitude distribution.

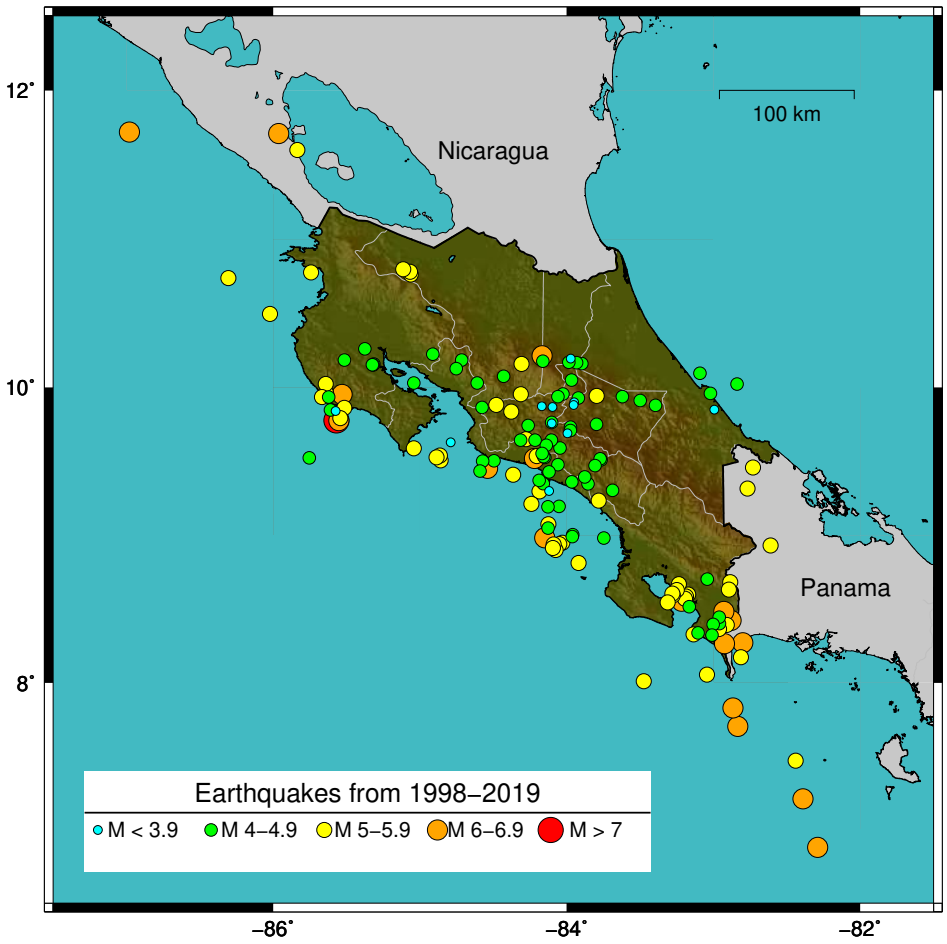

Figure 21: Epicenter location for the earthquakes recorded between 1998 and 2019.

3.6 Intensity measures

In addition to the database and the catalog, we estimated a series of intensity measures (IMs) based on ground motion time-histories (Table 9) and peak responses (Table 10). The IMs for each record are also available in the LIS-UCR website (http://www.crsmd.lis.ucr.ac.cr/?id=BD). The IMs based on time histories are available in a single table where each column represents a single IM. In the case of the IMs based on peak responses, they were calculated with a 5% damping and are presented in single tables as a function of several oscillator periods.

Table 9: List of intensity measures based on ground motion time histories.

Intensity measure	Acronym	Formulation	Units
Peak ground acceleration	PGA_{N00E}	$max\,\lvert a_{N00E}(t)\rvert$	cm/s^2
	PGA_{N90E}	$max\,\lvert a_{N90E}(t)\rvert$	
	PGA_Z	$max\,\lvert a_Z(t)\rvert$	
Larger value of the two horizontal components of acceleration	$PGA_{Larger(2)}$	$max\begin{bmatrix}\max\lvert a_{N00E}(t)\rvert \\ \max\lvert a_{N90E}(t)\rvert\end{bmatrix}$	cm/s^2
Larger value of the three components	$PGA_{Larger(3)}$	$max\begin{bmatrix}\max\lvert a_{N00E}(t)\rvert \\ \max\lvert a_{N90E}(t)\rvert \\ \max\lvert a_Z(t)\rvert\end{bmatrix}$	cm/s^2
Geometric mean of the PGA of the two horizontal components	PGA_{GM}	$[PGA_{N00E}\cdot PGA_{N90E}]^{1/2}$	cm/s^2
Peak ground velocity	PGV	$max\,\lvert v(t)\rvert$	cm/s
PGV-to-PGA ratio	PGV/PGA	$max\,\lvert v(t)\rvert\ /max\,\lvert a(t)\rvert$	s
Arias intensity	I_A	$\frac{\pi}{2g}\int_{t_i}^{t_f} a(t)^2dt$	cm/s
Root-mean-square (RMS) of acceleration	acc_{RMS}	$\sqrt{\frac{1}{\Delta}\int_{t_{5\%}}^{t_{95\%}} a(t)^2dt}$	g
Root-mean-square (RMS) of velocity	vel_{RMS}	$\sqrt{\frac{1}{\Delta}\int_{t_{5\%}}^{t_{95\%}} v(t)^2dt}$	cm/s
Specific energy density	SED	$\int_{t_i}^{t_f} v(t)^2dt$	cm^2/s
Characteristic intensity	I_C	$(acc_{RMS})^{1.5}\sqrt{t_f}$	-
Cumulative absolute velocity	CAV	$\int_{t_i}^{t_f}\lvert a(t)\rvert\,dt$	cm/s
Significant duration	Δ	5-95% of Arias intensity	s
Duration-PGV intensity	$I_{\Delta-PGV}$	$PGV^{\alpha}\Delta^{\beta}$	-

- $a(t)$ and $v(t)$ represents the acceleration and velocity time histories of an earthquake.
- t_i is the beginning of the record, t_f is the total duration of the record.
- 5% and 95% of the Arias intensity marks the beginning (t_5%) and end ($t_9$5%) of the strong phase.

We used the acceleration time-histories to calculate the IMs in Table 9. They have been widely used in the development of ground-motion prediction equations and seismic hazard studies (Boore et al., 1997; Watson-Lamprey and Boore, 2007; Mezcua et al., 2008; Schmidt-Díaz, 2014; Douglas, 2017), as well as in the evaluation of expected damage (Park et al., 1987; Kostinakis et al., 2015; Muin and Mosalam, 2017; Pinzón et al., 2020a). Figure 22 shows the relation between PGA and hypocentral distance in the database. There are 7413 individual time-histories corresponding to the 2471 records. Of them, 39.5% have a PGA larger than 10 cm/s^2. Comparing the mean values of several PGA definitions, we got differences of 1.45% between $PGA_{Larger(3)}$ and $PGA_{Larger(2)}$, and 12.5%, 15.6% and 14.0% between $PGA_{Larger(2)}$ and PGA_{N00E}, PGA_{N90E}, and PGA_{GM} respectively. Figure 23 shows the relation for the rest of the IMs with hypocentral distance.

Table 10: List of intensity measures based on peak responses.

Intensity measure	Definition
SA_{N00E} & SA_{N90E}	Response spectra of the as-recorded horizontal orthogonal components
SA_{Larger}	The larger of the two horizontal components (Douglas, 2003; Beyer and Bommer, 2006; Bradley and Baker, 2015)
SA_{GM}	Geometric mean of the response spectra of the as-recorded horizontal components (Beyer and Bommer, 2006; Boore and Kishida, 2016)
$SA_{GMRotDpp}$	Percentile (pp) value of the geometric mean of the response spectra of the two as-recorded horizontal components rotated onto all non-redundant azimuths (Boore et al., 2006; Boore and Kishida, 2016)
$SA_{GMRotIpp}$	Percentile (pp) value of the geometric mean of the response spectra of the two as-recorded horizontal components rotated onto all non-redundant period-independent azimuths (Boore et al., 2006; Boore and Kishida, 2016)
SA_{RotDpp}	Percentile (pp) values of the response spectra of the two as-recorded horizontal components rotated onto all non-redundant azimuths (Boore, 2010; Pinzón et al., 2018a)

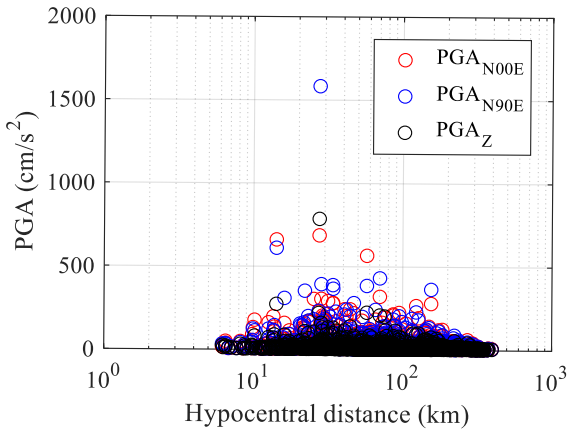

Figure 22: Peak ground acceleration as a function of the hypocentral distance for the three as-recorded components.

The IMs from peak responses in Table 10 are commonly used in the development of GMPE and hazard maps (Douglas, 2017). The SA_{GM} (where GM means geometric mean) has gained popularity in the development of GMPEs in recent years (Douglas, 2003; Campbell and Bozorgnia, 2007; Bindi et al., 2011) because the dispersion in the averaging procedure in GMPE is significantly reduced (Baker and Cornell, 2006; Watson-Lamprey and Boore, 2007; Stewart et al., 2011). However, this IM has a dependence on the recording sensor orientation (this means that if the recording sensor is oriented along the polarization direction, the GM of the response spectra of the as-recorded ground motion would be zero, Boore et al. (2006)). The $SA_{GMRotDpp}$ and the $SA_{GMRotIpp}$ developed by Boore et al. (2006) (where GM means geometric mean, Rot: rotation, D and I: period-dependent and independent rotations, and pp is the percentile) were proposed in order to eliminate the sensor orientation dependency of the SA_{GM}. The IM $SA_{GMRotIpp}$, for the 50th percentile ($SA_{GMRtI50}$), was used as an intensity parameter in the Next Generation Attenuation (NGA) project (Chiou et al., 2008; Power et al., 2008). Later on, Boore (2010) proposed the usage of the orientation-independent SA_{RotDpp} and SA_{RotIpp} IMs without computing the geometric mean. Finally, the SA_{RotD50} IM was used to develop the NGA-West2 (Boore et al., 2013; Bozorgnia et al., 2014) and NGA-East (PEER, 2015) GMPEs models.

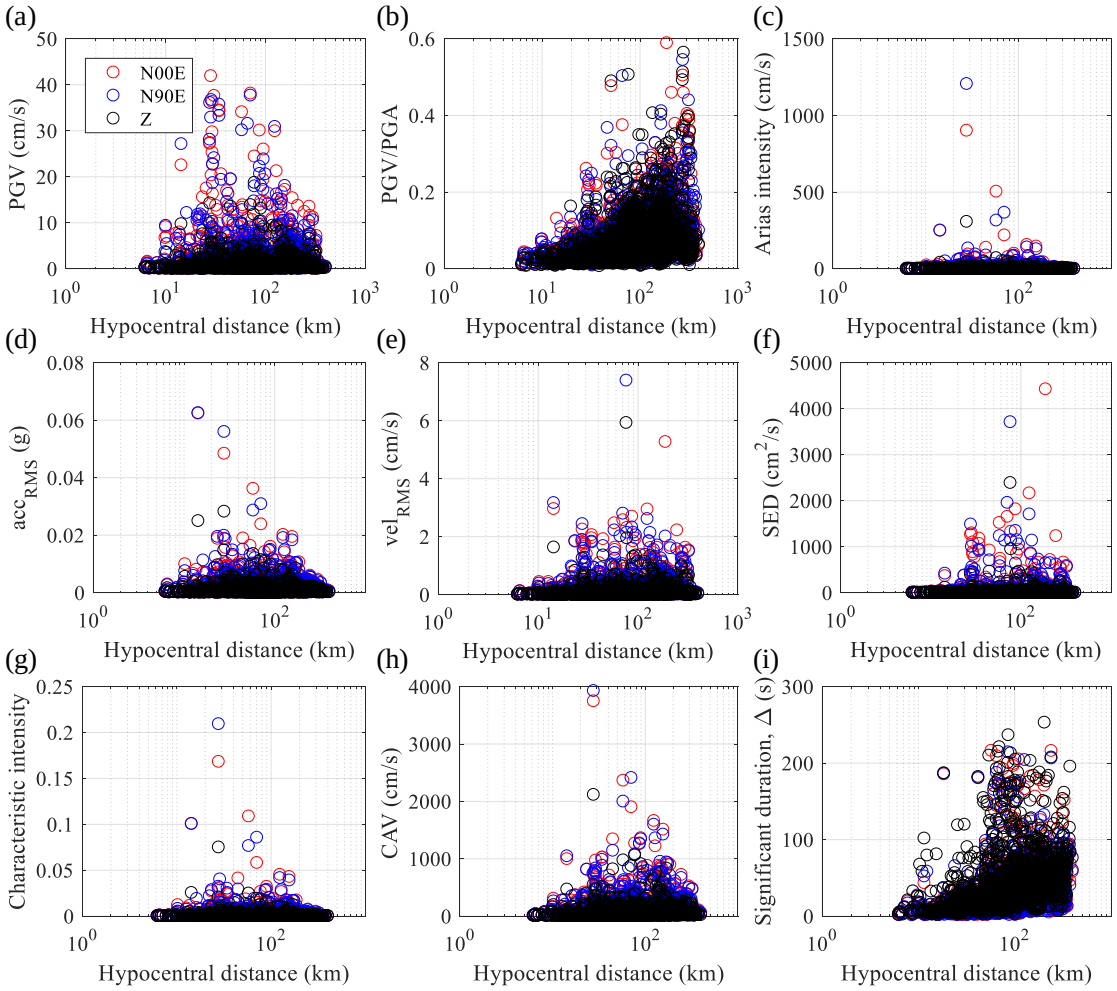

Figure 23: Several intensity measures as a function of the hypocentral distance: (a) PGV, (b) PGV/PGA, (c) Arias intensity, (d) acc$_{RMS}$, (e) vel$_{RMS}$, (f) Specific Energy Density, (g) Characteristic intensity, (h) Cumulative Absolute Velocity and (i) Significant duration.

Figure 24 shows a comparison between the rotated spectra (Boore, 2010) and the SA$_{RotD100}$ IM for the 2012 Nicoya earthquake at GNSR station. It is clear from the figure that the SA$_{RotD100}$ is the envelope of the rotated spectra. Because this IM represents the maximum value of the vector composition, it could be used for the design (or risk assessment) of structures of special importance such as historical-cultural heritage buildings or other high-risk constructions (Pinzón et al., 2018b).

Figure 25 shows the rest of IMs: SA$_{RotD100}$, SA$_{Larger}$, SA$_{GMRotD50}$, SA$_{GMRotI50}$, SA$_{RotD50}$, and SA$_{GM}$ calculated in the range of [0.10 0.25] s. SA$_{GMRotD50}$, SA$_{GMRotI50}$ and SA$_{RotD50}$ correspond to the median values of the rotated spectra and have similar values compared to SA$_{GM}$. SA$_{RotD100}$ and SA$_{Larger}$ represent the maximum spectral values. SA$_{RotD100}$ is 9% larger than SA$_{Larger}$ on average for the entire database. A statistical summary for all the IMs can be found on the LIS-UCR website.

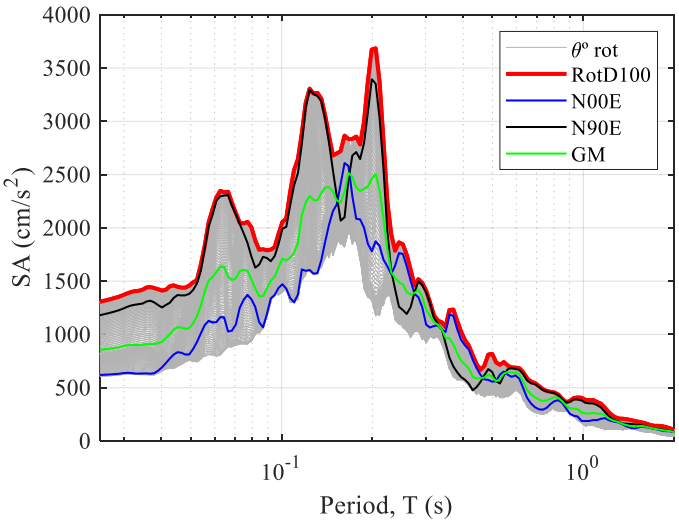

Figure 24: Comparison of the 5% damped response spectra estimated with RotD100, GM, horizontal acceleration components (N00E and N90E) and the rotated components (θ^o rot) from the 7.6 M_W Nicoya earthquake recorded at station GNSR, which occurred on 5 September 2012.

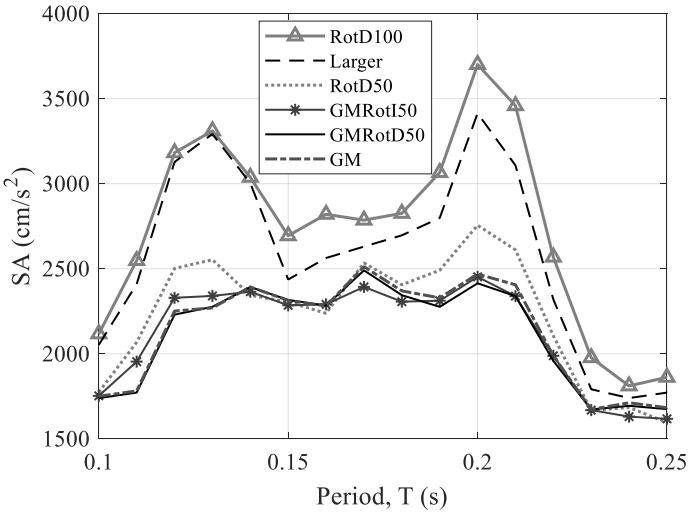

Figure 25: Comparison of the 5% damped response spectra estimated with RotD100, Larger, RotD50, GMRotI50, GMRotD50 and the GM using the 7.6 M_W Nicoya earthquake recorded at station GNSR, which occurred on 5 September 2012.

3.7 Conclusions

The database presented in this paper contains 2471 three-component digitally recorded strong-motion records from the last 20 years in Costa Rica. They correspond to 155 earthquakes with maximum hypocentral distances of 400 km. Data will continue to be added as new earthquakes get recorded by the LIS-UCR network. In addition, a catalog with earthquake and station metadata is also available. Several time-history IMs and peak responses were also calculated for each component. The IMs will be useful for developing new seismic hazard studies for the region or for updating the current GMPEs established for Costa Rica. The database, the catalog with the metadata, and the estimated IMs are available at the LIS-UCR website (http://crsmd.lis.ucr.ac.cr/).

4 An efficient method for considering the directionality effect of earthquakes on structures

Based on the published article: Pinzón, L. A., Diaz, S. A., Pujades, L. G., & Vargas-Alzate, Y. F. (2019). An efficient method for considering the directionality effect of earthquakes on structures. *Journal of Earthquake Engineering*, in-press, 1–30. doi: 10.1080/13632469.2019.1597783
Journal URL: www.tandfonline.com/doi/abs/10.1080/13632469.2019.1597783
FUTUR UPC URL: futur.upc.edu/24473665

4.1 Abstract

Recent researches have proven the importance of considering the directionality effect on the expected seismic damage of structures. However, it demands a high computational effort if the nonlinear dynamic analysis (NLDA) is used to estimate the seismic response. This paper presents a simplified approach to obtain peak response parameters for a building subjected to ground motions considering the directionality effect. To do so, the maximum and median response spectra, considering all the non-redundant response spectra, of several ground motion pairs are calculated. Afterwards, a spectral matching technique is applied to these spectra and new acceleration components are obtained. A series of NLDA are performed with these new components and the roof displacement and base shear values are calculated. These results are compared with the maximum and median values, calculated by performing a series of NLDA, after rotating the earthquakes records by considering increments of 1° in the interval 0°-180°. The results agree with both approaches validating the efficiency of the simplified proposed approach.

4.2 Introduction

When an earthquake occurs, the accelerations generated by the event are usually recorded in three orthogonal components corresponding to two horizontals and a vertical one. These three components represent the translational motion of the point where the sensor is located, but they do not necessarily allow capturing the maximum seismic demand of a structural system. It is because ground motions will depend on the position and orientation of the sensor with respect to a given reference system (Boore et al., 2006). Consequently, for estimating the dynamic response of a structure is commonly recommended to find the angle producing the peak demand to be conservative (Athanatopoulou, 2005; Lucchini et al., 2011; Kostinakis et al., 2018). Notice that, the predominant acceleration acting on a structure will also depend on its azimuthal orientation. This effect has been widely studied focusing on the expected performance and damage in structures and on the seismic hazard (Lagaros, 2010; Mackie et al., 2011; Nguyen and Kim, 2013; Torbol and Shinozuka, 2014; Bradley and Baker, 2015; Vargas-Alzate et al., 2018; Pinzón et al., 2018a).

The present study is focused on the building performance variation induced by the directionality effect of earthquakes. At this respect, several methodologies to obtain the rotated ground motion record which generates the maximum response of the structure have been developed to date (Rigato and Medina, 2007; Cantagallo et al., 2012). In these methodologies, the horizontal acceleration components of an earthquake are rotated, ranging from 0° to 180°, for regular buildings and from 0° to 360°, for irregular ones, generally considering increments of 1°. Then, 180 or 360 dynamic analyses should be performed, respectively. Once the dynamic analyses have been performed, one can obtain the seismic response for any percentile. However, such approach is computationally expensive. In

order to reduce the high computational effort involved, a simplified method to predict the building response for any percentile is developed herein.

This method is based on the combination of two techniques widely used in the last decade namely the sensor-orientation-independent intensity measures (RotDpp IMs) proposed by Boore (2010) and the spectral matching technique, which is summarized in section 4.3.3. To simplify the implementation of the simplified method, an application named MatchPercentile has been developed. This app is useful to obtain new ground motion pairs which are consistent with any demand percentile by considering the sensor-orientation-independent intensity measures mentioned above.

The simplified presented approach is tested against the more computational effort method, through the nonlinear dynamic analysis (NLDA), in order to demonstrate its advantages. To do so, a regular 4-story steel building and a L-shape irregular 4-story steel building, both with a structural system of special moment frames (SMF), modeled with Ruaumoko 3D software (Carr, 2002), have been developed. A total of 20 ground motion pairs recorded in Italy were used as seismic input. The results obtained with both approaches were compared and similar results have been obtained.

4.3 Methodology

In this section are presented two methods to evaluate the behavior of a building by considering the effect of the seismic directionality. The first method is the most commonly used when the directionality effect is evaluated over a structure and will be named 'complete rotational method', CRM. In this method, a series of NLDA should be performed with the rotated ground motions, by considering increments of 1°, until reaching 180°. Thus, a total of 180 dynamic analyses per ground motion pair should be performed. In this way, a distribution of any output variable can be obtained allowing to estimate any percentile level. The second method will be named 'predictive percentile method', PPM. This method seeks to predict any percentile level of an output variable, from a new pair of ground motions which has been adjusted by considering the RotDpp IM and the spectral matching technique. This efficient approach will significantly reduce the computational effort as will be shown below.

4.3.1 Complete rotational method

Some recent researches have shown that the maximum ductility demand of an elastoplastic single-degree-of-freedom system could occur at a different angle from the as-recorded one (Garcia-Soto et al., 2012). Similar conclusions have been observed when estimating the maximum displacement response and maximum expected damage of 3D multi-degree-of-freedom building models (Kostinakis et al., 2015, 2018; Vargas-Alzate et al., 2018). To analyze this effect for a particular building and earthquake, by considering the CRM, the following steps should be achieved:

1. A 3D model of the building should be created.

2. The horizontal components of the earthquake are rotated to the first considered angle. Notice that, the first calculation will be performed for the as-recorded components, i.e. θ=0 (see Equations 12 and 13).

3. A NLDA is computed for the rotated components.

4. Steps 2 and 3 are repeated with increments of 1° in the range of 0° to 180°. Depending on the structural irregularity, the analysis should be performed to 360°.

The rotated horizontal components, accx(θ) and accy(θ), are obtained by using linear combinations of the as-recorded components (acc$_x$ and acc$_y$) as a function of the rotational angle (θ), through the following equations:

$$acc_x(\theta) = acc_x \cdot cos(\theta) + acc_y \cdot sin(\theta) \tag{12}$$

$$acc_y(\theta) = -acc_x \cdot sin(\theta) + acc_y \cdot cos(\theta) \tag{13}$$

In order to illustrate how much can vary the spectral ordinates of an earthquake as a function of the rotational angle, Figure 26 shows the 180 response spectra calculated for each one of the rotated components of the earthquake of Umbria (see earthquake 2 in Table 13). In this figure is also illustrated the RotD100 and the RotD50, which are intensity measures related to the maximum and median spectrum, respectively. It is important to mention that the calculation time induced by the rotational analysis of the signal can be reduced if the linear combination of equations 12 and 13 are performed by using the oscillator time series responses instead of the as-recorded acceleration components.

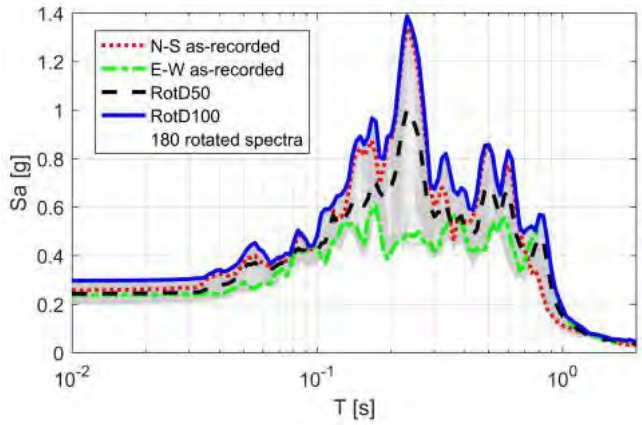

Figure 26: 180 rotated response spectra from Umbria, Italy earthquake (October 30, 2016). In blue the spectrum corresponding to de maximum demand (RotD100), in black the median (RotD50) and the as-recorded components, N-S and E-W, in red and green respectively.

As a result of the directionality analysis based on CRM, it can be obtained relationships between several output variables such as the roof displacement (δ) and the base shear (V$_B$) as a function of the rotation angle (θ). However, the high computational cost of performing hundreds of NLDA makes difficult to include the directionality effect. For this reason, it would be of practice interest to develop a simplified methodology allowing to obtain similar results to those based on the CRM, but with a fraction of the computational effort.

4.3.2 Predictive percentile method

As mentioned above, the aim of the PPM is to reduce the high computational cost involved when applying the CRM. PPM is based on the spectral matching technique in combination with the sensor-orientation-independent intensity measure, RotDpp (Boore, 2010). The intrinsic logic of this simplified method is that one can predict the maximum response of a structure to a given rotated ground motion, if the frequency content of the pair of horizontal records is modified to fit the response spectra related to the RotD100. In a general sense, one can predict the response of the structure to any percentile

(pp), only by adjusting the frequency content of the earthquake record, in such a way that the spectra of the ground motions are compatible with the response spectra of the desired demand percentile. In this way, the computational time can be highly reduced since only two NLDA should be performed. Notice that in the case of the RotD100 the calculation can be simplified using the Root-sum-of-squares (RSS) or the vector composition (mpVC) measures (Pinzón et al., 2018b).

To apply the PPM for a particular building and for a specific ground motion pair the following steps should be considered:

1. As in the CRM, a 3D model of the structure should be created.

2. **Case 1.** If the aim is to find the maximum response, the RSS spectrum must be computed. This spectrum represents the maximum spectral response for all the oscillator periods of the rotated ground motions used as input.
   Case 2. If the response for a specific percentile wants to be found, the RotDpp spectrum for the percentile pp should be estimated.

3. **Spectral matching.** The response spectrum defined in the previous step is used as a target spectrum and, by using a spectral matching method (Atik and Abrahamson, 2010; Hancock et al., 2006; Jayaram et al., 2011), two new ground motions compatible with the target spectrum are obtained (N-S matched and E-W matched). In this study, the spectral matching technique applied is described in section 4.3.3.

4. **Dynamic analyses.** The new pair of ground motions is applied in the main directions of the building. Two NLDA are performed alternating the accelerograms in each direction of the building. **NLDA 1.** N-S matched ground motion component applied in the X axis of the building and the E-W matched acceleration component applied in the Y axis of the building. **NLDA 2.** E-W matched ground motion component applied in the X axis of the building and the N-S matched acceleration component applied in the Y axis of the building.

To facilitate the implementation of the proposed simplified method, one application named MatchPercentile has been developed by using the commercial software MATLAB (see Figure 27). The users of the created software neither need to be proficient users of MATLAB nor to have the software installed. It is because the created program is a stand-alone version in .exe format and it works with Windows OS. MatchPercentile is useful to find ground motions compatibles with the response spectrum for a specific percentile depending on the angle to which the ground motion is rotated. As input parameters, it is required to enter the two acceleration horizontal components, the critical damping for the calculation of the response spectrum, the interval period of the spectrum, the expected demand to the desired percentile and the number of iterations allowing a better fitting of the target spectrum (a minimum of 10 iterations is recommended). The two acceleration components are obtained by using the equations 12 and 13, with increments of 1°, in the range between 0° and 180°. For each component of the earthquake record, the response spectrum is estimated. When the 180 spectra are obtained, the spectral values of all the rotational angles are sorted for each oscillator period. In this way, the ppth percentile of the ground motion can be obtained. Once the response spectrum for a specific percentile is obtained, it becomes the target spectrum. Afterwards, the spectral matching technique is applied to the as-recorded ground motions in such a way to fit the target spectrum (see section 4.3.3). In this way, two new horizontal components are obtained which can be used to perform the NLDA. It is expected that the results obtained with this approach fit quite well those obtained with the CRM.

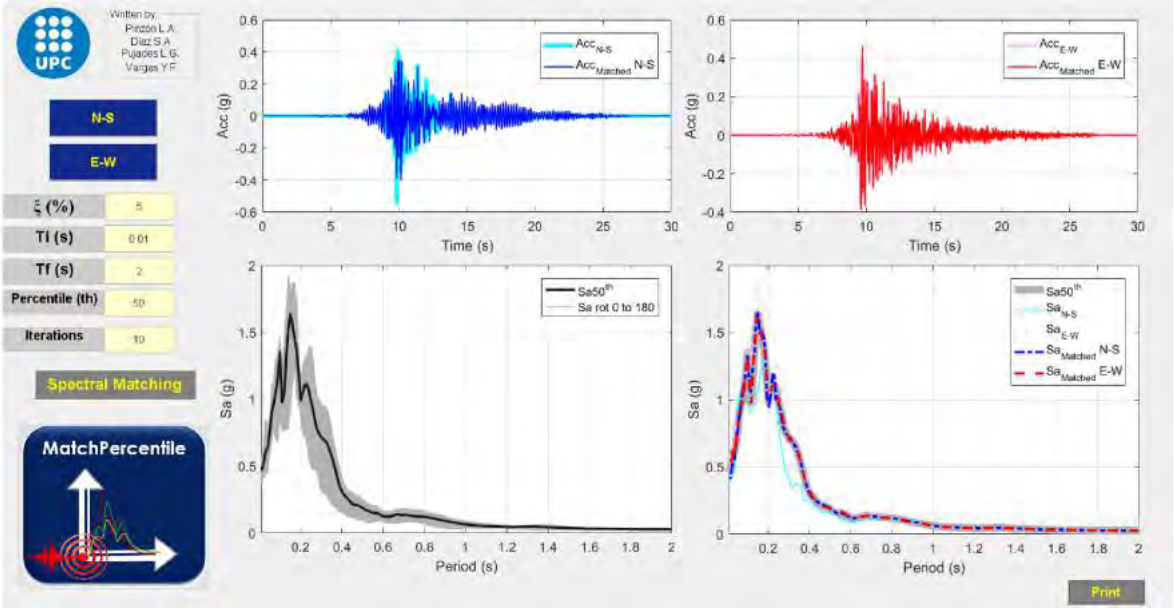

Figure 27: Main screen of the MatchPercentile application.

4.3.3 Spectral matching technique

The increasing capabilities of modern computers have increased the importance and usefulness of dynamic analyses both for designing new structures and for assessing the expected performance of existing ones. Therefore, the availability of accelerograms fulfilling specific requirements is an issue of broad interest, especially when design or assessment are tackled from a probabilistic point of view. For this purpose, the spectral matching technique properly modifies the Fourier amplitude spectrum of a seed accelerogram so that the response spectrum is compatible with a predefined target spectrum, usually a code, prescribed or recommended, design spectrum.

Given an actual accelerogram, the key of the spectral matching method entails modifying its Fourier amplitude spectrum so that the response spectrum coincides with a target one. In an ideal world and for undamped systems, replacing the Fourier spectrum amplitudes by the target undamped velocity response spectrum would lead to a reasonable estimate of the solution of the problem. In practice and for any response spectrum, spectral matching involves an iterative process. This iterative process is necessary due to the nonlinearity of the response.

This iterative process may be applied to adjust acceleration, as well as velocity and displacement response spectra whichever the damping be since each iteration adequately modifies the Fourier spectrum according to the target spectrum. Thus, the spectral matching is done according to the following steps: Step 1) substitute the Fourier amplitude spectrum by the target spectrum; Step 2) calculation of the response spectrum SR, of the accelerogram; Step 3) a Factor function F_{jk} is defined as follows:

$$F_{jk} = \frac{SR_{obj}}{SR_{jk}} \begin{cases} j = 1 \cdots N_{freq} \\ k = 1 \cdots N_{Iter} \end{cases} \tag{14}$$

subscript j refers to the j^{th} coordinate of both target spectrum (SR_{obj}) and response spectrum (SR); the subscript k refers to the k^{th} iteration; Step 4) a new accelerogram is defined by multiplying the Fourier amplitude spectrum by the factor F_{jk}; the inverse Fast Fourier Transform (FFT) provides the new accelerogram; Step 5): error analysis to end the iterative process or, eventually, to go back to Step 2. The iterative process may be concluded when an error criterion is fulfilled or a maximum

number of iterations is met. It must be noted that Step 1) is optional and can be omitted; sometimes Step 1 speeds up the convergence of the iteration process, but the improvement of the final result of the spectral matching is not guaranteed. There are two crucial numerical aspects of accomplishing Step 3: i) modifying the Fourier spectrum should be done carefully and adequately. The FFT defines N FFT samples; the first $N/2$ correspond to positive frequencies between zero and the Nyquist frequency the rest of samples correspond to negative frequencies. The way for assigning the factor F_{jk} of Equation 14 is through a new function Θ_{ik} defined as follows:

$$\Theta_{ik} = F_{jk} \begin{cases} i = 1 & j = \frac{N}{2}; \\ i = 2, \cdots, \frac{N}{2} + 1 & j = 1 \cdots \frac{N}{2}; \\ i = \frac{N}{2} + 2, \cdots, N & j = N + 1 - i; \end{cases} \tag{15}$$

where N is the number of points of the accelerogram. Note that $N/2$, in Equation 15, is equal to N_{freq} in Equation 14. Thus, once the function Θ_{ik} is defined it suffices to multiply the amplitude of the Fourier transform by Θ_{ik}. ii) Simply because of round-off errors the modified Fourier transform may not be conjugate symmetric; that is $X(-\omega) \neq X^*(\omega)$. This feature should be carefully controlled in the computing platform used; MATLAB allows the *symmetric* option for the inverse FFT to ensure that the inverse transform is a real function.

4.4 Building's application model

Two 4-story steel buildings are analysed in this paper; namely regular (rectangular shape in plan, Figure 28) and irregular (L-shape in plan, Figure 29) buildings, with Special Moment Frames (SMF). Steel W type sections (wide flange American section) are used for beams and columns, which are joined by means of prequalified connections (ANSI/AISC 358-10, 2010) of Fully Restrained (FR) type. The buildings were designed for office use based on the provisions given in the ANSI/AISC 341-102010 (ANSI/AISC 341-10, 2010).

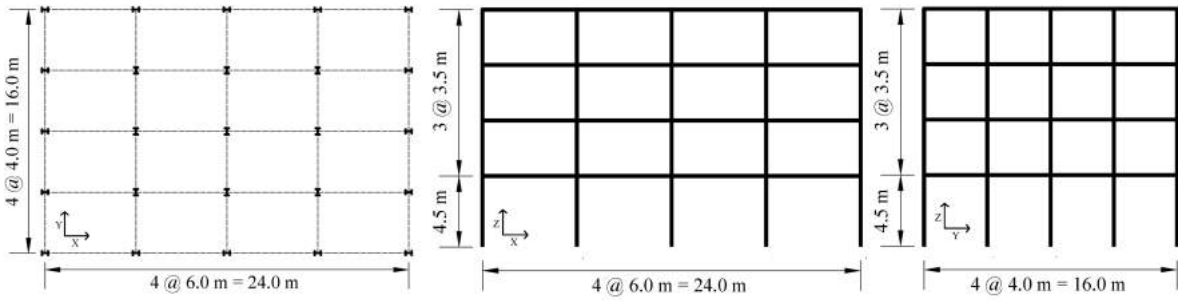

Figure 28: Regular steel frame model dimensions used to study the directionality effect.

Both buildings have column sections type W16X89 and beam sections type W14X68 according to the ASTM A992. The buckling in columns was controlled in the design. The design of the SMFs satisfies the AISC criterion "strong- column-weak-beam" and the structural sections of the columns meet the slenderness criterion presented in ANSI/AISC341-102010 (ANSI/AISC 341-10, 2010).

The NLDAs are performed with Ruaumoko 3D software (Carr, 2002). The weight of the structure, as well as that of the architectural finishes and facilities, were considered as dead loads (DL), while the live loads values (LL) were selected according to ASCE-7 (ASCE, 2010) provisions for office use. Notice that beams and columns were modelled as frame type members, with plastic hinges at their ends. Plastic hinges follow the Bi-Linear Hysteresis rule with hardening and strength reduction based

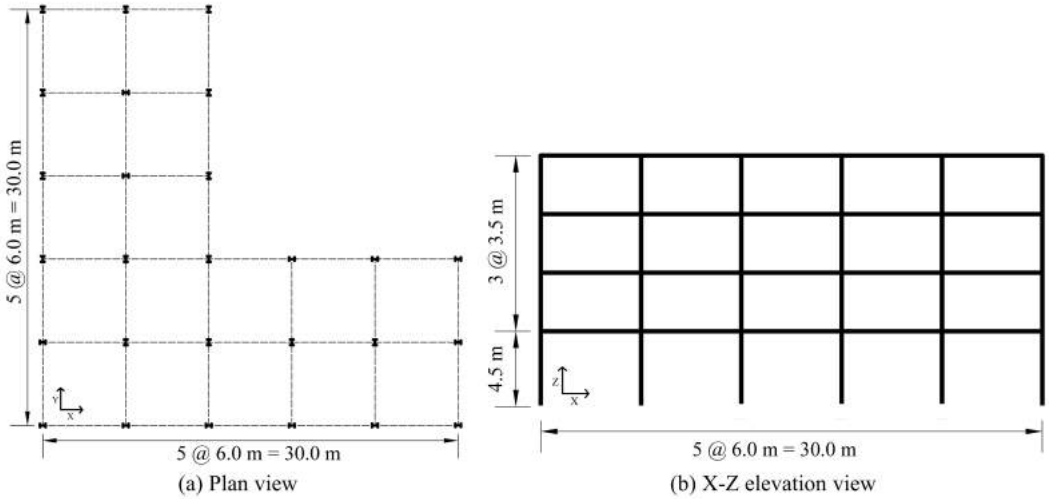

Figure 29: Irregular steel frame model dimensions used to study the directionality effect.

on the ductility factor (Carr, 2002). Moreover, the values of strength and ductility for the hysteresis rule were calculated according to the modified Ibarra–Medina–Krawinkler (IMK) model (Ibarra et al., 2005; Lignos and Krawinkler, 2011, 2013; Diaz et al., 2017).

The interaction force between the two horizontal directions is considered in the nonlinear structural model. To do so, regarding the restoring stiffness forces, the interaction between the element forces in both horizontal directions is considered through the interaction yielding surface proposed by Chen and Atsuta (Chen and Atsuta, 1976) for columns type section W, which is given by the following equation:

$$\frac{\left(\frac{M_z}{MY_z}\right)^{\alpha}}{1-\left(\frac{P}{P_y}\right)^{\beta}} + \frac{M_y}{MY_y} + \left(\frac{P}{P_y}\right)^{\gamma} = 1 \tag{16}$$

where P_y is the axial yielding load; MY_z and MY_y are the bending yielding moments about the Z and Y axes of the structural section; P, M_z and M_y are the acting axial load and bending moments about the Z and Y axes; α, β and γ are the interaction terms defining the yielding surface in the transition between principal axes.

P-Delta effects have been considered in all the simulations to take into account the global stability of the structure. The panel zones were modelled by the rotational stiffness in the connections according to the model proposed by Krawinkler (1978) and presented in FEMA 355C (2000). In all cases, as recommended for steel structures, for the first and last vibration mode under consideration (SAC, 1996), a value of 2% of damping was considered; the Rayleigh damping model was used in all the calculations. The main modal properties of the buildings are summarized in Tables 11 and 12.

Table 11: Values of T_1, W, PF_1 and α_1 of the regular building.

Dir.(1)	T_1(2) [s]	W(3) [kN]	PF_1(4)	α_1(5)
X	0.89	12460	1.28	0.881
Y	1.04	12460	1.20	0.885

(1) Building principal axes.
(2) Building fundamental period in seconds.
(3) Total weight in kN.
(4) Modal participation factor.
(5) Modal mass coefficient for fundamental period.

Table 12: Values of T, PF, α_x and α_y of the irregular building.

Dir.[6]	T[7] [s]	PF[8]	α_x[9]	α_y[10]
1	1.41	0.74	0.49	0.01
2	0.92	0.44	0.31	0.07
3	0.87	1.07	0.01	0.77

(6) Vibration mode.
(7) Building period in seconds.
(8) Modal participation factor.
(9) Modal mass coefficient in x-axis.
(10) Modal mass coefficient in y-axis.

4.5 Ground motions selection

A ground motion selection process has been made with the aim of obtaining a group of records with diverse characteristics. The Italian accelerometric archive (ITACA) (Luzi et al., 2017) has been considered for this purpose. A total of 20 ground motions pairs (GMP) recorded in Italy were used according to the following conditions: a) Site conditions A (2 GMP), B (6 GMP), C (10 GMP) and E (2 GMP), following the Eurocode 8 specifications; b) Earthquakes Type 1 (11 GMP) and 2 (9 GMP), following the Eurocode 8 specifications; c) Peak ground acceleration (PGA) $\geq$ 0.05 g; d) Depth $\leq$ 10 km. Table 13 shows the 20 ground motion pairs selected and their principal characteristics.

Figure 30 shows the particle acceleration motions of the 20 ground motion pairs selected. In this figure, different cases of polarization can be observed. Notice that most of them exhibit circularly motions. There are some cases as, for instance, ground motions 7, 17 and 18, in which a more linearly polarized behavior can be detected. Moreover, for the 20 ground motions, the maximum acceleration is also highlighted in this figure and it can be appreciated that it occurs for a different angle respect to the as-recorded one.

4.6 Results

The NLDA results obtained after performing the CRM and the PPM, which have been found after analyzing both regular and irregular 4-story SMF 3D models, with the 20 pairs of ground motion presented in Table 13, are presented in this section.

4.6.1 Regular building

To prove the effectiveness of the PPM, the Umbrian earthquake of October 30, 2016, recorded at T1220 station, was used as example. This earthquake registered a PGA of 0.26 g in the N-S component and 0.24 g in the E-W. In Figure 31 the horizontal acceleration records of the described earthquake are shown.

Firstly, these as-recorded components were used to compute the CRM in the regular building. Therefore, 180 NLDA were performed and the roof displacement and the base shear were calculated for each rotational angle. Figures 32 and 33 show the results obtained based on this method. The angle producing the maximum roof displacement in the X-Direction is 175° and in the Y-Direction is 103° (see Figure 32). The base shear is maximum in the X-Direction for an angle equal to 5° and in the Y-Direction for an angle equal to 110° (see Figure 33). It is important to mention that the plastic hinges occurring in the structure generally appear at the ends of the beams. Notice that this location varies from record-to-record and depend on the rotational angle.

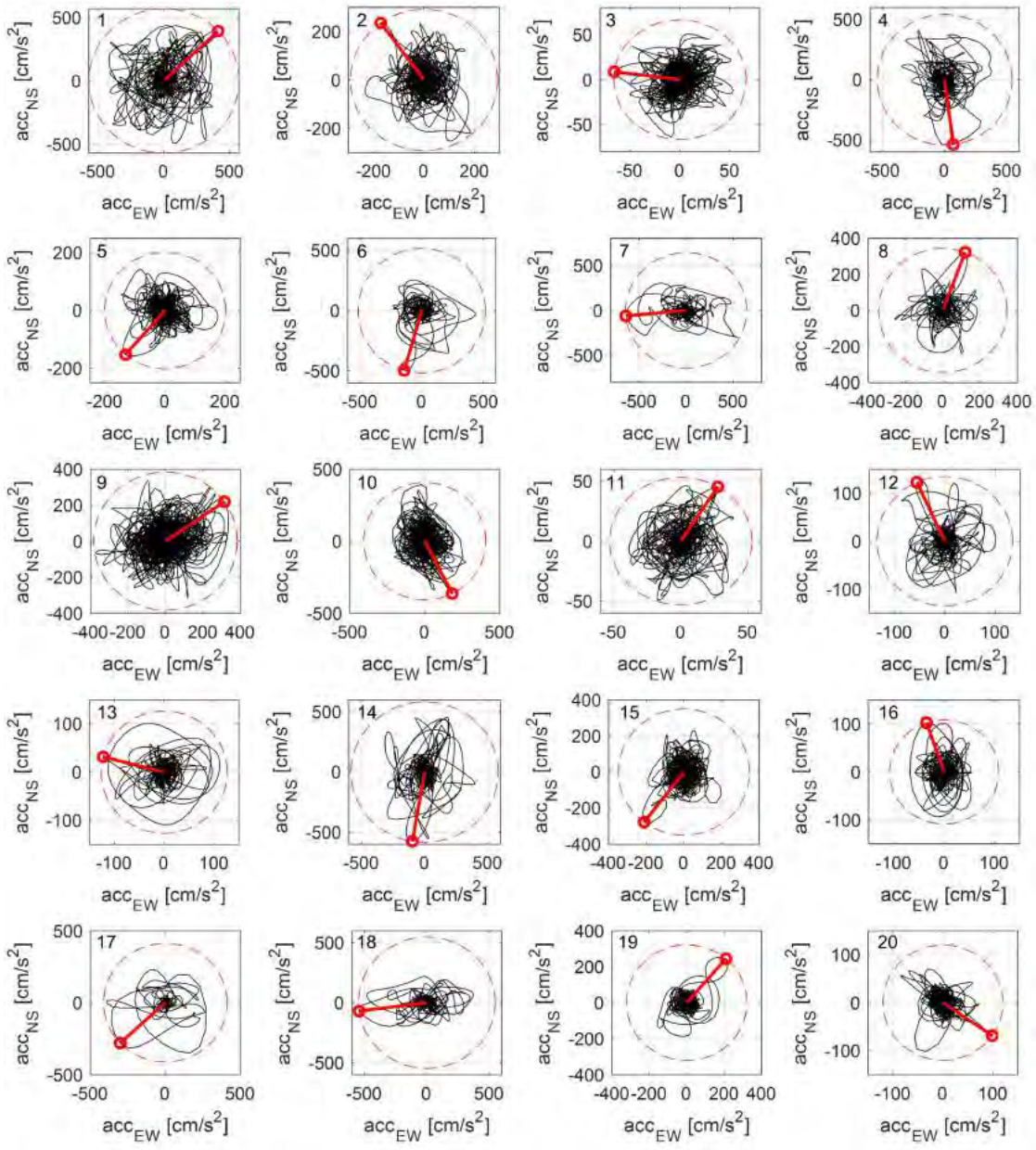

Figure 30: Particle acceleration motions of the 20 selected accelerograms.

Table 13: Ground motions selection from ITACA database.

#	Region	Station[10]	Event date	Time [HH:MM:SS]	M_W[11]	Epi.[12] [km]	Depth [km]	PGA N-S[13] [g]	PGA E-W[14] [g]	Fault	Soil EC8[15]
1	Umbria	NCR	26/09/1997	09:40:30	6.0	10.9	6.0	0.50	0.42	Normal	E
2	Umbria	T1220	30/10/2016	06:40:18	6.5	30.9	9.2	0.26	0.24	Normal	B
3	Lazio	SPM	24/08/2016	01:36:32	6.0	39.6	8.1	0.06	0.07	Normal	A
4	Marche	MCV	26/10/2016	19:18:06	5.9	14.0	7.5	0.55	0.38	Normal	B
5	Umbria	GAG1	30/10/2016	06:40:18	6.5	45.2	9.2	0.16	0.18	Normal	B
6	Medolla	T0814	29/05/2012	07:00:02	6.0	9.3	8.1	0.51	0.44	Thrust	C
7	Marche	CMI	26/10/2016	19:18:06	5.9	7.1	7.5	0.31	0.65	Normal	C
8	Lazio	FOC	24/08/2016	01:36:32	6.0	45.7	8.1	0.33	0.26	Normal	C
9	Umbria	FOC	30/10/2016	06:40:18	6.5	27.8	9.2	0.34	0.38	Normal	C
10	Umbria	ACT	30/10/2016	06:40:18	6.5	25.6	9.2	0.40	0.28	Normal	C
11	Lazio	BVG	24/08/2016	01:36:32	6.0	57.2	8.1	0.05	0.04	Normal	C
12	Marche	CLO	26/10/2016	17:10:36	5.4	8.5	8.7	0.13	0.10	Normal	A
13	Umbria	NCR	14/10/1997	15:23:00	5.6	23.5	7.0	0.11	0.12	Normal	E
14	Abruzzo	PCB	18/01/2017	10:14:12	5.5	5.6	9.1	0.59	0.41	Normal	B
15	Abruzzo	MSCT	18/01/2017	10:25:26	5.4	4.9	8.9	0.29	0.23	Normal	B
16	Abruzzo	RQT	18/01/2017	10:25:26	5.4	35.4	8.9	0.10	0.07	Normal	B
17	Umbria	CLC	16/10/1997	12:00:31	4.3	1.3	0.9	0.36	0.39	Strike-slip	C
18	Marche	CNE	26/10/2016	17:10:36	5.4	2.6	8.7	0.22	0.56	Normal	C
19	Medolla	MIR01	29/05/2012	10:55:56	5.5	7.6	4.4	0.26	0.23	Thrust	C
20	Abruzzo	ACT	18/01/2017	10:25:26	5.4	31.9	8.9	0.10	0.10	Normal	C

(10) Accelerometric stations code.
(11) Moment magnitude.
(12) Epicentral distance in km.
(13) Peak ground acceleration recorded in N-S horizontal component.
(14) Peak ground acceleration recorded in E-W horizontal component.
(15) Site condition following the Eurocode 8 specifications.

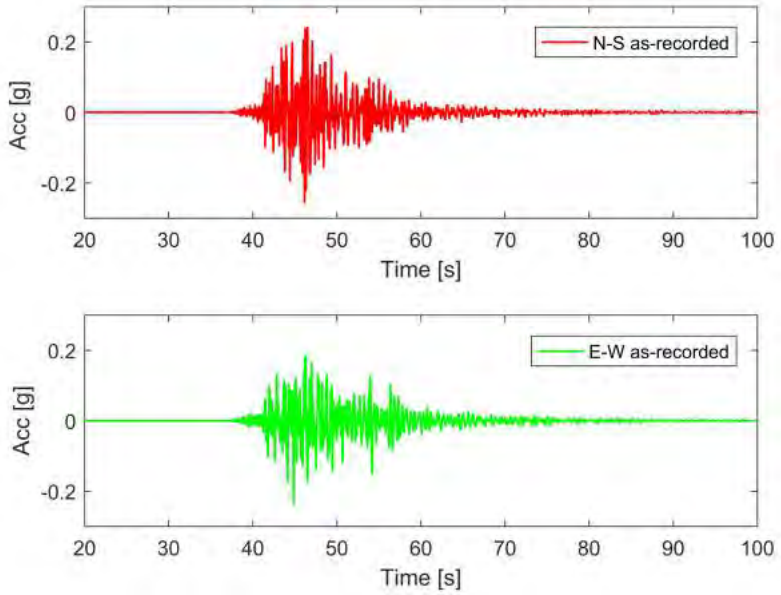

Figure 31: Accelerograms of the as-recorded N-S and E-W horizontal components from Umbria, Italy earthquake (October 30, 2016) recorded in T1220 station.

For the PPM, the horizontal as-recorded components of acceleration were used as input for the MatchPercentile application. The analysis was performed with a damping ratio equal to 2%; this value is recommended for steel frame buildings (Paz and Leigh, 2003). In Figure 34, the RotD100 (MaxRotD100), RotD50 (MedianRotD50) and the as-recorded components spectra are compared. The spectra corresponding to RotD100 and RotD50, become target spectra and the as-recorded ground motions are adjusted accordingly. Once adjusted, two new ground motions are generated, whose response spectra are RotD100 and RotD50, respectively. The new acceleration components are compared to the original ones in Figure 35.

The matched accelerograms N-S $\text{Max}_{RotD100}$ and E-W $\text{Max}_{RotD100}$ are used as input to perform the NLDA and to estimate the maximum expected demand. The N-S Median_{RotD50} and E-W Median_{RotD50} are also used as input to estimate the median demand. After the NLDAs are performed, for the two cases mentioned above, two demand values were obtained for each direction. These values represent the maximum and the median response of the building. Figures 36 and 37 show the comparison between the results obtained with the CRM and PPM, respectively.

The results obtained with the proposed method show a good agreement with the maximum and median values obtained with the CRM (Figure 38). Regarding the maximum roof displacement, in the X-Direction, a value of 17.40 cm was obtained with CRM and 17.83 cm with PPM; in the Y-Direction, the values obtained are 6.89 and 7.23 cm, respectively. The difference between these values is approximately 2% for the X-Direction and 5% for the Y-direction. In the case of the median roof displacement values, in the X-Direction, a value of 16.25 cm was obtained with CRM and 16.10 cm with PPM; in the Y-Direction values of 5.00 cm and 5.15 cm were obtained, respectively. Differences of 1% (X-Direction) and 3% (Y-Direction) were obtained.

Regarding the maximum base shear, in the X-Direction, a value of 7587 kN was achieved with the CRM and 7770 kN with the PPM; in the Y-Direction values of 2397 kN and 2513 kN were obtained, respectively. Such results represent differences of 2% in the X-Direction and 5% in the Y-Direction.

Finally, comparing the median base shear with the CRM, values of 7282 kN and 1858 kN were obtained for the X and Y directions, respectively. With PPM, values of 7267 kN and 1829 kN were

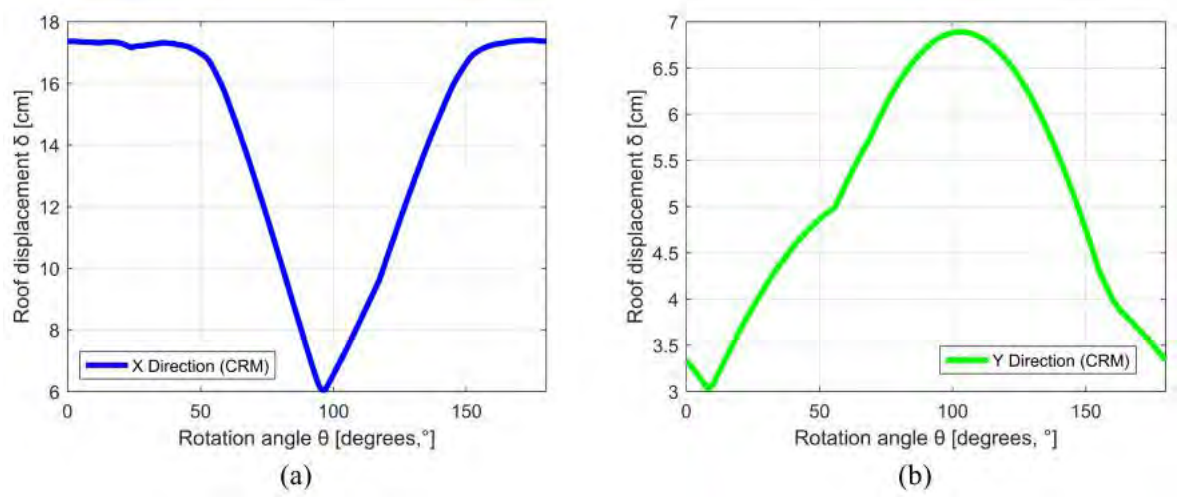

Figure 32: Influence of the angle of incidence on (a) roof displacement in X-Direction and (b) roof displacement in Y-Direction of the regular building.

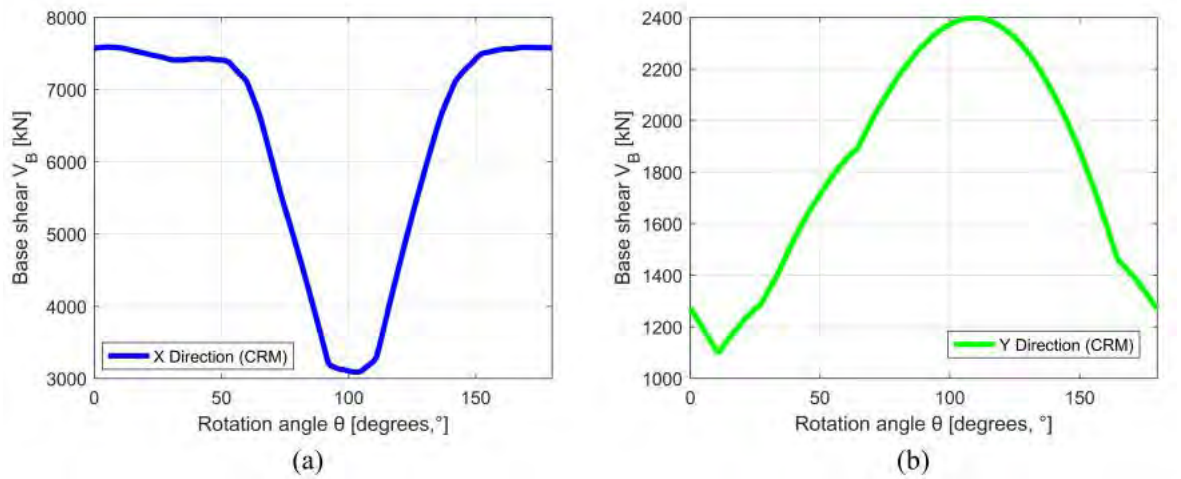

Figure 33: Influence of the angle of incidence on (a) base shear in X-Direction and (b) base shear in Y-Direction of the regular building.

obtained for the X and Y directions, respectively. These results represent differences of less than 1% in the X-Direction and 1.5% in the Y-Direction. In general, the differences obtained with the 20 GMP are in average of 4% for the roof displacement and 5% for the base shear values. A summary of the results obtained for the 20 GMP pairs can be seen in Tables A1, A2, A3 and A4 from Appendix A.

4.6.2 Irregular building

In the same way as the regular building, the as-recorded components, and the matched accelerograms N-S $\text{Max}_{RotD100}$ and E-W $\text{Max}_{RotD100}$, were used to compute the CRM and the PPM in the irregular one, respectively. Instead of 180 NLDA, 360 were performed with the CRM, due to the irregularity of the building. The roof displacement and the base shear were also estimated for each rotational angle. The maximum values obtained with the CRM were compared with the obtained ones using the PPM. As an example, Figure 39 shows the results obtained with the ground motions of the Umbrian earthquake occurred on October 30, 2016, and recorded at T1220 station.

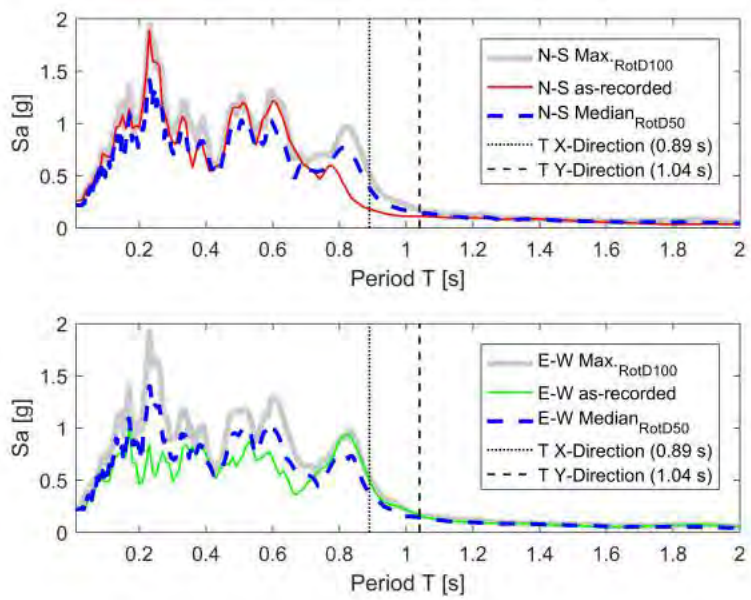

Figure 34: Regular building principal axes fundamental period (T X-Direction and Y-Direction), 2% damped response spectra corresponding to the maximum demand ($\text{Max}_{RotD100}$), median demand (Median_{RotD50}), and the as-recorded N-S and E-W horizontal components from Umbria, Italy earthquake (October 30, 2016) recorded in T1220 station.

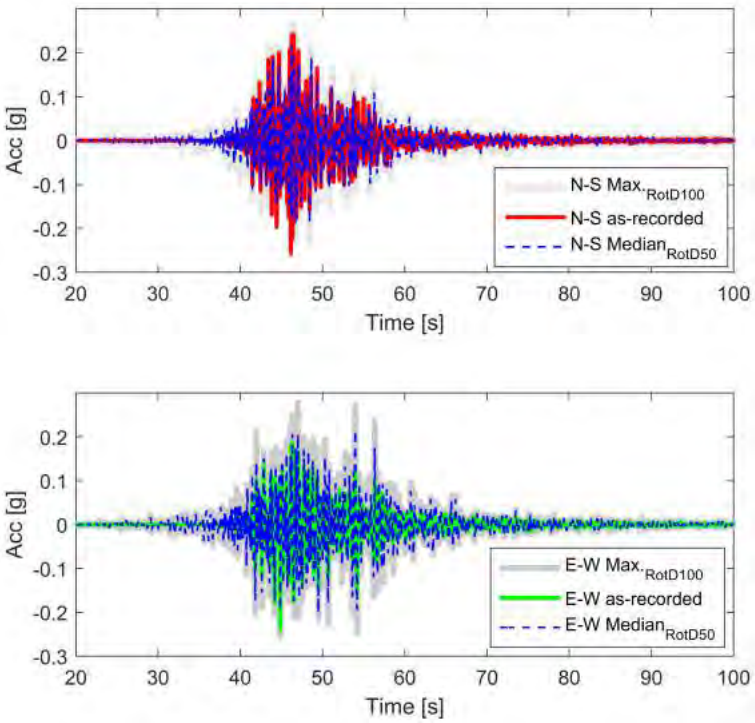

Figure 35: Matched accelerograms spectra corresponding to the maximum demand ($\text{Max}_{RotD100}$), median demand (Median_{RotD50}) and the as-recorded N-S and E-W horizontal components from Umbria, Italy earthquake (October 30, 2016) recorded in T1220 station.

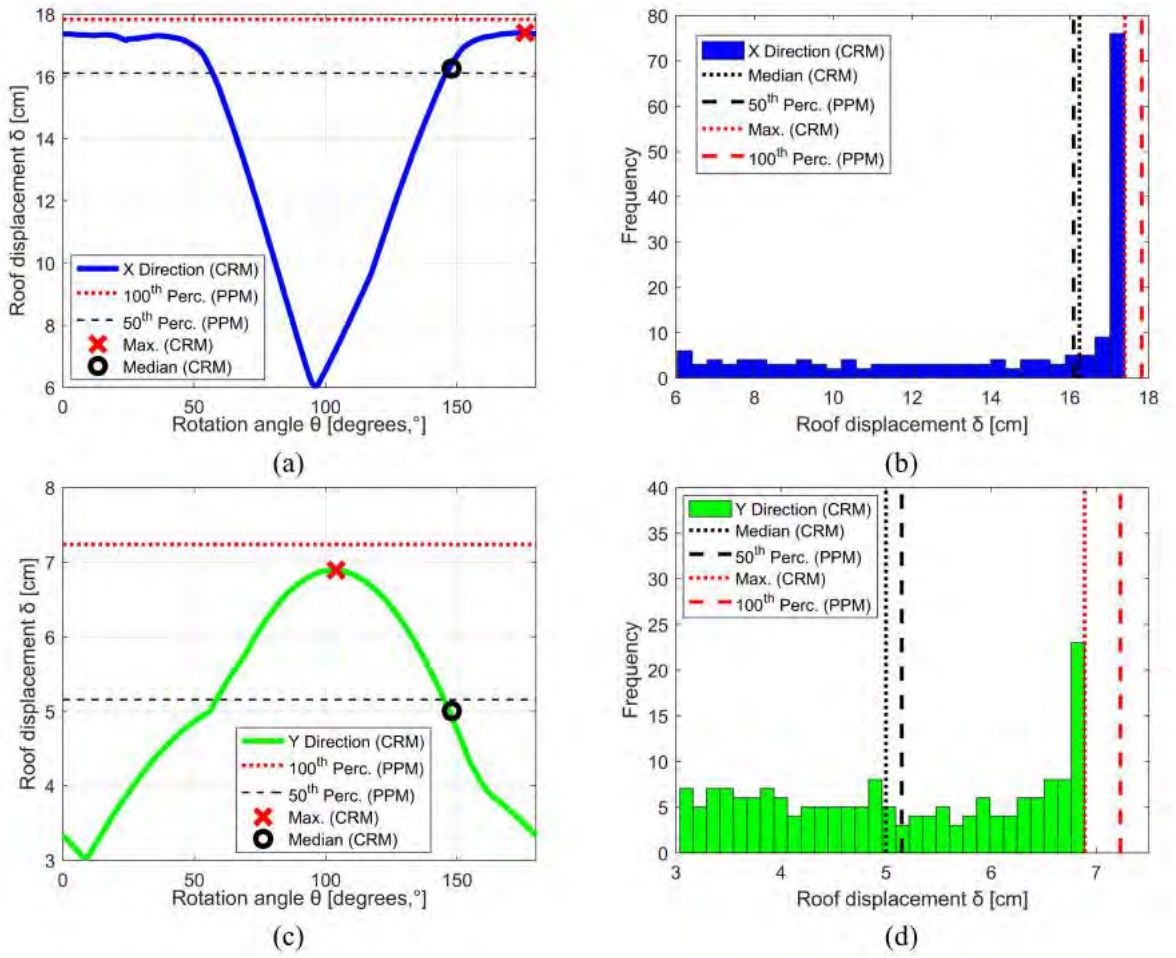

Figure 36: Comparison between the roof displacement results from both CRM and PPM method for the regular building. Values of the median and maximum response in (a) roof displacement as a function of the rotation angle in X-Direction; (b) histogram of roof displacement values in X-Direction; (c) roof displacement as a function of the rotation angle in Y-Direction; (d) histogram of roof displacement values in Y-Direction.

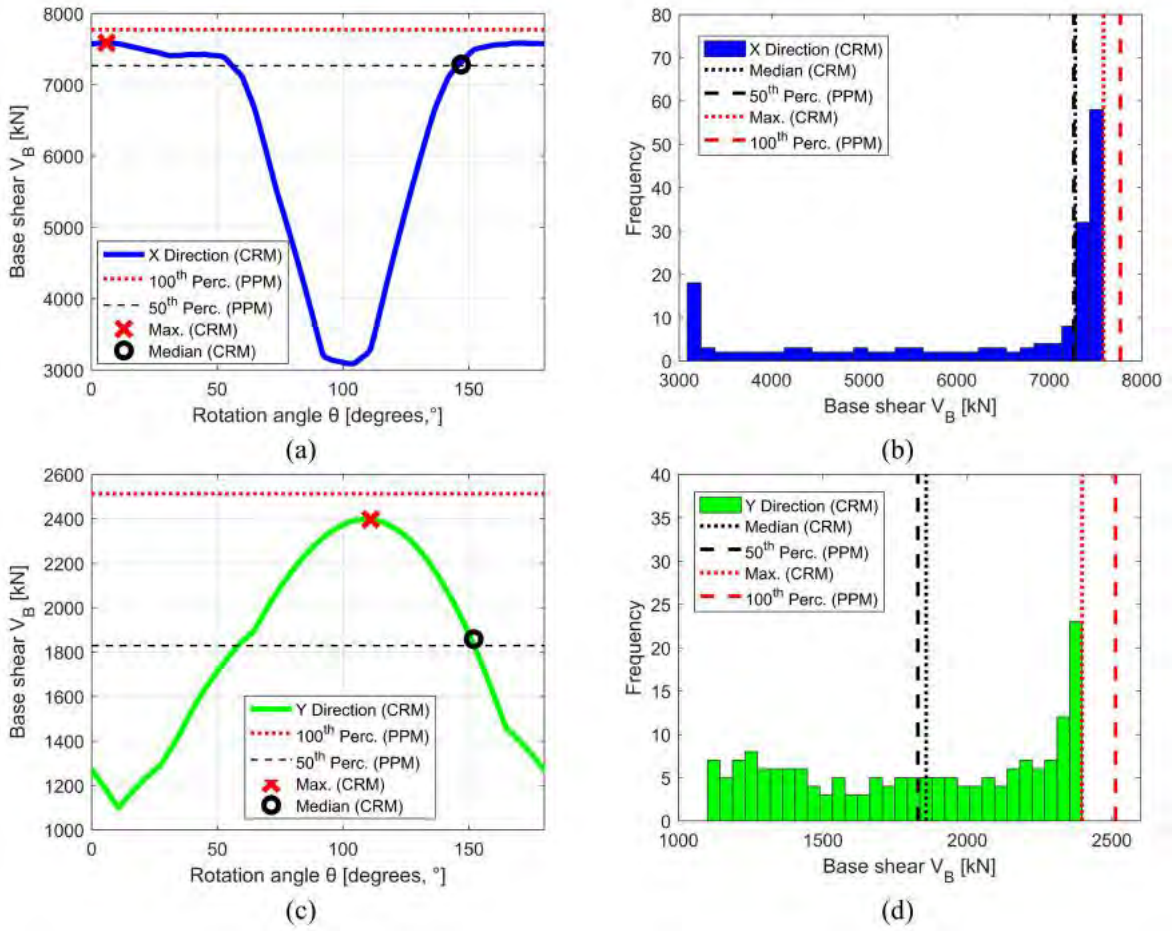

Figure 37: Comparison between the base shear results from both CRM and PPM method for the regular building. Values of the median and maximum response in (a) base shear as a function of the rotation angle in X-Direction; (b) histogram of base shear values in X-Direction; (c) base shear as a function of the rotation angle in Y-Direction; (d) histogram of base shear values in Y-Direction.

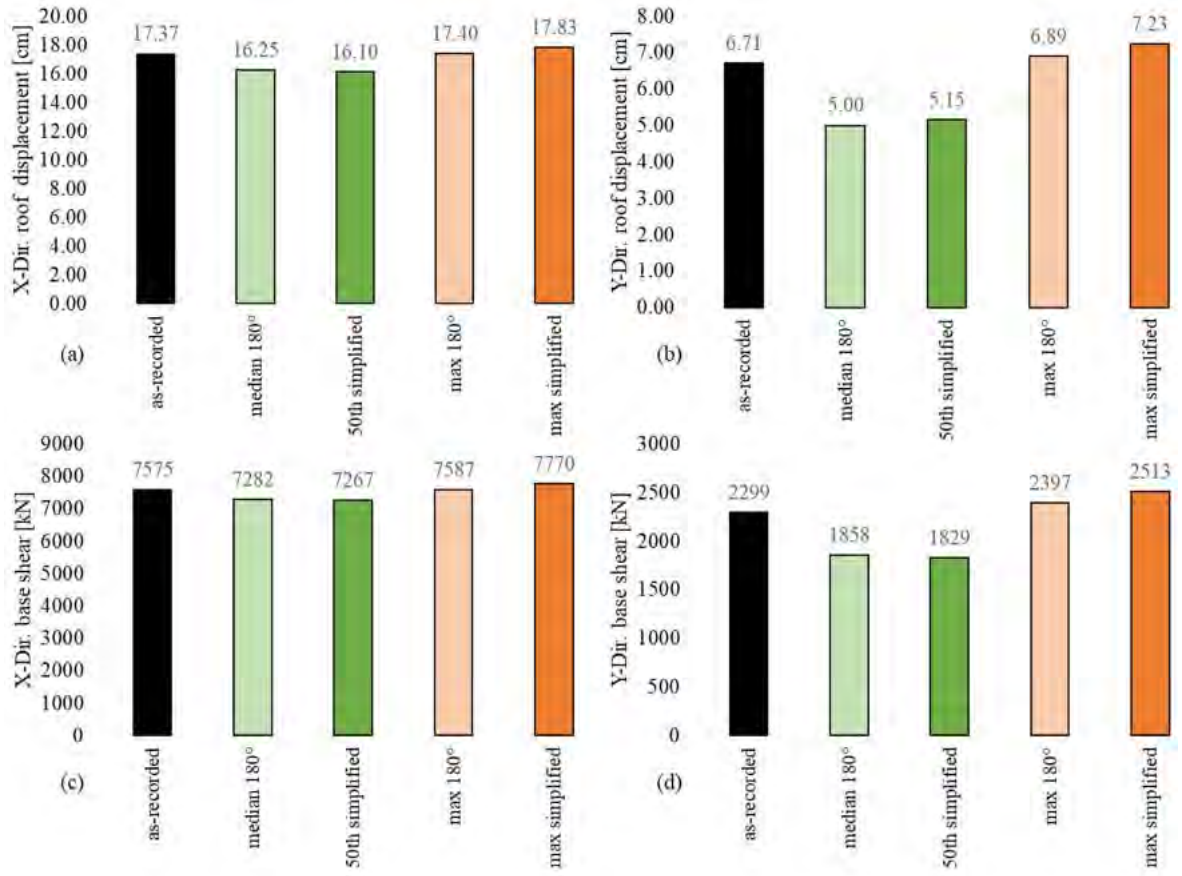

Figure 38: Bar graphics comparing the CRM and the PPM for the regular building. Values of the as-recorded, median and maximum response of (a) roof displacement in X-Direction and (b) roof displacement in Y-Direction (c) base shear in X-Direction and (d) base shear in Y-Direction.

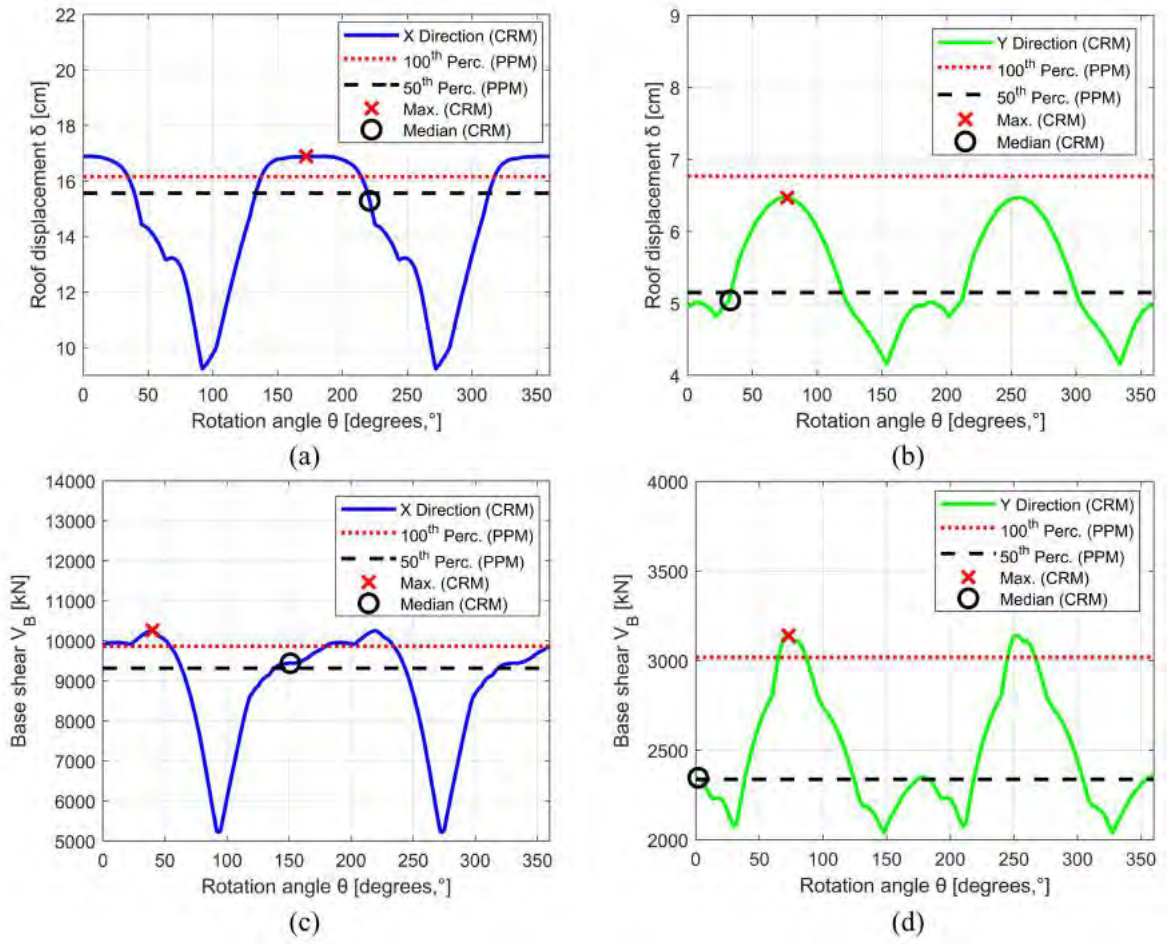

Figure 39: Comparison between the base shear results from both CRM and PPM method for the irregular building. Values of the median and maximum response in (a) base shear as a function of the rotation angle in X-Direction; (b) same in Y-Direction; (c) base shear as a function of the rotation angle in X-Direction; (d) same in Y-Direction.

The maximum roof displacement, in the X-Direction, registered a value of 16.89 cm was obtained with CRM and 16.15 cm with PPM; in the Y-Direction, the values obtained are 6.47 and 6.76 cm, respectively. The difference between these values is approximately 4% for the X-Direction and 5% for the Y-direction. The difference increases 2% in the X-direction compared to the regular building analysis. In the case of the median values of roof displacement, in the X-Direction, a value of 15.29 cm was obtained with CRM and 15.56 cm with PPM; in the Y-Direction values of 5.04 cm and 5.15 cm were obtained, respectively. Differences of 2% in both directions were obtained. Similar results were obtained with the regular building.

Regarding the maximum base shear, in the X-Direction, a value of 10260 kN was achieved with the CRM and 9869 kN with the PPM; in the Y-Direction values of 3140 kN and 3018 kN were obtained, respectively. These results represent differences of 4% in the X-Direction and 4% in the Y-Direction. Finally, comparing the median base shear with the CRM, values of 9443 kN and 2346 kN were obtained for the X and Y directions, respectively. With PPM, values of 9317 kN and 2338 kN were obtained for the X and Y directions, respectively. These results represent differences of 1% in both directions. Similar results were obtained with the regular building.

In general, the differences obtained with the 20 GMP are in average of 4% for the roof displacement and 6% for the base shear values, almost the same as the regular building. A summary of the results obtained for the 20 GMP can be seen in Tables A5, A6, A7 and A8 from Appendix A.

4.6.3 Performance in the non-linear range

To evaluate the performance of the buildings and to validate the PPM approach in the non-linear range, the analyses have been performed with scaled ground motions. To ensure that the buildings are in the non-linear range, the 20 GMP from Table 13 were scaled to achieve a damage index between 0.2 and 0.5 in each structure (Diaz et al., 2017). The results obtained after performing the CRM and the PPM for the maximum values can be seen in Tables 14 and 15 for the regular building and Tables 16 and 17 for the irregular one.

The results obtained with the proposed method are very close to those obtained through the CRM. Regarding the maximum roof displacement, in the X-Direction, differences of 4% and 3% (in average) were obtained for the regular and irregular buildings, respectively, when comparing the CRM and PPM results. In the Y-Direction, the differences are 4% and 5% for the regular and irregular, respectively. Comparing the maximum base shear obtained with the CRM and PPM, in the X-Direction, differences of 3% (in average) for both, regular and irregular building, were found. Finally, for the Y-Direction, differences of 4% and 3% in the maximum base shear were obtained for the regular and irregular buildings, when comparing the results of both methods.

4.6.4 Near- and far-fault earthquakes

Near-fault earthquakes ground motion records are very different compare to far-fault ground motions. Near-fault records are characterized by having a long-period pulse in the velocity time history of the normal-fault component due to the directivity effect of these kind of events (Chopra and Chintanapakdee, 2001). In Figure 40, the ground motion time-histories of the earthquake of Abruzzo (2017) recorded in the MSCT station are shown as an example of a near-fault earthquake (GMP 15 from Table 13). A clear pulse can be observed in the histories of velocities and displacements. Also, Figure 41 displays the 5% damped elastic response spectra in acceleration, velocity and displacement for the same GMP. Another characteristic of the near-fault earthquakes' records is that the response spectra of the horizontal components are very different (Chopra and Chintanapakdee, 2001).

Table 14: Regular building results; roof displacement and base shear in X-Direction for the 20 scaled ground motion pairs selected from the ITACA database.

X-Direction	Roof displacement (δ) [cm]		Base Shear (V_B) [kN]	
#	Max. (CRM)	100th Perc. (PPM)	Max. (CRM)	100th Perc. (PPM)
1	18.3	20.2	9150	9261
2	17.4	17.8	7587	7770
3	18.0	18.6	8135	7827
4	19.8	19.9	8684	8606
5	20.0	21.5	8506	8300
6	19.7	20.0	9061	8604
7	21.6	21.2	8922	8685
8	10.9	9.9	9135	8953
9	17.8	18.6	9290	9154
10	19.2	18.7	8916	8722
11	18.4	18.8	7029	7119
12	16.9	16.9	7395	7054
13	19.4	20.8	8960	8537
14	13.3	13.8	7058	7137
15	14.8	15.1	7638	7859
16	20.2	21.5	8491	8276
17	22.3	20.3	9766	8738
18	14.2	14.1	9330	8912
19	16.7	18.1	8484	8704
20	18.0	19.0	8823	8405

Table 15: Regular building results; roof displacement and base shear in Y-Direction for the 20 scaled ground motion pairs selected from the ITACA database.

Y-Direction	Roof displacement (δ) [cm]		Base Shear (V_B) [kN]	
#	Max. (CRM)	100th Perc. (PPM)	Max. (CRM)	100th Perc. (PPM)
1	19.0	20.8	5981	5897
2	6.9	7.2	2397	2513
3	19.2	18.3	6900	6600
4	15.8	17.1	6520	6340
5	17.4	17.2	5537	5799
6	19.6	19.7	5919	5738
7	22.7	21.3	6560	6500
8	8.5	8.7	6041	6140
9	12.0	11.4	7016	6706
10	22.2	22.4	6042	6018
11	17.9	17.6	5383	5637
12	20.5	19.2	6569	6060
13	16.5	16.5	7059	7055
14	14.9	14.9	6308	5680
15	22.0	22.0	6445	6559
16	19.7	20.8	6584	6148
17	19.8	20.0	6826	6266
18	15.0	15.4	6975	6875
19	17.7	18.5	6261	6387
20	18.4	17.4	5911	6016

Table 16: Irregular building results; roof displacement and base shear in X-Direction for the 20 scaled ground motion pairs selected from the ITACA database.

X-Direction	Roof displacement (δ) [cm]		Base Shear (V_B) [kN]	
#	Max. (CRM)	100th Perc. (PPM)	Max. (CRM)	100th Perc. (PPM)
1	16.7	16.7	10727	10379
2	16.9	16.2	10264	9869
3	19.7	20.4	11451	11035
4	19.1	18.3	13234	13520
5	21.2	22.4	11119	10880
6	18.4	18.1	12170	12158
7	18.7	19.5	11475	11453
8	10.0	10.0	12454	11575
9	19.6	20.2	13209	13341
10	17.9	18.0	11334	11458
11	18.1	18.8	10430	10678
12	15.4	15.8	8582	9215
13	16.3	16.6	13183	12872
14	14.8	15.3	10966	10793
15	14.2	15.0	10362	10169
16	18.2	18.6	12646	12870
17	21.8	21.3	13051	13135
18	9.0	9.2	11741	11598
19	15.3	16.7	13263	13702
20	17.4	16.8	11780	12325

Table 17: Irregular building results; roof displacement and base shear in Y-Direction for the 20 scaled ground motion pairs selected from the ITACA database.

Y-Direction	Roof displacement (δ) [cm]		Base Shear (V_B) [kN]	
#	Max. (CRM)	100th Perc. (PPM)	Max. (CRM)	100th Perc. (PPM)
1	12.3	12.0	5508	6042
2	6.5	6.8	3132	3018
3	16.2	16.6	8246	8358
4	17.3	18.4	8508	8596
5	15.2	16.4	7025	6540
6	18.3	16.5	7084	6698
7	17.4	16.8	7194	7180
8	8.1	7.5	7873	7943
9	15.1	15.6	9228	9435
10	15.2	14.7	8233	7620
11	15.6	16.0	5068	5228
12	15.2	13.8	7094	7123
13	17.8	16.5	9333	9453
14	11.4	10.8	8174	8067
15	16.4	16.7	7644	7477
16	16.9	17.4	8406	8764
17	19.5	19.0	7562	7608
18	8.1	8.3	8921	8476
19	14.7	16.2	7208	7659
20	15.1	15.0	8593	8578

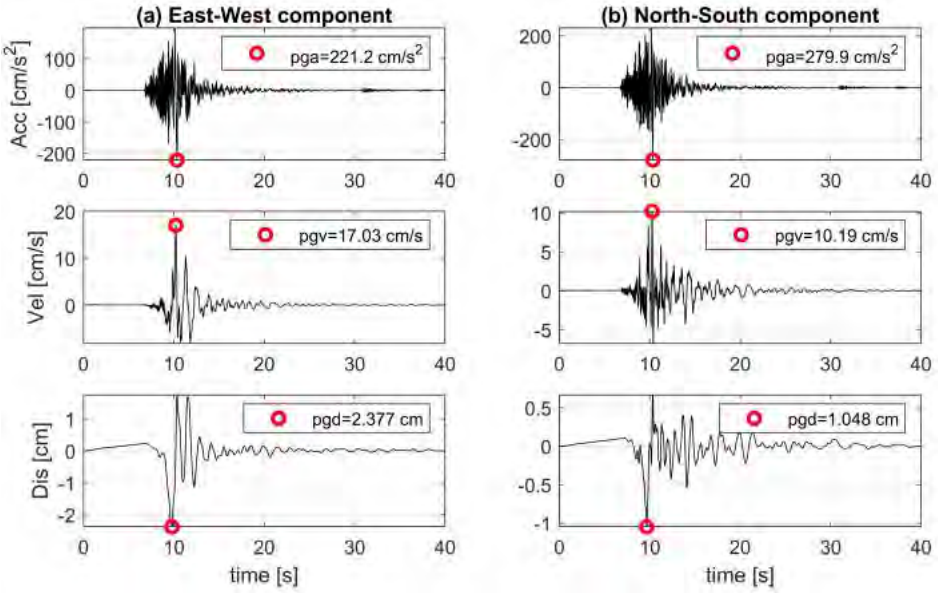

Figure 40: (a) E-W and (b) N-S as-recorded components of ground motions recorded at MSCT station, 2017 Abruzzo earthquake.

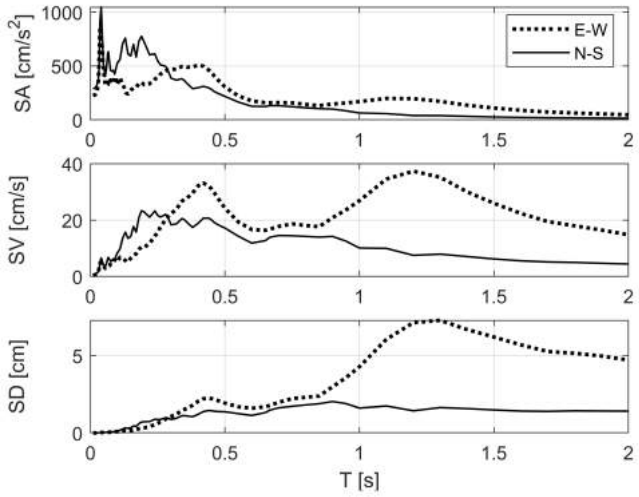

Figure 41: Response spectra for as-recorded ground motions components of MSCT station, 2017 Abruzzo earthquake; damping ratio = 5%.

The impulsive characteristic of these earthquakes has attracted the attention of researchers when assessing the seismic response of a structure. For this reason, the 20 GMP used in this study have been grouped according to their proximity to the fault. The objective is to validate the PPM for both types of records, near and far-fault, by analyzing the results independently. Table 18 present the hypocentral distance, peak ground acceleration (PGA), peak ground velocity (PGV), peak ground displacement (PGD) and fault proximity (NF: near-fault and FF: far-fault) for the 20 GMP. The selection has been made according to the study of Chopra and Chintanapakdee (Chopra and Chintanapakdee, 2001). A total of 10 near-fault and 10 far-fault earthquakes were obtained after the characterization.

Notice that the average error in percentage (%, 1-CRM/PPM) found after comparing the maximum values of roof displacement and base shear by considering the non-scaled and scaled GMP, for the regular and irregular buildings, are compared in Table 19. The results indicate that the average error in near-fault events are relatively higher in most cases, with exception of the non-scaled analysis for the irregular building where similar errors were observed.

Recent research has shown the importance of considering the directionality effect when estimating the seismic response of structures. It has been demonstrated that the structural response strongly varies depending on the orientation of the structure with respect to the seismic action. For instance, Vargas-Alzate et al. (2018) and Pinzón et al. (2018a) demonstrated how buildings with very similar structural system and dimensions, located very close to each other, had different damage states depending on their orientation respect to the earthquake source.

4.7 Discussion and conclusions

As can be seen in this study, neglecting the directionality effect could underestimate the actual demand about 30%, in some cases (see results of ground motion 1 in Tables A1 to A8). This fact reaffirms the importance of considering the directionality effect in the structural analysis. Moreover, it should be regarded in structural seismic codes since it allows to improve the evaluation of the expected seismic damage in structures. For instance, for special facilities such as nuclear plants, hospitals, schools and other facilities that need to be operating after an earthquake, the RotD100 matched accelerograms should be used to estimate the seismic demand. Therefore, it will be guaranteed that the maximum seismic demand will be considered in the structural analysis.

The predictive percentile method provides a simplified alternative to obtain any percentile response without the need of performing hundreds of NLDA; this represents a decrease from 180, if the increment for rotating the records is 1°, to only two NLDA. It is important to note that the PPM is useful to obtain a very good estimation of the variables analyzed when compared to the CRM, but this value do not always overestimate the one obtained with the CRM. For instance, note that in Table A1 the roof displacement under ground motion No. 8 and 18 are underestimated by using PPM. The same occurs in Table A2 in which the PPM leads to an underestimation of the roof displacement under ground motion No. 5. Moreover, the values presented in Tables 14-17 confirm that the estimation of the engineering demand parameters are randomly lower and higher than the one obtained with the CRM. However, as it has been mentioned above, the values obtained with the PPM are very close to the ones obtained through the CRM. Noteworthy, the differences in average are less than 5% when applying the PPM.

Notice that the simplified method could be easily extended to improve seismic structural codes when considering non-scaled ground motions in the NLDA. In this respect, many authors have reported increments of about 10% when estimating the RotD100 to their matched spectra, using spectrally matched ground motions instead of scaled or as-recorded ones (Carballo, 2000; Seifried, 2013; Baker et al., 2015).

Table 18: Hypocentral distance, PGA, PGV, PGD and source-type of the selected ground motions.

#	Hypo. [km]	PGA N-S [cm/s^2]	PGA E-W [cm/s^2]	PGV N-S [cm/s]	PGV E-W [cm/s]	PGD N-S [cm]	PGD E-W [cm]	Source
1	12.44	492.17	414.96	32.57	28.73	2.60	2.30	NF
2	32.24	252.48	234.25	16.39	15.60	2.45	3.04	FF
3	40.42	63.55	65.95	3.04	2.39	1.46	0.73	FF
4	15.88	538.79	377.21	17.13	12.70	2.50	1.47	NF
5	46.13	157.41	175.02	6.68	8.44	1.67	1.68	FF
6	12.33	495.60	435.68	21.12	23.58	5.70	4.58	NF
7	10.33	302.56	638.31	25.89	43.76	3.33	6.64	NF
8	46.41	322.54	256.20	10.18	8.10	1.34	0.83	FF
9	29.28	335.60	372.18	6.88	12.55	1.97	3.79	FF
10	27.20	392.65	273.69	10.04	5.59	6.68	2.39	FF
11	57.77	49.22	39.14	6.22	5.97	2.96	2.38	FF
12	12.16	125.18	100.48	4.79	5.24	0.70	0.85	NF
13	24.52	108.95	122.43	3.07	3.24	0.19	0.23	FF
14	10.69	575.00	400.43	21.03	16.91	2.18	1.32	NF
15	10.16	279.88	221.24	10.19	17.03	1.05	2.38	NF
16	36.50	102.53	67.72	2.07	1.93	0.18	0.23	FF
17	1.58	349.85	387.19	14.11	10.08	1.36	0.46	NF
18	9.08	219.47	545.57	8.42	17.34	0.71	1.23	NF
19	8.78	253.51	221.47	9.34	10.28	0.96	1.04	NF
20	33.12	101.97	98.54	2.01	3.22	0.19	0.20	FF

Table 19: Average error in percentage for near-fault and far-fault events comparing maximum values of the CRM and PPM.

Building	Source	Average error in % (1-CRM/PPM)	
		non-scaled analysis	scaled analysis
Regular	NF	5.81	3.85
	FF	4.54	3.63
Irregular	NF	5.24	3.58
	FF	5.26	3.32

This increment agrees with the obtained ones in this research when the peak parameters of the as-recorded values are compared with the maximum values; differences are 10% in average. At this respect, the analysis of 949 response spectra, corresponding to the ground motion pairs from the ITACA database, was performed with the aim of finding the average ratio between the RotD100 to the larger of the two response spectra of the as-recorded horizontal components (Larger IM). Once the 949 ratios were calculated, the geometric mean is estimated in order to obtain a single ratio. The geometric mean was used since it is a more natural estimator compared to the arithmetic mean (Shahi and Baker, 2014). The results show that the ratios are around 9% (see Figure 42). This proves why the simplified method works since the ratio between these two intensity measures remain, in average, when the roof displacement and the base shear values are calculated by using the PPM.

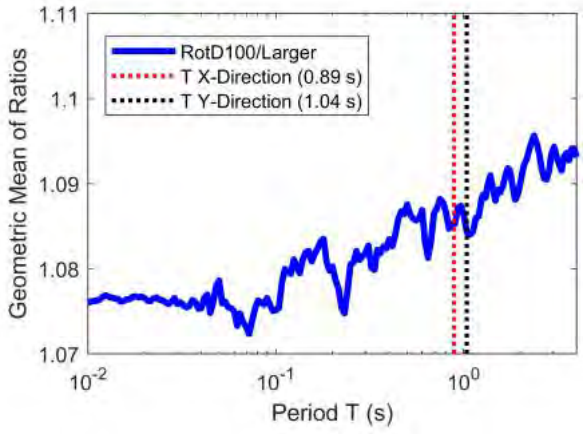

Figure 42: The geometric mean of RotD100/Larger ratio from 949 ground motion pairs of ITACA database.

Summarizing, the simplified method, PPM, provides satisfactory results when are compared to those obtained by using the complete rotational method, CRM, for the two buildings analyzed herein. It is worth to mention that this method cannot be generalized based on the results of this study. This approach should be proved with different structural typologies, building shapes, heights, among other properties that vary the dynamic behavior. Nonetheless, this simplified method has proven to be so far an efficient and simple alternative to include the directionality effect on the seismic performance of buildings. To implement the PPM, the application developed herein named MatchPercentile will be of interest, since it provides a friendly computational environment to calculate the new pair of ground motion records allowing estimating any percentile structural response. This software is a free distribution application compatible with Windows OS and it is available online in the following website: https://deca.upc.edu/en/projects/Earthquake_Engineering/matchpercentile.

5 Increased seismic hazard in Barcelona (Spain) due to soil-building resonance effects

Based on the published article: Pinzón, L. A., Pujades, L. G, Macau, A, & Figueras, S. (2019). Increased seismic hazard in Barcelona (Spain) due to soil-building resonance effects. *Soil Dynamics and Earthquake Engineering, 117*, 245–250. doi: 10.1016/j.soildyn.2018.11.022
Journal URL: www.sciencedirect.com/science/article/abs/pii/S0267726118309916
FUTUR UPC URL: futur.upc.edu/23633983

5.1 Abstract

In this study, previous microzonation studies in Barcelona (Spain) were revisited, and available data on the predominant periods of soils in the city were compiled to develop an updated microzonation map of the city. In addition, the building database was updated and used to create a map of building fundamental periods. The crossing of soil predominant period and building fundamental period maps led to the detection of areas in which resonance phenomena and, indeed, increased amplification of the structural response are expected. Thus, zones of Barcelona were identified in which the seismic hazard is probably greater due to resonance effects. The improved microzonation maps and the detection of soil-building resonance areas contribute significantly to enhanced precision and awareness of seismic hazard and risk in Barcelona.

5.2 Introduction

Seismic risk is defined as the probability or rate of the expected cost due to earthquakes in a specific period of time. Three aspects must be considered to study and develop knowledge of seismic risk in a specific area: the hazard, exposure/vulnerability, and the value of the exposed goods. The seismic hazard defines the annual probability or rate of earthquake occurrence which is determined by: 1) seismic source studies including the geometric distribution of faults, the focal mechanism, and earthquake recurrence models, 2) calculation of ground motion prediction equations (GMPE), and 3) characterization of local effects, including soil, topographic, and induced effects such as landslides and soil liquefaction (Franke et al., 2016; Li et al., 2018). The results of a hazard study allow us to determine the exceedance probabilities of a given threshold of ground motions during a specific time period. Ground motion thresholds may be quantified in terms of macroseismic intensity, peak ground acceleration, or spectral values of the structural response, among many other parameters.

Let us focus on the local effects, specifically on-site effects due to the soil response (Fatahi et al., 2014). Soil response maps usually have low resolution and they may be biased because of limitations in the quantity and geometric distribution of sampling points for which reliable information is available. It is known that anomalies can occur due to underground aquifers and/or ravines and streams responsible for draining rainwater from the highlands to the plains in large cities, among other factors. These underground anomalies are very common in most modern cities, particularly in those with rivers that cross them, those that are built on coasts, or those that have both characteristics. Typical examples of such cities in Spain, where seismic microzonation studies to evaluate site effects have been performed, are Malaga, Murcia, and Valencia (Goded et al., 2012; Navarro et al., 2014; Caselles et al., 2010).

There are two kinds of methods for characterizing the response of soil to a seismic action: experimental and numerical. The main objective of experimental methods is to determine the transfer

function or the fundamental period/frequency of the surface deposits through micro-tremor, seismic, or noise records. In this respect, the spectral H/V ratio is a well-known technique (Nakamura, 1989).

To consider the effects of soil in seismic hazard evaluations, areas with soils that behave in a very similar way when an earthquake occurs are grouped together. This zonation can be carried out according to parameters that describe the ground motion, such as macroseismic intensity, spectral acceleration, and, in the case of this study, the fundamental period of the soil.

Resonance is as an important factor to consider in the effects of local geology on the amplification of seismic action (Dikmen and Tanırcan, 2018; Kuo et al., 2018). Resonance is a well-known phenomenon in physics (Billah and Scanlan, 1991). It is produced when a vibrating object is subjected to a periodic force whose period is close to the characteristic period of the object. Hence, relatively small forces may cause great amplitudes of the oscillating system. Thus, the object progressively vibrates and increases the amplitude of the movement after each successive cycle of the force.

This phenomenon can also be found in buildings due to earthquake actions. In these cases, the building would be the "object" and the seismic action the "force". In a simplified way, each building can be defined as a damped single-degree-of-freedom system with a vibration period, T. With this simplification, a period can be assigned to each single building. In addition to the causative fault features and propagation path through rock formations, seismic actions are affected by soil amplification effects. The typical frequencies and amplitudes of seismic waves vary depending on the soil type. Rigid media, such as rocky and stiff soils, do not amplify the seismic motion, while soft soils amplify specific frequencies depending on the soil characteristics. By crossing building vibration eigen periods and predominant soil frequencies, resonant zones can be detected and analyzed, due to the similarity between the periods of the structures and the periods of the expected seismic actions. In civil engineering, the study of this effect complements the soil-structure interaction (SSI) field. SSI is a very important factor that must be considered in the seismic design of structures (Stanko et al., 2017; Tabatabaiefar et al., 2015; Fatahi et al., 2011).

In Barcelona, seismic microzonation studies first began at the end of the 1990s and early 2000s. Initial research took advantage of existing geological maps and geotechnical soundings (Cid et al., 2001; Jiménez et al., 2000; Figueras et al., 1995). Data concerning H/V spectral ratios (Alfaro et al., 2001) were also used. As a result of a soil response modelling process, four homogeneous and regular soil zones were defined in lines approximately parallel to the coast (Figure 43a). The first zone, with soft soils, is close to the coastline and the fourth one, of rocky outcrops and hard soils, is in the highest zone of the city (Figure 43b). The excellent correlation between elevation and soil type is evident. Intermediate soft and hard soil zones were defined by two areas that border the first and fourth zones respectively (Cid et al., 2001). In recent years, Cadet et al. (2011) used all the available information and complemented it with new array measurements to characterize each zone by means of fundamental resonance frequencies and shear-wave velocity profiles. These authors proposed an average soil for each zone and a standard reference rock site.

The aim of this study was to analyze seismic soil effects in Barcelona, including likely soil-building resonance effects. The starting point was the construction of a fundamental period map of buildings in Barcelona. A second objective was to develop an updated, improved seismic microzonation map of Barcelona, based on the integration of existing data. Finally, an analysis of soil and building predominant period maps was designed to detect and quantify areas in which resonance phenomena and amplification of the structural response are expected.

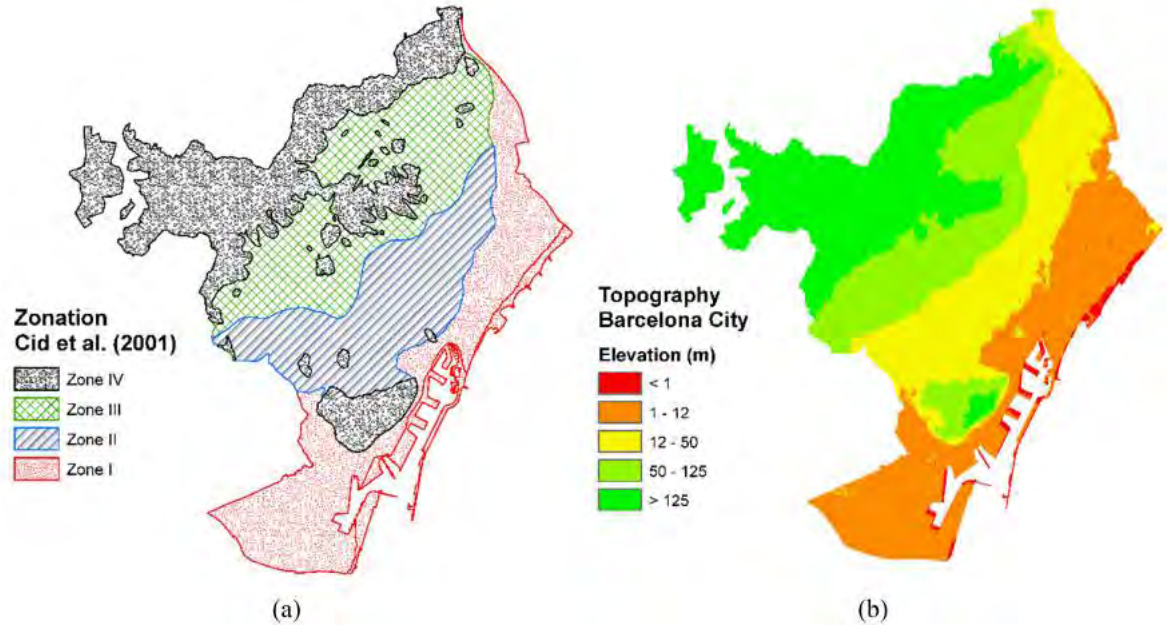

Figure 43: (a) Microzonation map of Barcelona city and (b) topography of the city.

5.3 Building period map

In Barcelona, approximately 71,000 of the 80,715 lots in the city are occupied by buildings. Our research group has an excellent database, provided by Barcelona City Council's Civil Protection Services, with detailed information on the typology, age, and geometric characteristics of over 90% of these buildings (Lantada et al., 2010). It is estimated that this information corresponds to over 96% of the city's residential buildings (Figure 44). We used this database to develop the map of fundamental periods.

Information on structural typology (masonry, concrete, wood, steel, and others) and the number of stories was used to estimate the fundamental periods of vibration. Then, the ArcMap GIS tool was used to generate the map of fundamental periods of the buildings. Before the periods were estimated, the buildings were separated into typologies.

For this purpose, the RISK-UE building typology matrix was used (Milutinovic and Trendafiloski, 2003). The identification of the typology of every building in Barcelona was previously defined by Lantada et al. (2010) (see Figure 45). Eight main typologies were used (see Table 20).

Table 20: Structural typologies and coefficient, C_t, used in this study. (URM: unreinforced masonry; RC: reinforced concrete)

Risk-UE Typologies	Description	C_t
M31	URM bearing walls with wooden slabs	0.050
M32	URM bearing walls with masonry vaults	
M33	URM bearing walls with composite steel and masonry slabs	
M34	URM bearing walls with RC slabs	
RC32	RC irregular frames with URM infill walls	0.075
S3	Steel frames with URM infill walls	0.085
S5	Steel and RC composite systems	
W	Wood structures	0.050

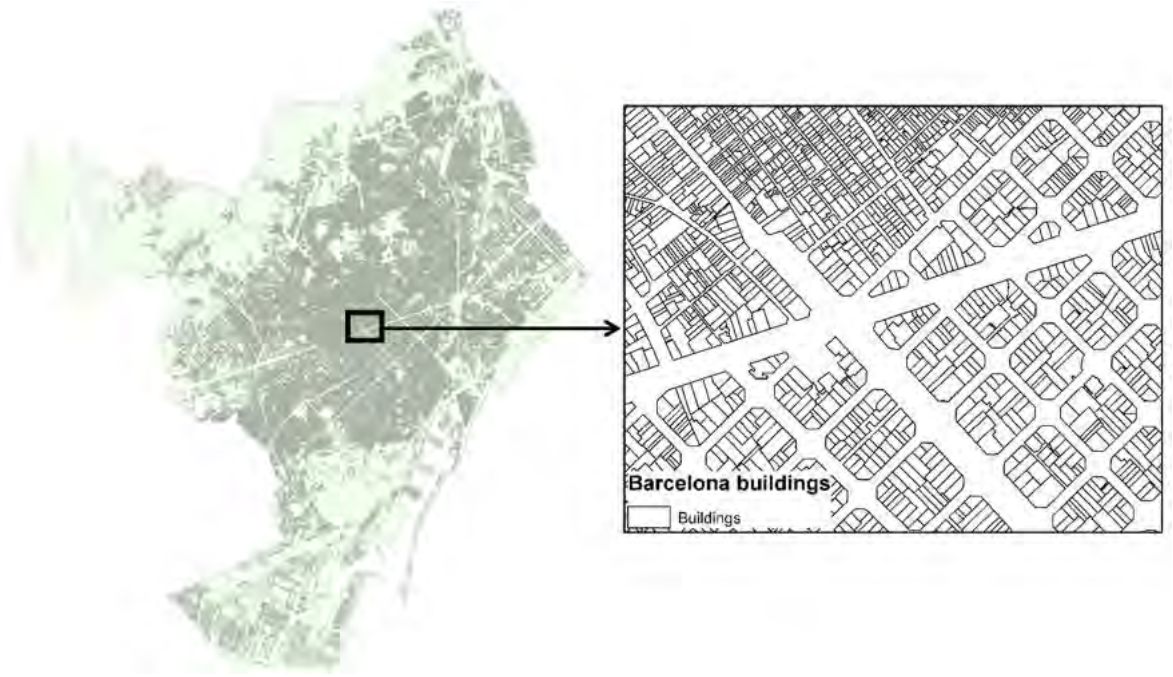

Figure 44: Example of building database for Barcelona City.

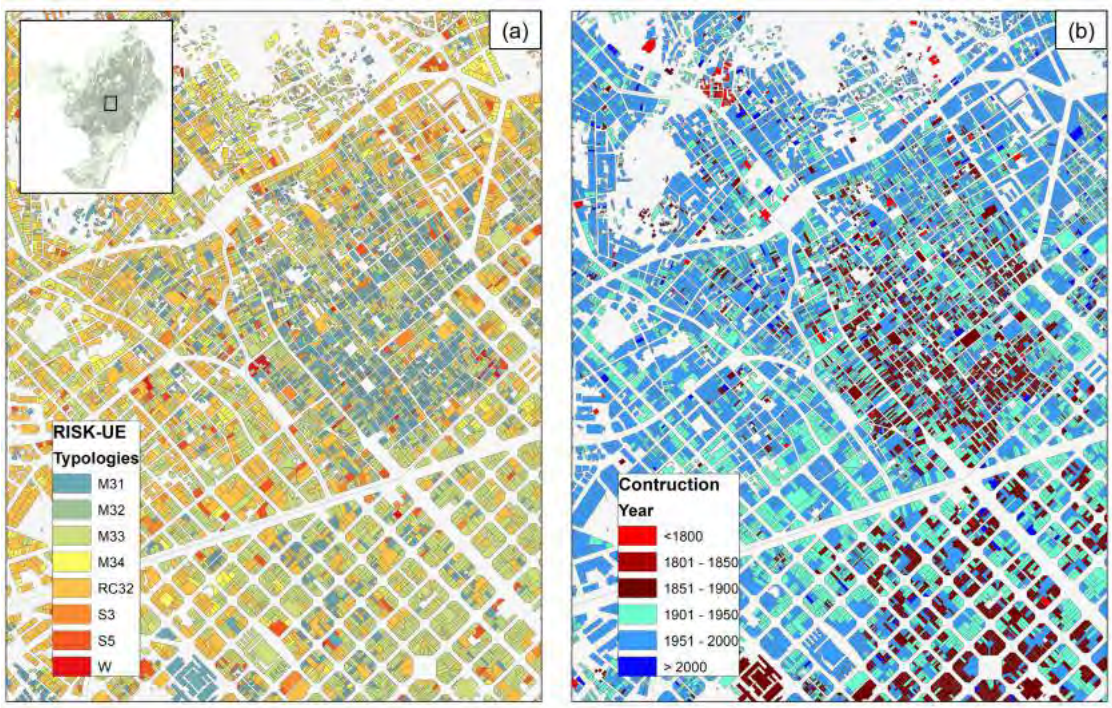

Figure 45: Example of building database map with the respective (a) structural typology and (b) construction year (zoom-in of Gracia district).

To estimate the fundamental periods of each building, the approximate equation of the Eurocode 8 (EC-8) (CEN, 2004) was used.

$$T_1 = C_t H^{3/4} \tag{17}$$

where C_t is the variation coefficient and H is the building height in meters (m). For each structural typology, a value of C_t was defined (see Table 20).

The approximate fundamental period of each building can also be obtained from other structural regulations (Kwon and Kim, 2010). Figure 46 shows the results obtained after the assignment of the period to each building. Different colors have been assigned to different ranges of periods.

5.4 Soil period map

One of the aims of this study was to develop an improved microzonation map based on soil response periods. As a starting point, we compiled all the information on Barcelona's soils that had been obtained by experimental methods. This information was integrated into a geo-referenced, homogeneous database including information on the fundamental soil period obtained by H/V measurements (Alfaro et al., 2001; Cadet et al., 2011; Santos-Assuncao et al., 2016; Macau et al., 2015). The available data, together with the corresponding references, are shown in Table 21.

Then, all the available data and ArcMap software were used to develop a new map of soil predominant periods in Barcelona (see Figure 47). The results show four clear soil zones for different ranges of periods. The first zone, in red, has the highest periods, and starts on the coastline. The last zone, in green, has the smallest periods and is in the highest zones of the city.

A comparison between the resulting map and the topography and microzonation map of Cid et al. (2001) showed interesting results (see Figure 48). A relationship was found between three parameters: soil period, soil type, and elevation. Rocky soils are present in the highest zones with the smallest periods (near zero), corresponding to Cid's zones III and IV; and soft soils are in areas near the coast with the highest periods, corresponding to Cid's zones I and II. With these results, a different range of periods could be assigned to each zone: Zone IV – T $<$ 0.2 s, Zone III – 0.2 s $\leq$ T $\leq$ 0.4 s, and Zones I and II – T $>$ 0.4 s.

The ranges of predominant frequencies obtained by Cadet et al. (2011) were similar to those obtained in this study. A summary of representative values of elevation, predominant period, predominant frequency (Cadet et al., 2011), geomorphology (Cid et al., 2001; Ventayol et al., 1978), and shear-wave velocity (Vs_{30}) (Cadet et al., 2011) for each zone is presented in Table 22.

5.5 Crossing period maps

The characteristics of the site affect the frequency and duration of ground motions. The site period (T) depends on the thickness of the layers (H) and on the corresponding shear-wave velocities (Vs), according to the following approximate equation: $T = 4H/Vs$. In most cases, structures built on rocky sites will be subjected to short-period excitations, while, under earthquake excitations, soft soils result in long-period motions. In addition, thin and soft soil layers over rigid bedrock may cause high-amplitude, short-period amplification. The ratio between the site period and the building period is important in estimating the resonance effects (Elnashai and Di Sarno, 2008).

Areas of increased hazard caused by interaction and resonance effects between the soil response and the structural response can be detected by crossing the obtained building period map with the soil period map. Figure 49 shows the results obtained by crossing both maps. Three zones were defined based on the similarity of the soil and building periods.

Figure 46: (a) Map with the estimated fundamental period of the building database of Barcelona, (b) zoom-in the cross between Diagonal Ave. and Passeig de Gracia street and (c) 3D view of (b).

Table 21: Available soil data from Barcelona used in this study.

Author	Technique	# points	Description of the study
Alfaro et al. (2001)	H/V	197	Micrometer field survey carried out in Barcelona using a high dynamic range accelerometer to obtain fundamental periods based on H/V. The H/V spectral ratio was computed in a range between 0.05 and 15 Hz.
Cadet et al. (2011)	H/V, array	17	Ambient noise array measurements in Barcelona with a Lennartz LE-3D sensor (cut-off frequency of 0.2 Hz) and CityShark acquisition system.
Santos-Assuncao et al. (2016)	H/V	220	GPR data were used to define the most probable area affected by streams and paleochannels, and geological data from geological maps and boreholes facilitated the recognition of possible targets (layers and shallow streams). Then, vibration measurement points were selected considering these previous results. After selection of the measurement point, the fundamental period of soil response was determined by the H/V method. The ambient noise measures were obtained with a Tromino seismometer.
Macau et al. (2015)	H/V, array	57	H/V measurements were estimated along the Llobregat Delta, Barcelona. The seismic ambient noise vibrations were recorded using a six-channel Cityshark datalogger connected to one Lennartz LE-3D 0.2 Hz triaxial sensor. The H/V ratio was calculated using Geopsy software (http://www.geopsy.org).

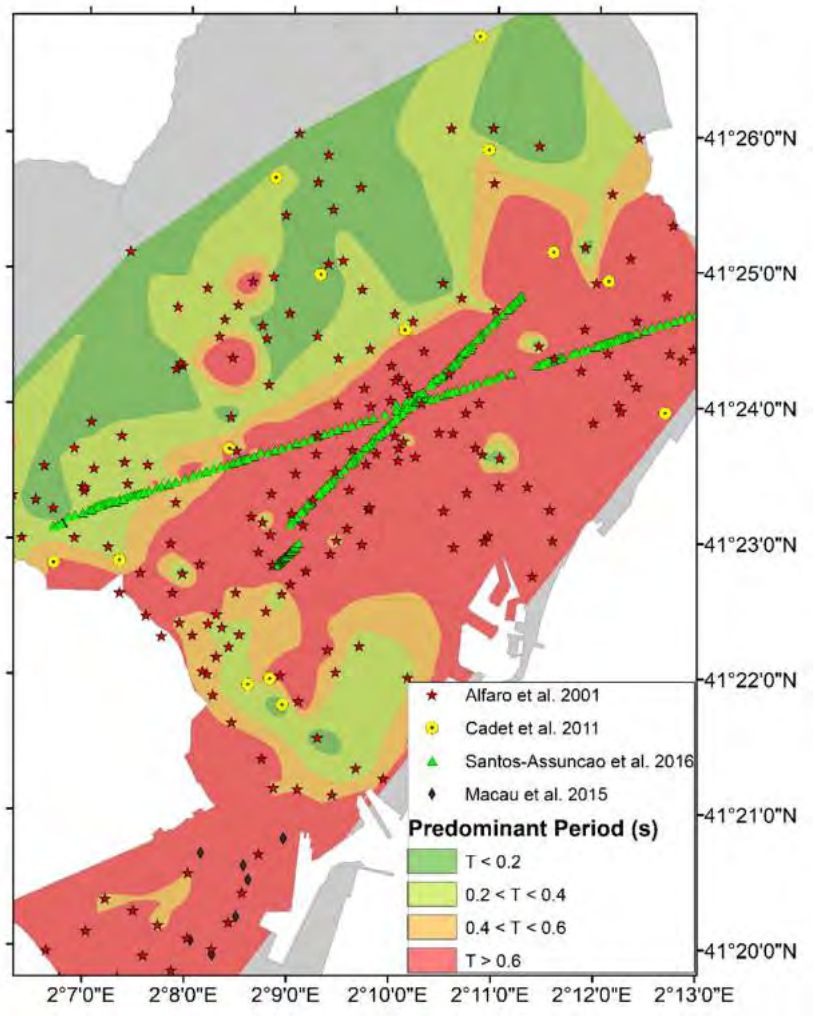

Figure 47: Microzonation map of Barcelona based on soil periods. The points represent the available experimental data.

Table 22: Summary of parameters of interest: microzonation zones, topography, geomorphology, Vs_{30}, predominant frequency and fundamental period obtained in this study.)

Zones (Cid et al., 2001)	I	II	III	IV
Elevation (m)	0 – 15	15 – 60	60 – 125	>125
Predominant period, T (s)	>0.40	>0.40	0.20 – 0.40	<0.20
Predominant frequency (Hz) from Cadet et al. (2011)	0.6 – 1.9	0.8 – 2.1	1.4 – 5.8	Unreliable
Geomorphology (Cid et al., 2001; Ventayol et al., 1978)	Recent quaternary	Ancient quaternary	Ancient quaternary and rocky outcrop	Rocky outcrop
Vs30 (m/s) from Cadet et al. (2011)	218	398	422	742

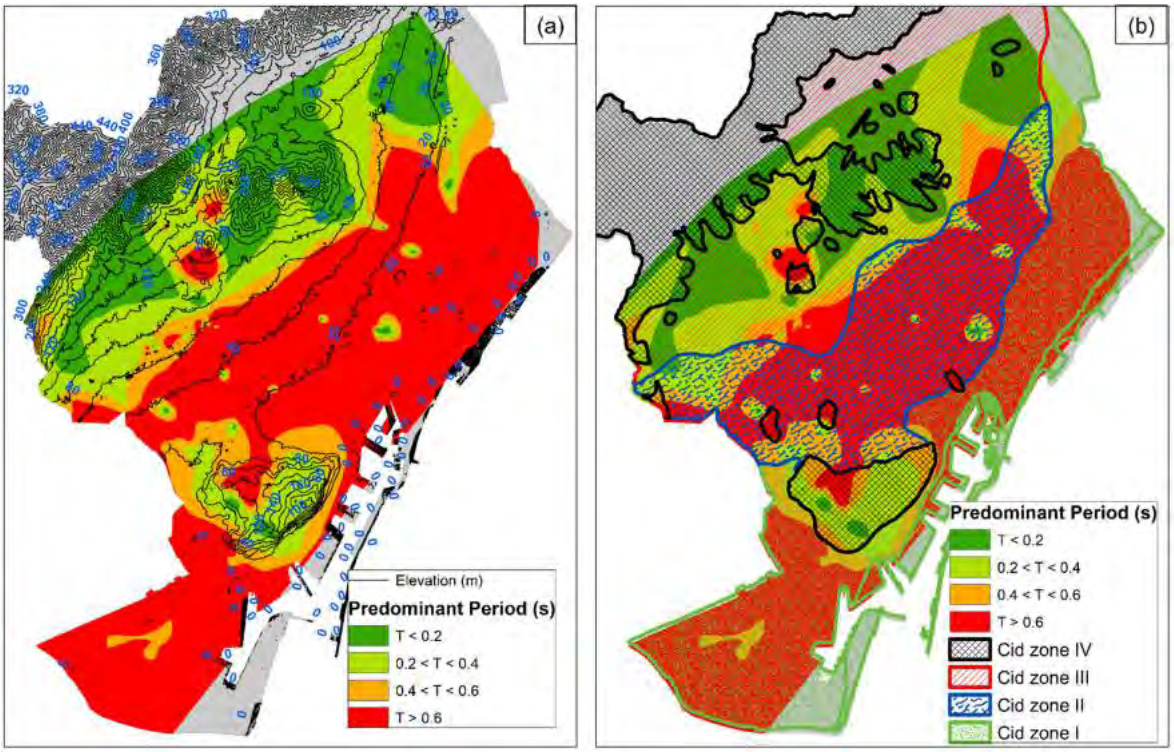

Figure 48: Microzonation map of Barcelona based on soil periods compared with (a) elevations of the city and (b) Cid *et al.* (2001) microzonation zones.

Zones with increased probability of amplification due to a resonance effect are shown in red. These zones present differences in the range of 0.20 s between the building and soil fundamental periods. This difference corresponds to the standard error of Equation 17 (Goel and Chopra, 1997, 1998). In the case of moderate resonance zones (yellow), differences of between ±0.21 and ±0.50 s were found. For the lower resonance zones (green), differences of ±0.51 s or higher were defined.

At first glance, the neighborhoods of Gràcia, Poble Sec, Sant Antoni, El Raval, and Sants are the most affected in the city center. These zones are correlated with the construction year and the structural typology previously shown in Figure 45. Most of the buildings were constructed in the 19th century and the predominant typology is URM. URM is the most commonly used structural typology for buildings worldwide and the one that has caused the most damage and death, due to its high vulnerability to seismic events (D'ayala, 2013; Pinzón et al., 2018a).

5.6 Discussion and Conclusions

Although Barcelona is a city located in a low-to-moderate seismic hazard region, the exposed value and vulnerability are high, so the seismic risk is significant and mitigation studies are highly recommended (Barbat et al., 2006). As the occurrence of an earthquake cannot be predicted, the only way to mitigate the effects generated by these events is to strongly influence prevention, in terms of structural safety in the design and seismic-resistant construction of buildings and infrastructures, and the planning and management of an emergency situation immediately after the occurrence of an earthquake.

In this study, soil and building period maps of Barcelona were generated. With the crossing and analysis of both maps, a new map was developed highlighting the areas where soil-building resonance phenomena are expected. This study makes a significant contribution to awareness of the seismic

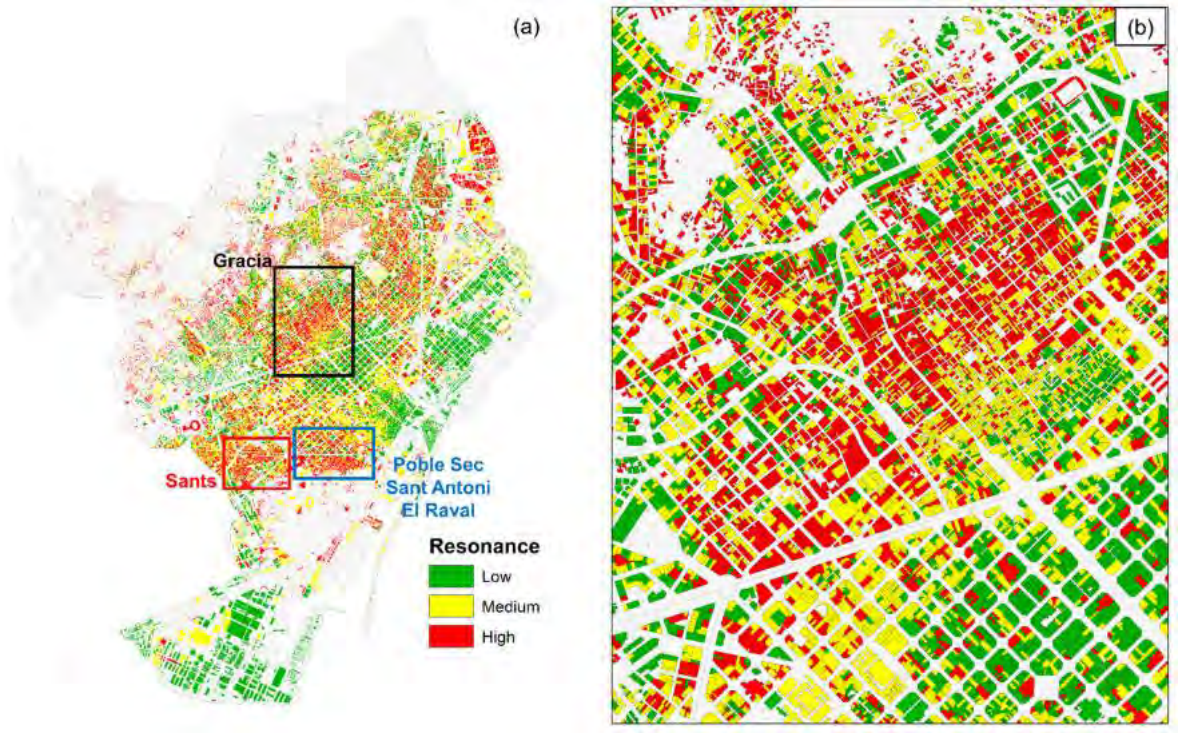

Figure 49: (a) Resonance zones in Barcelona and (b) zoom-in of Gracia district.

risk in the city, when local effects are considered in regional and local seismic hazard studies. The maps developed herein can help to reduce the seismic risk, since special attention can be devoted to structures that are vulnerable to resonance effects. In addition, a microzonation map, based on the predominant soil periods, can be implemented in structural regulations to develop improved design spectra based on the site-specific period, as in structural regulations for Mexico City (NTCDS-RCDF, 2017).

As mentioned in the introduction, these studies complement soil-structure interaction (SSI) analyses (Stanko et al., 2017; François et al., 2014). SSI effects refer to modification of the building response due to the characteristics of the site. This effect is generally seen in buildings constructed on soft soils (Bard et al., 2005). In addition, the SSI effect is defined as the process in which the soil's response modifies the response of the structure, and the structure influences the response of the soil (Tuladhar et al., 2008).

Conventional structural codes do not consider SSI effects, since in most cases it is more conservative to use structural regulations. However, the effect of SSI is prominent when the structure and soil periods are similar. Bard et al. (1996) demonstrated that the effects of the structure are greater when the soil-structure system period is close to the fundamental period of the ground. These effects should be considered, at least, with approaches such as that proposed in the National Institute of Standards and Technology (NIST) 12-917-21 report (NIST-GCR-12-917-21, 2012) report. Here, the structure-to-soil stiffness ratio, $r = h/(VsT)$, is a recommended measure that indicates when SSI effects become relevant. The h is the effective height to the center of mass for the first mode shape, Vs is the effective shear-wave velocity (e.g. the shear-wave velocity to a depth of 30 meters, Vs_{30}), and T is the fundamental period of vibration. Values of r above 0.1 would indicate that SSI effects should be considered.

Since Barcelona is a dense city, the site-city interaction (SCI) may also become relevant. The SCI

effect is defined as the global interaction between all the buildings in a city and its subsoil through ground motion (Bard et al., 2005). These multiple interactions may modify the response of the buildings and the subsoil. If SCI effects turn out to be significant, one immediate consequence is that erecting or destroying a building, or a group of buildings, could modify the seismic hazard for the neighborhood. In turn, this could lead to significant conceptual changes, especially concerning microzoning studies, land-use planning, and insurance policies (Bard et al., 2005).

When the SCI is relevant, normally the ground motion generated by every building modifies the motion of the structures that interact in the system. These multiple interactions become significant when the soil period or frequency match the structure's fundamental period, generating resonance effects (Kham et al., 2006). In addition, in the case of multiple interactions, the overall effects appear to be beneficial, reducing the ground motion in urban environments, particularly for homogeneous groups of buildings (Guéguen et al., 2012).

6 Seismic site classification from the horizontal-to-vertical response spectral ratios: use of the Spanish strong motion database

Based on the published article: Pinzón, L. A., Pujades, L. G, Macau, A, Carreño, E. & Alcalde, J. M. (2019). Seismic Site Classification from the Horizontal-to-Vertical Response Spectral Ratios: Use of the Spanish Strong-Motion Database. *Geosciences, 9*(7), 294. doi: 10.3390/geosciences9070294
Journal URL: www.mdpi.com/2076-3263/9/7/294
FUTUR UPC URL: futur.upc.edu/25801670

6.1 Abstract

Normally, the average of the horizontal-to-vertical (H/V) ratios of the 5% damped response spectra of ground motions is used to classify the site of strong-motion stations. In these cases, only the three-orthogonal as-recorded acceleration components are used in the analysis, and all the vector compositions that can generate a different response for each period oscillator are excluded. In this study, the Spanish strong-motion database was used to classify the sites of accelerometric stations based on the predominant periods through the average horizontal-to-vertical spectral ratios (HVSR) of recorded ground motions. Moreover, the directionality effects using the vector composition of the horizontal components of ground motions were also considered in the estimations of H/V ratios. This consideration is a relevant novelty compared to the traditional H/V ratios methods. Only earthquakes with magnitudes above 3.5 and hypocentral distances below 200 km were selected, which resulted in 692 ground-motion records, corresponding to 86 stations, from events in the period between 1993 and 2017. After the analysis, a predominant-period site classification was assigned to each station. On the whole, the obtained mean and standard deviation values of the spectral ratios are comparable to those shown by other researchers. Therefore, the advantages of the proposed procedure, which takes the directionality effects into account, can be summarized as follows: a) The obtained information is richer and gives enables more sophisticated and realistic analyses on the basis of percentiles and b) it is easier to detect anomalous stations, sites, and/or accelerograms. Moreover, the method eliminates the effect of directionality as a contributor to epistemic uncertainty.

6.2 Introduction

The Vs30 value (the time-averaged shear-wave velocity in the upper 30 meters) is a measure that is commonly used to define site classifications in seismic codes and ground-motion prediction equations (GMPEs) (Akkar et al., 2014; Cadet et al., 2011). Table 23 shows seismic site classifications based on the Vs30 from European (CEN, 2004), Spanish (NCSE-02, 2009), and American (ASCE, 2017) seismic codes and structural standards. However, researchers have reported some limitations and problems with this classification (Steidl, 2000; Zhao et al., 2006; Fukushima et al., 2007; di Alessandro et al., 2012). Some of these include i) the limited availability of near-surface shear-wave data at strong-motion sites, ii) the complexity of data acquisition, and iii) the fact that these classifications do not consider the effect of the thickness of soft sediments.

As an alternative to the Vs30 classification, a method based on horizontal-to-vertical (H/V) ratios of 5% damped response spectra, which can be used to obtain site predominant periods, was proposed by Zhao et al. (2006). This method was adapted to the seismic design of highway bridge regulations in Japan. After this paper, many authors presented studies based on the Zhao et al. (2006) method

Table 23: Classification based on Vs30 for seismic codes and standard regulations from Europe, Spain, and the United States.

Eurocode 8 (Europe)			**NCSE-02 (Spain)**			**ASCE 7-16 (USA)**		
Soil Type	**Description**	**Vs30 (m/s)**	**Soil Type**	**Description**	**Vs30 (m/s)**	**Soil Type**	**Description**	**Vs30 (m/s)**
A	Rock or other rock-like geological formation, including at most 5 m of weaker material at the surface.	Vs >800	I	Compact rock, very dense cemented or granular soil	Vs >750	A	Hard rock	Vs >1500
						B	Rock	750 <Vs ≤ 1500
B	Deposits of very dense sand, gravel, or very stiff clay, at least several tens of meters in thickness, characterized by a gradual increase of mechanical properties with depth.	360 <Vs ≤ 800	II	Very fractured rock, dense or cohesive hard granular soils.	400 <Vs ≤ 750	C	Very dense soil and soft rock	360 <Vs ≤ 750
C	Deep deposits of dense or medium dense sand, gravel, or stiff clay with thickness from several tens to many hundreds of meters.	180 <Vs ≤ 360	III	Granular soil of medium compactness or cohesive soil of firm consistency to very firm.	200 <Vs ≤ 400	D	Stiff soil profile	180 <Vs ≤ 360
D	Deposits of loose-to-medium cohesionless soil or of predominantly soft-to-firm cohesive soil.	Vs <180	IV	Loose granular soil or soft cohesive soil.	Vs <200	E	Soft soil profile	Vs <180
E	A soil profile consisting of a surface alluvium layer with vs values of type C or D and thickness varying between about 5 m and 20 m, underlain by stiffer material with vs >800 m/s.	-	-	-	-	F	Other. See ASCE 7-16 Table 20.3-1	
S1	Deposits consisting of or containing a layer at least 10 m thick of soft clays/silts with a high plasticity index (PI >40) and high water content.	Vs <100	-	-	-	-		-
S2	Deposits of liquefiable soils, sensitive clays or any other soil profile not included in types A–E or S1	-	-	-	-	-		-

with data from Europe–United States–Japan (Fukushima et al., 2007), Iran (Ghasemi et al., 2009), Italy (di Alessandro et al., 2012), and India (Chopra et al., 2017).

Ground motions during earthquakes are recorded in three orthogonal components: two horizontal and one vertical. Horizontal components are usually recorded in North-South (N-S) and East-West (E-W) directions, but other adequate directions are often used when, for instance, bridges, buildings, or other structures are instrumented. In these cases, longitudinal and transversal directions are normally preferred.

The as-recorded components do not necessarily represent the maximum intensity at the site. For instance, in addition to the response spectra of the two as-recorded accelerograms, namely E30°N and N30°W, Figure 50a shows the response spectra of the accelerograms corresponding to a rotated recording axis with increments of 1° in the range between 0° and 180°. The as-recorded components are rotated 30°, according to the data provided by the Spanish National Geographic Institute, since the sensor is installed with a 30° offset from the north. Figure 50b is a 3D representation of particle motion, showing how maximum recorded values strongly depend on the direction of the recording instruments. The following equation is used to obtain the rotated acceleration response time histories, $acc_{rot}(t, \theta, T, \xi)$:

$$acc_{rot}(t, \theta, T, \xi) = acc_1(t, 0, T, \xi) \cdot cos(\theta) + acc_2(t, 0, T, \xi) \cdot sin(\theta) \tag{18}$$

where t is time, θ is the rotation angle, T is the period of the oscillator and ξ is the damping ratio. Usually, $acc_1(t, 0, 0, 0)$ and $acc_2(t, 0, 0, 0)$ are the as-recorded accelerograms. Maximum values lead to the response spectra RotDpp where Rot means rotated, D means period-dependent and pp means percentile. For other details on directionality, see Pinzón et al. (2018b).

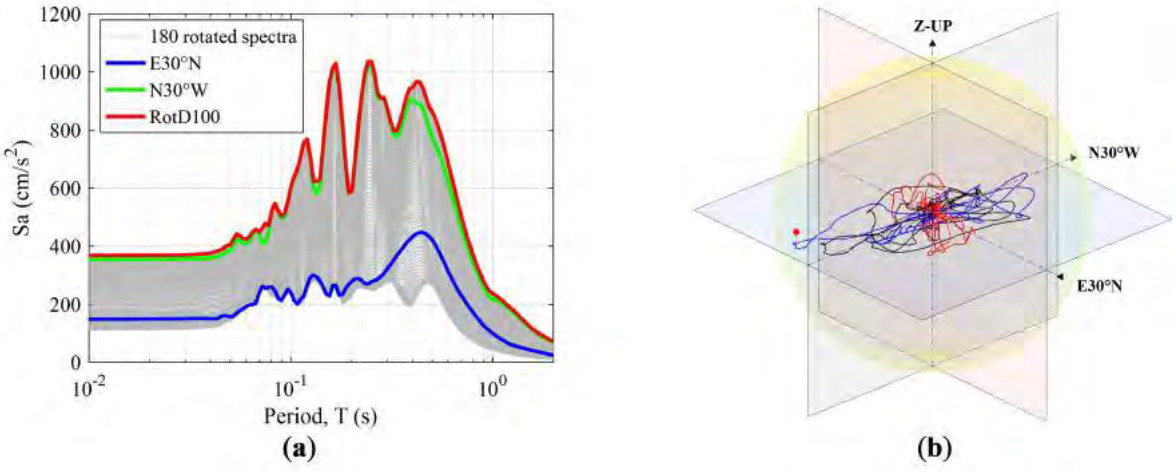

Figure 50: The 11 May 2011 Lorca (Spain) earthquake, 5.1 M_W at 18:47:00 local time. (a) Response spectra comparison and (b) 3D particle motion for the ground-motion record registered in LOR station. E30°N and N30°W correspond to the as-recorded accelerograms.

As can be seen in Figure 50a, the N30°W component has larger Sa values than E30°N but does not represent the RotD100 (Rot: rotated; D: period-dependent; 100: 100th percentile) spectrum well. RotD100 is the spectrum that represents the maximum (100th percentile) values of response spectra of the two as-recorded horizontal components rotated onto all non-redundant azimuths (Boore, 2010). This is due to the directionality effect of strong motion recordings, which is now considered in the GMPEs (Pinzón et al., 2018b; Shahi and Baker, 2014; Bozorgnia et al., 2014) and in the variability

of the performance of structures due to the angle of incidence of the seismic action (Lagaros, 2010; Torbol and Shinozuka, 2014; Vargas-Alzate et al., 2018; Pinzón et al., 2018a).

Directionality effects also play an important role in seismic site classification by means of H/V response spectral ratios (Zhao et al., 2006). Normally, the three as-recorded orthogonal components are used to perform the analysis. In some cases, the same site predominant period is captured with both horizontal components (see Figure 51a where a predominant period, T_g, of 0.61 s is obtained), but in other cases, as can be seen in Figure 51b, the predominant period varies for each horizontal component (T_g [N-S] = 1.11 s and T_g [E-W] = 0.95s). By considering the directionality effects, using the 50th percentile of all the rotated ratios, a single site predominant period is obtained in both cases (T_g = 0.61 s and T_g = 1.11 s for the ground motions of Lorca and Alhucemas respectively). This procedure reduces epistemic uncertainty, since all non-redundant orientations are considered.

Earthquakes such as those in Sicily (Italy) in 1693 (Bianca et al., 1999), Lisbon (Portugal) in 1755 (Baptista et al., 2010), and Messina (Italy) in 1908 (Amoruso et al., 2002) were highly destructive events that left their mark on the European continent in the past. Over the last decade, a considerable number of high-magnitude earthquakes have occurred, causing property damage and fatalities. In Italy, the earthquakes of L'Aquila (Italy) in 2009 (Çelebi et al., 2010) and the Central Italian events of 2016 (Fiorentino et al., 2018) caused around 600 fatalities and thousands lost their homes. In Spain, the Lorca 2011 earthquake is an example of how a moderate earthquake (M_W = 5.1) can produce significant damage with considerable economic loss, loss of homes, and fatalities (De Luca et al., 2014; Alfaro et al., 2012). This confirms the need to increase knowledge of earthquakes and provide advanced tools to improve the evaluation and management of seismic hazard and risk in Spain (Pinzón et al., 2019d).

The main aim of this study is to improve the seismic site classification of the accelerometric stations of the strong-motion network of Spain. The site classification method proposed by di Alessandro et al. (2012) is adopted, with the only difference being that directionality effects are taken into account. For this purpose, acceleration records from the Spanish strong-motion network (Spanish National Geographic Institute, IGN) are used. A predominant-period site classification is assigned to each strong-motion station and the results of the mean ratios are compared with those obtained by other researchers.

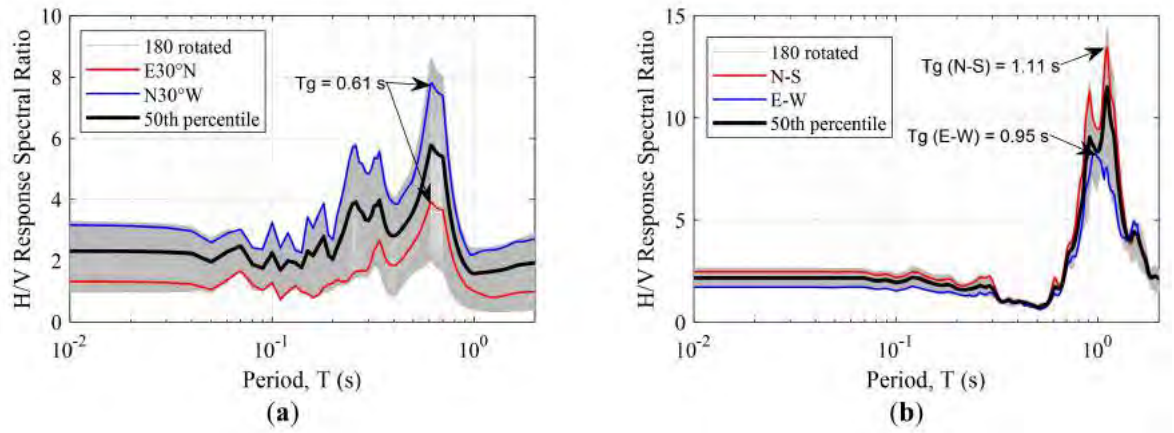

Figure 51: Horizontal-to-vertical (H/V) 5% damped response spectral ratio comparison for (a) the 11 May 2011 Lorca (Spain) earthquake recorded in the LOR station (5.1 M_W at 18:47:00 local time) and (b) the 24 February 2004 Alhucemas (Morocco) earthquake recorded in the ALG station (6.3 M_W at 02:27:47 local time).

6.3 Methodology

In this study, the method proposed by di Alessandro et al. (2012) is used to classify the sites of accelerometric stations. Furthermore, the Rotational H/V response spectral ratio (H/V Rot) is proposed as an extension of the method to consider the directionality effects. The aim of the H/V Rot method is to eliminate the contribution of sensor orientation uncertainty in the estimation of the response spectral ratios.

Instead of using only the three-orthogonal as-recorded components, the method considers directionality effects according to the following steps:

1. An estimation of 5% damped response spectra for each linear combination of the two horizontal orthogonal components between 0 and 180 degrees of rotation is computed (180 in total using Equation 18). In this study, a period range between 0 and 2 seconds is used to compute the spectra with increments of 0.01 s.
2. The H/V response spectral ratios are computed for the 180 response spectra.
3. The 50th percentile (median value) of the 180 H/V spectral ratios are computed, to obtain a single ratio for each record.

Zhao et al. (2006), Fukushima et al. (2007), and di Alessandro et al. (2012) proposed a seismic site classification method based on the site natural period at each station using H/V spectral ratios estimated with 5% damped response spectra. The criteria used by each researcher are shown in Table 24. In this table, T_g is the natural (predominant/fundamental) period of the site in seconds, SC refers to soil class and CL to site class. In this paper, the classification proposed by di Alessandro et al. (2012) (see Table 24) is applied to the strong-motion network of Spain.

Table 24: Comparison of the site classification definition based on the predominant period (T_g) proposed by Zhao *et al.* (2006), Fukushima *et al.* (2007), and di Alessandro *et al.* (2012).

Zhao et al. (2006)		**Fukushima et al. (2007)**		**di Alessandro et al. (2012)**	
Site	**Description**	**Site**	**Description**	**Site**	**Description**
SC-I	T_g <0.2 s	SC-1	T_g <0.2 s	CL-I	T_g <0.2 s
SC-II	0.2 s $\leq T_g < 0.4s$	SC-2	0.2 s $\leq T_g < 0.6s$	CL-II	0.2 s $\leq T_g < 0.4s$
SC-III	0.4 s $\leq T_g < 0.6s$	SC-3	0.6 s $\leq T_g$	CL-III	0.4 s $\leq T_g < 0.6s$
SC-IV	0.6 s $\leq T_g$	SC-4	T_g not identifiable and original rock site	CL-IV	0.6 s $\leq T_g$
-	-	SC-5	T_g not identifiable and original soil site	CL-V	T_g not identifiable with flat H/V ratio and amplitude <2
-	-	-	-	CL-VI	Broad amplification with multiple peaks @ T_g >0.2 s
-	-	-	-	CL-VII	T_g not identifiable with multiple peaks over all periods

6.4 Data

The complete analysis was performed using the accelerometric database of the Spanish strong-motion network from the Spanish National Geographic Institute (IGN). This database contains records from 1993 to 2017. Ground motions were carefully corrected through baseline removal and band-pass filtering (Butterworth fourth-order). Only ground motions with body-wave (mb) and/or moment

magnitudes (M_W) $\geq$ 3.5 and hypocentral distances 200 km were selected. M_W and mb magnitudes were used in the selection, since these were the magnitudes available in the database catalog. Magnitudes of earthquakes before 2010 were defined with mb and after this year they were defined with M_W. Thus, a dataset with 692 three orthogonal accelerograms, recorded at 86 stations, was segregated for the analysis.

The distribution of magnitude as a function of the hypocentral distance of the selected ground motions is displayed in Figure 52 and the earthquake locations are shown in Figure 53. Most records correspond to earthquakes with magnitudes below 4 and with a hypocentral distance between 20 and 30 km.

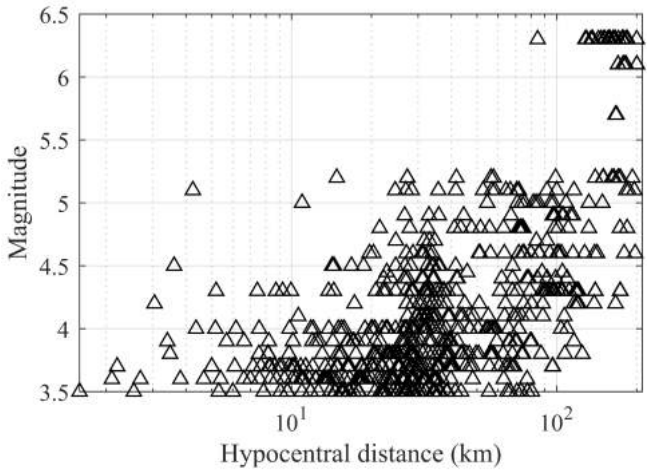

Figure 52: Magnitudes and hypocentral distances for selected earthquakes and stations.

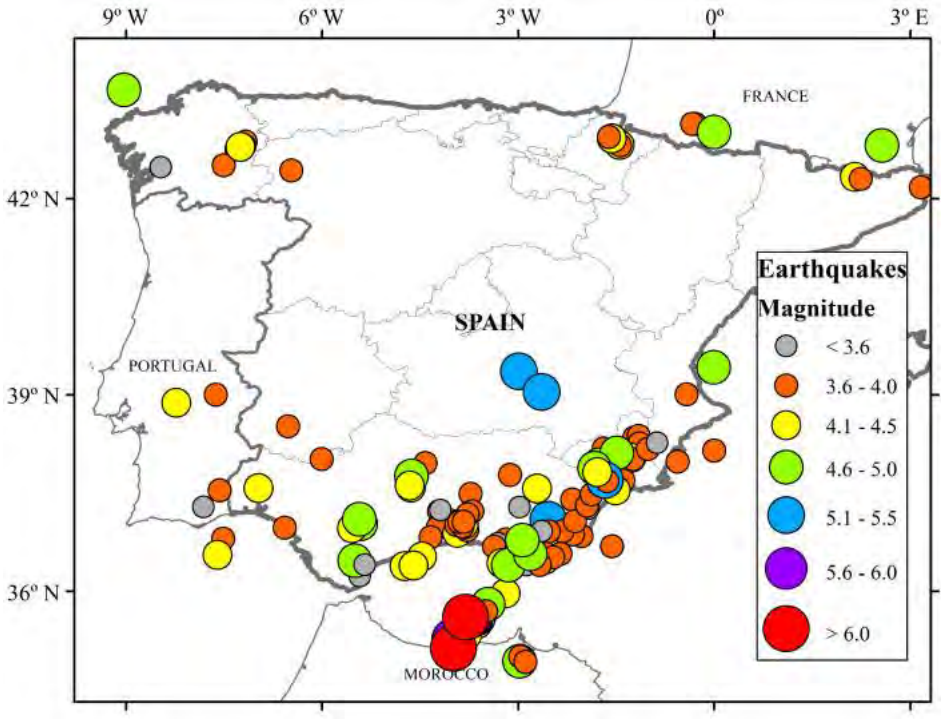

Figure 53: Location of the earthquakes used in the analysis.

From the 692 ground motion records, only one has a peak ground acceleration (PGA) higher than 0.30 g (high seismicity), the 2011 Lorca earthquake recorded in the LOR station with a PGA = 0.36 g (see Figure 51a). Figure 54 shows the results of the H/V spectral ratios of the LOR station using all the available records. The median predominant period is 0.46 s compared to the 0.61 s period obtained in Figure 51a. This difference in the period is due to the high PGA of the motion, producing high deformations and leading to a nonlinear response of the soil (Angina et al., 2018; Lo Presti et al., 2006; Fiorentino et al., 2019; Pinzón et al., 2019b).

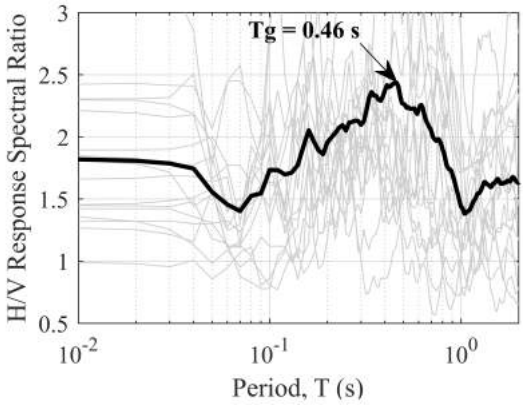

Figure 54: H/V response spectral ratios for the LOR station. Gray lines are the H/V ratios of all the ground motions recorded in LOR station and in black the 50th percentile. The predominant period found is 0.46 s.

6.5 Results

Once the complete database had been analyzed, a seismic site class was assigned to each strong-motion station. Seventy-three percent of the stations were classified in the first four categories corresponding to 78% of the ground-motion records (Table 25).

Table 25: Number of accelerometric stations and ground-motion records for each site class according to the di Alessandro *et al.* (2012) classification.

Number	CL-I	CL-II	CL-III	CL-IV	CL-V	CL-VI	CL-VII
Stations	9 (10.5%)	24 (27.9%)	16 (18.6%)	14 (16.3%)	2 (2.3%)	4 (4.6%)	17 (19.8%)
Records	167 (24.1%)	138 (20.0%)	176 (25.4%)	62 (9.0%)	31 (4.5%)	32 (4.6%)	86 (12.4%)

The location of the 86 analyzed stations are shown in Figure 55, and, in order to summarize the results obtained and to allow easy comparison with previous classifications, Table 26 shows the new and old site classifications. In this table, the classification based on the predominant periods, the geology (provided by the IGN), and the site classification published by Mezcua et al. (2008) are shown. For the geology classification, R refers to rock, H to hard soil, and S to soft soil. To characterize each site, Mezcua et al. (2008) used the crude site qualitative description provided for each station. Site class 1 corresponds to compact rocks, 2 refers to firm soil, and 3 applies to soft sedimentary deposits.

The geometric means (GM) of the H/V ratios of the 5% damped response spectra and their standard deviations were calculated for each site class. The results are shown in Figure 56 and in Tables 27 and 28. The shape of the GM ratio is similar to that obtained by Zhao et al. (2006) using the Japanese database and di Alessandro et al. (2012) using the Italian one.

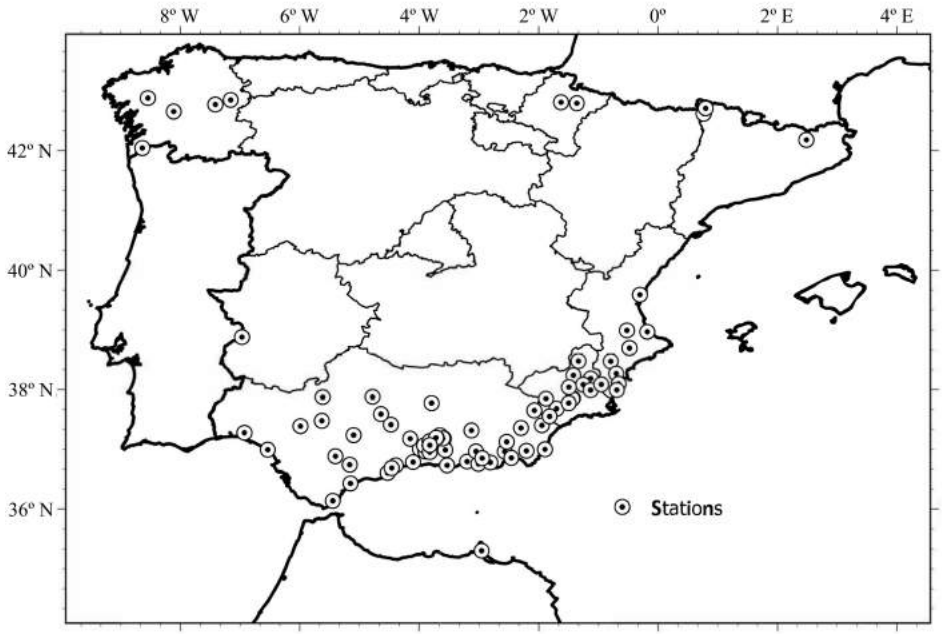

Figure 55: Location of accelerometric stations.

Differences in amplitudes of the GM of the ratios were also observed: Maximum values were around 4 with the Japanese dataset [see Figure 3 of Zhao et al. (2006)], 2.8 with the Italian dataset [see Figure 3 of di Alessandro et al. (2012)], and 2.3 in this study (see Figure 56). These differences are related to the range of magnitudes used and the number of records. The analysis for Japan was made with ground motions from earthquakes with magnitudes ≥ 5.0 and in Italy with magnitudes ≥ 4.0. In the case of the present study, most of the records were from earthquakes with a magnitude ≤ 4. For this reason, smaller amplitudes were found in the GM of ratios.

In the case of the standard deviations of the geometric mean of H/V response spectra ratios (Figure 56b), the results show values around 0.3 on average. These results are similar to those obtained by Zhao et al. (2006), Fukushima et al. (2007), Ghasemi et al. (2009), and di Alessandro et al. (2012).

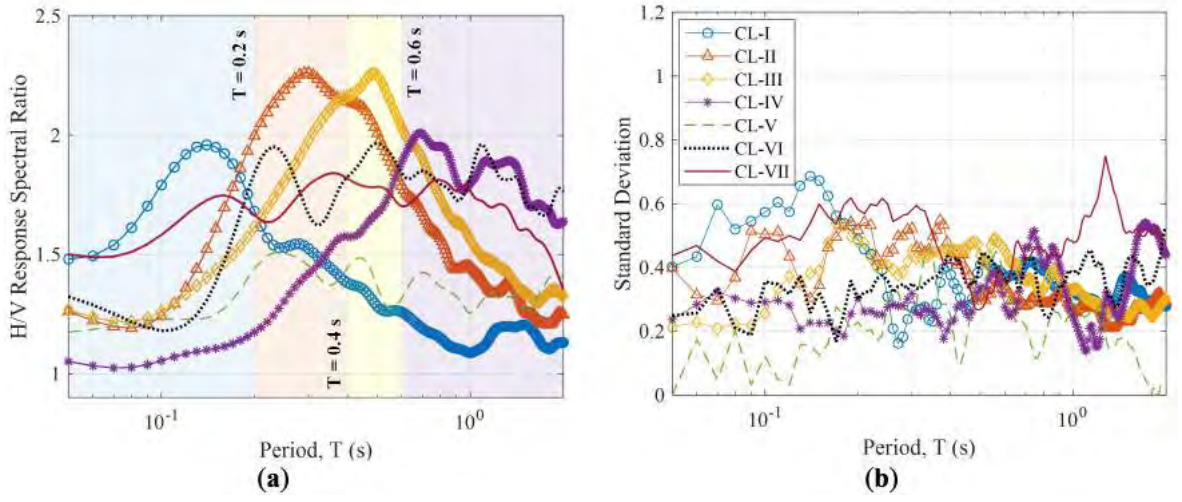

Figure 56: (a) Geometric means (GM) of the H/V ratios of the 5% damped response spectra for each site class. (b) The corresponding standard deviations.

Table 26: Site classification of the Spanish strong-motion stations.

Station code	Geology IGN	Site class Mezcua et al. (2008)	Site class of this study	Station code	Geology IGN	Site class Mezcua et al. (2008)	Site class of this study
ABU	H	3	IV	JAE	S	2	II
ADR	R	1	V	JAY	S	3	III
AGE	S	-	IV	JUM	S	2	VI
AGR	H	3	III	LA2	H	2	II
AHA	R	1	IV	LOJ	H	3	I
AHM	R	3	V	LOQ	S	3	I
ALB	H	3	III	LOR	R	2	III
ALC	H	2	VII	LUC	S	3	II
ALG	S	2	IV	M04	S	3	VII
ALH	R	1	IV	MAL	R	1	II
ALM	H	1	III	MEL	R	1	VI
AM2	S	-	VI	MON	H	1	IV
ARE	H	3	III	MOT	S	3	VII
AROQ	H	-	I	MPD	S	3	IV
ASAB	S	-	VII	MTC	S	3	II
ATIG	S	-	I	MUL	H	3	VII
BAD	S	3	VII	NIJ	R	2	IV
BEC	H	1	II	OLO	R	1	III
BNL	H	2	VI	OLU	H	2	II
CAB	R	3	IV	ORI	S	3	II
CAC	S	3	II	OSU	H	2	II
CAR	H	1	II	PAM	S	3	I
CBN	S	3	II	PTO	S	-	VII
CHI	H	2	III	PUI	H	2	III
CHU	S	3	III	RON	H	3	IV
CIE	S	3	VII	SAR	R	1	I
CNS	H	1	I	SCT	S	-	IV
COR	S	3	II	SEV	S	3	III
DIL	S	3	VII	SF2	S	-	III
DUR	S	3	II	STF	S	3	III
EJI	S	3	VII	STS	R	2	VII
ELD	S	2	IV	TOR	S	2	IV
ELX	S	2	III	TOT	H	-	VII
EST	H	3	IV	TUI	R	1	VII
FAC	R	3	II	UGI	H	-	II
FOR	S	-	II	VEN	S	3	VII
GAN	S	3	II	VER	H	3	III
GDX	S	3	II	VI3	S	2	I
GER	R	1	III	VIE	S	3	II
GUA	S	3	II	VLM	H	3	VII
HUE	S	3	VII	VLR	H	2	VII
HUO	S	-	II	XAT	H	3	II
ITO	H	1	I	ZAR	H	2	II

Table 27: Numerical values of the GM of the H/V ratios of the 5% damped response spectra for the site classes of the accelerometric stations based on the Spanish ground-motion database.

Period (s)	Geometric Mean Values of H/V Response Spectral Ratios						
	CL-I	CL-II	CL-III	CL-IV	CL-V	CL-VI	CL-VII
0.01	1.631	1.455	1.437	1.155	1.167	1.404	1.630
0.05	1.374	1.232	1.223	1.040	1.205	1.397	1.392
0.07	1.350	1.100	1.107	0.943	1.177	1.266	1.406
0.10	1.926	1.182	1.240	1.044	1.246	1.143	1.594
0.15	1.998	1.619	1.447	1.071	1.180	1.356	1.780
0.20	1.645	2.030	1.615	1.166	1.444	1.959	1.632
0.25	1.494	2.157	1.789	1.309	1.484	1.990	1.693
0.30	1.527	2.316	2.013	1.409	1.508	1.585	1.801
0.40	1.355	2.156	2.174	1.578	1.445	1.830	1.806
0.50	1.266	1.996	2.290	1.659	1.359	1.970	1.782
0.60	1.262	1.774	2.021	1.902	1.310	1.836	1.693
0.70	1.186	1.678	1.904	2.021	1.428	1.864	1.768
0.80	1.156	1.577	1.730	1.965	1.363	1.786	1.812
0.90	1.106	1.434	1.633	1.801	1.325	1.708	1.750
1.00	1.081	1.455	1.558	1.806	1.243	1.812	1.771
1.25	1.196	1.348	1.441	1.878	1.312	1.808	1.717
1.50	1.207	1.264	1.342	1.751	1.271	1.720	1.609
2.00	1.130	1.246	1.327	1.639	1.410	1.765	1.350

The spectral ratios (spectral amplification factors) obtained for each site class (see Figure 56a and Table 27) are used to compare the results with the elastic design spectra of the Eurocode 8 (EC-8) (CEN, 2004). To make this comparison, the spectral shapes of each site class are first normalized at the zero-sec-period and the EC-8 design spectrum for Type 2 earthquakes and soil type A (EC8-2A spectrum) (see Table 23) is used as a reference spectrum. This reference spectral shape was selected because of the low-to-moderate seismic hazard in Spain (Pinzón et al., 2019d) and the relatively low magnitudes of the events involved in this study (see Figure 52). Recall that Type 2 spectra are recommended for regions with earthquakes whose surface-wave magnitude (Ms) is no greater than 5.5 (low seismicity) (CEN, 2004). The EC8-2A design spectrum and the normalized spectral ratios are then multiplied to obtain the expected design spectrum at each site class. This procedure is equivalent to considering the normalized spectral ratios as transfer functions between the basement and the surface soils, when the EC8-2A design spectrum is the reference spectrum in the hard rock basement. Thus, each site class can also be compared with the EC-8 design spectra for different soil classes (Figure 57). Site classes CL-I, CL-V, and CL-VII match well with EC8-2A and EC8-2B soil types, while CL-II, CL-III, and CL-VI are a better fit with EC8-2B and EC8-2C soil types. Finally, the spectrum corresponding to the CL-IV site class has large amplitudes for higher periods and lower amplitudes for low periods so that the long period section is a good match with the spectra for EC8-2C and EC8-2D soil types, and the short period section, that is, periods below 0.3 s, is well fitted by the EC8-2B spectrum.

Table 29 summarizes and highlights similarities between the site classes of this study and the EC-8. However, we must be aware that it does not mean that site classes and EC-08 soils are equivalent but only that there exist significant similarities in the corresponding spectra, mainly in the long period range. In our view, the spectra for site classes must be preferred for assessment purposes, because they are based on actual strong motion recordings.

Table 28: Standard deviation of the GM of H/V ratios of the 5% damped response spectra for the site classes of accelerometric stations based on the Spanish ground-motion database.

Period (s)	**Standard Deviation of H/V Spectral Ratios**						
	CL-I	**CL-II**	**CL-III**	**CL-IV**	**CL-V**	**CL-VI**	**CL-VII**
0.01	0.325	0.376	0.269	0.263	0.128	0.226	0.480
0.05	0.403	0.397	0.213	0.237	0.000	0.250	0.437
0.07	0.597	0.296	0.209	0.324	0.051	0.335	0.420
0.10	0.573	0.503	0.256	0.291	0.120	0.355	0.493
0.15	0.672	0.344	0.390	0.225	0.125	0.323	0.599
0.20	0.488	0.518	0.483	0.305	0.230	0.300	0.582
0.25	0.309	0.446	0.406	0.276	0.295	0.358	0.600
0.30	0.276	0.523	0.453	0.319	0.258	0.351	0.581
0.40	0.377	0.443	0.460	0.228	0.244	0.425	0.416
0.50	0.409	0.310	0.438	0.338	0.314	0.438	0.269
0.60	0.371	0.332	0.454	0.277	0.335	0.364	0.353
0.70	0.412	0.279	0.359	0.460	0.215	0.428	0.429
0.80	0.389	0.288	0.331	0.405	0.161	0.258	0.453
0.90	0.329	0.322	0.371	0.413	0.255	0.336	0.436
1.00	0.324	0.266	0.332	0.244	0.288	0.385	0.478
1.25	0.253	0.240	0.271	0.254	0.239	0.385	0.705
1.50	0.369	0.229	0.246	0.330	0.165	0.424	0.509
2.00	0.279	0.293	0.301	0.438	0.028	0.526	0.482

Table 29: Main similarities among the classification obtained in this study for the Spanish strong motion database and the soil classification of the Eurocode 8.

Site Class	**EC-8 Soils with Similarities**
CL-I	A and B
CL-II	B and C
CL-III	B and C
CL-IV	B, C, and D
CL-V	A and B
CL-VI	B and C
CL-VII	A and B

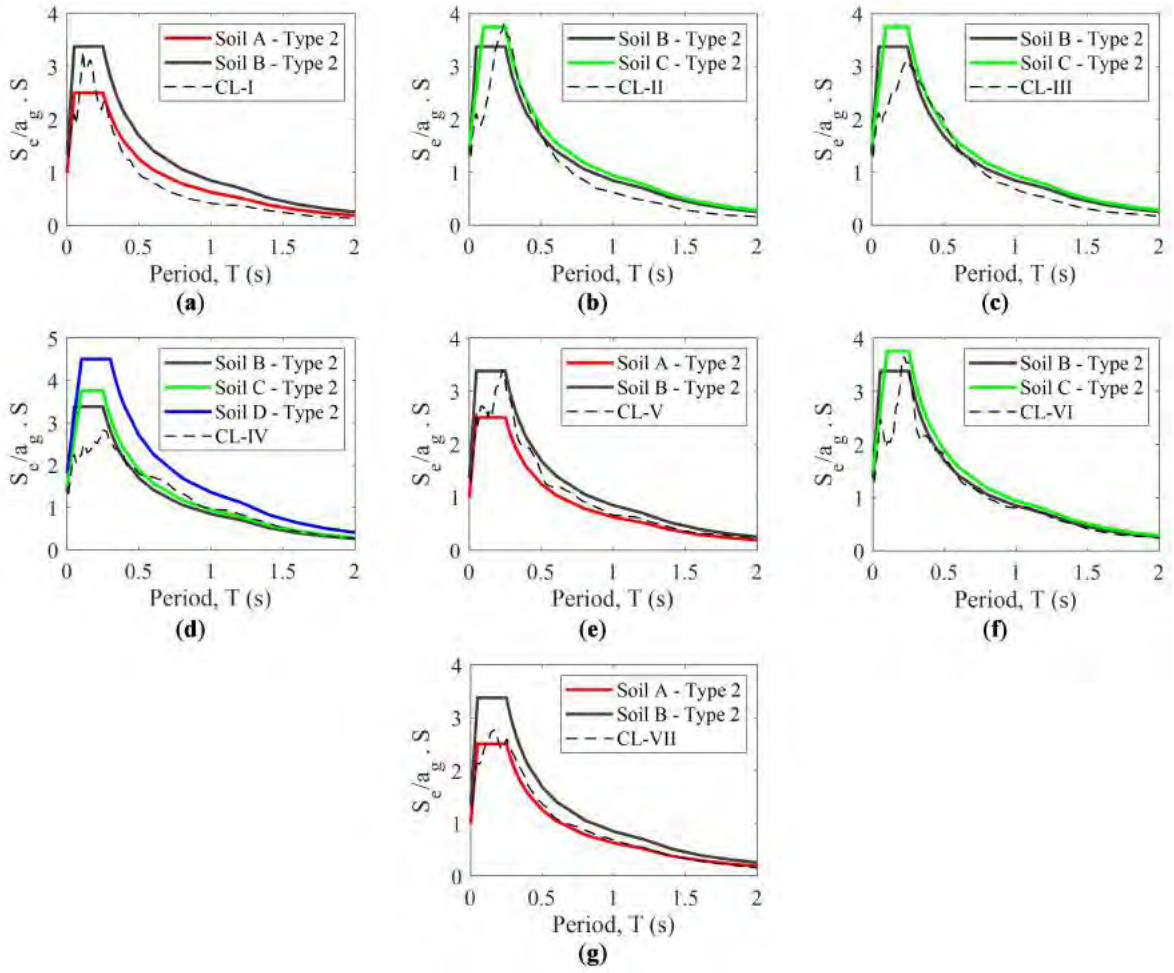

Figure 57: Comparison between the EC-8 Type 2 design spectra and the mean spectral shapes obtained for the site classes: (a) CL-I, (b) CL-II, (c) CL-III, (d) CL-IV, (e) CL-V, (f) CL-VI, and (g) CL-VII.

6.6 Conclusions

In this study, the Spanish ground-motion database was used to classify the site of each accelerometric station through the predominant period obtained using H/V ratios of the 5% damped response spectra. Directionality effects were also considered in the analysis through linear combinations of the horizontal components. For each ground motion, 180 H/V ratios were estimated (one per rotation angle). The 50th percentile was then selected to obtain a single ratio per ground motion. To determine the classification based on the site predominant period, the geometric mean of the ratios of each station was calculated to obtain one spectral shape per station. It is important to mention that is not usual to include the effects of directionality in H/V calculations. In most cases, the spectral quotients are only calculated with the orthogonal components.

Without considering directionality effects, this seismic site classification has previously been applied to ground motion databases from other countries. The application of this methodology to the Spanish network helps to improve the site classification of each station and fill the gap generated by the lack of information. One important novelty of this study is that it provides empirical information about the site response due to ground motions, complementing existing hypotheses based on geology maps. The proposed classification is made with data collected in the same station. It is not usual to classify an entire network according to a homogeneous common parameter, which is not a proxy from geology

or topography. In fact, most networks have few stations characterized by direct measurements such as Vs30 or the predominant frequency of the site.

This classification provides some advantages compared to others (e.g., Vs30-based). (i) The acquisition and processing of data are simple and automatic, since the network works continuously. (ii) This methodology may be easily exported to other networks, depending on the availability of strong motion databases. (iii) Moreover, this classification considers the real response of the site to actual seismic actions. This way, more realistic site conditions are obtained in comparison to the more general, simplified, and proxy classifications, which are used in seismic codes (e.g., Eurocode 8 site classification). (iv) When directionality is included, the method allows us to have information about the likely anisotropy of both the strong motion and the soil response. An additional value of the method is that the epistemic uncertainty decreases since all of the orientations are considered in the analysis.

In recent years, interest in the site conditions of installed stations has increased for research purposes and for engineering uses. From an engineering perspective, this classification plays an important role in the evaluation and design of structures, which can be useful, for instance, when actual accelerograms are needed for deterministic and/or probabilistic dynamic analyses, thus improving the results for specific areas and contributing to reducing epistemic uncertainties. Moreover, an equivalent classification to the Eurocode 8 soil classes was obtained using the design spectra and the spectral shapes of each station as transfer functions. This equivalence can be very useful if a study or project is carried out following the Eurocode 8 specifications, either for the earthquake resistant design or for assessment of existing structures.

Finally, the impact of these site classes on the development of new generation empirical ground motion predictive equations (GMPE) in comparison to the more traditional ones based on more simplified approaches that take into account the local site effects based on conventional rock/soil classifications remains a relevant and interesting issue.

7 Dynamic soil-structure interaction analyses considering directionality effects

Based on the published article: Pinzón, L. A., Mánica, M. A., Pujades, L. G & Alva, R. E. (2020). Dynamic soil-structure interaction analyses considering directionality effects. *Soil Dynamics and Earthquake Engineering, 130*, 106009. doi: 10.1016/j.soildyn.2019.106009
Journal URL: www.sciencedirect.com/science/article/abs/pii/S0267726119308966
FUTUR UPC URL: futur.upc.edu/26926910

7.1 Abstract

The paper investigates directionality effects of ground motions in the context of dynamic soil-structure interaction (DSSI) analyses. The problem addressed corresponds to a nonlinear soil deposit, overlaying firm ground, where the input motion was derived from an acceleration time history recorded at a rock outcrop. A simplified procedure is proposed to incorporate directionality effects. The main objective is to identify in advance the incidence angle producing the maximum response of a structure for a given earthquake. Results from the simplified procedure were evaluated by comparison with what is called here the complete rotational approach, where the behaviour of the structure, as a function of the incidence angle of the input motion, is derived through a large number of nonlinear dynamic soil-structure interaction analyses. The obtained results show the importance of considering directionality effects in DSSI analyses. The maximum response of the system was reasonably captured with the simplified approach.

7.2 Introduction

Earthquake ground-motions are recorded in three orthogonal components: two horizontal (normally N-S and E-W) and one vertical. These as-recorded time histories are usually employed to derive input motions for dynamic analyses (Mánica et al., 2014, 2016; Carbonari et al., 2011). However, the intensity of ground motions is not uniform in all directions. In the case of as-recorded accelerograms, their intensity will depend on the orientation of the sensor. Such orientation rarely corresponds to the direction in which maximum intensities occur and, therefore, the maximum response of a given system generally takes place for an intermediate unknown angle. This dependence on orientation is commonly known as directionality effect of ground motions.

Over the past two decades, directionality effects have received considerable attention. Research has been performed to assess these effects on recorded ground motions (Bradley and Baker, 2015; Pinzón et al., 2018a), intensity measures and their influences on the development of ground motion prediction equations (Shahi and Baker, 2014; Boore et al., 2006; Boore, 2010; Pinzón et al., 2018b), seismic demands of buildings (Rigato and Medina, 2007; Pinzón et al., 2019a; Fujii, 2016; Athanatopoulou, 2005; Cantagallo et al., 2012; Lagaros, 2010), probabilistic damage assessment (Vargas-Alzate et al., 2018), directivity effects in near-fault regions (Gordo-Monsó and Miranda, 2011; Huang et al., 2008; Garini and Gazetas, 2013), horizontal-to-vertical spectral ratios (Matsushima et al., 2017; Pinzón et al., 2019c; Stanko et al., 2017), seismic risk assessment of highways (Torbol and Shinozuka, 2014), and the performance of bridge foundations (Soltanieh et al., 2019).

As shown in Rigato and Medina (2007); Pinzón et al. (2019a); Lagaros (2010), directionality effects can be addressed in time-history-based dynamic analyses by using a number of linear combinations of the two horizontal as-recorded components as input motions. In this way, peak response parameters can be determined as functions of the rotation angle. This method is called here the complete rotational

approach (CRA). However, dynamic analyses are generally computationally expensive, especially when nonlinear behaviour is considered. For this reason, some simplified approaches have been developed to incorporate directionality effects without the need of performing a large number of analyses (Pinzón et al., 2019a; Diaz et al., 2018). For instance, a spectral matching technique was employed by Pinzón et al. (2019a) to derive input motions accounting for directionality. However, in most of these studies, directionality effects are taken into account in the seismic performance of buildings without considering the soil-structure interaction.

Let us consider the case of a dynamic soil-structure interaction analysis (DSSI), where a soil deposit (nonlinear) exists resting on firm ground (bedrock), and the input motion was derived from a ground motion recorded at a rock outcrop. In this case, directionality cannot be addressed directly in the input motion since site effects modify the response (Pinzón et al., 2019b). The angle where the maximum response of the structure occurs varies significantly from that estimated from the input motion applying simplified procedures. Certainly, directionality effects could be addressed applying the CRA; however, DSSI analyses are by far more computationally expensive compared to structural dynamic analyses preventing the use of the CRA in most cases.

In this paper, a simplified alternative is evaluated to incorporate directionality effects in DSSI by means of finite element (FE) analyses. The main objective is to identify in advance the angle that produces the maximum response of the soil-structure system for a given seismic action and, therefore, to perform only one DSSI analysis. Site effects are incorporated through free-field simulations, where the CRA is applied; free-field simulations are quite inexpensive compared to full DSSI analyses. The assumption explored is that the incidence angle that generates the maximum value of an intensity measure (IM), at the top of the soil deposit (free-field), will cause the maximum response of the structure. The IMs explored are: (1) the peak ground acceleration and peak ground velocity (PGA and PGV), (2) the PGV/PGA ratio, (3) the Arias intensity (AI), (4) the specific energy density (SED), (5) the cumulative absolute velocity (CAV), the angle that makes the response spectrum closest to RotD100 [i.e. the RotI100 spectrum as defined by Boore (2010)], and (7) the spectral response for the fundamental period of the structure (SA_{Tf}). RotD100 and RotI100 are orientation-independent intensity measures, proposed by Boore (2010), based on the spectral response of the rotated horizontal components. These intensity measures eliminate the effect of the sensor orientation as a component of epistemic uncertainty. Here, Rot refers to rotation, D and I means period-dependent and –independent respectively, and 100 refers to the 100th percentile of the rotated spectra (more details on these IMs are described in section 7.5.7). These IMs were selected since they are commonly employed, both in the development of seismic hazard studies (Baker and Bradley, 2017), and in the estimation of the expected damage of structures [e.g. correlations of these IMs with the Damage Index and Inter-storey Drift Ratios (Kostinakis et al., 2015), and with the Seismic Indices of Destructiveness (Garini and Gazetas, 2013)]. Results from the simplified procedure were evaluated by comparison with the CRA. In addition, the effect of different seismic actions, thicknesses of the soil deposit and the number of storeys were evaluated.

7.3 Case study

A sketch of the problem addressed is depicted in Figure 58, where the input motion, applied at the base of the FE model, is derived from an acceleration time history recorded at a rock outcrop; situations where the available accelerograms were recorded on top of the soil deposit are not considered here. The different incidence angles are obtained from the linear combination of the two horizontal as-recorded components of the considered acceleration time histories, by performing a usual coordinate transformation. The structure considered is a steel frame building rigidly connected to a concrete

raft foundation. The soil deposit corresponds to a medium to dense sandy layer overlying a bedrock. Analyses were performed using the FE code PLAXIS 2D (Brinkgreve et al., 2017), where the soil was characterised using an elastoplastic constitutive model. Details regarding the input motion, the surface structure, and the FE model are given in the following sections.

In the base case, a 30 m thick soil deposit was considered since the average shear wave velocity over the top 30 m (V_{S30}) is a commonly used parameter for site classification in seismic codes (CEN, 2004; ASCE, 2017). The influence of parameters such as the soil layer thickness, the input motions, and the number of storeys were also studied in this research. Three different groups of analyses were considered (see Table 30). In the first group, the 30 m thick soil and three different acceleration records were employed. In the second, the soil layer thickness was varied, and values of 10, 20, and 30 m were considered; one of the seismic actions of the first group was used here. Finally, in the third group, the analyses were performed with buildings of 3, 4 and 5 storeys using the same seismic action as the one used in the second group analyses.

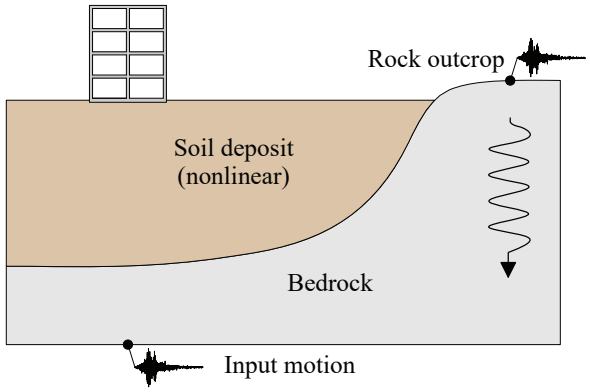

Figure 58: Input motion for DSSI analyses from an acceleration history recorded at a rock outcrop.

Table 30: Cases studied.

Group	Soil thickness (m)	Seismic actions	Building	Building fundamental period, T_f (s)
1	30	Friuli Campania Umbria	4-storey	0.95
2	10 20 30	Friuli	4-storey	0.95
3	30	Friuli	3-storey 4-storey 5-storey	0.80 0.95 1.11

7.3.1 Input motions

Input motions were derived from horizontal as-recorded components of the Friuli (1976), Campania (1980), and Umbria (1997) earthquakes in Italy. The recording stations are all located on rock outcrops, which are assumed to correspond to the bedrock underlying the soil deposit. The ground motion records and site specifications were obtained from the European Strong-Motion database (Ambraseys et al., 2000). In this work, ground motions were selected considering only their capacity

to excite significantly the soil-structure system. For more specific cases, for which the specific site is known, site-specific ground motions should be used according to the seismic hazard of the area.

Figure 59 shows the acceleration time histories of the two horizontal components of the selected accelerograms. The Friuli earthquake ground motion was recorded at the TLM1 station on May 6, 1976. The earthquake had a moment magnitude (M_W) of 6.5 and a recorded PGA of 350 cm/s^2 (obtained from the as-recorded components). The Campania earthquake (M_W = 6.9) was recorded at the STR station (November 23, 1980) and registered a PGA of 316.8 cm/s^2. Finally, the Umbria earthquake was recorded at the NCR station on September 26, 1997 with M_W = 6.0 and a PGA of 745.4 cm/s^2.

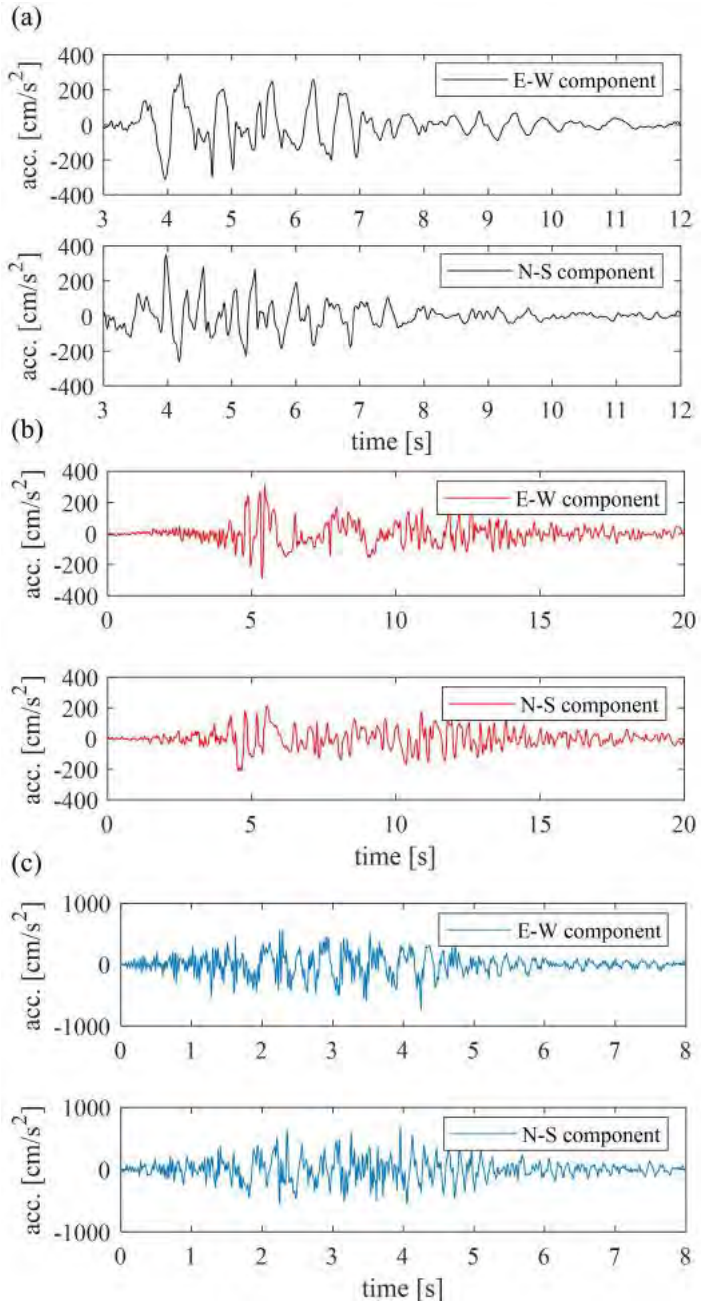

Figure 59: As recorded ground motion horizontal components of the earthquakes considered: (a) Friuli in 1976, (b) Campania in 1980, and (c) Umbria in 1997.

On the other hand, ground motion accelerations show great variability in time and space. For instance, if we ignore the vertical component, this variation takes place only on the horizontal plane. Then, the maximum acceleration will generally occur at an orientation that is different from those observed in the as-recorded accelerograms. These features can be observed in Figure 60, where the acceleration hodogram for the two horizontal accelerograms recorded at TLM1 station, after the Friuli earthquake, is depicted. The true PGA is 463.3 cm/s^2 and occurs at an azimuth of 319°. For Campania and Umbria records, the true PGA are 326.6 and 834.4 cm/s^2 respectively.

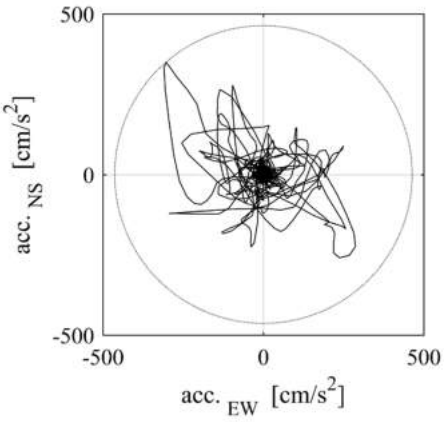

Figure 60: Particle acceleration motion of the accelerograms of the Friuli earthquake.

Thus, in order to account for different incidence angles, rotated input motions, $a_1'(t,\theta)$ and $a_2'(t,\theta)$, were derived from linear combinations of the two horizontal as-recorded components, $a_1(t)$ and $a_2(t)$, as a function of the rotation angle θ:

$$a_1'(t,\theta) = a_1(t) \cdot cos\,\theta + a_2(t) \cdot sin\,\theta \tag{19}$$

$$a_2'(t,\theta) = -a_1(t) \cdot sin\,\theta + a_2(t) \cdot cos\,\theta \tag{20}$$

where t is the time. Pairs of a_1' and a_2' represent different relative orientations between the ground motion and the considered structure. However, as only two-dimensional analyses are being considered in this work, only one of the rotated components is employed to derive the input motions for the analyses. Therefore, iteration in the range of 0-180° degrees is required to consider all possible, no redundant, actions in the analysed frame.

7.3.2 Surface structure

As mentioned before, the considered surface structures consist of a 2-, 3- and 4-storey steel frame buildings founded on a 0.30 m thick concrete raft foundation. The columns and beams are assumed to correspond to American wide-flange sections W16x89 and W14x68 respectively (ASTM A992 / A992M - 11, 2015). These sections have been modelled through 2D plate-type elements, with three degrees of freedom per node (two translational and one rotational) that follow Mindlin's theory (Mindlin, 1951). The behaviour of all structural elements was assumed linear elastic and the connections between them are fully restrained (ANSI/AISC 358-10, 2010). Dimensions of the 4-storey building model are shown in Figure 61a. The dimensions of the 3- and 5-storey buildings are the same, only removing and adding a storey respectively. The weight of the structure, including architectural finishes and facilities, were

considered as dead loads. Live loads magnitudes were selected according to ASCE7–10 (ASCE, 2010) provisions for office use. 100% of dead loads and 25% of live loads have been considered as inertial mass in the dynamic analyses (ASCE, 2010). To account for energy dissipation in the structural elements, Rayleigh damping was included with α and β coefficients selected to obtain a 2% damping ratio in the fundamental period of the structure; a 2% damping ratio is generally recommended for steel frame buildings (Paz and Leigh, 2003). Note that the employed structures have been calibrated with the 3D model used by Pinzón et al. (2019a) to achieve equivalent dynamic performance.

7.3.3 Main features of the finite element model

As mentioned before, the soil deposit is characterised as a 30 m thick medium to dense sandy layer, with a deep water table, overlaying a bedrock; thicknesses of 20 and 10 m were also considered. The full soil-structure system was modelled in the FE code PLAXIS 2D (Brinkgreve et al., 2017), assuming plane strain conditions. The FE mesh and main boundary conditions (for the 30 m thick soil deposit) are depicted in Figure 61b. The mesh comprises 4225 triangular 15-noded finite elements with fourth-order interpolation and 12 integration points. The mesh is more refined in the 70 m long zone directly under the building, where the soil-structure interaction (SSI) phenomenon mainly takes place. The latter was verified by comparing the obtained surface response from the free field simulation and from those considering the building. The lateral extension of the model was considered large enough so that any unwanted wave reflections are damped before reaching the zone where the SSI effects are relevant. Absorbing boundaries were also considered to account for the semi-infinite nature of the ground. For the lateral faces, free-field boundaries were employed. They consist of one-dimensional elements (for 2D problems) where the free-field response is computed. They are coupled to the main grid through viscous dashpots, which apply normal and shear stresses to account for the difference between the movement of the main grid (at the boundary) and the free-field elements. At the bottom face, a compliant base was prescribed (Lysmer and Kuhlemeyer, 1969) based on the use of independent dashpots in the normal and shear directions. They provide adequate means to absorb waves approaching the boundary. Both free-field and compliant boundary conditions are succinctly described in Brinkgreve et al. (2017).

Since negligible modifications of the outcrop motions occur by their deconvolution through the rock to the desired elevation, the original accelerograms recorded at rocky outcrops were directly employed to derive input motions at the base of the FE models (Mejia and Dawson, 2006). However, since a compliant base was prescribed at this boundary, absorbing the downward propagating waves, only the upward component of the motions must be applied. This is obtained by taking half of the outcrop motions. In addition, since an acceleration history (or velocity, or displacement) would nullify the absorbing effect of the compliant base, the input motion is given in terms of a shear stress time history, computed as:

$$\tau = 2\,\rho\,V_s\,\dot{u}_x^u \tag{21}$$

where ρ is the density, V_s is the shear wave velocity, and $\dot{u}_x^u$ is the horizontal particle velocity of the upward propagating motion. The factor of two is added because half of the stress is absorbed by the viscous dashpots.

The Plaxis Hardening Soil model with small-strain stiffness was employed to account for the non-linear response of the soil (Brinkgreve et al., 2017). The model is formulated within the framework of elastoplasticity and includes features like small-strain stiffness degradation, a hyperbolic hardening law, a volumetric yield cap, and a Mohr-Coulomb type limit surface. A detailed description of the model can be found in Brinkgreve et al. (2017, 2007).

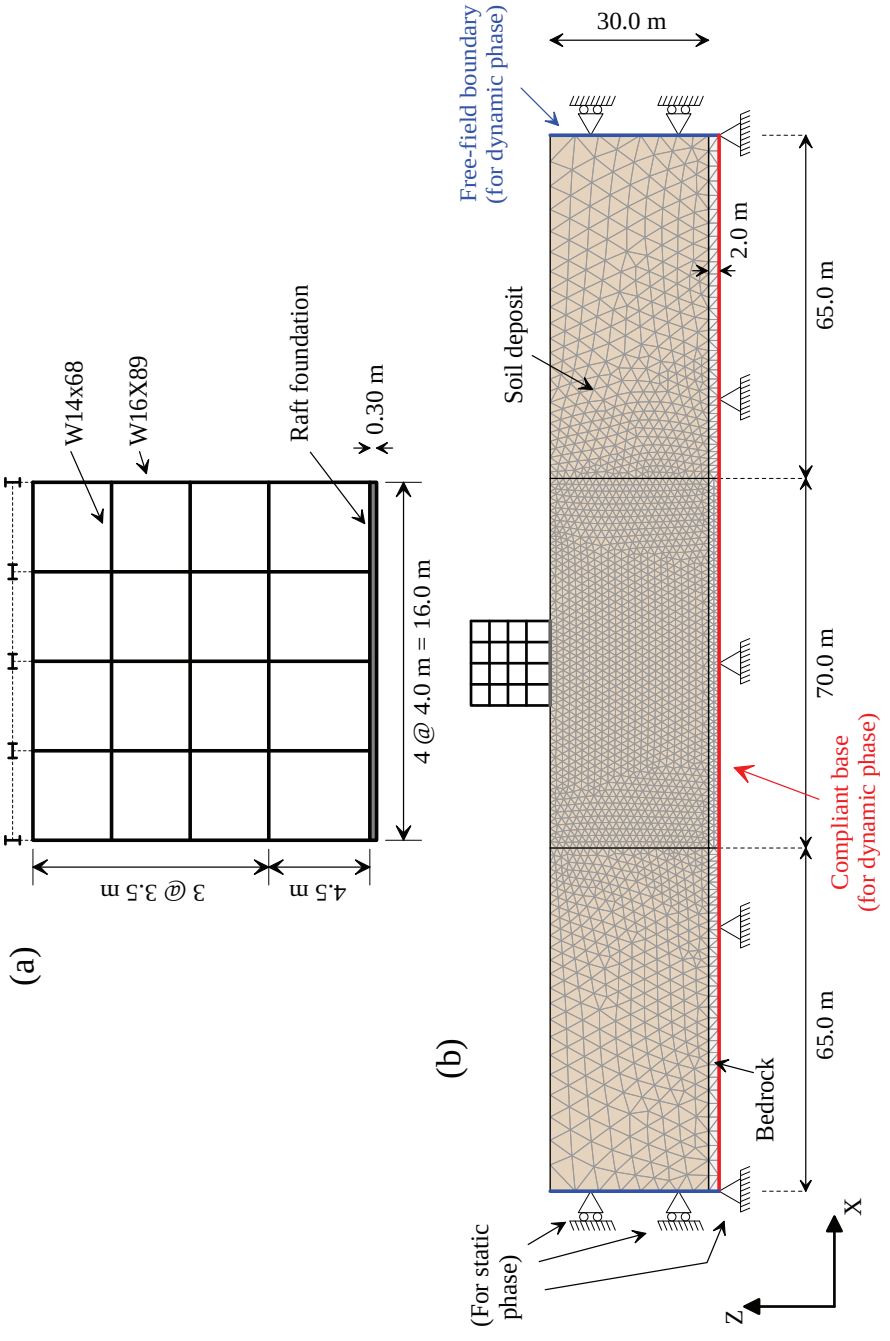

Figure 61: (a) Building geometry and (b) soil-building FE model employed.

Employed parameters are shown in Table 31. They were chosen to represent a medium to dense sand deposit. Energy dissipation occurs in the model due to both small-strain stiffness degradation and plastic strains. However, for small strain amplitudes, damping is generally underestimated (Brinkgreve et al., 2007). Therefore, Rayleigh damping was also included in the soil elements, with α and β coefficients selected to obtain a 2% damping ratio at the fundamental vibration period of the soil deposit. The small layer considered for the bedrock (Figure 61b), required to apply the proper input motion, was characterised as a linear elastic material.

Table 31: Soil parameters

Parameter	Symbol	Units	Value
Unit weight	γ	kN/m^3	20
Small strain shear stiffness	G_0^{ref}	kN/m^2	125000
Shear strain at 0.7 G_0	$\gamma_{0.7}$	-	1.5E-4
Triaxial compression stiffness	E_{50}^{ref}	kN/m^2	40000
Primary oedometric stiffness	E_{oed}^{ref}	kN/m^2	32000
Unloading/reloading stiffness	E_{ur}^{ref}	kN/m^2	120000
Poisson's ratio for unloading/reloading	υ_{ur}	-	0.2
Reference pressure	p_{ref}	kN/m^2	100
Rate of stress-dependency	m	-	0.5
Cohesion	c	kN/m^2	0
Friction angle	ϕ	^{o}	35
Dilatancy angle	ψ	^{o}	5
Failure ratio	R_f	-	0.9
Stress ratio for normal consolidation	K_0^{nc}	-	0.426

After stress initialisation, a static phase was considered where the building and its foundation were activated. Then, the dynamic analyses described in this work were performed.

7.4 Complete rotational approach - CRA

As mentioned before, directionality effects can be studied in DSSI analyses by performing simulations with a number of linear combinations of the two horizontal acceleration components of the input motion (Equation 19) (the vertical component is generally neglected). Increments of 1^o are usually employed, in the range of 0^o and 180^o. Then, the distribution of any output variable can be plotted as a function of the incidence angle allowing the determination of the most critical orientation for the system. However, this method entails high computational costs, and it would be of practical interest to develop a simplified approach to assess directionality effects with fewer computational resources.

In this work, the CRA approach was applied to all considered cases to serve as a benchmark to evaluate the results of the simplified procedure. For each case analysed, 90 2D DSSI analyses (using increments of 2^o) were performed resulting in 630 analyses. The main monitored variable was the horizontal roof displacement relative to the base of the building. This demand parameter can be related to the level of structural damage (Pinzón et al., 2019a).

Results obtained for the different cases are shown in Figure 62 as maximum relative roof displacement values. In the first group of analyses (Figure 61a), results using different input motions are compared. The seismic motions of the Friuli earthquake resulted in the largest displacements and showed the largest difference between maximum and minimum values as functions of the incidence angle. It is also important to notice that the variation with orientation is quite different for each seismic action and, therefore, unconservative designs might result from using the as-recorded components depending on the selected ground motion.

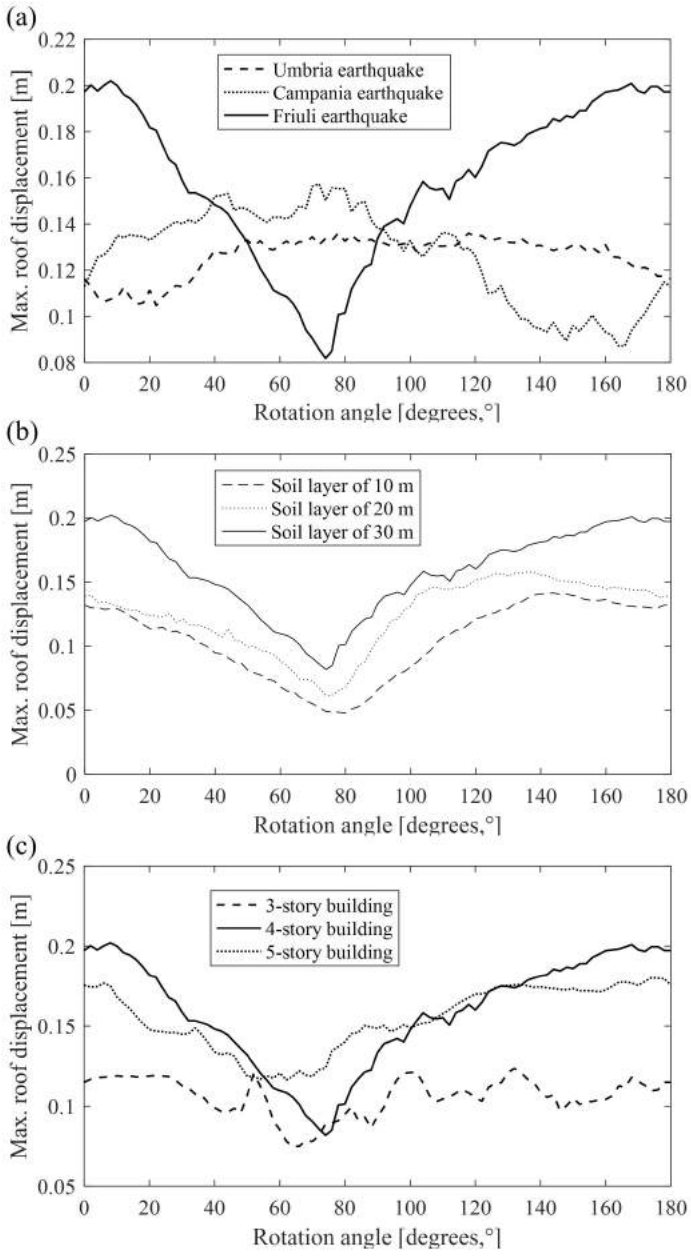

Figure 62: Maximum relative roof displacement as a function of the rotation angle obtained from the CRA for groups 1 (a), 2 (b) and 3 (c).

In the second group of analyses (Figure 62b), motions of the Friuli earthquake are also employed in combination with layer thicknesses of 10 and 20 m. Although the shape of the variation is somewhat similar for the different cases, the maximum relative roof displacements occur at different orientations for each of them even though the same input motion is being employed. This result stresses the fact that directionality effects cannot be addressed directly in the input motion in the presence of soil deposits.

Finally, in the third group (Figure 62c), analyses were performed using the seismic action from Friuli, but considering 3- and 5-storey buildings as surface structures. Again, the variation with orientation differs significantly among the different analyses since the dynamic response of each model depends on the dynamic properties of the structure. The 4-storey building resulted in the largest displacements although, depending on the incidence angle, larger displacements can occur in the 5-storey building. Nevertheless, note that, unlike the 3-storey building, the location of the maxima is well defined for the 4- and 5-storey buildings, and the angles where the maxima occur are relatively similar.

Results shown in Figure 62 were obtained from approximately 3000 hours of computing time on Intel Core i7-4712HQ 2.67 GHz CPUs; certainly, an excessive amount of time for conventional engineering projects.

7.5 Simplified rotational approach - SRA

A simplified approach is pursued here for the prediction of the incidence angle producing the peak response of a soil-structure system. By deriving this angle in advance, only one DSSI analysis is required for a given seismic action compared to the large number of analyses involved in the CRA. The assumption explored is that the angle that generates the maximum value of an intensity measure, at the top of the soil deposit (free-field motion), would also cause the maximum response of the structure. The motion at the surface is obtained through free-field site response analyses, where the CRA is applied; in this way, site effects are introduced. Then, IMs, as functions of the rotation angle, can be determined from the motion computed at the surface of the soil deposit and from which the critical orientation between the seismic action and the soil-structure-system may be predicted.

7.5.1 Free-field seismic actions computations

The application of the CRA to the free-field response implies conducting site response analyses for each rotation angle considered. They are usually performed using frequency-domain methodologies, to reduce calculation times, where nonlinearity is introduced through iterative procedures (Schnabel et al., 1972). However, the elastoplastic constitutive law employed here prevents the use of frequency-domain approaches. The free-field response is addressed here through dynamic FE analyses. However, they demand much fewer computational resources compared to full DSSI analyses since only a slender column of soil, with special boundary conditions, is required (Mánica et al., 2014).

The geometry and mesh of the free-field FE model (for the 30 m thick soil deposit) are depicted in Figure 63. This model shares most of the features of the full DSSI model (Figure 61b) except for the lateral boundary conditions, where tied degrees of freedom were employed. With these conditions, the nodes of the left and right boundaries at the same elevation are connected so that they are characterised by the same vertical and horizontal displacements (Zienkiewicz et al., 1988).

In Figure 64, the acceleration records of the as-recorded components (E-W $\theta = 0^{o}$, N-S $\theta = 90^{o}$) and the rotated component for $\theta = 50^{o}$ of the Friuli earthquake are compared with the results of the free-field simulations at the surface.

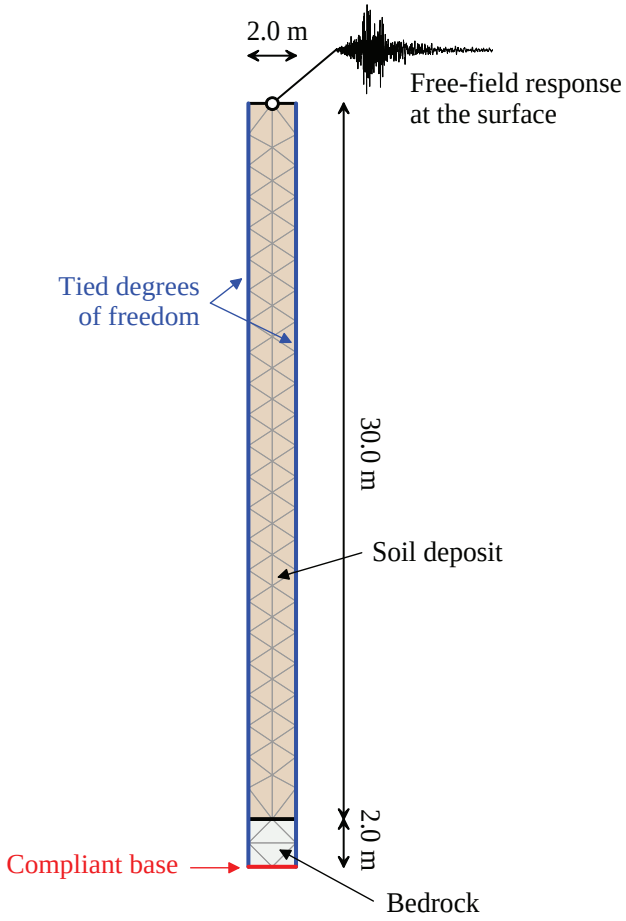

Figure 63: Geometry, mesh, and boundary conditions of the free-field FE simulation.

Clearly, an amplification of the signal occurs in the three cases due to site effects. This amplification is also evident in the response spectra (Figure 65), where considerably larger spectral ordinates are obtained from the free-field simulations.

7.5.2 Intensity measures

From the free-field time histories at the surface, the angles that produce the maximum value of each IM are identified. The IMs explored are: (1) the peak ground acceleration and velocity, (2) the PGV/PGA ratio, (3) the Arias intensity, (4) the specific energy density, (5) the cumulative absolute velocity, (6) the angle that corresponds to the RotI100 response spectrum, and (7) the spectral response for the fundamental period of the building. Then, the obtained orientations can be compared with those from the CRA to assess the performance of each IM.

In the following sections, the determination of the critical angle, for each IM, is described. Only results for the first group of analyses (different seismic actions) are shown. However, the obtained results for different soil layer thicknesses (second group of analyses) and different number of storeys (third group of analyses) are also compared with the CRA later on.

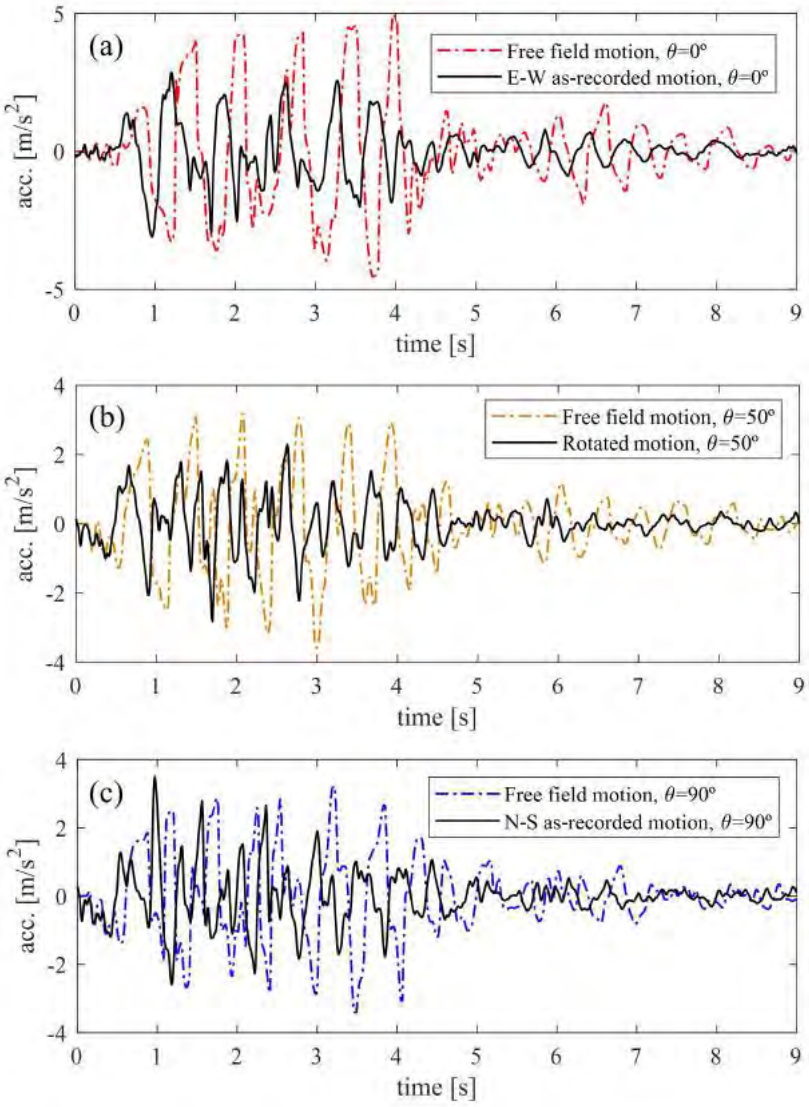

Figure 64: Time histories from the recorded motion and the free-field motion at the Surface for the accelerograms of the Friuli earthquake. Rotation angles of (a) $\theta = 0°$, (b) $\theta = 50°$, and (c) $\theta = 90°$.

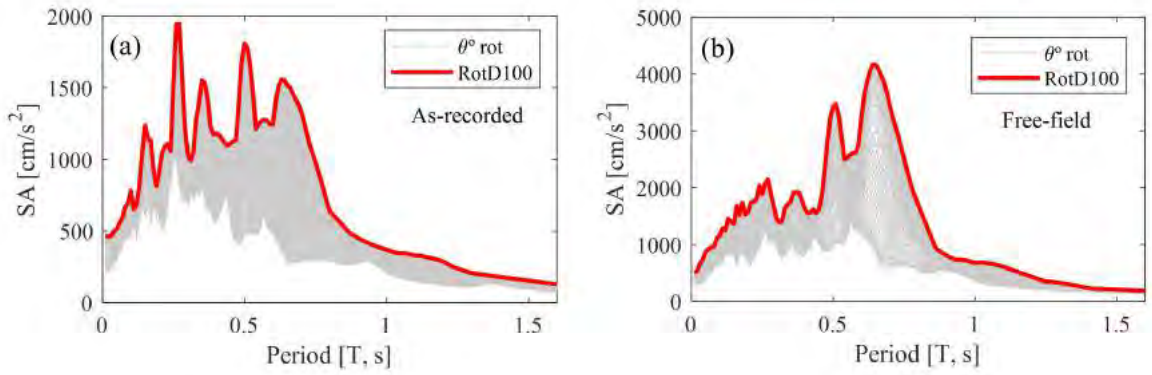

Figure 65: Response spectra from the rotated histories and their envelope (RotD100) for the (a) recorded motion and (b) the free-field motion at the surface.

7.5.3 Peak ground acceleration, peak ground velocity, and PGV/PGA ratio

For a given time, the magnitude of acceleration or velocity components of a recorded motion depends on the considered incidence angle θ. Therefore, peak values can be determined as a function of θ as follow:

$$PGA_{rot}(\theta) = max\,|acc_{rot}(t,\theta)|_{for\,t} \quad \text{for } \theta \in [0\,180] \tag{22}$$

$$PGV_{rot}(\theta) = max\,|vel_{rot}(t,\theta)|_{for\,t} \quad \text{for } \theta \in [0\,180] \tag{23}$$

where acc_{rot} and vel_{rot} are the rotated acceleration and velocity time histories of the horizontal components. Figure 66 shows the variation of PGA_{rot} and PGV_{rot} (normalised by the maximum value) for the three ground motions considered; locations of the maxima are indicated with circles in the figure. The variations of these two IMs are significantly different, but their maximum values occur at somewhat similar orientations.

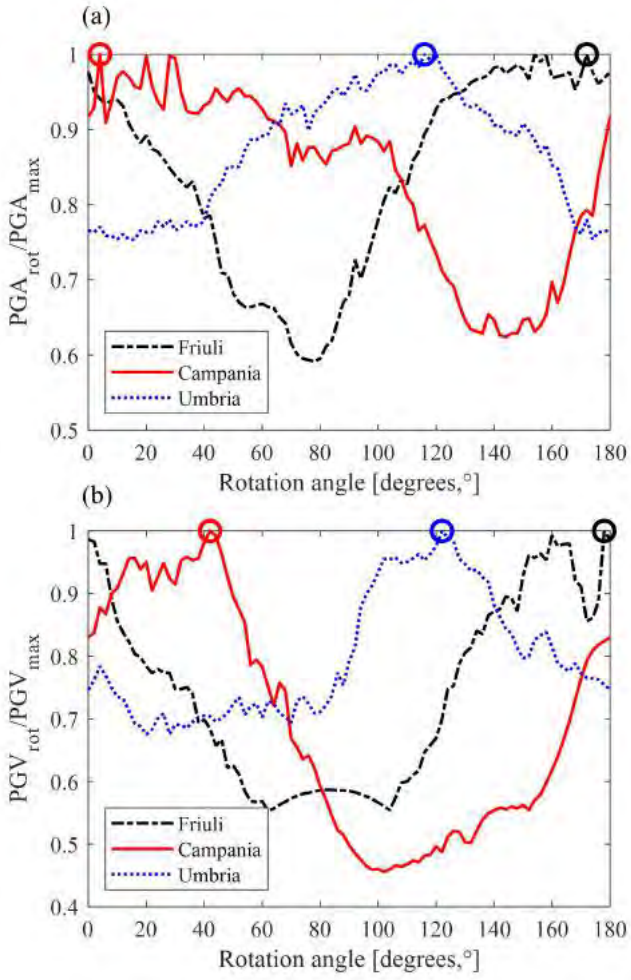

Figure 66: Normalised (a) peak ground acceleration and (b) peak ground velocity as a function of the rotation angle for the Friuli, Campania, and Umbria seismic actions (group 1).

Tso et al. (1992) use the PGV/PGA ratio as a measure of the frequency content of an earthquake ground motion. Sucuoğlu and Nurtuğ (1995) correlated this ratio to the seismic energy dissipation since it is linked to the duration of the dominant acceleration pulse of a near-fault impulsive motion.

Bommer et al. (2000) used this ratio to estimate corner periods at which the constant acceleration ends and the constant displacement begins on code spectra. For each rotation angle, the PGV/PGA ratio can be defined as:

$$PGV_{rot}(\theta)/PGA_{rot}(\theta) = \frac{max\,|vel_{rot}(t,\theta)|_{for\,t}}{max\,|acc_{rot}(t,\theta)|_{for\,t}} \text{ for } \theta \in [0\,180] \tag{24}$$

The variation of this IM is shown in Figure 67. The angles that generate the maximum normalised ratios are 2°, 42° and 126° for the Friuli, Campania, and Umbria seismic actions respectively. Note that the problem has a periodicity of 180° and, therefore, results for angles close to 0° are, in fact, similar to those close to 180°. Consequently, similar orientations are obtained compared to Figure 66 even though the shapes of the curves are quite different.

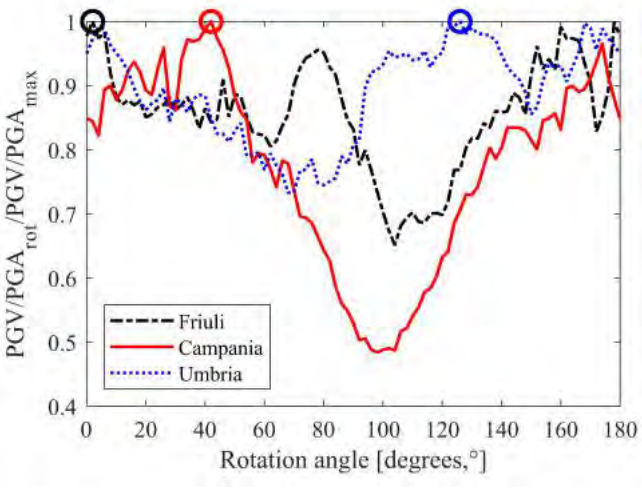

Figure 67: Normalised PGV/PGA ratio as a function of the rotation angle for the Friuli, Campania, and Umbria seismic actions (group 1).

7.5.4 Arias intensity - *AI*

The AI is a measure of the severity of a ground motion defined as the total energy per unit weight stored by a set of undamped simple oscillators at the end of a strong seismic action due to an earthquake (Arias, 1970). The AI, for a given rotated motion, is computed in the following way:

$$AI_{rot}(\theta) = \frac{\pi}{2g}\int_0^{t_f} acc_{rot}(t,\theta)^2 dt \tag{25}$$

where g is the acceleration due to gravity and t_f is the total duration of the record. The variation of AI as a function θ is shown in Figure 68. The angles producing the maximum value for this IM for the first group of analyses are 164°, 44° and 104° for the Friuli, Campania, and Umbria earthquakes.

7.5.5 Specific energy density - *SED*

The SED (Sarma, 1971; Sarma and Yang, 1987) is defined as the integral of the squared velocity time history vel_{rot} for the total duration of the motion t_f (Equation 26); therefore, this IM is, to some

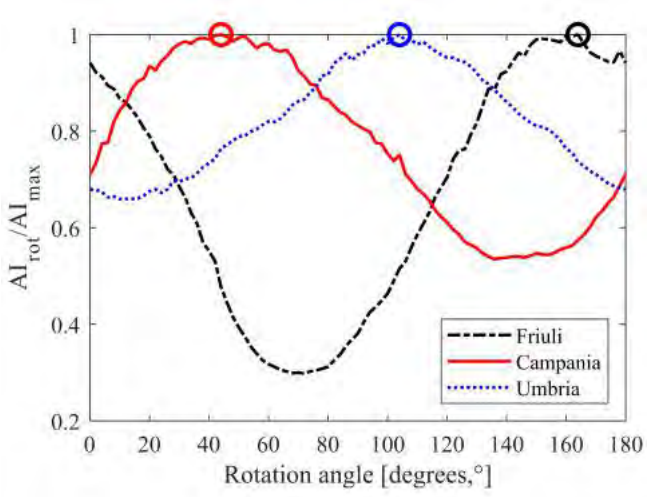

Figure 68: Normalised Arias intensity as a function of the rotation angle for the Friuli, Campania, and Umbria seismic actions (group 1).

extent, analogous to the AI (Equation 25).

$$SED_{rot}(\theta) = \int_0^{t_f} vel_{rot}(t,\theta)^2 dt \tag{26}$$

In Figure 69, the variation of the SED, as a function of the rotation angle, is shown. For the first group of analyses, the angles where the maxima SED_{rot} occur are 162°, 14° and 104° for the seismic actions of Friuli, Campania and Umbria earthquakes respectively.

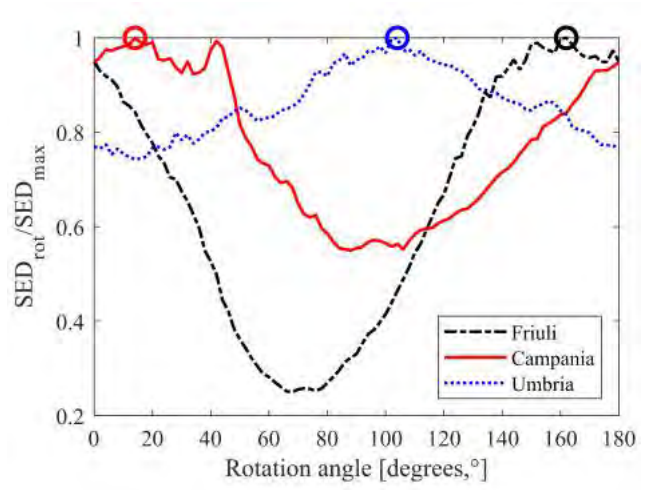

Figure 69: Normalised specific energy density as a function of the rotation angle for the Friuli, Campania, and Umbria seismic actions (group 1).

7.5.6 Cumulative absolute velocity - *CAV*

The CAV is an IM proposed by Reed and Kassawara (1990), and it has been used to estimate the destructive potential of strong ground motions. It is defined in the following way:

$$CAV_{rot}(\theta) = \int_0^{t_f} |acc_{rot}(t,\theta)|\, dt \tag{27}$$

The normalised CAV, as a function of θ is shown in Figure 70. The angles where the maximum value is achieved are 164°, 52° and 128° for the accelerograms recorded during the Friuli, Campania and Umbria earthquakes, respectively.

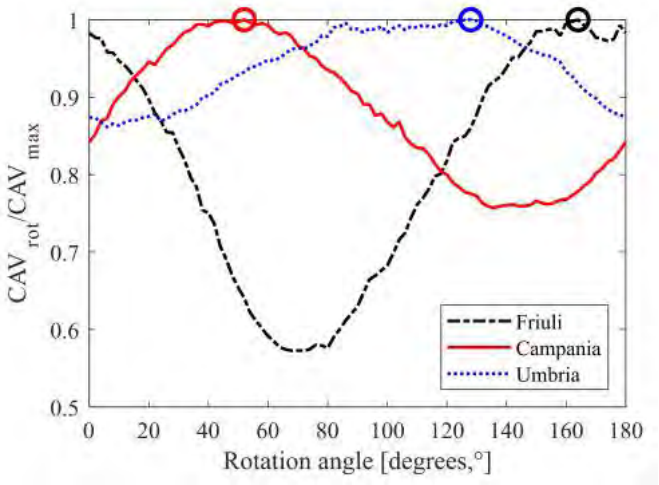

Figure 70: Normalised cumulative absolute velocity as a function of the rotation angle for the Friuli, Campania, and Umbria seismic actions (group 1).

7.5.7 Maximum spectral response

The aim is to find the angle that generates spectral accelerations closest to the RotD100 spectrum within a given range of vibration periods; the range considered is related to the fundamental period of the system. The response spectrum, for a given θ, is estimated using Equation 28. The RotD100 spectrum is the envelope of all spectra from the rotated motions (Figure 71b and Figure 71d).

$$SA_{rot}(T,\xi,\theta) = max\, |\ddot{u}_{rot}(t,T,\xi,\theta)|_{for\, t} \tag{28}$$

where SA_{rot} is a spectral acceleration from a rotated motion, $\ddot{u}_{rot}$ is the acceleration response of a single-degree-of-freedom damped oscillator, T is the vibration period, and ξ is the damping ratio. A penalty function is computed as follows:

$$penalty(\theta) = \frac{1}{N_{per}} \sum_{i=1}^{N_{per}} \left[\frac{SA_{rot}(T_i,\xi,\theta)}{SA_{RotD100}(T_i,\xi)} - 1 \right]^2 \tag{29}$$

where $SA_{RotD100}$ are the spectral ordinates of the RotD100 spectrum, and N_{per} is the number of sample period between T_1 and T_2. Then, the RotI100T_1T_2 spectrum is defined as the one obtained from the rotated motion that minimises the penalty function. This orientation is assumed as the critical θ for this IM.

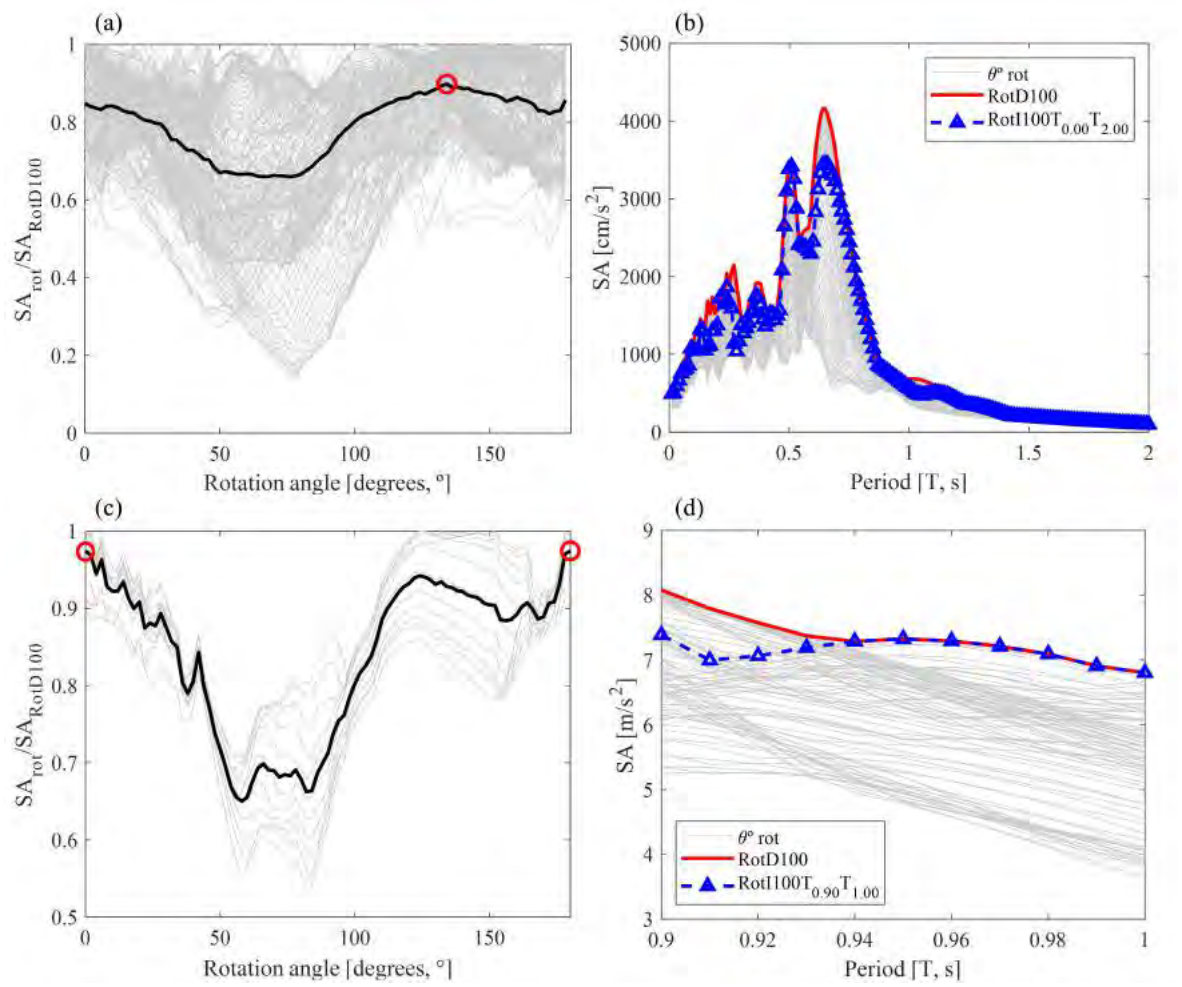

Figure 71: $SA_{rot}/SA_{RotD100}$ spectral ratio as a function of the rotation angle for the Friuli earthquake for vibration periods (a) between 0.0 and 2.0 s and (c) between 0.9 and 1.0 s. Response spectra from the rotated motions, the RotD100 spectrum, and the RotI100T_1T_2 spectrum for the Friuli seismic actions for vibration periods (b) between 0.0 and 2.0 s and (d) between 0.9 and 1.0 s.

In Figure 71, an example of the determination of the RotI100T_1T_2 spectrum, using strong motion data from Friuli earthquake, is presented. Figure 71a and Figure 71b show the results obtained for a wide range of periods (between 0.0 and 2.0 s). The studied building has a predominant period of 0.95 s and, therefore, a range between 0.9 and 1.0 s has also been considered to calculate the RotI100T_1T_2 spectrum. The obtained results are shown in Figure 71c and Figure 71d. Note that the critical angle varies considerably depending on the period range considered. In this study, a range of ±0.05 s of the predominant period of the buildings was used.

7.5.8 Spectral response for the fundamental period of the building - SA_{Tf}

An IM highly used in both seismic hazard studies and structural analyses is the spectral response at the building's fundamental period. This measure is defined as the maximum acceleration response of a 5% damped single-degree-of-freedom linear oscillator, as shown in the following equation:

$$SA_{Tf(rot)}(T_f, \xi, \theta) = max\,|\ddot{u}_{rot}(t, T_f, \xi, \theta)|_{for\,t} \tag{30}$$

In fact, this approach coincides with that of section 7.5.7 if the period range is reduced to a single value. The variation of this IM is shown in Figure 72 for the considered seismic actions. For the Friuli earthquake, the critical angle is 0° (or 180°), which is the same result obtained in Figure 71c.

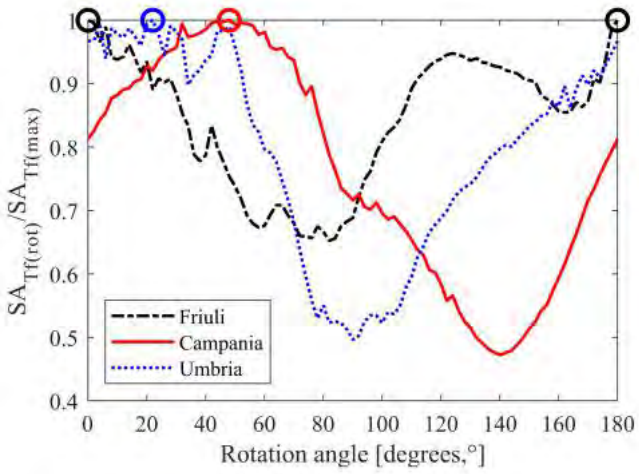

Figure 72: Normalised spectral response for the fundamental period of the building ($T_f = 0.95s$) as a function of the rotation angle for the Friuli, Campania, and Umbria seismic actions (group 1).

7.6 CRA and SRA comparison

In this section, the critical angles predicted with the SRA are compared with the CRA. Figure 73 shows the relative roof displacement, as a function of the rotation angle, obtained through the CRA for the group of analyses 1 (30 m soil layer and different input motions); the position of the maximum values is indicated with a black square. The values obtained with the SRA, for the different IMs, are also indicated in the figure with red circles. For the Friuli earthquake, the SRA captured reasonably the angle where the maximum response of the building occurs (in terms of relative roof displacements) with all the IMs (recall that the 180° periodicity implies that angles close to 180° are also close to 0°). For the other two earthquakes, a larger dispersion is observed between the different IMs. The PGV and the PGV/PGA ratio predicted the angles closest to the CRA for the three earthquakes considered. The obtained critical orientations from all the analyses performed are summarised in Table 32. In the second group of analyses (different soil thickness and Friuli seismic actions), the PGV and PGV/PGA ratio also showed the closest values to the CRA. Finally, in the third group of analyses (different buildings and Friuli seismic actions), the RotI100T_1T_2 IM produced, on average, the closest values to the CRA, followed by the PGV and the PGV/PGA ratio respectively. Results are coherent since RotI100T_1T_2 takes into account the variation of the structure (structural behaviour) using the maximum spectral response in a range of period close to the fundamental period of each building.

The maximum displacements obtained through the CRA and SRA are compared in Table 33; the relative error with respect to the CRA approach is also indicated (a negative sign implies an underestimation of the relative roof displacement). The lowest mean error (averaged over all the considered cases) was obtained with the PGV (-2.476%), which is also the IM capturing the closest critical angle (see Table 32). The PGV/PGA ratio, the RotI100T_1T_2 and the AI also achieved similar error magnitudes. Nevertheless, the latter shows larger differences with respect to the critical angle (Table 32). The worst performing IM was the SA_{Tf}, with a mean relative error of -11.892%.

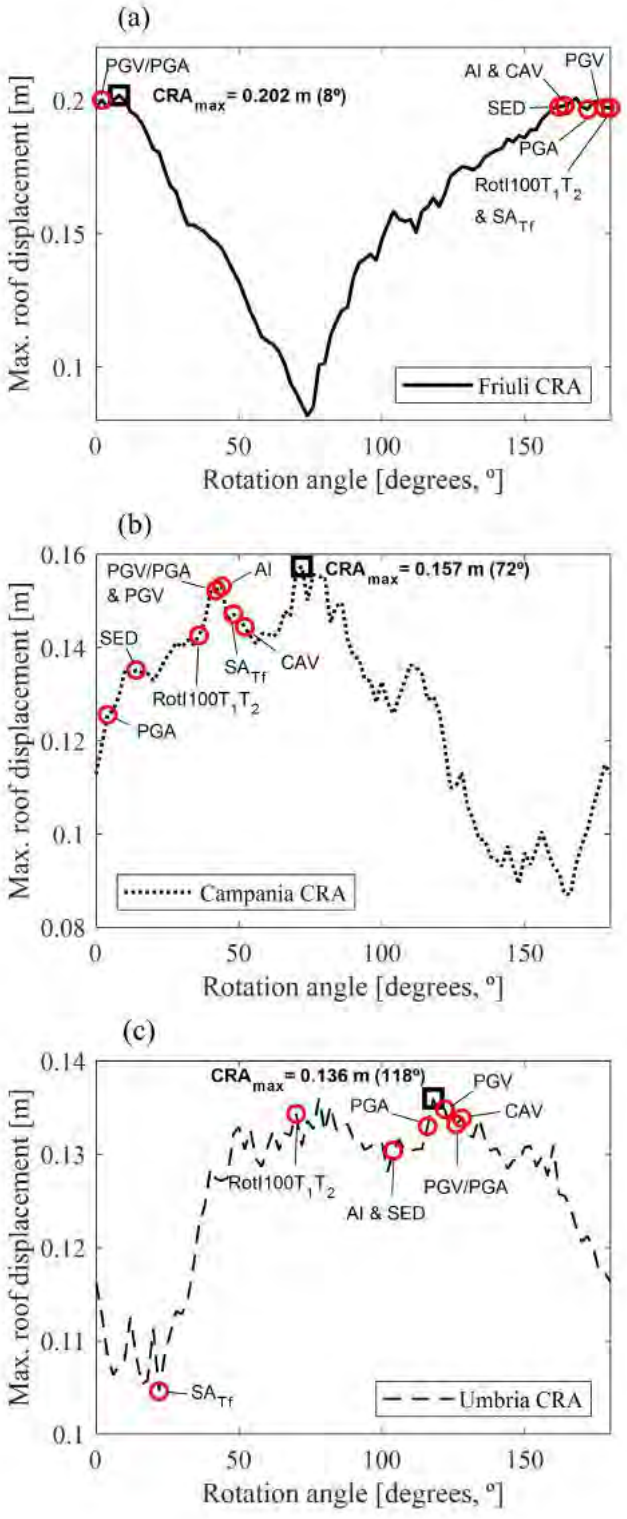

Figure 73: Comparison between the relative roof displacements obtained from the CRA and SRA for the (a) Friuli, (b) Campania, and (c) Umbria seismic actions (group 1).

Table 32: Critical incidence angles where the maximum relative roof displacement occurred with the CRA and the SRA.

Approach	Group 1			Group 2			Group 3		
	Friuli	Campania	Umbria	10 m	20 m	30 m	3-storey	4-storey	5-storey
CRA	8°	72°	118°	144°	136°	8°	132°	8°	175°
SRA with PGA	172°	4°	116°	148°	164°	172°	172°	172°	172°
SRA with PGV	178°	42°	122°	148°	146°	178°	178°	178°	178°
SRA with PGV/PGA	2°	42°	126°	150°	146°	2°	2°	2°	2°
SRA with AI	164°	44°	104°	154°	142°	164°	164°	164°	164°
SRA with SED	162°	14°	104°	166°	140°	162°	162°	162°	162°
SRA with CAV	164°	52°	128°	154°	142°	164°	164°	164°	164°
SRA with SA_{Tf}	0°	48°	22°	36°	174°	0°	142°	0°	178°
SRA with RotI100T_1T_2	0°	36°	70°	154°	146°	0°	134°	0°	178°

Table 33: Comparison between the relative roof displacements obtained through the CRA and SRA.

Approach	Roof displacement	Group 1			Group 2			Group 3			Mean relative error (δ in %)*
		Friuli	Campania	Umbria	10 m	20 m	30 m	3-storey	4-storey	5-storey	
CRA	max. (m)	0.202	0.157	0.136	0.141	0.158	0.202	0.123	0.202	0.180	-
SRA with PGA	max. (m)	0.189	0.126	0.133	0.141	0.145	0.189	0.113	0.189	0.178	-6.551
	δ with CRA_{max} (%)	-6.436	-19.745	-2.206	0.000	-8.228	-6.436	-8.130	-6.436	-1.111	
SRA with PGV	max. (m)	0.197	0.152	0.135	0.141	0.151	0.197	0.115	0.197	0.180	-2.476
	δ with CRA_{max} (%)	-2.475	-3.185	-0.735	0.000	-4.430	-2.475	-6.504	-2.475	0.000	
SRA with PGV/PGA	max. (m)	0.200	0.152	0.133	0.140	0.151	0.200	0.117	0.200	0.174	-2.819
	δ with CRA_{max} (%)	-0.990	-3.185	-2.206	-0.709	-4.430	-0.990	-4.878	-0.990	-3.333	
SRA with AI	max. (m)	0.198	0.153	0.130	0.136	0.155	0.198	0.113	0.198	0.177	-3.455
	δ with CRA_{max} (%)	-1.980	-2.548	-4.412	-3.546	-1.899	-1.980	-8.130	-1.980	-1.667	
SRA with SED	max. (m)	0.198	0.135	0.130	0.131	0.156	0.198	0.107	0.198	0.175	-6.364
	δ with CRA_{max} (%)	-1.980	-14.013	-4.412	-7.092	-1.266	-1.980	-13.008	-1.980	-2.778	
SRA with CAV	max. (m)	0.198	0.144	0.134	0.136	0.155	0.198	0.113	0.198	0.177	-3.853
	δ with CRA_{max} (%)	-1.980	-8.280	-1.471	-3.546	-1.899	-1.980	-8.130	-1.980	-1.667	
SRA with SA_{Tf}	max. (m)	0.197	0.147	0.105	0.102	0.142	0.197	0.106	0.197	0.18	-11.892
	δ with CRA_{max} (%)	-2.475	-6.369	-22.794	-27.660	-10.127	-2.475	-13.821	-2.475	0.000	
SRA with RotI100T_1T_2	max. (m)	0.197	0.143	0.134	0.136	0.151	0.197	0.121	0.197	0.18	-3.209
	δ with CRA_{max} (%)	-2.475	-8.917	-1.471	-3.546	-4.430	-2.475	-1.626	-2.475	0.000	
Mean relative error (δ in %)		-2.599	-8.280	-4.963	-5.762	-4.589	-2.599	-8.028	-2.599	-1.320	

*The Friuli, the 30 m and the 4-storey analyses from group 1, 2 and 3 respectively are the same analysis, therefore only are considered once in the mean error estimation.

Although the SRA is not able to predict exactly neither the critical angle nor the maximum relative roof displacement obtained with the CRA, the errors are much smaller compared to those obtained using the as-recorded components (Table 34), which is the customary practice. The mean errors obtained using the E-W and the N-S components for all analysed cases are 10.334% and -25.353% respectively. When the recorded motion is polarised with one of the horizontal principal directions of the accelerometer, the errors would be small. This situation occurred in the E-W component of the Friuli earthquake seismic actions, where a relative error of -2.475% (4-storey case) and -2.222% (5-storey case) were estimated. However, this is generally not the case and the relative roof displacements can be underestimated as much as 50% if directionality effects are not properly addressed.

7.7 Conclusions

In this study, the importance of considering directionality effects of ground motions in 2D DSSI analyses has been highlighted. Two-dimensional models are widely used to perform DSSI analyses, since they are less computationally expensive than a three-dimensional (3D) one (Tabatabaiefar and Fatahi, 2014; Tabatabaiefar et al., 2015; Kham et al., 2006; Genes and Kocak, 2005; Sáez et al., 2013). On the other hand, an important deficiency in DSSI analyses, usually performed, is that only the as-recorded components of ground motions are adopted, without considering other angles that could lead to a more severe structural response. These effects can be addressed by analysing the considered problem with a number of linear combinations of the input motions for different incidence angles. Then, the orientation producing the maximum response of the structure can be determined; this procedure was termed here the CRA. It was found that, if directionality effects are overlooked and only the as-recorded components are employed to derive the input motions for the analyses, the building response (in terms of relative roof displacements) can be underestimated as much as 50%.

On the other hand, DSSI analyses are computationally expensive preventing the use of the CRA in most cases. In addition, already established simplified procedures to incorporate directionality effects for structural analyses cannot be employed directly to the input motions for DSSI analyses since site effects tend to modify the response. A simplified procedure has been proposed here to identify, in advance, the angle that produces the maximum response of a structure for a given seismic action and, therefore, to perform only one DSSI analysis. Site effects are incorporated by applying the CRA to free-field site response simulations, since they are quite inexpensive compared to full DSSI analyses. Then, the critical orientation is predicted from the maximum value of a given IM, as a function of the rotation angle, from the motions computed at the surface of the free-field simulations. Different IMs were evaluated, and the PGV resulted in critical angles and relative roof displacements closest to the CRA. Although the exact values were not predicted, the mean relative differences with respect to the CRA, in terms of roof displacements, were only -2.476% (mean value of the considered cases); much smaller than those obtained using the as-recorded directions.

The proposed simplified approach, using the PGV as IM, appears to be an attractive and economical alternative to incorporate directionality effects in DSSI analyses. The high computational cost of DSSI analyses, where the soil is characterised with an elastoplastic constitutive model, prevents the use of a large number of earthquake records. Three acceleration pairs, leading to 630 nonlinear dynamic analyses, have been considered adequate for the purpose of the paper, i.e. to propose a simplified approach to predict the worst angle orientation, thus avoiding such large number of costly dynamic analyses. Nevertheless, the procedure must be further validated under different conditions, such as different characteristics of the soil deposit, additional seismic actions corresponding to different kinds of earthquakes, and, of course, different surface structures. In addition, future analyses should be performed considering 3D models and the non-linearity properties and damage of the structure.

Table 34: Comparison between the relative roof displacements obtained through the CRA and the as-recorded components.

Approach	Roof displacement	Group 1			Group 2			Group 3			Mean relative error (δ in %)*
		Friuli	Campania	Umbria	10 m	20 m	30 m	3-storey	4-storey	5-storey	
CRA	max. (m)	0.202	0.157	0.136	0.141	0.158	0.202	0.123	0.202	0.180	-
As-recorded (AR)	0^o max. (m)	0.197	0.113	0.116	0.132	0.139	0.197	0.115	0.197	0.176	-10.334
	δ with CRA_{max} (%)	-2.475	-28.025	-14.706	-6.383	-12.025	-2.475	-6.504	-2.475	-2.222	
	90^o max. (m)	0.133	0.138	0.132	0.066	0.106	0.133	0.093	0.133	0.148	-25.353
	δ with CRA_{max} (%)	-34.158	-12.102	-2.941	-53.191	-32.911	-34.158	-24.390	-34.158	-17.778	
Mean relative error (δ in %)		-18.317	-20.064	-8.824	-29.787	-22.468	-18.317	-15.447	-18.317	-10.000	

*The Friuli, the 30 m and the 4-storey analyses from group 1, 2 and 3 respectively are the same analysis, therefore only are considered once in the mean error estimation.

Although the effects of directionality should always be considered for earthquake-resistant design and assessment, it is important to mention that using the most unfavourable incidence angle, in each of the selected ground-motion records, could lead to over-conservative results. The specific way in which directionality must be considered for design is not discussed in this work and deserves further research. Nonetheless, the proposed approach, to economically determine the most unfavourable orientation in DSSI analyses, might serve as a tool for such kind of studies.

8 A drift-correlated ground motion intensity measure: application to steel frame buildings

Based on the published article: Pinzón, L. A., Vargas-Alzate, Y. F., Pujades, L. G & Diaz, S. A. (2020). A drift-correlated ground motion intensity measure: application to steel frame buildings. *Soil Dynamics and Earthquake Engineering, 132*, 106096. doi: 10.1016/j.soildyn.2020.106096
Journal URL: www.sciencedirect.com/science/article/abs/pii/S0267726119309029
FUTUR UPC URL: futur.upc.edu/27020273

8.1 Abstract

Estimations of seismic risk in urban areas should include quantification of the expected damage to civil structures subjected to earthquakes. In buildings, this quantification depends on the maximum inter-story drift (MIDR), among other aspects. In this study, the correlation between several intensity measures (IMs) and the maximum inter-story drift of steel structures was investigated. Three steel frame buildings of 3, 7 and 13 stories were used as a testbed. These buildings were modelled as 2D framed structures. For the seismic hazard, forty strong ground motion pairs were selected (80 individual horizontal components) from the Italian database. These records were scaled to a specific peak ground acceleration (PGA) and matched to a design spectrum from Eurocode 8. Nonlinear dynamic analysis was used to estimate the seismic response of the structures. Thus, 720 nonlinear dynamic analyses (NLDA) were performed [3 structures (80 as recorded accelerograms + 80 scaled records + 80 matched records)]. Preliminary results indicate that PGA and MIDR show the worst correlation. A higher correlation was observed for peak ground velocity, root-mean-square velocity and specific energy density intensity-based measures. Finally, a new IM, which is highly correlated with MIDR, is proposed. This IM is called $I_{\Delta-PGV}$ and considers both the PGV and the duration.

8.2 Introduction

Over the last decade, a number of high-magnitude earthquakes have caused hundreds of thousands of fatalities, made millions of people homeless and caused considerable economic losses. Earthquakes such as those in Maule (Chile, 2010), Christchurch (New Zealand, 2011), Tohoku (Japan, 2011), Emilia (Italy, 2012), Umbria (Italy, 2016), Ecuador (Ecuador, 2016) and Mexico City (Mexico, 2017) generated economic losses in the order of $400 billion (National Geophysical Data Center / World Data Service (NGDC/WDS), 2018). Moreover, depending on the vulnerability of the stricken area, a single earthquake can cause hundreds of thousands of fatalities. This was the case in the 2010, M_W=7.0, Haiti earthquake (DesRoches et al., 2011). The examples confirm the need for further research on the negative consequences of these geohazards. Advanced tools to improve the estimation of seismic risk could contribute significantly to mitigating the negative consequences of earthquakes.

In this context, identification of the potential destructiveness of an earthquake is a topic that has captured the attention of seismologists and engineers for almost a century. Accurate characterization of the seismic potential of a region is fundamental for estimating and reducing its seismic risk. Currently, acceleration response spectra functions (Biot, 1933, 1941, 1943) are the preferred method in the design of new structures and assessments of the performance of existing ones. For design purposes, the design response spectrum (DRS) is used, which is related to the location of the structure. The DRS is generally provided by the seismic codes and guidelines of the construction area. For assessment purposes, the uniform hazard spectrum (UHS) is normally used to quantify the seismic hazard of the area. Over the years, a set of damage-related intensity measures (IMs) have also been developed.

To a greater or lesser extent, these IMs are related to the expected seismic damage of a structure. Identifying the IM that is most strongly correlated to the expected damage of a structure is of interest, since it can contribute to improving the estimation of seismic risk.

The degree of correlation between several IMs and the expected damage of a structure were studied. To achieve this, three steel frame buildings with varying numbers of stories were analyzed through nonlinear dynamic analyses (NLDA). Eighty horizontal accelerograms (40 records, two horizontal components) from the Italian Accelerometric Archive (ITACA) (Pacor et al., 2011) were used to characterize the seismic actions. These ground motion records were carefully selected in terms of the duration of the strong phase to identify whether this variable influences the building performance. However, the NLDA was performed using the original, scaled and spectrum-matched records as will be explained later. Thus, 720 NLDA were carried out and the MIDR and the damage index of Park and Ang, PA, (Park and Ang, 1985) were calculated. Then, the correlations between the IMs and the MIDR were estimated and compared. Finally, a new IM, which is highly correlated with the MIDR, was proposed. This new IM is a combination of two well-known seismic parameters: the peak ground velocity (PGV) and the significant duration. The use of more than one seismic parameter to define the damage potential of earthquakes to structures is a significant novelty, allowing alternative methods such as Artificial Neural Networks to be undertaken (de Lautour and Omenzetter, 2009; Morfidis and Kostinakis, 2017). The performance of this IM was also validated through probabilistic NLDA. One of its main advantages is its independence from the properties of the analyzed structure and its high correlation with the MIDR.

8.3 Intensity measures

The efficiency of some IMs as indicators of potential structural damage were evaluated in this study. For this purpose, several IMs were estimated (see Table 35). They were selected because they are the most commonly used in the development of seismic hazard studies through ground motion prediction equations (Douglas, 2017), and in the estimation of expected damage (Kostinakis et al., 2015; Garini and Gazetas, 2013). In the following section, the IMs that were considered are described briefly.

Table 35: List of intensity measures used in this study (see also explanation in the text).

Intensity measure	Acronym	Formulation	Units
Arias intensity	I_A	$\frac{\pi}{2g}\int_{t_i}^{t_f} a(t)^2 dt$	cm/s
Root mean square (RMS) of acceleration	acc_{RMS}	$\sqrt{\frac{1}{\Delta}\int_{t_{5\%}}^{t_{95\%}} a(t)^2 dt}$	g
Root mean square (RMS) of velocity	vel_{RMS}	$\sqrt{\frac{1}{\Delta}\int_{t_{5\%}}^{t_{95\%}} v(t)^2 dt}$	cm/s
Specific energy density	SED	$\int_{t_i}^{t_f} v(t)^2 dt$	cm^2/s
Characteristic intensity	I_C	$(acc_{RMS})^{1.5}\sqrt{t_f}$	-
Cumulative absolute velocity	CAV	$\int_{t_i}^{t_f} \lvert a(t)\rvert \, dt$	cm/s
Peak ground acceleration	PGA	$max\,\lvert a(t)\rvert$	$\mathrm{cm/s}^2$
Peak ground velocity	PGV	$max\,\lvert v(t)\rvert$	cm/s
Spectral acceleration for the fundamental period	SA_{T1}	$max\,\lvert \ddot{u}(T_1,\xi)\rvert$	$\mathrm{cm/s}^2$

8.3.1 Intensity measures based on ground motion time histories

Benioff (1934) defined an earthquake's destructiveness measure in terms of the energy obtained through the relative displacement response spectrum. After this paper, several measures were devised based on the energy content of the signal. For instance, Arias intensity (Arias, 1970) is a measure of the severity of the ground motion and is defined by the following equation:

$$I_A = \frac{\pi}{2g} \int_{t_i}^{t_f} a(t)^2 dt \tag{31}$$

where g is the acceleration due to gravity, t_i is the beginning of the record, t_f is the total duration of the record and $a(t)$ represents the acceleration time history of the earthquake.

Many authors used this measure to define the significant duration (Δ) of a ground motion (Husid, 1969; Bolt, 1973; Housner, 1975; Trifunac and Brady, 1975). Significant duration is based on the energy accumulation and is defined as the interval over which some proportion of the total energy is accumulated (Bommer and Martínez-Pereira, 1999). This interval is considered the "strong phase" of a ground motion. In this study, the thresholds of 5% and 95% of Arias intensity mark the beginning ($t_{5\%}$) and end ($t_{95\%}$) of the phase, as proposed by Trifunac and Brady (1975) (see Figure 74).

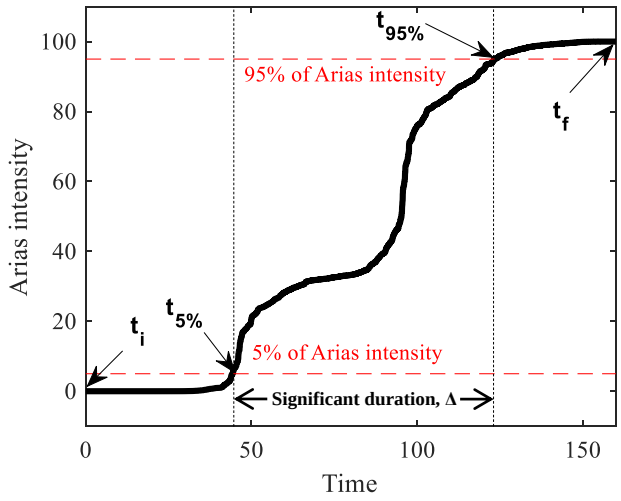

Figure 74: Definition of the significant duration of a single accelerograms using the Husid plot (Husid, 1969) [accumulative energy (%) in terms of Arias intensity vs. time (s)].

Housner (1975) and Dobry et al. (1978) suggested that ground motion can be characterized by the quadratic mean of the acceleration time histories (see Equation 32).

$$acc_{RMS} = \sqrt{\frac{1}{\Delta} \int_{t_{5\%}}^{t_{95\%}} a(t)^2 dt} \tag{32}$$

where Δ is the duration of the strong phase (5–95% of Arias intensity), also known as the significant duration, $t_{5\%}$ is the initial time of the strong phase and $t_{95\%}$ is the final time of the strong phase of an acceleration time history, $a(t)$. Moreover, the root mean square of the velocity time histories, $v(t)$, has been associated with damage in several studies (Kostinakis et al., 2015; Garini and Gazetas, 2013)(see Equation 33).

$$vel_{RMS} = \sqrt{\frac{1}{\Delta} \int_{t_{5\%}}^{t_{95\%}} v(t)^2 dt} \tag{33}$$

Another interesting measure is the Specific Energy Density (SED) (Sarma, 1971; Sarma and Yang, 1987), which is defined as the integral of the square velocity time history $v(t)$ in the interval $t_i - t_f$ (see Equation 34).

$$SED = \int_{t_i}^{t_f} v(t)^2 dt \tag{34}$$

Park et al. (1987) developed a relationship between the destructiveness potential of an earthquake ground motion (Characteristic intensity, I_C) and the structural damage of reinforced concrete buildings, using the damage index proposed by Park and Ang (1985). The I_C was defined by means of the following equation:

$$I_C = (acc_{RMS})^{1.5} \sqrt{t_f} \tag{35}$$

The Cumulative Absolute Velocity (CAV) intensity measure was proposed by Reed and Kassawara (1990) and has also been used to state the destructive potential of earthquakes.

$$CAV = \int_{t_i}^{t_f} |a(t)|\, dt \tag{36}$$

8.3.2 Intensity measures based on peak responses

Another group of IMs based on the peak response of a single-degree-of-freedom (SDOF) system has been considered in assessments of the seismic behaviour of structures. These IMs have been used to build up the design response spectrum in many seismic regulations. Thus, the Peak Ground Acceleration (PGA), the Peak Ground Velocity (PGV) and the elastic spectral acceleration at the fundamental period of the structure, Sa_{T1}, were included in the correlation analysis. These IMs are listed in Table 35.

Note that the IMs described in Table 35 have been correlated with expected seismic structural damage (Kostinakis et al., 2015; Elenas, 2000; Hancock and Bommer, 2006; Muin and Mosalam, 2017). In these studies, the aim was to obtain an IM that properly represents the destructive potential of an earthquake. Such a measure would help in the development of more accurate seismic hazard studies and, therefore, more precise seismic design methods. Thus, the described IMs will be correlated with the MIDR. Note that this engineering demand parameter (EDP) has been widely correlated with damage states in seismic risk assessment methods, such as Hazus (Federal Emergency Management Agency (FEMA), 2002).

8.4 Structural models

Three steel buildings of 3, 7 and 13 stories were analysed in this study (Figure 75). The buildings have special moment frames as a seismic-force-resisting system with "wide flange" sections for beams and columns, according to ASTM A992 (ASTM A992 / A992M - 11, 2015) (Figure 75). These elements are joined through prequalified connections (ANSI/AISC 358-10, 2010) of fully restrained type. The buildings were designed for office use based on the provisions in AISC-341-10 (ANSI/AISC 341-10, 2010). Buckling in columns was controlled in the design. The special moment frames satisfy the AISC criterion strong-column-weak-beam and the structural sections of the columns meet the slenderness criterion presented in AISC-341-10 (ANSI/AISC 341-10, 2010). The weight of the structure, the architectonic finishes and facilities were considered as dead loads. The live loads were selected according to ASCE 7-10 (ASCE, 2010) provisions for office use. These buildings were modelled as frame type members with plastic hinges at their ends using Ruaumoko 2D software (Carr, 2002).

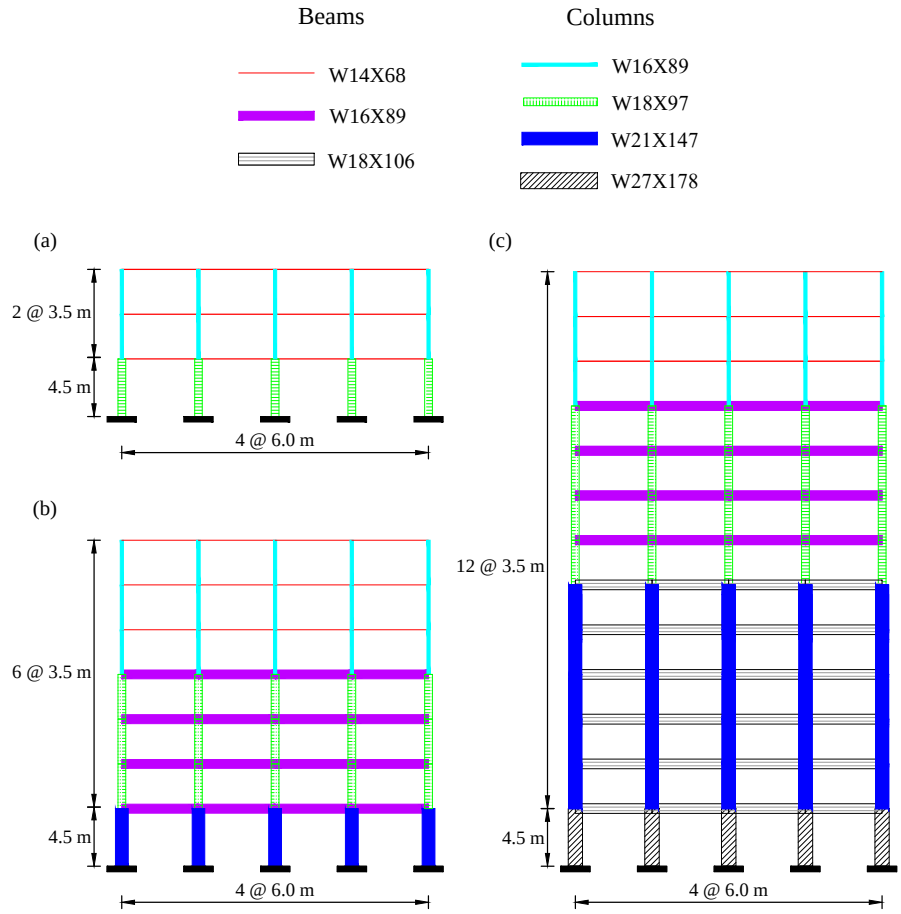

Figure 75: Steel moment frame model dimensions for (a) 3-story, (b) 7-story and (c) 13-story buildings.

The plastic hinges follow a Bilinear Hysteresis rule with hardening and strength degradation based on the ductility factor. The strength and ductility values for the hysteresis rule were calculated according to the modified Ibarra-Medina-Krawinkler (IMK) model (Ibarra et al., 2005; Lignos and Krawinkler, 2011, 2013). The backbone curve of the modified IMK model is defined by three strength parameters (M_y = effective yield moment, M_c = capping moment strength or post-yield strength ratio $M_c/M_y = 1.1$ and $M_r = k * My$, $k = 0.4$, residual moment). These strength parameters are obtained from the steel section's properties: the plastic modulus (depends on the W type sections used), yield strength (345 MPa), and elastic modulus (200,000 MPa). The ductility of the structural sections in the modified IMK model are defined by the four deformation parameters: θ_y = yield rotation, θ_p = pre-capping plastic rotation for monotonic loading –difference between yield rotation and rotation at the maximum moment, θ_{pc} = post-capping plastic rotation difference between rotation at the maximum moment and rotation at complete loss of strength and θ_u = ultimate rotation capacity. Two per cent Rayleigh damping was used for the first and last vibration modes as recommended for steel structures. Input motions were applied directly at the base of the buildings. The base of the resisting frames is fixed with all degrees of freedom restrained.

$P - \Delta$ effect was considered in the analysis. Ruaumoko allows modelling structures where the displacements are sufficient to require a large displacement analyses or where the axial forces in members affect their stiffness. In large displacement analyses the coordinates, as well as the axial forces in the beam or wall members and the changes in geometry in the members, are updated at

every time-step. This procedure is computationally expensive, but is important if the structure is undertaking large displacements. As the response of the buildings analyzed herein can achieve MIDR significantly greater than 1%, this approach has been considered within the simulations to consider the $P-\Delta$ effect. The predominant periods of the buildings are 0.6 (3-story), 1.2 (7-story) and 1.9 (13-story) seconds. Further details about the modelling considerations can be found in (Diaz et al., 2018).

8.5 Ground motion records

To perform the NLDAs, a set of ground motion records were selected as a function of the duration of their strong phase. The ITACA database was used for this purpose. The horizontal components of the records were used in the analysis. Records were considered with a duration of around 4, 5, 7 and 30 seconds (see Table 36). This selection criterion was aimed at evaluating the influence of the duration of the earthquake record on the damage of buildings. The record set included 40 component pairs of horizontal ground motions (80 individual components, see Table 36). Note that the duration values used for selecting the earthquake records were taken directly from the database catalogue. In the database, the effective duration (Bommer and Martínez-Pereira, 1999) is used as reference. Then, we estimated the significant duration for each component. As mentioned above, the analyses were performed using original, scaled and spectrally matched ground motions. The significant duration was recalculated for the spectrally matched records. In order to obtain the scaled records, the selected ones were normalized by the peak ground acceleration (PGA) and multiplied by 700 cm/s^2. The 700 cm/s^2 value is used as a reference, since buildings begin to be damaged around this PGA. The spectrally matched records were adjusted to an elastic design spectrum defined in Eurocode 8 (CEN, 2004). Namely, the design spectrum for rock, a base acceleration of 700 cm/s^2, a seismically active region type I (earthquake magnitudes over 5.5) and a 5% damping value was used as a target. The spectral matching method used in this paper was developed by Pujades (personal communication, 2015) and has been used in previous studies (Pinzón et al., 2019a; Diaz et al., 2017). A comparison showing the effectiveness of the matching procedure can be seen in Figure 76.

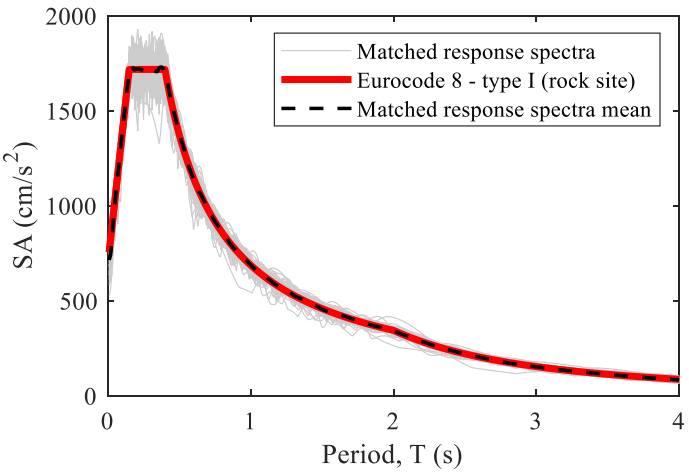

Figure 76: Five per cent damped response spectra, corresponding to the 80 selected accelerograms, matched to the design spectrum of Eurocode 8 for earthquakes with M > 5.5 (type I) located in rock.

Table 36: Ground motions selection from the ITACA database.

Event id	Date and time	Station	M_W	Site EC8	Epi. (km)	PGA (cm/s^2) E-W	PGA (cm/s^2) N-S	Eff. dur. (s)	Sig. dur., Δ (s) E-W	Sig. dur., Δ (s) N-S
EMSC-20161027_0000072	25/08/16 3:17 AM	NRCA	4.3	B	4.6	100.9	122.0	3.8	3.8	3.1
IT-2009-0095	07/04/09 9:26 AM	AQV	5.1	B	5.8	184.5	96.2	3.8	2.6	3.7
IT-1998-0054	03/04/98 7:26 AM	NOCE	5.1	B	6.4	276.4	566.8	3.9	3.9	2.1
IT-2012-0033	31/05/12 2:58 PM	T0826	3.7	C	5.8	60.7	107.1	3.9	2.0	1.3
IT-1976-0024	11/09/76 4:31 PM	GMN	5.2	B	6.1	152.0	186.8	3.9	3.3	3.9
IT-2009-0140	09/04/09 7:38 PM	RM11	5.2	B	7.1	165.8	166.5	4.0	3.0	2.0
IT-2009-0105	07/04/09 9:34 PM	RM07	4.5	B	4.5	171.6	106.8	4.0	2.6	4.0
IT-1977-0008	16/09/77 11:48 PM	SMU	5.3	B	7.1	79.5	179.4	4.0	3.1	1.7
IT-2005-0145	08/11/05 9:10 PM	CSN	3.6*	B	1.9	88.3	111.1	4.1	2.1	3.0
EMSC-20160824_0000050	24/08/16 4:06 AM	NRCA	4.4	B	7.0	123.8	153.1	4.1	4.1	3.6
IT-1997-0163	19/10/97 4:00 PM	CESV	4.2	C	4.5	101.2	141.9	4.9	3.4	3.2
IT-1976-0024	11/09/76 4:31 PM	FRC	5.2	B	16.6	109.7	95.0	4.9	4.8	4.6
EMSC-20170118_0000119	18/01/17 1:33 PM	MSC	5.0	B	8.0	123.4	153.9	5.0	3.8	3.9
EMSC-20161026_0000133	26/10/16 9:42 PM	CLO	4.5	A	7.9	96.1	84.5	5.0	3.1	5.0
IT-2009-0102	07/04/09 5:47 PM	MI05	5.5	A	3.6	651.5	304.1	5.0	3.6	5.0
IT-2010-0032	16/08/10 12:54 PM	ILLI	4.7	A	11.4	323.0	382.2	5.1	5.1	4.7
EMSC-20161026_0000095	26/10/16 7:18 PM	CNE	5.9	C	2.5	527.0	373.1	5.2	4.5	5.2
EMSC-20161026_0000095	26/10/16 7:18 PM	MCV	5.9	B	14	377.2	538.8	5.4	5.2	4.3
IT-1997-0004	26/09/97 12:33 AM	CLF	5.7	D	2.8	251.7	271.4	5.5	5.2	5.5
IT-1997-0004	26/09/97 12:33 AM	NCR	5.7	E	13.2	250.9	387.4	5.5	4.1	5.5
EMSC-20161026_0000077	26/10/16 5:10 PM	CNE	5.4	C	2.6	545.6	219.5	6.5	3.9	6.5
IT-2012-0011	29/05/12 7:00 AM	T0813	6.0	C	11.3	361.2	331.9	6.6	5.9	6.6
EMSC-20161030_0000029	30/10/16 6:40 AM	T1214	6.5	B	11.4	593.2	413.0	6.8	6.8	6.4
IT-2012-0011	29/05/12 7:00 AM	SAN0	6.0	C	6.1	170.9	216.7	6.8	6.7	6.8
EMSC-20161026_0000077	26/10/16 5:10 PM	FOC	5.4	C	24.9	331.2	196.8	6.9	3.9	5.6
IT-2012-0011	29/05/12 7:00 AM	MIRE	6.0	C	4.1	173.3	265.5	7.1	7.1	6.9
IT-2012-0011	29/05/12 7:00 AM	MIRH	6.0	C	4.5	146.8	265.0	7.1	7.1	6.7
IT-2012-0011	29/05/12 7:00 AM	MIR01	6.0	C	0.5	411.4	373.0	7.2	6.6	7.2
IT-2012-0011	29/05/12 7:00 AM	T0802	6.0	C	9.9	258.8	290.7	7.3	7.3	7.2
IT-2012-0011	29/05/12 7:00 AM	T0800	6.0	C	14.4	330.6	248.9	7.3	6.2	7.3
IT-2012-0010	29/05/12 10:55 AM	MIR07	5.5	C	26.8	31.0	32.1	29.7	21.3	23.0
EMSC-20170118_0000037	18/01/17 10:25 AM	CNO	5.4	B	74.4	9.4	10.9	29.8	24.5	22.8
EMSC-20161026_0000077	26/10/16 5:10 PM	MNTP	5.4	B	39.9	21.5	21.1	29.9	20.5	20.8
IT-2012-0008	20/05/12 2:03 AM	MLD	6.1	C	107.6	22.2	19.9	29.9	20.5	22.6
EMSC-20160824_0000006	24/08/16 1:36 AM	SRL	6.0	C	96.3	18.1	25.7	29.9	21.1	15.3
EMSC-20161026_0000095	26/10/16 7:18 PM	ATFO	5.9	B	68.1	10.2	9.1	29.9	29.9	26.4
EMSC-20160824_0000006	24/08/16 1:36 AM	BVG	6.0	C	57.2	39.1	49.2	30.2	29.8	28.7
IT-2006-0272	26/10/06 2:28 PM	VBV	5.8	B	53.3	12.4	8.2	30.2	30.2	29.5
EMSC-20161026_0000095	26/10/16 7:18 PM	IT.SNG	5.9	C	86.7	45.5	52.7	30.6	22.7	25.6
IT-2012-0011	29/05/12 7:00 AM	CAS0	6.0	C	28.1	66.2	42.0	30.7	18.2	19.7

* Value estimated with local magnitude (M_L).

8.6 Correlation between the IMs and the MIDR

The IMs were estimated massively with a program developed in MATLAB (The MathWorks, 2017) and they were checked with the commercial software SeismoSignal (Seismosoft, 2018), with excellent agreement. The correlation values between the IMs listed in Table 35 and the MIDR obtained after performing the 720 NLDAs [3 structures (80 as-recorded accelerograms + 80 scaled records + 80 matched records)] are presented in Figure 77. The square of the correlation coefficient (R^2), which is also called the coefficient of determination, was used as an indicator. The results as a function of the PGA are shown in Figure 77a. In this figure, the results corresponding to the scaled records can be clearly identified at a PGA value of 700 cm/s^2. It is interesting that earthquakes with similar PGA values may produce very different MIDR. SA_{T1}, acc_{RMS}, I_A, I_C and CAV present an R^2 value of around 0.80. For the IM SA_{T1}, note that a better correlation would have been obtained if the regression analyses were carried out independently for each building. Although 0.80 is a good enough correlation, there are other IMs with higher correlation values. Actually, the IMs with better correlation values are the PGV, vel_{RMS} and SED. Among these highly correlated IMs, the PGV is the easiest to obtain. Thus, the PGV seems to be a good measure to predict expected damage since it is directly obtained from the ground motion and is independent of the period of the buildings.

In Table 37, a summary of the R^2 values obtained after performing correlations with different groups of ground motion records is shown. Values obtained with the original records reflect similar results to the correlation obtained with all the records. As expected, when the records are scaled to the same PGA, the correlation with this IM is lost. The values obtained with the matched ground motions has shown that the correlation is null between IMs and the MIDR, since IMs are conditioned to a target spectrum.

Finally, the values obtained with the group of original plus scaled records reveal that the correlation is maintained when the matched records are added (although these have no correlation with the MIDR). This is because the matched records generate similar MIDR values and therefore similar values on IMs, which avoids a decrease in the correlation with all the records. Table 38 shows the type of equation used and the coefficient that fulfils the minimization condition from the 720 NLDA. In the next section, a new IM which is highly correlated with the MIDR and is based on the PGV and the significant duration is presented.

Table 37: R^2 value obtained from the correlation of each IM with the MIDR.

Records	PGA	PGV	SA_{T1}	acc_{RMS}	vel_{RMS}	I_A	I_C	SED	CAV
Original	0.469	0.895	0.807	0.614	0.924	0.759	0.722	0.929	0.825
Scaled	0.008	0.865	0.749	0.361	0.870	0.692	0.686	0.887	0.591
Matched	0.016	0.011	0.285	0.003	0.000	0.031	0.030	0.022	0.024
Original + Scaled	0.546	0.916	0.822	0.682	0.938	0.796	0.771	0.939	0.816
All	0.630	0.928	0.846	0.739	0.941	0.834	0.818	0.950	0.828

8.7 New IM

In this section a new IM is proposed based on the results after performing the correlations with the MIDR. This IM is based on the PGV but also includes the significant duration (Δ, between 5–95% of the Arias intensity) as a variable (see Equation 37) and is called $I_{\Delta-PGV}$. This IM is independent of the period of the oscillator. This new IM was proposed because there is certain level of correlation between the MIDR and the significant duration of the scaled records (see Figure 78). Thus, based on

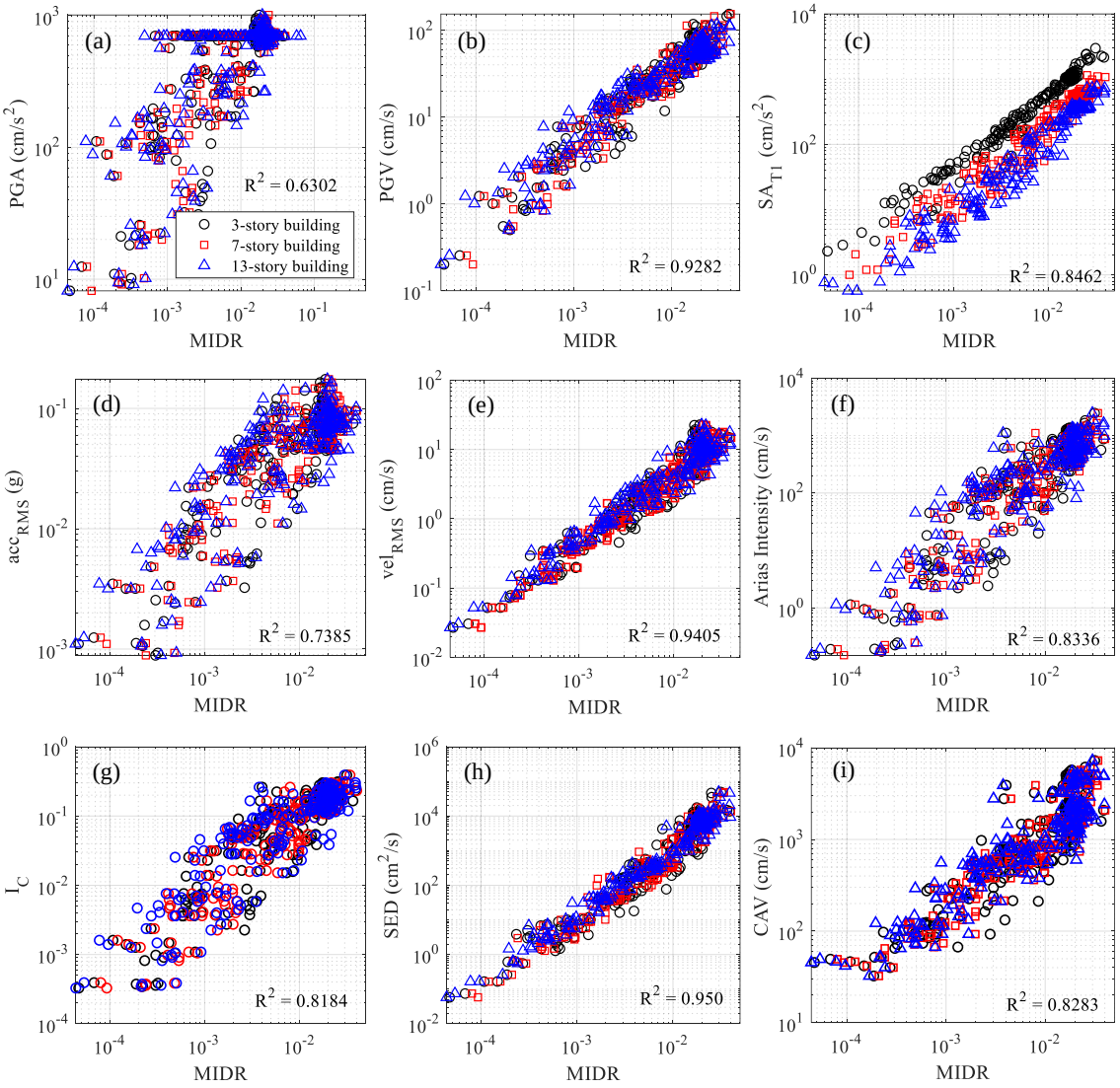

Figure 77: Correlation between the maximum drift and several intensity measures: (a) PGA, (b) PGV, (c) SA_{T1}, (d) acc_{RMS}, (e) vel_{RMS}, (f) Arias intensity, (g) Characteristic intensity, (h) Specific Energy Density and (i) Cumulative Absolute Velocity.

Table 38: Equation and coefficients used in the minimization (720 NLDA).

Equation	$IM = a \cdot MIDR^b$								
IM	PGA	PGV	SA_{T1}	acc_{RMS}	vel_{RMS}	I_A	I_C	SED	CAV
a	7309.9	1990.5	53622.0	1.2	492.4	165823.0	11.3	2.00E+07	48208.0
b	0.581	0.879	1.165	0.684	1.015	1.414	1.049	2.075	0.799

this correlation and considering the high correlation between the PGV and the MIDR, this new IM is defined according to the following equation:

$$I_{\Delta-PGV} = PGV^{\alpha} \cdot \Delta^{\beta} \tag{37}$$

where α and β are coefficients obtained by minimizing the mean square error between the MIDR and the values provided by this equation. PGV is in m/s and Δ in s. After the minimization procedure, $\alpha = 1.5$ and $\beta = 0.5$. Notably, in this IM the significant duration is a relevant variable.

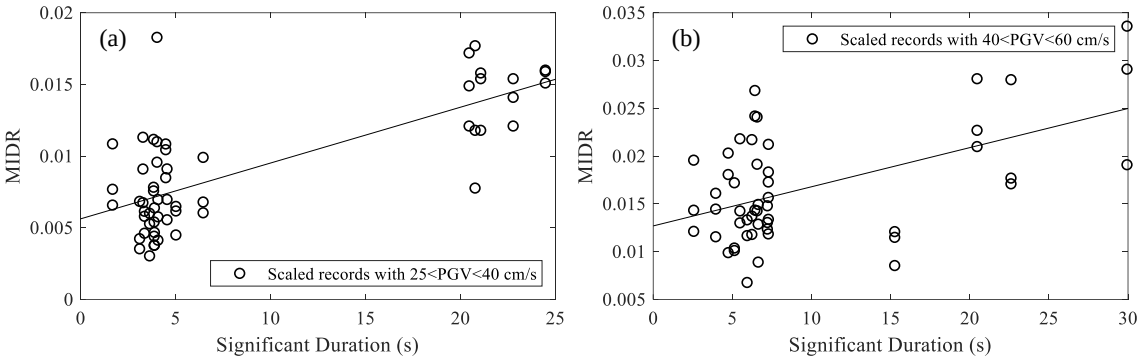

Figure 78: Influence of duration on the maximum drift for scaled accelerograms and ranges of PGV: (a) 25<PGV<40 cm/s and (b) 40<PGV<60 cm/s.

The results obtained after correlating the $I_{\Delta-PGV}$ with the MIDR are shown in Figure 79. From these results it can be concluded that the proposed IM is highly correlated with the MIDR. Actually, the highest coefficients of determination were obtained after the regression analysis, compared with all the IMs studied (see Tables 37 and 39). In Figure 79b, damaged buildings are highlighted in red whilst those that do not suffer damage are in black. This identification is based on the damage index (DI) of Park and Ang. Therefore, if DI $>$ 0.1 then the point will be red otherwise it will be black. Most of the buildings suffered damage (DI $>$ 0.1) when the inter-story drift reached the threshold of 0.015. Regarding $I_{\Delta-PGV}$ values, damage appears at a value close to 1 whilst the maximum value is around 6.

Finally, Figure 80 shows the distribution of the R^2 values according to the IM for each building type. The R^2 values for the proposed IM are very similar regardless of the building analyzed and the types of simulations performed. The same is true of SED, PGV and vel_{RMS}. SA_{T1} has very good correlation values if each independent building is analyzed. This makes sense due to the period dependence of this IM.

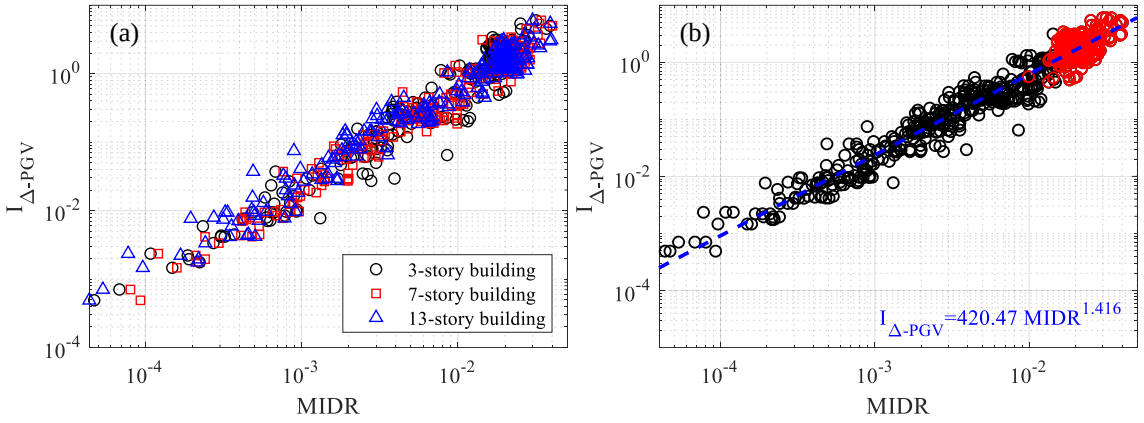

Figure 79: (a) Comparison between the maximum drift and the proposed intensity measure $I_{\Delta-PGV}$. (b) In red, damaged buildings (with DI $>$ 0.1) and in black, buildings that did not suffer damage.

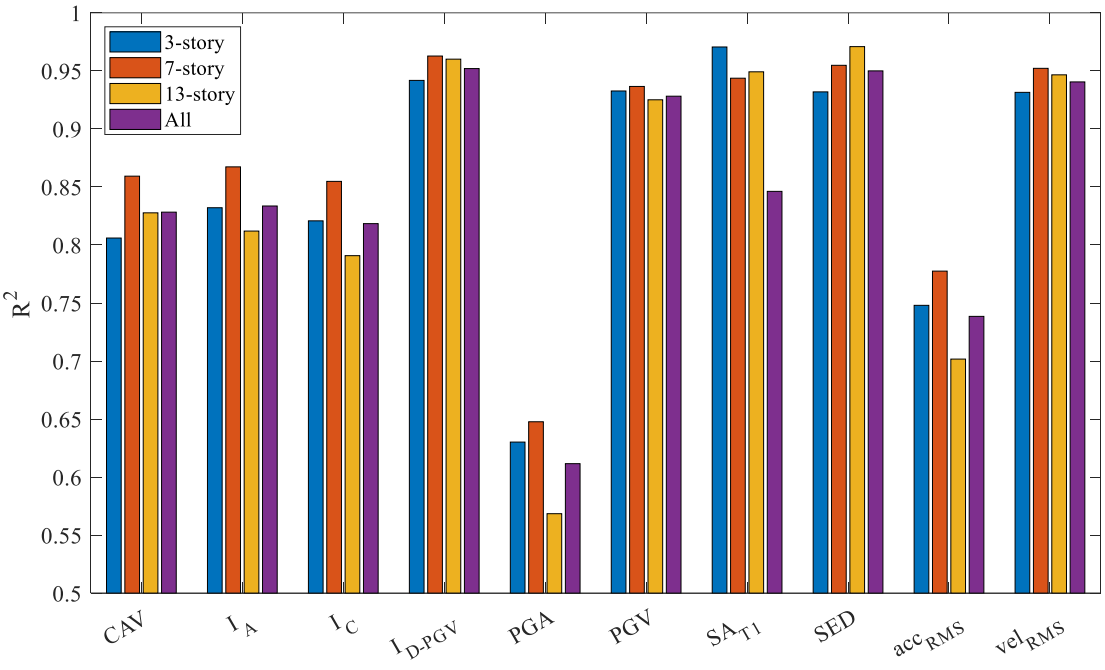

Figure 80: Coefficient of determination (R^2) for the comparison of different IMs with the MIDR drift corresponding to the results obtained by performing the NLDAs for the 3-story building, 7-story building, 13-story building and all the buildings.

Table 39: R^2 values obtained from the correlation of $I_{\Delta-PGV}$ IM and MIDR.

Records	R^2
Original	0.9341
Scaled	0.8793
Matched	0.0000002
Original + Scaled	0.9437
All	0.952

8.8 Correlation between IMs

The correlation between the IMs was determined. For this purpose, a linear correlation using all the available records was performed. The results are shown in Table 40 in a correlation matrix. Strong correlations were found for the pairs $CAV - I_A$ (0.978), $CAV - I_C$ (0.89), $I_A - I_C$ (0.934), $I_A - SED$ (0.856), $I_C - acc_{RMS}$ (0.854), $I_{\Delta-PGV} - PGV$ (0.909), $I_{\Delta-PGV} - SED$ (0.878) and $acc_{RMS} - vel_{RMS}$ (0.856). The high correlation between the $I_{\Delta-PGV}$ and SED is interesting, since these two IMs have the highest correlations with the MIDR and both are independent from the period of the buildings.

Table 40: Linear correlation of the IMs used in this study for all the available records (original + scaled + matched).

IMs	CAV	I_A	I_C	$I_{\Delta-PGV}$	PGA	PGV	SA_{T1}	SED	acc_{RMS}	vel_{RMS}
CAV	1.000									
I_A	0.978	1.000								
I_C	0.890	0.934	1.000							
$I_{\Delta-PGV}$	0.778	0.820	0.801	1.000						
PGA	0.514	0.554	0.724	0.558	1.000					
PGV	0.594	0.662	0.752	0.909	0.692	1.000				
SA_{T1}	0.572	0.609	0.635	0.717	0.487	0.723	1.000			
SED	0.811	0.856	0.742	0.878	0.399	0.683	0.629	1.000		
acc_{RMS}	0.553	0.626	0.854	0.582	0.780	0.683	0.509	0.444	1.000	
vel_{RMS}	0.619	0.678	0.831	0.802	0.652	0.844	0.671	0.667	0.856	1.000

In addition, a correlation analysis was performed for the groups of records (original, scaled and matched). The results are shown in Figure 81. Here, the square of the linear correlation (R^2) was used to avoid negative (-) values of correlations. The results obtained with the original records were greater than the overall results. The scaled records correlations decreased and a null correlation with the PGA was found, as expected. In the case of the matched records, most correlations decreased significantly, except for $CAV - I_A$, $CAV - SED$, $I_A - I_C$, $I_A - SED$ and $acc_{RMS} - vel_{RMS}$, for which high correlations were obtained. In Table 41, strong correlations with values > 0.80 are indicated.

8.9 Validation through probabilistic NLDA

In the first approach, only uncertainties related to seismic action were considered. However, modelling the random variation in building-to-building structural characteristics within a structural typology is standard practice. In this section, we introduce these sources of uncertainties to validate more fully the new intensity measure ($I_{\Delta-PGV}$). Vargas-Alzate (2020) developed an algorithm that can be used to generate probabilistic multi-degree-of-freedom systems. Although they developed the algorithm for reinforced concrete models, it can easily be adapted to generate structural steel models that are compatible with those analyzed above. The algorithm is a product of the KaIROS project (Vargas et al., 2019), which is focused on maintaining and increasing the resilience and sustainability of communities against earthquakes.

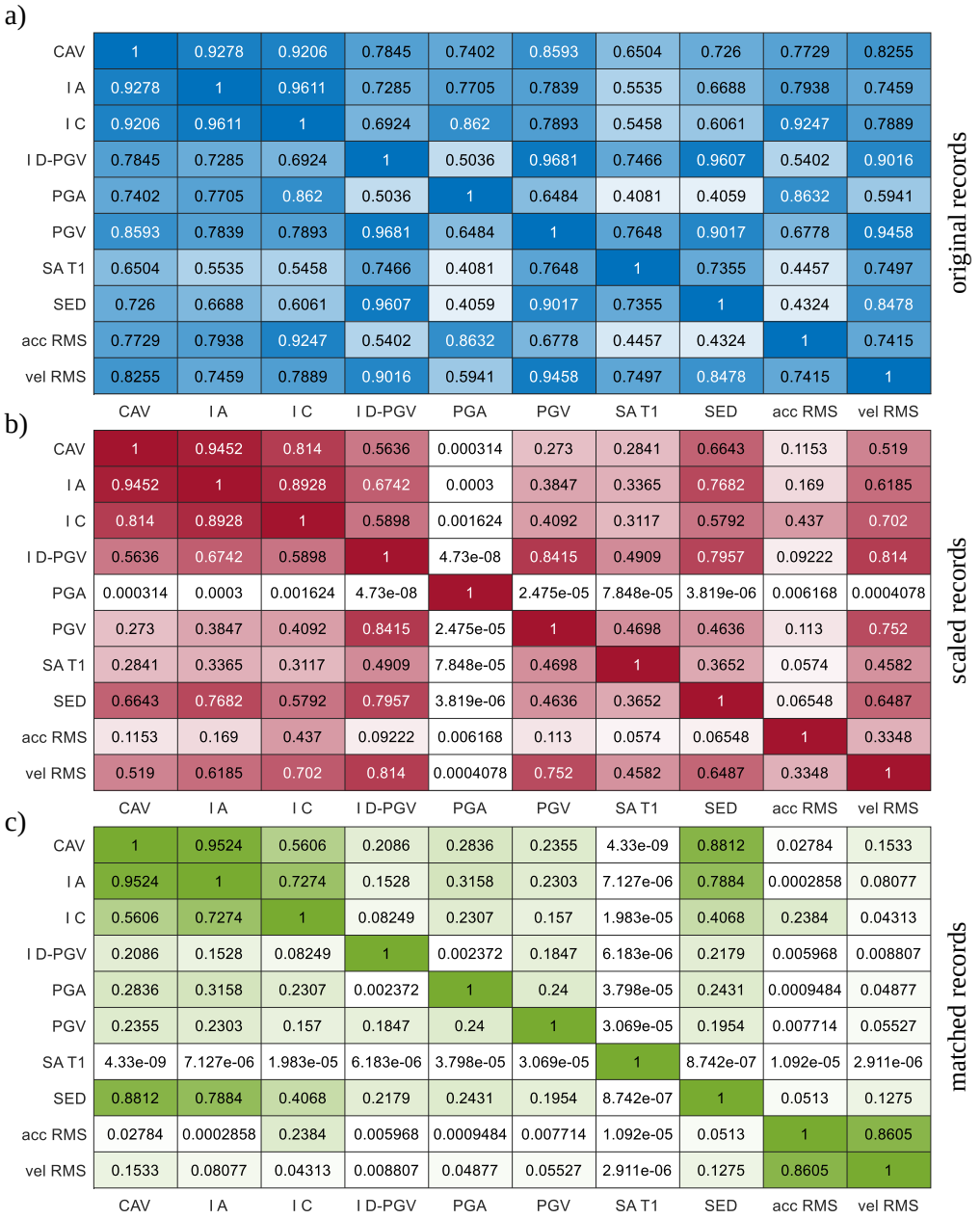

Figure 81: Matrices of R^2 from the correlation between the IMs used in this study for the (a) original records, (b) scaled records and (c) the matched records.

Table 41: IMs with correlations values > 0.80.

Correlation	Original records	Scaled records	Match records	All
$CAV - I_A$	o	o	o	o
$CAV - I_C$	o	o	-	o
$CAV - I_{\Delta-PGV}$	o	-	-	-
$CAV - PGA$	o	-	-	-
$CAV - PGV$	o	-	-	-
$CAV - SA_{T1}$	o	-	-	-
$CAV - SED$	o	o	o	o
$CAV - acc_{RMS}$	o	-	-	-
$CAV - vel_{RMS}$	o	-	-	-
$I_A - I_C$	o	o	o	o
$I_A - I_{\Delta-PGV}$	o	-	-	o
$I_A - PGA$	o	-	-	-
$I_A - PGV$	o	-	-	-
$I_A - SA_{T1}$	-	-	-	-
$I_A - SED$	o	o	o	o
$I_A - acc_{RMS}$	o	-	-	-
$I_A - vel_{RMS}$	o	-	-	-
$I_C - I_{\Delta-PGV}$	o	-	-	o
$I_C - PGA$	o	-	-	-
$I_C - PGV$	o	-	-	-
$I_C - SA_{T1}$	-	-	-	-
$I_C - SED$	o	-	-	-
$I_C - acc_{RMS}$	o	-	-	o
$I_C - vel_{RMS}$	o	o	-	o
$I_{\Delta-PGV} - PGA$	-	-	-	-
$I_{\Delta-PGV} - PGV$	o	o	-	o
$I_{\Delta-PGV} - SA_{T1}$	o	-	-	-
$I_{\Delta-PGV} - SED$	o	o	-	o
$I_{\Delta-PGV} - acc_{RMS}$	-	-	-	-
$I_{\Delta-PGV} - vel_{RMS}$	o	o	-	o
$PGA - PGV$	o	-	-	-
$PGA - SA_{T1}$	-	-	-	-
$PGA - SED$	-	-	-	-
$PGA - acc_{RMS}$	o	-	-	-
$PGA - vel_{RMS}$	o	-	-	-
$PGV - SA_{T1}$	o	-	-	-
$PGV - SED$	o	-	-	-
$PGV - acc_{RMS}$	o	-	-	-
$PGV - vel_{RMS}$	o	o	-	o
$SA_{T1} - SED$	o	-	-	-
$SA_{T1} - acc_{RMS}$	-	-	-	-
$SA_{T1} - vel_{RMS}$	o	-	-	-
$SED - acc_{RMS}$	-	-	-	-
$SED - vel_{RMS}$	o	o	-	-
$acc_{RMS} - vel_{RMS}$	o	-	o	o

Using this algorithm, we generated 500 structural steel models whose number of stories, Nst, number of spans, Nsp, story height, Hst, and span length, Sl, were considered as input random variables. Nst followed a uniform, discrete distribution in the interval (3, 13); Nv also followed a uniform, discrete distribution in the interval (3, 6). Hst was distributed uniformly in the interval (3.3, 3.7) m. Sl was distributed uniformly in the interval (5, 7) m. In order to assign the cross-sectional properties of the structural elements of the first floor, the values presented in Table 42 were adopted. For the upper stories, the size of the columns and beams decreases systematically each 3 stories, to values associated with a building with a lower number of stories. Table 43 presents the main properties of a group of variables that were also considered as random within the analysis. Figure 82 shows twenty structural models generated by considering the geometrical properties mentioned above.

Table 42: Beam and column sections of the first floor per number of stories. American wide flanges steel sections - ASTM A992.

N. of stories	Beam sections	Area (m^2)	Inertia (m^4)	Column sections	Area (m^2)	Inertia (m^4)
3	W14x68	1.30E-02	3.03E-04	W18x97	1.84E-02	7.26E-04
4	W14x74	1.41E-02	3.34E-04	W18x106	2.01E-02	7.95E-04
5	W18x86	1.64E-02	6.42E-04	W18x119	2.26E-02	9.12E-04
6	W18x86	1.64E-02	6.42E-04	W21x132	2.50E-02	1.34E-03
7	W16x89	1.71E-02	5.50E-04	W21x147	2.79E-02	1.51E-03
8	W16x89	1.71E-02	5.50E-04	W24x146	2.77E-02	1.91E-03
9	W18x97	1.84E-02	7.26E-04	W24x146	2.77E-02	1.91E-03
10	W18x97	1.84E-02	7.26E-04	W27x161	3.06E-02	2.61E-03
11	W18x97	1.84E-02	7.26E-04	W27x161	3.06E-02	2.61E-03
12	W18x106	2.01E-02	7.95E-04	W30x173	3.28E-02	3.41E-03
13	W18x106	2.01E-02	7.95E-04	W30x173	3.28E-02	3.41E-03

Table 43: Properties of the variables considered in the probabilistic NLDA.

Variable	μ (kPa)	σ (kPa)
LL	2.0	0.2
SL	3.50	0.175
fy	4.2E+06	2.1E+05
Es	2 E+08	2 E+07

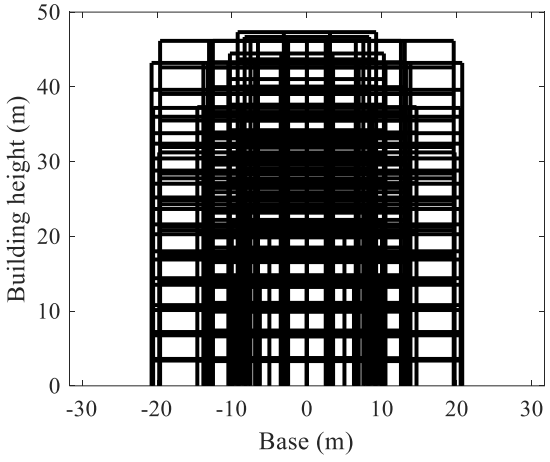

Figure 82: Twenty 2-D steel-frame building models.

One of the main sources of uncertainty in estimations of the seismic risk of structures is the random variability of the ground motion. There are several methodologies to properly select ground motion records that are consistent with the site-dependent spectral shape. However, the main objective of this paper was not to assess the seismic risk of an area, but to develop a simplified procedure for estimating EDPs, like those obtained with NLDAs.

With this objective in mind, the most important requirement was to have earthquakes that demand the structural models at different intensity levels. To achieve this, based on the fundamental period range of the generated models, groups of earthquakes were selected whose mean spectral acceleration, in the interval (0.9–1.3) s, was between a band limited by two intensity levels. The intensity levels defining the upper and lower limits of each band range from 0 to 1.5 g at intervals of 0.15 g. The objective was to obtain 500 records (as many as generated structural models) whereby 50 earthquake records per interval should be found. The database of Ambraseys et al. (2000) was used for the earthquake selection. Figure 83 shows the response spectra of the 500 earthquake records selected according to the described procedure.

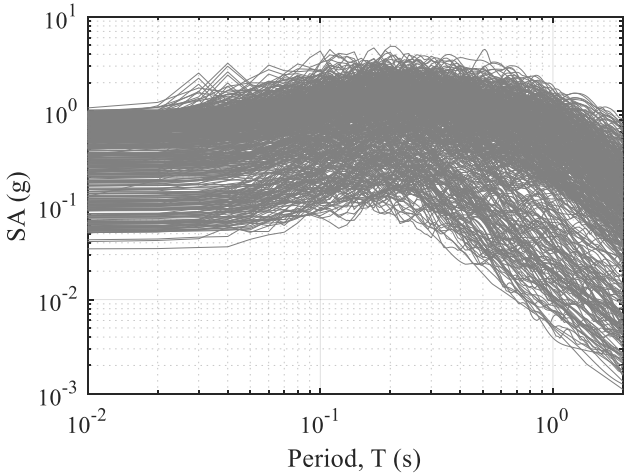

Figure 83: Response spectra of the selected ground motion records for the probabilistic analysis.

Due to the high number of earthquakes requested to fulfil the interval condition, several will be scaled versions of those that naturally meet this condition. Thus, if an interval does not contain 50 earthquake records because there are not enough records in the database, the number of missing records will be selected from the previous interval. This criterion avoids excessive scaling of the earthquake records. After performing the 500 NLDA, the MIDR was correlated with the studied IMs. In Figure 84 the proposed IM ($I_{\Delta-PGV}$) is plotted against the MIDR. As this figure shows, $I_{\Delta-PGV}$ maintained a high correlation with the MIDR despite variations in the geometry and mechanical properties of buildings. Table 44 shows a comparison of the new coefficients of determination, from the probabilistic analysis obtained through the first analysis. The new values were consistent with those obtained in the first analysis. Note that the PGA correlation increased considerably in the probabilistic calculation. This is because the bias introduced when scaling the earthquakes to a fixed PGA in the first approach has been eliminated. However, in both cases, the PGA exhibited one of the lowest R^2 values. The intensity measures that generated the highest correlation were still the PGV, vel_{RMS}, SED and $I_{\Delta-PGV}$. Notably, the proposed IM maintained the highest correlation with respect to other intensity measures, in spite of the sources of uncertainties considered. This demonstrates the effectiveness of this IM as an estimator of the potential damage of an earthquake.

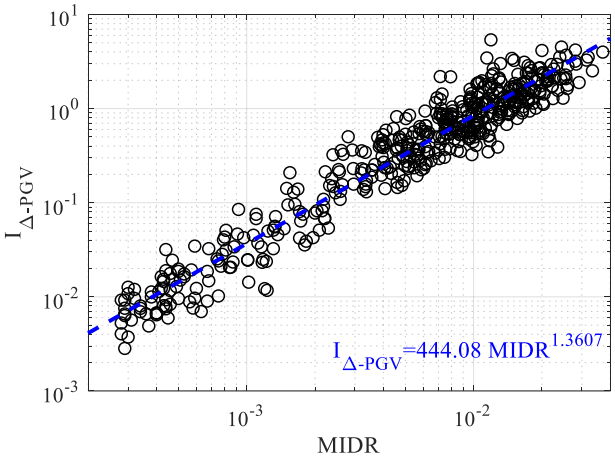

Figure 84: Results after performing the 500 NLDA. Relation between the MIDR and the proposed intensity measure $I_{\Delta-PGV}$.

Table 44: Comparison of R^2 values from the correlation of the studied IMs and MIDR obtained through the first approach and probabilistic NLDA.

IMs	R^2 – First approach	R^2 - Probabilistic NLDA
PGA	0.630	0.783
PGV	0.928	0.924
SA_{T1}	0.856	0.873
acc_{RMS}	0.739	0.768
vel_{RMS}	0.940	0.919
I_A	0.834	0.862
I_C	0.818	0.802
SED	0.950	0.928
CAV	0.828	0.853
$I_{\Delta-PGV}$	0.952	0.932

8.10 Conclusions

In this study, the destructiveness potential of a group of well-known IMs was analysed. To achieve this, three structural models and a record set including 40 component pairs of horizontal ground motions (80 individual components) were performed. NLDA were performed using the structural models and by scaling and matching the accelerograms of the record set based on different criteria. After performing the NLDA, the MIDRs were calculated for each analysis. The MIDR has been widely used as a good indicator to estimate structural damage due to earthquakes (Ghobarah et al., 1999; Raghunandan et al., 2015). This condition is very important because some of the IMs analysed in this article are good predictors of the MIDR. Therefore, the usefulness of the new IM proposed here becomes clear. As the MIDR is highly correlated with the damage, measures that have a high correlation with the MIDR will also be highly correlated with the damage. Thus, the levels of correlation between the MIDR and the IMs were calculated. Based on these results and considering the correlation between the PGV and the significant duration, a new intensity measure that is highly correlated with the MIDR, called $I_{\Delta-PGV}$, is proposed. $I_{\Delta-PGV}$ works well for the three buildings studied.

The preliminary results indicate that the inter-story height is an important variable to consider in the analysis. In the first part of this study, the inter-story heights were the same for all studied buildings. For this reason, the building-to-building structural characteristic variations were considered through probabilistic NLDA and therefore the use of the proposed IM, $I_{\Delta-PGV}$, was validated. A total of 500 NLDA were performed, varying the geometry and mechanical properties of the building models. The results validate those obtained using the first approach and therefore confirm the effectiveness of the proposed IM.

Only two-dimension symmetrical buildings were analysed in this study. Further analyses should be performed with other structural typologies, three-dimensional and non-symmetrical building models, to validate the general performance. The coefficients α and β, presented in Equation 37, should be recalibrated when other building typologies are analysed. If this measure could be validated for different structural typologies, it would be effective to perform seismic hazard and risk analyses. In addition, the earthquake-resistant design approach used in this study protects the structures against failures due to second order effects. Thus, future research studies should be carried out to analyze the evolution of and coefficients by considering different types of design conditions.

Finally, one of the main advantages of $I_{\Delta-PGV}$ is that it is independent of the building period. In future research, the potential of the proposed IM should be compared with other IMs that consider the structural behaviour through the period elongation of buildings (Theophilou et al., 2017; Zhou and Li, 2015; Kohrangi et al., 2017; Bojórquez and Iervolino, 2011; Bojórquez et al., 2017).

9 Discussion and conclusions

Although, this PhD thesis has been structured in three main parts, or blocks, all of them concern to important issues related to seismic risk, which is the glue, joining them, in an integrated environment, to provide new insights, methods and tools for seismic risk assessments, guided to earthquake *protection* and *prevention*. The words "*prevention*" and "*protection*" have been taken from the nice book by Coburn and Spence (2002).

The main issues tackled are related to: I) directionality effects in expected seismic actions and in the expected damage in buildings, II) microzonation and soil-building resonance effects, seismic site classification of accelerometric stations and directionality effects in the dynamic soil-structure interaction. In this second part a new intensity measure which is well correlated with drift, has been proposed, too. Four case studies related respectively to soil-structure interaction, to directionality effects and to site classification of accelerometric stations are included in the part III of this dissertation. One of the reasons for this structure of the document is the fact that each chapter and appendix is supported by a publication, mainly journal paper, but also proceedings of relevant meetings and internal reports. Therefore, the document has been prepared in the format foreseen for article-based-PhD-thesis at the Polytechnic University of Catalonia.

In this last chapter, after a short review of, and a discussion on the main results obtained, the main conclusions, coming from the analyses done, are highlighted. Also, quite a few of remaining open questions are pointed out and some suggestions for future research are given.

9.1 Main results and discussion

Significant and valuable results concerning directionality effects in expected seismic actions (Chapters 2 and 3, Block I.1, and Appendix C, Block III), are the following:

- Directionality effects in Italy and in Costa Rica have been investigated using large and wide strong ground motion databases. New sensor orientation-independent IMs, which are based on the maximum values of the time history obtained by a previous combination the two horizontal components, rather than on the combination of the two maximum values of each component, have been proposed. These new IMs have been called LRotDpp for the Larger measure, and mpGM, mpGMRotDpp, and mpGMRotDpp for the IMs involving geometric mean values.

- Geometric mean of the peak values (GM) is conservative in comparison to the mpGM. Also, it has been found that vector composition of the time histories, mpVC, is identical to RotD100 and LRotD100. In fact, mpVC, RotD100, and LRotD100 can be considered as the maximum response, corresponding to the most unfavourable case. These IMs would be useful for the design or risk assessments of structures of special importance such as historical-cultural heritage buildings or other high-risk constructions.

- From statistical analyses of great databases of strong motion recordings, as the ones of Italy and Costa Rica, it has been shown that, in average, the impact of the directionality effects on existing GMPE developed without considering directionality effects, although significant, is not very high. More specifically, the ratios GMRotD50/GM GMRotI50/GM and RotD50/GM, take values between 1.01 and 1.02 in the range of periods 0.01-2 s but, the ratio RotD50/GM takes values around 1.015 in the range of periods 0.1-1.0 s and values between 1.02 and 1.04 in the range of periods between 0.1 and 2 s. Anyhow, ratios between other intensity measures as, for instance, Larger/GM and LRotD50/GM take values between 1.15 and 1.20, but LRotD100/GM takes values in the range

between 1.23 and 1.30. For details on other ratios, please see Chapters 2 and 3, where the specific studies for Italy and Costa Rica are detailed.

- Thus, the sensor orientation-independent IMs, GMRotD50, GMRotI50, and RotD50 are generally larger than the as-recorded GM, and, although the differences between GMRotD50, GMRotI50, RotD50, and GM are small, orientation-independent measures should be used as they reduce epistemic uncertainties in the ground motion predictive equations (GMPE).
- The results obtained in this study are of significant interest in the improvement of the GMPEs in PSHA and in seismic design and risk assessments. In this respect, a simple theoretical model has been developed. This directionality model for Italy can be used to improve existing GMPEs as it allows us to include directionality effects, by means of simple ratios, into equations obtained without any consideration of directionality.
- Directionality effects are more important for low magnitude near events.

Concerning general analyses related to directionality effects on buildings (Chapter 4, Block I2. a), main results are:

- When one deals with a single accelerometric station, directionality may be very important, producing a great variability with the orientation of the two orthogonal horizontal components. This is why the expected damage in a specific building, submitted to a concrete two-component horizontal acceleration time histories, may have a great variability.
- A simplified approach to consider directionality effects on structures has been presented (see Chapter 4). The results indicate that neglecting the directionality effect could underestimate the actual demand about 30%. This fact reaffirms the importance of considering the directionality effect in the structural analysis.
- The predictive percentile method (PPM) provides a simplified alternative to obtain any percentile response without the need of performing hundreds of NLDA; this represents a decrease from 180, if the increment for rotating the records is 1°, to only two NLDA. The values obtained with the PPM are very close to the ones obtained through the complete rotational method. Noteworthy, the differences, in average, are less than 5%.
- Directionality effects should be regarded in structural seismic codes too, since it allows to improve the evaluation of the expected seismic damage in structures. For instance, for special facilities such as nuclear plants, hospitals, schools and other facilities that need to be operating after an earthquake, the RotD100 matched accelerograms should be used to estimate the seismic demand. This way, it will be guaranteed that the maximum seismic demand is considered in the structural analyses.

In reference to the M_W 7.8 Ecuador earthquake occurred on April 16, 2016 earthquake (Appendix C, Block III):

- Directionality effects have been evaluated, in both orthogonal directions of a seriously damaged building.
- The ground motion records at a close accelerometric station, located 5 km away from the building, has been used to estimate the expected damages. The directionality analysis has shown that probably the directionality effect was responsible for an increased damage because in spite of both main axes of the building showed similar strength, a strongest seismic action, hit one of them.

- A very good agreement has been found between the numerical analyses and the damage observed.
- This study, has allowed us to test the parametric model, and to verify the robustness and usefulness of the Park and Ang damage index.
- The importance and relevance of considering directionality effects in expected damage and risk assessments of specific building has been clearly highlighted.
- Directionality effects on the peak ground-motion produced by this event in the country, were also evaluated, obtaining nice and relevant results. This event reaffirms the need and importance of keeping developing research to reduce the seismic risk in Ecuador.

Regarding to the case study of a building severely damaged during the 19 September M_W 7.1, 2017 Mexico earthquake (Appendixes E and F, Block III):

- The anomalous seismic performance of a specific building in a multifamily residential area, which was the only one collapsed in the complex, was mainly attributed to directionality effects. In this case, assuming seismic actions recorded close to the building, the direction producing the strongest seismic action was the same as the one of the weak axis of the building.
- Thus, in damage and risk assessments, the direction in which the strongest seismic actions hit the buildings, directionality, should be considered, as similar buildings, located in the same place, may suffer very different damage grades, depending only of their specific orientation.
- In addition, concerning seismic hazard, the results show how the response spectra predicted by the SASID A v4.0.2.0 application, are lower than those corresponding to the seismic actions produced by this earthquake. This fact confirms that it is important to incorporate the results of directionality studies into the GMPEs by means of sensor orientation-independent measures.
- Anyhow, the consideration of maximum seismic actions could lead to excessively conservative GMPE. Median values or specific percentiles should be considered.
- Regarding design spectra, seismic regulations in Mexico City have been improved in recent years. However, latter design spectra were still surpassed by several accelerograms recorded during this earthquake. Noticeable, these excesses were due to directionality effects.
- Thus, an important conclusion of this study is that directionality effects must be considered in PSHA, in damage assessments, and in design regulations. Specific studies on directionality effects should be performed in urban areas located in high seismic hazard zones. However, studies undertaken in different countries may be also useful as the ratios RotD100/GM and RotD100/Larger, found are similar among them.

Concerning microzonation studies in Barcelona city (Chapter 5, Block II.1a):

- Previous work done in the city has been revisited and reviewed. An updated microzonation map of soils have been obtained. Also, a detailed map of predominant periods of buildings has been depicted. This way, crossing both maps, areas where soil-building resonance phenomena are expected has been highlighted. These maps can help to prevent and to reduce the seismic risk, since special attention can be devoted to vulnerable structures located on areas where soil-building resonance effects are likely (See Chapter 5 for details).
- Old towns located in the present-day neighbourhoods of *Gràcia*, *Poble Sec*, *Sant Antoni*, *El Raval*, and *Sants* are the most affected in the city. buildings in these neighbourhoods were built at the

same period of time and have similar structural typologies. Most of them were constructed in the late 19th century and the predominant typology is unreinforced masonry. This structural typology is one of the most commonly used buildings worldwide and the one that has caused the most damage and death, due to its high vulnerability to earthquakes.

- The microzonation map, based on predominant soil periods, can be implemented in structural regulations to develop improved design spectra based on the site-specific spectral response. Some structural codes do not consider SSI effects, since in most cases it is more conservative to use structural regulations. However, the effect of SSI may be prominent when structure and soil periods are similar.

In reference to the site classification of accelerometric stations (Chapter 6, Block II.1b and Appendix D, Block III):

- The Spanish strong-motion database has been used to classify the site of each accelerometric station, of the Spanish strong motion network, by means of the predominant period obtained using H/V ratios of the 5% damped response spectra. Directionality effects were considered too. This study strongly enforces the knowledge on the network which beforehand was based only on geological maps (see Chapter 6 for details).

- The sites of the accelerometric stations of the Costa Rica strong motion recording network has been also classified (see Appendix D).

- These classifications provide several advantages compared to others. The acquisition and processing of data are simple and automatic since network work continuously. This methodology may be easily exported to other networks, depending on the availability of strong motion databases. Moreover, this classification considers the real response of the site to actual seismic actions. This way, more realistic site conditions are obtained in comparison to the more general, simplified, and proxy classifications, which are used in seismic codes.

- Moreover, additional information on the likely anisotropy of both the strong motion and the soil response is also available, since directionality effects have been considered, and, for the same reason, epistemic uncertainties decrease because all the orientations are considered in the analysis.

- Finally, from an engineering point of view, this classification plays an important role in the evaluation and design of structures, which can be useful, for instance, when actual accelerograms are needed for deterministic and/or probabilistic dynamic analyses, thus improving the results for specific areas and contributing to reducing epistemic uncertainties.

With respect to dynamic soil-structure interaction (DSSI) analyses (Chapter 7 in Block II.2a and Appendix B in Block III):

- The importance of considering directionality effects of ground motions in 2D DSSI analyses has been highlighted. An important shortage in DSSI analyses, usually performed, is that only the as-recorded components of ground motions are considered, without any consideration to other rotated time-histories that could lead to more severe structural responses.

- It has been shown that directionality effects can be properly addressed by analysing the considered problem with a number of linear combinations of the input motions for different incidence angles. Then, the orientation producing the maximum response of the structure can be determined; this procedure was termed the CRA. If directionality effects are overlooked and only the as-recorded

components are employed to derive the input motions for the analyses, the maximum relative roof displacements of the building can be underestimated as much as 50%.

- DSSI analyses are computationally expensive preventing the use of the CRA in most of the cases. Already established simplified procedures to incorporate directionality effects for structural analyses cannot be employed directly with the input motions for DSSI analyses, since site effects tend to modify the input. Thus, a simplified procedure has been proposed here to identify, in advance, the angle that produces the maximum response of a structure for a given seismic action and, therefore, allowing us to get good results with only one DSSI analysis. Site effects are incorporated by applying the CRA to free-field site response simulations, since they are quite inexpensive compared to full DSSI analyses. Then, the critical orientation is predicted from the maximum value of a given IM, as a function of the rotation angle, from the motions computed at the surface of the free-field simulations.

- Different IMs were evaluated, and the PGV resulted in critical angles and relative roof displacements closest to the CRA. Although the exact values were not exactly predicted, the mean relative differences with respect to the CRA results, in terms of roof displacements, were smaller than those obtained using the as-recorded directions.

- Although directionality effects should always be considered for earthquake-resistant design and seismic damage and risk assessments, it is important to mention that using the most unfavourable incidence angle, in each of the selected ground-motion records, could lead to over-conservative results.

Concerning drift-correlated intensity measures (Chapter 8, Block II.2b):

- From a correlation analysis between the maximum inter-story drift (MIDR) and a group of well-known IMs, related to the destructiveness potential of earthquakes, it was found an important correlation between MIDR, PGV and the significant duration.

- Then a new intensity measure, which is highly correlated with the MIDR, called $I_{\Delta-PGV}$, has been proposed.

- The building-to-building structural characteristic variations were considered by means of a probabilistic approach, varying the geometry and mechanical properties of the building models to perform 500 probabilistic NLDA. This way the new IM, $I_{\Delta-PGV}$, was validated. An important finding and one of the main advantages of $I_{\Delta-PGV}$ is that this new IM is independent of the building fundamental period.

9.2 Recommendations and future trends

The knowledge on topics covered in this PhD thesis is, nowadays, relatively limited, so that these topics keep on having relevant interest in engineering seismology and in earthquake engineering, as well. Research never stops, each issue addressed opens the door to new exciting dares deserving to be investigated. This way, at the end of each research stage there emerge methods and procedures which are worthy of being improved and new questions deserving to be answered. This is why the present backgrounds, tools, resources and attainments are far from the ones which were available only several years ago. This section is devoted to point out and to highlight spots being the natural development and maturation of the job done and to propose new trends in the same road of the issues investigated. Also, several ideas and guidelines for future research are depicted.

Concerning directionality in expected seismic actions, several suggestions follow:

- The quantity, quality and availability of strong motion databases, is increasing day by day. It is very important to keep on this effort in the maintenance of such big-data.
- To analyse more databases would help to improve and to refine the lessons and conclusions coming of this type of studies.
- The impact on ground-motion predictive equations and on PSHA of the new intensity measures based on the prior-combination of the acceleration time histories, which in our opinion has more physical sense, should be investigated deeper. A criterion of the goodness of the fits may be the dispersion in the predictive equations.
- An interesting issue would be to model the directionality effects from source to site, including the fault rupture and directivity. It would be interesting to study the similarities/dissimilarities of directionality effects for normal-, strike-slip-, thrust type faults.
- The variation of directionality effects with the distance to the causing fault is considered worthy to be investigated too. Very likely, seismic waves responsible for the strong motion may be different at short and long distances.
- The influence of site effects on directionality is another interesting issue. In this study, directionality effects in different soil conditions have been analysed. However, the fact that results obtained by others did not considered soil's effects advised us to do the comparison without considering them. Further comparative analyses considering site effects are recommended.

Concerning directionality effects on expected seismic damage on specific structures subjected to a specific strong motion, the following hints are highlighted:

- Concerning the simplified method to consider the directionality effects on structures (see Chapter 4), it is worth to mention that this approach should be proved with different structural typologies, building shapes and heights, among other properties, that may influence the dynamic behaviour. More work is needed to go towards more general conclusions.
- Few studies have been carried out on effects of the azimuthal orientation of buildings in the expected damage. It seems clear that if the strong action hits the weak axis the damage will be greater. However, it would be interesting to see how damage probability matrices corresponding to both main axes are combined to get a global damage probability matrix. A reasonable assumption could be to use the Bayes theorem concerning to prior knowledge of conditions related to the event. To check for this assumption, to combine 2D non-linear static analyses and 3D incremental dynamic analyses is suggested.
- In this sense, it is proposed to analyze different 3D building configurations, having high variability in the fundamental periods in the directions of their main axes, with the aim of evaluating their susceptibility to directionality effects. It would be interesting as well to examine and to compare the response of such buildings to different seismic demands, through nonlinear dynamic analyses, using, for instance, only one acceleration component and the two orthogonal components, simultaneously. It is also suggested to analyze more realistic situations considering the vertical acceleration in addition to the two horizontal ones.

Concerning microzonation studies:

- In many cities, located in low-to-moderate seismic hazard regions, like Barcelona is, the seismic risk may become high because of the huge population density, the great exposed value and the high vulnerability of the built environment. Seismic risk studies in those cities are strongly recommended. Moreover, in these very dense cites, it is important to determine likely soil-structure-resonant areas.

- In dense cities too, it is strongly recommended to analyse Soil-Structure-Interaction (SSI) and Soil-City-Interaction (SCI) effects. The SCI effect is defined as the global interaction between urban fabric and its subsoil through ground motion (Bard et al., 2005). These multiple interactions may modify the response of the buildings and the one of the subsoils itself. If SCI effects turn out to be significant, one immediate consequence is that erecting or destroying a building, or a group of buildings, could modify the seismic hazard for the neighbourhood affected.

- Macau et al. (2015) found that H/V measures in shallow quaternary layers in the delta of the Llobregat river at the south-eastern part of Barcelona, exhibit a second peak at which significant amplification may occur. Additional research on this finding and on its influence on buildings' response is suggested.

Concerning site classifications:

- The procedure for classification of the site of accelerometric stations, which has been applied to accelerometric networks of Spain and Costa Rica, can be easily implemented to other networks.

- It would be interesting to go further in the directionality related issues and, to study the anisotropy of both the strong motion and the soil response. It would be challenging also to evaluate this anisotropy in the non-linear range.

- The impact of this site classifications on the development of new GMPEs, in comparison to the more traditional ones based on more simplified approaches that consider the local site effects based on conventional rock/soil classifications, remains as a relevant and interesting issue.

Related to the Dynamic Soil-Structure Interaction (DSSI) analyses:

- The procedure presented in this study that incorporates directionality effects in DSSI analysis, requires further validation by means of new analyses under different conditions, such as different characteristics of the soil deposit, additional seismic actions, corresponding to different kinds of earthquakes, and, of course, different surface structures.

- More analyses should be performed considering 3D models and the non-linear properties and expected damage of the structures.

In reference to the new Drift-correlated intensity measure ($I_{\Delta-PGV}$):

- $I_{\Delta-PGV}$ is a linear combination of two well-known seismic parameters: peak ground velocity (PGV) and significant duration. The use of more than one parameter to define the potential damage of earthquakes to structures is a noteworthy novelty. This finding suggests that alternative methods, such as for instance Artificial Intelligence and Neural Networks, can be used in future similar studies.

- $I_{\Delta-PGV}$ was validated for 2D symmetric steel frame buildings. Further analyses, with other structural typologies and 3D asymmetric buildings, are needed to establish its broad soundness.

- As well, coefficients, α and β, of the linear combination, should be recalibrated with other building types. If this intensity measure holds for different structural types, it would be very useful and effective for seismic hazard and risk assessments.
- One of the main advantages of $I_{\Delta-PGV}$ is that it is independent of the fundamental period of the building. In future research, the potential of this IM should be compared with other IMs that consider the structural behaviour by means of the elongation of the buildings' periods.

9.3 Conclusions and final remarks

There are many remarks and conclusions that can be inferred from the work done, mainly because the extensive number of issues tackled in this dissertation. For detailed conclusions and remarks on the different topics, the reader is invited to have a look into the corresponding paper, which forms each chapter. Here, only a short number of conclusions/remarks are stressed.

- Directionality effects in expected seismic actions are relevant. For probabilistic seismic hazard analysis, predictive equations of strong ground motion can and should be improved.
- Other ways of combining maximum IMs or peak values, as for instance, the ones based on prior combinations of the time-histories, may also help to have more realistic estimates, and with more physical sense, of the expected seismic actions.
- Expected damage in a specific building strongly may depend on the azimuthal orientations of its main axes with respect to the strong motion in the site.
- Even when located in low-to-moderate seismic hazard regions, detailed risk assessments must be done in big cities, including detailed microzonation analyses, soil-building resonant zones detection, SSI and SCI studies. Because of the high population density, the high vulnerability of the built environment, and because of the high concentration of facilities, infrastructures and services, the seismic risk of these cities may become very high.
- With the availability of huge databases of strong motion recordings, site characterization of accelerometric stations can be done in an easy and expedite way. Additional value studies concerning anisotropy of the site response and the one of the seismic actions can also be tackled.
- The available big-data concerning to accelerograms and the increasing computational power of modern devices and tools, also allows us to search for more and more reliable IMs related to drift, so that they may become excellent forecasts of the seismic performance of buildings and of damage expected. Artificial intelligence emerges as an interesting means to search for new IMs, connecting highly correlated parameters of seismic actions to those of the structural performance and response.

Final thought

And that's all, it is over...

Unfortunately, earthquakes are turning on great catastrophes, and they will be keeping on doing that. Many are the reasons for this apparent failure of the present-day civil engineering community. But, as it has been shown in recent earthquakes, like the 2010 Haiti, M_W 7.7, earthquake, the dimension of an earthquake disaster goes beyond technical aspects, involving many other socioeconomic and, even, political issues. Discrimination, poverty and societal inequalities greatly increase the catastrophic breadth of earthquakes. In any case, the main motivation of my PhD research has been to provide new insights in the right road towards more knowledge-based, sustainable, safe and resilient communities around the planet Earth, for sure, the most beautiful of our solar system but, also the one most needing special care to protect the wonderful life it shelters.

Bibliography

Abrahamson, N., Atkinson, G., Boore, D. M., Bozorgnia, Y., Campbell, K., Chiou, B., Idriss, I. M., Silva, W., and Youngs, R. (2008). Comparisons of the NGA ground-motion relations. *Earthquake Spectra*, 24(1):45–66.

Akkar, S., Sandıkkaya, M. A., and Bommer, J. J. (2014). Empirical ground-motion models for point- and extended-source crustal earthquake scenarios in Europe and the Middle East. *Bulletin of Earthquake Engineering*, 12(1):359–387.

Alfaro, A., Pujades, L. G., Goula, X., Susagna, T., Navarro, M., Sanchez, J., Canas, J. A., and Sánchez, J. (2001). Preliminary map of soil's predominant periods in Barcelona using microtremors. *Pure and Applied Geophysics*, 158(12):2499–2511.

Alfaro, P., Delgado, J., García-Tortosa, F. J., Lenti, L., López, J. A., López-Casado, C., and Martino, S. (2012). Widespread landslides induced by the Mw 5.1 earthquake of 11 May 2011 in Lorca, SE Spain. *Engineering Geology*, 137-138(May 2011):40–52.

Alvarado, G. E., Benito, B., Staller, A., Climent, A., Camacho, E., Rojas, W., Marroquín, G., Molina, E., Talavera, J. E., Martínez-Cuevas, S., and Lindholm, C. (2017). The new Central American seismic hazard zonation: Mutual consensus based on up to day seismotectonic framework. *Tectonophysics*, 721(October):462–476.

Ambraseys, N. N., Smit, P. M., Beradi, R., Rinaldis, D., Cotton, F., and Berge, C. (2000). Dissemination of European Strong-Motion Data, CD ROM collection, European Commission, Directorate-General XII, Environmental and Climate Programme, ENV4-CT97-0397.

Amoruso, A., Crescentini, L., and Scarpa, R. (2002). Source parameters of the 1908 Messina Straits, Italy, earthquake from geodetic and seismic data. *Journal of Geophysical Research: Solid Earth*, 107(B4):ESE 4–1–ESE 4–11.

Angina, A., Steri, A., Stacul, S., and Lo Presti, D. (2018). Free-Field Seismic Response Analysis: The Piazza dei Miracoli in Pisa Case Study. *International Journal of Geotechnical Earthquake Engineering*, 9(1):1–21.

ANSI/AISC 341-10 (2010). Seismic Provisions for Structural Steel Buildings.

ANSI/AISC 358-10 (2010). Prequalified connections for special and intermediate steel moment frames for seismic applications.

Arias, A. (1970). A measure of earthquake intensity. *Cambridge, MA, The M.I.T. Press*, pages 438 – 483.

Arroyo, M., Godínez, K., and Linkimer, L. (2017). Completitud del catálogo de la red sismológica nacional de Costa Rica durante 1975-2014. *Boletin de Geologia*, 39(3):87–98.

ASCE (2010). *Minimum Design Loads for Buildings and Other Structures, ASCE/SEI 7-10*. American Society of Civil Engineers/Structural Engineering Institute, Reston, Virginia.

ASCE (2017). *Minimum Design Loads and Associated Criteria for Buildings and Other Structures, ASCE/SEI 7-16*.

ASTM A992 / A992M - 11 (2015). Standard Specification for Structural Steel Shapes. Technical report.

Athanatopoulou, A. M. (2005). Critical orientation of three correlated seismic components. *Engineering Structures*, 27(2):301–312.

Atik, L. A. and Abrahamson, N. A. (2010). An improved method for nonstationary spectral matching. *Earthquake Spectra*, 26(3):601–617.

Baker, J. W. and Bradley, B. A. (2017). Intensity Measure Correlations Observed in the NGA-West2 Database, and Dependence of Correlations on Rupture and Site Parameters. *Earthquake Spectra*, 33(1):145–156.

Baker, J. W. and Cornell, C. A. (2006). Which Spectral Acceleration Are You Using? *Earthquake Spectra*, 22(2):293–312.

Baker, J. W., Haselton, C. B., Luco, N., Stewart, J. P., and Zimmerman, R. B. (2015). Updated ground motion spectral matching requirements in the 2015 NEHRP Recommended Seismic Provisions. In *6th International Conference on Earthquake Geotechnical Engineering*, number November, pages 1–8.

Baptista, M. A., Miranda, J. M., Chierici, F., and Zitellini, N. (2010). New study of the 1755 earthquake source based on multi-channel seismic survey data and tsunami modeling. *Natural Hazards and Earth System Science*, 3(5):333–340.

Barbat, A. H., Pujades, L. G., and Lantada, N. (2006). Performance of buildings under earthquake in Barcelona, Spain. *Computer-Aided Civil and Infrastructure Engineering*, 21:573–593.

Bard, P.-Y., Chazelas, J. L., Guéguen, P., Kham, M., and Semblat, J. F. (2005). *Site-city interaction, Chapter 5. pp 91-114*. Assessing and Managing Earthquake Risk, C. S. Oliveira, A. Roca, and X. Goula (Editors), Springer, New York, New York, 530 pp.

Bard, P.-Y., Guéguen, P., and Wirgin, A. (1996). A note on the seismic wavefield radiated from large building structures into soft soils. *11th World Conference on Earthquake Engineering*, (May 2014).

Benioff, H. (1934). The physical evaluation of seismic destructiveness. *Bulletin of the Seismological Society of America*, pages 398–403.

Beyer, K. and Bommer, J. (2006). Relationships between median values and between aleatory variabilities for different definitions of the horizontal component of motion. *Bulletin of the Seismological Society of America*, 96(4A):1512–1522.

Bianca, M., Monaco, C., Tortorici, L., and Cernobori, L. (1999). Quaternary normal faulting in southeastern Sicily (Italy): A seismic source for the 1693 large earthquake. *Geophysical Journal International*, 139(2):370–394.

Bilek, S. L. (2010). Invited review paper: Seismicity along the South American subduction zone: Review of large earthquakes, tsunamis, and subduction zone complexity. *Tectonophysics*, 495(1-2):2–14.

Billah, K. Y. and Scanlan, R. H. (1991). Resonance, Tacoma Narrows bridge failure, and undergraduate physics texbookls. *American Journal of Physics*, 59:118–124.

Bindi, D., Pacor, F., Luzi, L., Puglia, R., Massa, M., Ameri, G., and Paolucci, R. (2011). Ground motion prediction equations derived from the Italian strong motion database. *Bulletin of Earthquake Engineering*, 9(6):1899–1920.

Biot, M. (1933). Theory of Elastic Systems Vibrating Under Transient Impulse with an Application to Earthquake – Proof Buildings. In *Proc. National Academy of Sciences*, volume 19, pages 262–268.

Biot, M. (1941). A Mechanical Analyzer for the Prediction of Earthquake Stresses. *Bulletin of the Seismological Society of America*, 31(2):151–171.

Biot, M. (1943). Analytical and Experimental Methods in Engineering Seismology. *Transactions of the American Society of America*, 108:365–385.

Bojórquez, E., Chávez, R., Reyes-Salazar, A., Ruiz, S. E., and Bojórquez, J. (2017). A new ground motion intensity measure IB. *Soil Dynamics and Earthquake Engineering*, 99(April 2016):97–107.

Bojórquez, E. and Iervolino, I. (2011). Spectral shape proxies and nonlinear structural response. *Soil Dynamics and Earthquake Engineering*, 31(7):996–1008.

Bolt, B. A. (1973). Duration of strong ground motion. In *5th World Conference on Earthquake Engineering*, volume 1, pages 1304–1313.

Bommer, J. J., Abrahamson, N. A., Strasser, F. O., Pecker, A., Bard, P.-Y., Bungum, H., Cotton, F., Fah, D., Sabetta, F., Scherbaum, F., and Studer, J. (2004). The Challenge of Defining Upper Bounds on Earthquake Ground Motions. *Seismological Research Letters*, 75(1):82–95.

Bommer, J. J., Elnashai, A.-S., and Weir, A. G. (2000). Compatible acceleration and displacement spectra for seismic design codes. In *12th World Conference on Earthquake Engineering*, page paper no. 207, Auckland, New Zealand.

Bommer, J. J. and Martínez-Pereira, A. (1999). The effective duration of earthquake strong motion. *Journal of Earthquake Engineering*, 3(2):127–172.

Boore, D. M. (2010). Orientation-independent, nongeometric-mean measures of seismic intensity from two horizontal components of motion. *Bulletin of the Seismological Society of America*, 100(4):1830–1835.

Boore, D. M., Joyner, W. B., and Fumal, T. E. (1997). Equations for estimating horizontal response spectra and peak acceleration from western North American earthquakes: A summary of recent work. *Seismological Research Letters*, (68):128–153.

Boore, D. M. and Kishida, T. (2016). Relations between some horizontal-component ground-motion intensity measures used in practice. *Bulletin of the Seismological Society of America*, 107(1):334–343.

Boore, D. M., Stewart, J. P., Seyhan, E., and Atkinson, G. M. (2013). NGA-West2 Equations for Predicting Response Spectral Accelerations for Shallow Crustal Earthquakes.

Boore, D. M., Watson-Lamprey, J., and Abrahamson, N. A. (2006). Orientation-independent measures of ground motion. *Bulletin of the Seismological Society of America*, 96(4A):1502–1511.

Bothara, J. K., Dhakal, R. P., and Mander, J. B. (2010). Seismic performance of an unreinforced masonry building: An experimental investigation. *Earthquake Engineering Structural Dynamics*, 39:45–68.

Bozorgnia, Y., Abrahamson, N. A., Al Atik, L., Ancheta, T. D., Atkinson, G. M., Baker, J. W., Baltay, A., Boore, D. M., Campbell, K. W., Chiou, B. S. J., Darragh, R. B., Day, S., Donahue, J. L., Graves, R. W., Gregor, N., Hanks, T., Idriss, I. M., Kamai, R., Kishida, T., Kottke, A. R., Mahin, S. A., Rezaeian, S., Rowshandel, B., Seyhan, E., Shahi, S., Shantz, T., Silva, W., Spudich, P., Stewart, J. P., Watson-Lamprey, J., Wooddell, K., and Youngs, R. (2014). NGA-West2 research project. *Earthquake Spectra*, 30(3):973–987.

Bozorgnia, Y., Abrahamson, N. A., Campbell, K., Rowshandel, B., and Shantz, T. (2012). NGA-West2: A comprehensive research program to update ground motion prediction equations for shallow crustal earth- quakes in active tectonic regions. In *15th World Conf. on Earthquake Engineering, Lisbon, Portugal, 6 pp.*

Bradley, B. A. and Baker, J. W. (2015). Ground motion directionality in the 2010–2011 Canterbury earthquakes. *Earthquake Engineering and Structural Dynamics*, 44:371–384.

Brady, A. G. (2009). Strong-motion accelerographs: Early history. *Earthquake Engineering and Structural Dynamics*, 38:1121–1134.

Braga, F., Dolce, M., and Liberatore, D. (1982). A Statistical Study on Damaged Buildings and an Ensuing Review of the MSK-76 Scale. In *Proceedings of the Seventh European Conference on Earthquake Engineering*, pages 431–450, Athens, Greece.

Braga, F., Dolce, M., and Liberatore, D. (1986). Assessment of the relationships between Macroseismic Intensity, Type of Building and Damage, based on the recent Italy Earthquake Data. In *Proceedings of the 8th European Conference on Earthquake Engineering*, pages 39–46, Lisbon.

Brinkgreve, R. B. J., Kappert, M. H., and Bonnier, P. G. (2007). Hysteretic damping in a small-strain stiffness model. In Pande, G. N. and Pietruszczak, S., editors, *10th International Symposium on Numerical Models in Geomechanics*, pages 737–742, Rhodes, Greece. CRC Press.

Brinkgreve, R. B. J., Kumarswamy, S., and Swolfs, W. M. (2017). PLAXIS 2D.

BSSC (2009). *NEHRP Recommended Seismic Provisions for New Buildings and Other Structures (FEMA P-750)*. Building Seismic Safety Council of the National Institute of Building Sciences.

Cadet, H., Macau, A., Benjumea, B., Bellmunt, F., and Figueras, S. (2011). From ambient noise recordings to site effect assessment: The case study of Barcelona microzonation. *Soil Dynamics and Earthquake Engineering*, 31(3):271–281.

Calvi, G. M., Pinho, R., and Crowley, H. (2006). State-of-the-knowledge on the period elongation of RC buildings during strong ground shaking. *First European Conference on Earthquake Engineering and Seismology*, (September):3–8.

Campbell, K. W. and Bozorgnia, Y. (2007). *NGA ground motion relations for the geometric mean horizontal component of peak and spectral ground motion parameters*. PEER Report 2007/02, Pacific Earthquake Engineering Research Center.

Cantagallo, C., Camata, G., and Spacone, E. (2012). Demand of Reinforced Concrete Structures. In *15th World Conference on Earthquake Engineering, Lisbon Portugal*.

Carballo, J. E. (2000). Probabilistic seismic demand analysis: spectrum matching and design. Technical report, Dept. of Civil and Environmental Engineering, Stanford University, Stanford, CA.

Carbonari, S., Dezi, F., and Leoni, G. (2011). Linear soil-structure interaction of coupled wall-frame structures on pile foundations. *Soil Dynamics and Earthquake Engineering*, 31(9):1296–1309.

Carr, A. J. (2002). Ruaumoko 2D and 3D - Inelastic Dynamic Analysis Program.

Casapulla, C., Maione, A., and Argiento, L. (2017). Seismic analysis of an existing masonry building according to the multi-level approach of the Italian guidelines on cultural heritage. *Ingegneria Sismica*, 34(1):40–59.

Caselles, J. O., Pérez-Gracia, V., Franklin, R., Pujades, L. G., Navarro, M., Clapes, J., Canas, J. A., and García, F. (2010). Applying the H/V method to dense cities. A case study of Valencia city. *Journal of Earthquake Engineering*, 14(2):192–210.

Çelebi, M. (2008). Seismic monitoring to assess performance of structures in near-real time: Recent progress. *AIP Conference Proceedings*, 1020(PART 1):848–855.

Çelebi, M., Bazzurro, P., Chiaraluce, L., Clemente, P., Decanini, L., Desortis, A., Ellsworth, W., Gorini, A., Kalkan, E., Marcucci, S., Milana, G., Mollaioli, F., Olivieri, M., Paolucci, R., Rinaldis, D., Rovelli, A., Sabetta, F., and Stephens, C. (2010). Recorded motions of the 6 April 2009 Mw 6.3 L'Aquila, Italy, earthquake and implications for building structural damage: Overview. *Earthquake Spectra*, 26(3):651–684.

CEN (2004). *Eurocode 8: design of structures for earthquake resistance – Part1: general rules, seismic actions and rules for buildings*. Comité Européen de Normalisation Brussels, May, http://www.cen.eu/cenorm/homepage.htm.

CFIA (2016). *Código Sísmico de Costa Rica 2010 (Revisión 2014). Editorial Tecnológica de Costa Rica, Cartago, Costa Rica*.

Chen, W. and Atsuta, T. (1976). *Theory of Beam-Columns, Volume 1: In-Plane Behavior and Design*. McGraw-Hill, Inc., New York. 513.

Chiou, B., Darragh, R., Gregor, N., and Silva, W. (2008). NGA project strong-motion database. *Earthquake Spectra*, 24(1):23–44.

Chopra, A. K. (2017). *Dynamics of Structures: Theory and Applications to Earthquake Engineering, 5th Edition*. Pearson Prentice Hall.

Chopra, A. K. and Chintanapakdee, C. (2001). Comparing response of SDF systems to near-fault and far-fault earthquake motions in the context of spectral regions. *Earthquake Engineering and Structural Dynamics*, 30:1769–1789.

Chopra, S., Kumar, V., Choudhury, P., and Yadav, R. B. S. (2017). Site classification of Indian strong motion network using response spectra ratios. *Journal of Seismology*, 22:419–438.

Chávez-García, F. J. and Bard, P.-Y. (1994). Site effects in Mexico City eight years after the September 1985 Michoacan earthquakes. *Soil Dynamics and Earthquake Engineering*, 13(4):229–247.

Cid, J., Susagna, T., Goula, X., Chavarria, L., Figueras, S., Fleta, J., Casas, A., and Roca, A. (2001). Seismic zonation of Barcelona based on numerical simulation of site effects. *Pure and Applied Geophysics*, 158(12):2559–2577.

Coburn, A. and Spence, R. (2002). *Earthquake Protection*. John Wiley & Sons, Ltd., Chichester, West Sussex, second edition.

Cosenza, E. and Manfredi, G. (2000). Damage indices and damage measures. *Progress in Structural Engineering and Materials*, 2(1):50–59.

D'ayala, D. (2013). Assessing the seismic vulnerability of masonry buildings. In Tesfamariam, S. and Goda, K., editors, *Handbook of Seismic Risk Analysis and Management of Civil Infrastructure Systems*, chapter 13, pages 334–365. Woodhead Publishing Series in Civil and Structural Engineering.

de Lautour, O. R. and Omenzetter, P. (2009). Prediction of seismic-induced structural damage using artificial neural networks. *Engineering Structures*, 31(2):600–606.

De Luca, F., Verderame, G. M., Gómez-Martínez, F., and Pérez-García, A. (2014). The structural role played by masonry infills on RC building performances after the 2011 Lorca, Spain, earthquake. *Bulletin of Earthquake Engineering*, 12(5):1999–2026.

DeShon, H. R., Schwartz, S. Y., Bilek, S. L., Dorman, L. M., Gonzalez, V., Protti, J. M., Flueh, E. R., and Dixon, T. H. (2003). Seismogenic zone structure of the southern Middle America Trench, Costa Rica. *Journal of Geophysical Research: Solid Earth*, 108(B10).

DesRoches, R., Comerio, M., Eberhard, M., Mooney, W., and Rix, G. J. (2011). Overview of the 2010 Haiti earthquake. *Earthquake Spectra*, 27(SUPPL. 1):1–21.

di Alessandro, C., Bonilla, L. F., Boore, D. M., Rovelli, A., and Scotti, O. (2012). Predominant-period site classification for response spectra prediction equations in Italy. *Bulletin of the Seismological Society of America*, 102(2):680–695.

Diaz, S. A., Pujades, L. G., Barbat, A. H., Vargas, Y. F., and Hidalgo-Leiva, D. A. (2017). Energy damage index based on capacity and response spectra. *Engineering Structures*, 152:424–436.

Diaz, S. A., Pujades, L. G., Pinzón, L. A., and Vargas, Y. (2018). An alternative approach to consider the effect of seismic directionality. *Revista Ingeniería de Construcción*, 33(3):279–290.

Dikmen, S. and Tanırcan, G. (2018). Site amplification and resonance frequency in the urban environment. *Soil Dynamics and Earthquake Engineering*, 105(April 2017):160–170.

Dobry, R., Idriss, I. M., and Ng, E. (1978). Duration characteristics of horizontal components of strong-motion earthquake records. *Bulletin of the Seismological Society of Americas*, 68(5):1487–1520.

Douglas, J. (2003). Earthquake ground motion estimation using strong-motion records: a review of equations for the estimation of peak ground acceleration and response spectral ordinates. *Earth-Science Reviews*, 61(12):43–104.

Douglas, J. (2017). *Ground motion prediction equations 1964-2016*. University of Strathclyde, Glasgow, UK.

Elenas, A. (2000). Correlation between seismic acceleration parameters and overall structural damage indices of buildings. *Soil Dynamics and Earthquake Engineering*, 20:93–100.

Elnashai, A. S. and Di Sarno, L. (2008). *Fundamentals of Earthquake Engineering*. John WileySons, Ltd., Chichester, United Kingdom, 337 pp.

Espinoza, F. (1999). *Determinación de características dinámicas de estructuras*. PhD thesis, Universitat Politècnica de Catalunya (UPC).

Fan, G., Beck, S. L., and Wallace, T. C. (1993). The seismic source parameters of the 1991 Costa Rica aftershock sequence: evidence for a transcurrent plate boundary. *Journal of Geophysical Research*, 98(B9):15759.

Fatahi, B., Tabatabaiefar, H. R., and Samali, B. (2011). Performance Based Assessment of Dynamic Soil-Structure Interaction Effects on Seismic Response of Building Frames. In *Georisk 2011: Geotechnical Risk Assessment & Management*, pages 344–351, Atlanta, Georgia. American Society of Civil Engineers.

Fatahi, B., Tabatabaiefar, H. R., and Samali, B. (2014). Soil-structure interaction vs Site effect for seismic design of tall buildings on soft soil. *Geomechanics and Engineering*, 6(3):293–320.

Federal Emergency Management Agency (FEMA) (2002). HAZUS'99 (SR 2) technical manual. Technical report, Federal Emergency Management Agency.

FEMA (2004). *NEHRP Recommended Provisions for Seismic Regulations for New Buildings and Other Structures (FEMA 450), Part 1: Provisions*. Building Seismic Safety Council, National Institute of Building Sciences, Washington, D.C., 308 pp.

FEMA 355C (2000). State of the Art Report on System Performance of Steel Moment Frames Subject to Earthquake Ground Shaking. Technical report, SAC Joint Venture Partnership for the Federal Emergency Management Agency. Washington.

Figueras, S., Schmidt-Díaz, V., Susagna, T., Fleta, J., Goula, X., and Roca, A. (1995). Preliminary study of microzonation of Barcelona (Spain). In *Fifth Int. Conf. on Seismic Zonation*, pages 731–738, Nice, France.

Fiorentino, G., Forte, A., Pagano, E., Sabetta, F., Baggio, C., Lavorato, D., Nuti, C., and Santini, S. (2018). Damage patterns in the town of Amatrice after August 24th 2016 Central Italy earthquakes. *Bulletin of Earthquake Engineering*, 16(3):1399–1423.

Fiorentino, G., Quaranta, G., Mylonakis, G., Lavorato, D., Pagliaroli, A., Carlucci, G., Sabetta, F., Monica, G. D., Lanzo, G., Aprile, V., Marano, G. C., Briseghella, B., Monti, G., Squeglia, N., Bartelletti, R., and Nuti, C. (2019). Seismic reassessment of the leaning tower of Pisa: Dynamic monitoring, site response, and SSI. *Earthquake Spectra*, 35(2):703–736.

François, S., Galvín, P., Museros, P., Lombaert, G., and Degrande, G. (2014). Dynamic soil-structure interaction analysis of a telescope at the Javalambre Astrophysical Observatory. *Soil Dynamics and Earthquake Engineering*, 65:165–180.

Franke, K. W., Ulmer, K. J., Ekstrom, L. T., and Meneses, J. F. (2016). Clarifying the differences between traditional liquefaction hazard maps and probabilistic liquefaction reference parameter maps. *Soil Dynamics and Earthquake Engineering*, 90:240–249.

Fujii, K. (2016). Assessment of pushover-based method to a building with bidirectional setback. *Earthquake and Structures*, 11(3):421–443.

Fukushima, Y., Bonilla, L. F., Scotti, O., and Douglas, J. (2007). Site classification using horizontal-to-vertical response spectral ratios and its impact when deriving empirical ground-motion prediction equations. *Journal of Earthquake Engineering*, 11(5):712–724.

Garcia-Soto, A. D., Hong, H. P., and Gómez, R. (2012). Effect of the orientation of records on displacement ductility demand. *Canadian Journal of Civil Engineering*, 39(4):362–373.

Garini, E. and Gazetas, G. (2013). Damage potential of near-fault records: Sliding displacement against conventional "Intensity Measures". *Bulletin of Earthquake Engineering*, 11(2):455–480.

Genes, M. C. and Kocak, S. (2005). Dynamic soil-structure interaction analysis of layered unbounded media via a coupled finite element/boundary element/scaled boundary finite element model. *International Journal for Numerical Methods in Engineering*, 62(6):798–823.

Ghasemi, H., Zare, M., Fukushima, Y., and Sinaeian, F. (2009). Applying empirical methods in site classification, using response spectral ratio (H/V): A case study on Iranian strong motion network (ISMN). *Soil Dynamics and Earthquake Engineering*, 29(1):121–132.

Ghobarah, A., Abou-Elfath, H., and Biddah, A. (1999). Response-based damage assessment of structures. *Earthquake Engineering and Structural Dynamics*, 28(1):79–104.

Givens, M. J. (2013). *Dynamic soil-structure interaction of instrumented buildings and test structures*. Ph.D. Dissertation, University of California, Los Angeles, 367 pp.

Goded, T., Buforn, E., and Macau, A. (2012). Site effects evaluation in Málaga city's historical centre (Southern Spain). *Bulletin of Earthquake Engineering*, 10(3):813–838.

Goel, R. K. and Chopra, A. K. (1997). Period Formulas for Moment-Resisting Frame Buildings. *Journal of Structural Engineering*, 123(11):1454–1461.

Goel, R. K. and Chopra, A. K. (1998). Period formulas for concrete shear wall buildings. *Journal of Structural Engineering*, 124(4):426–433.

Goes, S. D., Velasco, A. A., Schwartz, S. Y., and Lay, T. (1993). The April 22, 1991, Valle de la Estrella, Costa Rica (Mw=7.7) earthquake and its tectonic implications: a broadband seismic study. *Journal of Geophysical Research*, 98(B5):8127–8142.

Goldstein, P., Dodge, D., Firpo, M., and Minner, L. (2003). SAC2000: Signal processing and analysis tools for seismologists and engineers. In Lee, W. H., Kanamori, H., Jennings, P. C., and Kisslinger, C., editors, *International Handbook of Earthquake and Engineering Seismology*, chapter 85.5, pages 1613–1614. Academic Press, London.

Gordo-Monsó, C. and Miranda, E. (2011). Bulletin of Earthquake Engineering Significance of Directivity Effects During the 2011 Lorca Earthquake in Spain.

Guendel, F. and Protti, M. (1998). Sismicidad y sismotectónica de América Central. *Física de la Tierra*, 10(0214-4557):19–51.

Guéguen, P., Bard, P.-Y., and Chávez-García, F. J. (2002). Site-city seismic interaction in Mexico City - Like environments: An analytical study. *Bulletin of the Seismological Society of America*, 92(2):794–811.

Guéguen, P., Bard, P.-Y., and Oliveira, C. S. (2000). Experimental and numerical analysis of soil motions caused by free vibrations of a building model. *Bulletin of the Seismological Society of America*, 90(6):1464–1479.

Guéguen, P., Semblat, J. F., Bard, P.-Y., and Chazelas, J. L. (2012). Site-city interaction: Experimental and numerical approaches. *Bull. Lab. Ponts Chaussées*, 279:35–46.

Haji-Soltani, A. and Pezeshk, S. (2017). Relationships among various definitions of horizontal spectral accelerations in Central and Eastern North America. *Bulletin of the Seismological Society of America*, 108(1):409–417.

Hancock, J. and Bommer, J. J. (2006). A State-of-Knowledge Review of the Influence of Strong-Motion Duration on Structural Damage. *Earthquake Spectra*, 22(3):827–845.

Hancock, J., Watson-Lamprey, J. A., Abrahamson, N. A., Bommer, J. J., Markatis, A., McCoyh, E., and Mendis, R. (2006). An improved method of matching response spectra of recorded earthquake ground motion using wavelets. *Journal of Earthquake Engineering*, 10(1):67–89.

Hassani, B. and Atkinson, G. M. (2016). Applicability of the site fundamental frequency as a VS30 proxy for Central and Eastern North America. *Bulletin of the Seismological Society of America*, 106(2):653–664.

Hidalgo-Leiva, D. A., Pujades, L. G., Barbat, A. H., Diaz, S. A., Vargas, Y., and Pinzón, L. A. (2018). Damage index for structures with elements of high flexural stiffness and/or brittle behavior. In *16th European Conference on Earthquake Engineering*, pages 1–12.

Hidalgo-Leiva, D. A., Pujades, L. G., Diaz, S. A., Barbat, A. H., and Gonzalez-Drigo, J. R. (2017). Orientation-Independent Measures of Ground Motion for a Database of Central America. In *16th World Conference on Earthquake Engineering, 16WCEE 2017*.

Housner, G. W. (1975). Measures of severity of earthquake ground shaking. In *Proc. U.S. Natl. Conf. Earthquake Eng.*, pages 25–33.

Huang, Y., Whittaker, A., and Luco, N. (2008). Maximum spectral demands in the near-fault region. *Earthquake Spectra*, 24:319–341.

Huang, Y.-N., Whittaker, A. S., and Luco, N. (2010). *Establishing maximum spectral demand for performance-based earthquake engineering: collaborative research with the University of Buffalo and the USGS*. US Geol. Surv. Tech. Rept.

Husid, L. R. (1969). Características de terremotos. Análisis general. *Revista del IDIEM*, 8(1):21–42.

Ibarra, L. F., Medina, R. A., and Krawinkler, H. (2005). Hysteretic models that incorporate strength and stiffness deterioration. *Earthquake Engineering and Structural Dynamics*, 34(12):1489–1511.

Jayaram, N., Lin, T., and Baker, J. W. (2011). A Computationally efficient ground-motion selection algorithm for matching a target response spectrum mean and variance. *Earthquake Spectra*, 27(3):797–815.

Jiménez, M. J., García-Fernández, M., Zonno, G., and Cella, F. (2000). Mapping soil effects in Barcelona, Spain, through an integrated GIS environment. *Soil Dynamics and Earthquake Engineering*, 19(4):289–301.

Kham, M., Semblat, J. F., Bard, P.-Y., and Dangla, P. (2006). Seismic site-city interaction: Main governing phenomena through simplified numerical models. *Bulletin of the Seismological Society of America*, 96(5):1934–1951.

Kobayashi, H., Vidal, F., Feriche, M. D., Samano, T., and Alguacil, G. (1996). Evaluation of Dynamic Behavior of Building Structures with Microtremors for Seismic Microzonation Mapping. In *11th World Conf. on Earthquake Engineering*, page Paper No. 1769, Acapulco, Mexico.

Kohrangi, M., Bazzurro, P., Vamvatsikos, D., and Spillatura, A. (2017). Conditional spectrum-based ground motion record selection using average spectral acceleration. *Earthquake Engineering & Structural Dynamics*, 46:1667–1685.

Kose, M. M. (2009). Parameters affecting the fundamental period of RC buildings with infill walls. *Engineering Structures*, 31(1):93–102.

Kostinakis, K. G., Athanatopoulou, A. M., and Morfidis, K. (2015). Correlation between ground motion intensity measures and seismic damage of 3D R/C buildings. *Engineering Structures*, 82:151–167.

Kostinakis, K. G., Manoukas, G. E., and Athanatopoulou, A. M. (2018). Influence of seismic incident angle on response of symmetric in plan buildings. *KSCE Journal of Civil Engineering*, 44:1919–1937.

Kostoglodov, V. and Pacheco, J. F. (1999). *One hundred years of seismicity in Mexico*. Inst. de Geofís., Univ. Nac. Autónoma de Mexico, Mexico City.

Krawinkler, H. (1978). Shear in beam-column joints in seismic design of steel frames. *Engineering Journal*, 15(3):82–91.

Kuo, C. H., Wen, K. L., Lin, C. M., Hsiao, N. C., and Chen, D. Y. (2018). Site amplifications and the effect on local magnitude determination at stations of the surface–downhole network in Taiwan. *Soil Dynamics and Earthquake Engineering*, 104(March 2017):106–116.

Kwon, O. S. and Kim, E. S. (2010). Evaluation of building period formulas for seismic design. *Earthquake engineering and structural dynamics*, 39:1569–1583.

Lagaros, N. D. (2010). The impact of the earthquake incident angle on the seismic loss estimation. *Engineering Structures*, 32:1577–1589.

Lantada, N., Irizarry, J., Barbat, A. H., Goula, X., Roca, A., Susagna, T., and Pujades, L. G. (2010). Seismic hazard and risk scenarios for Barcelona, Spain, using the Risk-UE vulnerability index method. *Bulletin of Earthquake Engineering*, 8(2):201–229.

Laurenzano, G., Priolo, E., Gallipoli, M. R., Mucciarelli, M., and Ponzo, F. C. (2010). Effect of vibrating buildings on free-field motion and on adjacent structures: The Bonefro (Italy) case history. *Bulletin of the Seismological Society of America*, 100(2):802–818.

Li, B., Cai, Z., Xie, W. C., and Pandey, M. (2018). Probabilistic seismic hazard analysis considering site-specific soil effects. *Soil Dynamics and Earthquake Engineering*, 105(November 2017):103–113.

Lignos, D. G. and Krawinkler, H. (2011). Deterioration Modeling of Steel Components in Support of Collapse Prediction of Steel Moment Frames under Earthquake Loading. *Journal of Structural Engineering*, 137(11):1291–1302.

Lignos, D. G. and Krawinkler, H. (2013). Development and Utilization of Structural Component Databases for Performance-Based Earthquake Engineering. *Journal of Structural Engineering*, 139(8):1382–1394.

Lo Presti, D. C., Lai, C. G., and Puci, I. (2006). ONDA: Computer Code for Nonlinear Seismic Response Analyses of Soil Deposits. *Journal of Geotechnical and Geoenvironmental Engineering*, 132(2):223–236.

Lucchini, A., Monti, G., and Kunnath, S. (2011). Nonlinear response of two-way asymmetric single-story building under biaxial excitation. *Journal of Structural Engineering*, 137(1):34–40.

Luzi, L., Pacor, F., and Puglia, R. (2016a). *Italian Accelerometric Archive v 2.1.* . Istituto Nazionale di Geofisica e Vulcanologia, Dipartimento della Protezione Civile Nazionale.

Luzi, L., Pacor, F., and Puglia, R. (2017). *Italian Accelerometric Archive v 2.2.* . Istituto Nazionale di Geofisica e Vulcanologia, Dipartimento della Protezione Civile Nazionale.

Luzi, L., Puglia, R., and Russo, E. (2016b). *Engineering Strong Motion Database, version 1.0.* Istituto Nazionale di Geofisica e Vulcanologia, Observatories Research Facilities for European Seismology.

Lysmer, J. and Kuhlemeyer, L. (1969). Finite dynamic model for infinite media. *J. of the Eng. Mech. Div.*, 95(4):859–878.

Macau, A., Benjumea, B., Gabàs, A., Figueras, S., and Vilà, M. (2015). The Effect of Shallow Quaternary Deposits on the Shape of the H/V Spectral Ratio. *Surveys in Geophysics*, 36(1):185–208.

Mackie, K. R., Cronin, K. J., and Nielson, B. G. (2011). Response sensitivity of highway bridges to randomly orientes multi-component earthquake excitation. *Journal of Earthquake Engineering*, 15(6):850–876.

Mánica, M. A., Ovando, E., and Botero, E. (2014). Assessment of damping models in FLAC. *Computers and Geotechnics*, 59:12–20.

Mánica, M. A., Ovando-Shelley, E., and Botero Jaramillo, E. (2016). Numerical study of the seismic behavior of rigid inclusions in soft Mexico City Clay. *Journal of Earthquake Engineering*, 20(3):447–475.

Matsushima, S., Kosaka, H., and Kawase, H. (2017). Directionally dependent horizontal-to-vertical spectral ratios of micrometers at Onahama, Fukushima, Japan. *Earth Planets Space*, 69:96.

Mejia, L. H. and Dawson, E. M. (2006). Earthquake deconvolution for FLAC. In *Forth iternational FLAC symposium*, Madrid.

Meli, R. and Faccioli, E. (1996). Seismic instrumentation of a tall building in México city. In *11th World Conf. on Earthquake Engineering*, page Paper No. 1422, Acapulco, Mexico.

Menglin, L., Haifeng, W., Cheng, X., and Yongmei, Z. (2011). Structure-soil-structure interaction: Literature review. *Soil Dynamics and Earthquake Engineering*, 31:1724–1731.

Mezcua, J., García Blanco, R. M., and Rueda, J. (2008). On the strong ground motion attenuation in Spain. *Bulletin of the Seismological Society of America*, 98(3):1343–1353.

Milutinovic, Z. V. and Trendafiloski, G. S. (2003). RISK-UE: an advanced approach to earthquake risk scenarios with applications to different European towns. WP04 Vulnerability of current buildings.

Mindlin, R. D. (1951). Influence of rotatory inertia and shear flexural motions of isotropic elastic plates. *J. Appl. Mech.*, 18:31–38.

Montero, W. (2001). Neotectónica De La Región Central De Costa Rica. *Revista Geologica de America Central*, 24:29–56.

Morfidis, K. and Kostinakis, K. (2017). Seismic parameters' combinations for the optimum prediction of the damage state of R/C buildings using neural networks. *Advances in Engineering Software*, 106:1–16.

Moya Fernández, A. (2006). Nuevo formato de datos para el Laboratorio de Ingeniería Sísmica del Instituto de Investigaciones en Ingeniería de la Universidad de Costa Rica. *Revista Ingeniería*, 16(2):63–74.

Moya Fernández, A. (2018). Accelerographic Monitoring System of the Earthquake Engineering Laboratory. *Revista Ingeniería*, 28(1):96–114.

Moya-Fernández, A., Pinzón, L. A., Schmidt-Díaz, V., Hidalgo-Leiva, D. A., and Pujades, L. G. (2020). A Strong-Motion Database of Costa Rica: 20 Years of Digital Records. *Seismological Research Letters*, under-review.

Muin, S. and Mosalam, K. M. (2017). Cumulative Absolute Velocity as a Local Damage Indicator of Instrumented Structures. *Earthquake Spectra*, 33(2):641–664.

Mylonakis, G., Gazetas, G., Nikolaou, S., and Michaelides, O. (2000). The role of soil on the collapse of 18 piers of the Hanshin expressway in the Kobe earthquake. In *12th World Conf. on Earthquake Engineering, Auckland, New Zealand, Paper Number 1074, 7 pp.*

Nagashima, F., Matsushima, S., Kawase, H., Sánchez-Sesma, F. J., Hayakawa, T., Satoh, T., and Oshima, M. (2014). Application of horizontal-to-vertical spectral ratios of earthquake ground motions to identify subsurface structures at and around the K-NET site in Tohoku, Japan. *Bulletin of the Seismological Society of America*, 104(5):2288–2302.

Nakamura, Y. (1989). A method for dynamic characteristics estimation of subsurface using microtremor on the ground surface. *Quarterly Report of the Railway Technical Reasearch Institute*, 30:25–33.

National Geophysical Data Center / World Data Service (NGDC/WDS) (2018). Significant Earthquake Database. National Geophysical Data Center, NOAA.

Navarro, M., García-Jerez, A., Alcalá, F. J., Vidal, F., and Enomoto, T. (2014). Local site effect microzonation of Lorca town (SE Spain). *Bulletin of Earthquake Engineering*, 12(5):1933–1959.

NCSE-02 (2009). *Norma de Construcción Sismorresistente: Parte general y edificación.*

Nguyen, V. T. and Kim, D. (2013). Influence of incident angles of earthquakes on inelastic responses of asymmetric-plan structures. *Structural Engineering and Mechanics*, 45(3):373–389.

Nigam, N. C. and Jennings, P. C. (1969). Calculation of response spectra from strong-motion earthquake records. *Bulletin of the Seismological Society of America*, 59:909–922.

NIST-GCR-12-917-21 (2012). *Soil-Structure Interaction for Building Structures*. NEHRP consultants Joint Venture and National Institute of Standards and Technology, U.S. Department of Commerce, 292 pp.

Norabuena, E., Dixon, T. H., Schwartz, S., DeShon, H., Newman, A., Protti, M., Gonzalez, V., Dorman, L. R., Flueh, E. R., Lundgren, P., Pollitz, F., and Sampson, D. (2004). Geodetic and seismic constraints on some seismogenic zone processes in Costa Rica. *Journal of Geophysical Research: Solid Earth*, 109(11):1–25.

NTCDS-RCDF (2004). *Normas Técnicas Complementarias para el Diseño por Sismo*. Government of Mexico City, Mexico City.

NTCDS-RCDF (2017). *Normas Técnicas Complementarias para el Diseño por Sismo*. Government of Mexico City, Mexico City.

Pacor, F., Paolucci, R., Ameri, G., Massa, M., and Puglia, R. (2011). Italian strong motion records in ITACA: overview and record processing. *Bulletin of Earthquake Engineering*, 9:1741–1759.

Park, Y. and Ang, A. H. (1985). Mechanistic Seismic Damage Model for Reinforced Concrete. *Journal of Structural Engineering*, 111(4):722–739.

Park, Y. J., Ang, A. H., and Wen, Y. K. (1987). Damage-Limiting Aseismic Design of Buildings. *Earthquake Spectra*, 3(1):1–26.

Paz, M. and Leigh, W. (2003). *Structural Dynamics: Theory And Computation*.

PEER (2015). *NGA- East: Median ground-motion models for the central and eastern North America region, PEER 2015/04*. Pacific Earthquake Engineering Research Center, Berkeley, California, 351 pp.

Pinzón, L. A. (2014). *Evaluación de medidas de intensidad del movimiento del suelo independientes de la orientación del sensor para una base de datos con acelerogramas de Costa Rica, El Salvador y Nicaragua*. Universitat Politècnica de Catalunya. Retrieved from http://upcommons.upc.edu/pfc/handle/2099.1/24352.

Pinzón, L. A., Diaz, S. A., Pujades, L. G., and Vargas, Y. F. (2019a). An efficient method for considering the directionality effect of earthquakes on structures. *Journal of Earthquake Engineering*, in-press(0):1–30.

Pinzón, L. A., Mánica, M. A., Pujades, L. G., and Alva, R. E. (2019b). A simplified approach to account for directionality effects on 2D dynamic soil-structure interaction analysis. In Silvestri, F. and Moraci, N., editors, *Earthquake Geotechnical Engineering for Protection and Development of Environment and Constructions*, pages 4490–4497, Rome, Italy. CRC Press, Taylor & Francis Group.

Pinzón, L. A., Mánica, M. A., Pujades, L. G., and Alva, R. E. (2020a). Dynamic soil-structure interaction analyses considering directionality effects. *Soil Dynamics and Earthquake Engineering*, 130:106009.

Pinzón, L. A., Pujades, L. G., Diaz, S. A., and Alva, R. E. (2018a). Do Directionality Effects Influence Expected Damage? A Case Study of the 2017 Central Mexico Earthquake. *Bulletin of the Seismological Society of America*, 108(5A):2543–2555.

Pinzón, L. A., Pujades, L. G., Diaz, S. A., and Alva, R. E. (2020b). Reply to " Comment on ' Do Directionality Effects Influence Expected Damage ? A Case Study of the 2017 Central Mexico Earthquake ' by Luis A. Pinzón, Luis G. Pujades, Sergio A. Diaz, and Rodrigo E. Alva" by Eduardo Reinoso, Pablo Quinde, Danny Arroyo, Mar. *Bulletin of the Seismological Society of America*, 110(1):393–396.

Pinzón, L. A., Pujades, L. G., Hidalgo-Leiva, D. A., and Diaz, S. A. (2018b). Directionality models from ground motions of Italy. *Ingegneria Sismica*, 35(3):43–63.

Pinzón, L. A., Pujades, L. G., Macau, A., Carreño, E., and Alcalde, J. M. (2019c). Seismic Site Classification from the Horizontal-to-Vertical Response Spectral Ratios: Use of the Spanish Strong-Motion Database. *Geosciences*, 9(7):294.

Pinzón, L. A., Pujades, L. G., Macau, A., and Figueras, S. (2019d). Increased seismic hazard in Barcelona (Spain) due to soil-building resonance effects. *Soil Dynamics and Earthquake Engineering*, 117:245–250.

Pinzón, L. A., Vargas-Alzate, Y. F., Pujades, L. G., and Diaz, S. A. (2020c). A drift-correlated ground motion intensity measure: application to steel frame buildings. *Soil Dynamics and Earthquake Engineering*, 132:106096.

Power, M., Chiou, B. S. J., Abrahamson, N. A., Bozorgnia, Y., Shantz, T., and Roblee, C. (2008). An overview of the NGA project. *Earthquake Spectra*, 24(1):3–21.

Pujades, L. G., Vargas-Alzate, Y. F., Barbat, A. H., and González-Drigo, J. R. (2015). Parametric model for capacity curves. *Bulletin of Earthquake Engineering*, 13(5):1347–1376.

Quintero, R. and Güendel, F. (2000). Stress field in Costa Rica, Central America. *Journal of Seismology*, 4(3):297–319.

Raghunandan, M., Liel, A. B., and Luco, N. (2015). Aftershock collapse vulnerability assessment of reinforced concrete frame structures. *Earthquake Engineering and Structural Dynamics*, 44:419–439.

Reed, J. W. and Kassawara, R. P. (1990). A criterion for determining exceedance of the Operating Basis Earthquake. *Nucl. Eng. Des.*, 123(2-3):387–396.

Reinoso, E., Quinde, P., Arroyo, D., Ordaz, M., and Terán-Gilmore, A. (2020). Comment on "Do Directionality Effects Influence Expected Damage? A Case Study of the 2017 Central Mexico Earthquake" by Luis A. Pinzón, Luis G. Pujades, Sergio A. Díaz, and Rodrigo E. Alva. *Bulletin of the Seismological Society of America*, 110(1):387–392.

Rigato, A. B. and Medina, R. A. (2007). Influence of angle of incidence on seismic demands for inelastic single-storey structures subjected to bi-directional ground motions. *Engineering Structures*, 29(10):2593–2601.

SAC (1996). Analytical and Field Investigations of Buildings Affected by the Northridge Earthquake of January 17, 1994. Technical report, Report No. SAC-95-04.

Sáez, E., Lopez-Caballero, F., and Modaressi-Farahmand-Razavi, A. (2013). Inelastic dynamic soil-structure interaction effects on moment-resisting frame buildings. *Engineering Structures*, 51:166–177.

Santos-Assuncao, S., Perez-Gracia, V., Salinas, V., Caselles, J. O., González-Drigo, J. R., Pujades, L. G., and Lantada, N. (2016). GPR Backscattering Intensity Analysis Applied to Detect Paleochannels and Infilled Streams for Seismic Nanozonation in Urban Environments. *IEEE Journal of Selected Topics in Applied Earth Observations and Remote Sensing*, 9(1):167–177.

Sarma, S. K. (1971). Energy flux of strong earthquakes. *Tectonophysics*, 11(3):159–172.

Sarma, S. K. and Yang, K. S. (1987). An evaluation of strong motion records and a new parameter A95. *Earthquake Engineering and Structural Dynamics*, 15:119–132.

Schmidt-Díaz, V. (2011). Soil classification based on spectral ratios where Central American accelerographic stations are located. Cases of El Salvador, Nicaragua and Costa Rica. *Revista Geológica de América Central*, (44):9–26.

Schmidt-Díaz, V. (2014). Ground motion prediction models for Central America using data from 1972 to 2010. *Revista Geológica de América Central*, 50:7–37.

Schnabel, P. B., Lysmer, J., and Seed, B. H. (1972). SHAKE, a computer program for earthquake response analysis of horizontal layered sites. Technical report, Earthquake Engineering Reserach Center, University of California, Berkeley.

Seifried, A. (2013). *Response spectrum compatibilization and its impact on structural response assessment. Ph.D. Thesis.* PhD thesis, Stanford University, Stanford, CA.

Seismosoft (2018). SeismoSignal - A computer program for signal processing of time-histories.

Semblat, J. F., Kham, M., and Bard, P.-Y. (2008). Seismic-wave propagation in alluvial basins and influence of site-city interaction. *Bulletin of the Seismological Society of America*, 98(6):2665–2678.

Semblat, J. F., Kham, M., Bard, P.-Y., and Guéguen, P. (2004). Could "site-city interaction" modify site effects in urban areas? In *13th World Conf. on earthquake engineering.*

Semblat, J. F., Kham, M., Guéguen, P., Bard, P.-Y., and Duval, M. (2002). Site-city interaction through modification of site effects. In *EERI, 7th US Conf. on Earthquake Engineering.*

Shahi, S. K. and Baker, J. W. (2014). *NGA-West2 models for ground-motion directionality. PEER 2013/10.* . Pacific Earhquake Engineering Research Center, Berkeley, California. 73 pp.

Shrivastava, M. N., González, G., Moreno, M., Reddy, C., Salazar, P., Yáñez, G., González, J., de la Llera, J. C., and Báez, J. C. (2016). Coseismic and Afterslip of the Mw 8.3 Illapel Earthquake 2015 from Continuous GPS data. *Geophysical Research Letters*, 43:10710—-10719.

Singaucho, J. C., Aurore, L., Viracucha, C., and Ruiz, M. (2016). Observaciones del sismo del 16 de abril de 2016 de magnitud Mw 7.8. Intensidades y aceleraciones. *Informe de referencia de datos RENAC*, (1):1–20.

Singh, S. K., Mena, E., and Castro, R. (1988). Some aspects of source characteristics of the 19 September 1985 Michoacan earthquake and ground motion amplification in and near Mexico City from strong motion data. *Bulletin of the Seismological Society of America*, 78(2):451–477.

Soltanieh, S., Memarpour, M. M., and Kilanehei, F. (2019). Performance assessment of bridge-soil-foundation system with irregular configuration considering ground motion directionality effects. *Soil Dynamics and Earthquake Engineering*, 118(July 2017):19–34.

Spudich, B. P., Chiou, B., Graves, R., Collins, N., and Somerville, P. (2004). *A Formulation of Directivity for Earthquake Sources Using Isochrone Theory*. U.S. Geol. Surv. Open-File Rept. 2004-1268, 54 pp.

Stanko, D., Markušić, S., Strelec, S., and Gazdek, M. (2017). HVSR analysis of seismic site effects and soil-structure resonance in Varaždin city (North Croatia). *Soil Dynamics and Earthquake Engineering*, 92(October 2016):666–677.

Steidl, J. H. (2000). Site response in southern California for probabilistic seismic hazard analysis. *Bulletin of the Seismological Society of America*, 90(6):149–169.

Stewart, J. P., Abrahamson, N. A., Atkinson, G. M., Baker, J. W., Boore, D. M., Bozorgnia, Y., Campbell, K. W., Comartin, C. D., Idriss, I. M., Lew, M., Mehrain, M., Moehle, J. P., Naeim, F., and Sabol, T. A. (2011). Representation of bidirectional ground motions for design spectra in building codes. *Earthquake Spectra*, 27(3):927–937.

Sucuoglu, H. and Erberik, A. (1997). Performance evaluation of a three-storey unreinforced masonry building during the 1992 Erzincan earthquake. *Earthquake Engineering Structural Dynamics*, 26(3):319–336.

Sucuoğlu, H. and Nurtuğ, A. (1995). Earthquake ground motion characteristics and seismic energy dissipation. *Earthquake Engineering & Structural Dynamics*, 24(9):1195–1213.

Tabatabaiefar, H. R. and Fatahi, B. (2014). Idealisation of soil-structure system to determine inelastic seismic response of mid-rise building frames. *Soil Dynamics and Earthquake Engineering*, 66:339–351.

Tabatabaiefar, H. R., Fatahi, B., Ghabraie, K., and Zhou, W.-H. (2015). Evaluation of numerical procedures to determine seismic response of structures under influence of soil-structure interaction. *Structural Engineering and Mechanics*, 56(1):27–47.

Tarquis, F. and Roesset, J. (1988). Structural response and design response spectra for the 1985 Mexico City earthquake. Technical report, University of Texas, Austin, Texas.

The MathWorks (2017). MATLAB and Statistics Toolbox Release 2016b,The MathWorks, Inc.,Natick, Massachusetts, United States.

Theophilou, A. A. I., Chryssanthopoulos, M. K., and Kappos, A. J. (2017). A vector-valued ground motion intensity measure incorporating normalized spectral area. *Bulletin of Earthquake Engineering*, 15(1):249–270.

Thusoo, S., Modi, K., Kumar, R., and Madarhar, H. (2015). Response of buildings with soil-structure interaction with varying soil types. *Int. J. Civil Environ. Eng.*, 9(4):414–418.

Torbol, M. and Shinozuka, M. (2014). The directionality effect in the seismic risk assessment of highway networks. *Structure and Infrastructure Engineering*, 10:175–188.

Torkamani, M. A. M. and Ahmadi, A. K. (1988). Stiffness Identification of a Tall Building During Construction Period Using Ambient Tests. *Earthquake Engineering and Structural Dynamics*, 16:1177–1188.

Trifunac, M. D. and Brady, A. G. (1975). A study on the duration of strong earthquake ground motion. *Bulletin of the Seismological Society of America*, 65(3):581–626.

Tso, W. K., Zhu, T. J., and Heidebrecht, A. C. (1992). Engineering implication of ground motion A/V ratio. *Soil Dynamics and Earthquake Engineering*, 11(3):133–144.

Tuladhar, R., Maki, T., and Mutsuyoshi, H. (2008). Cyclic behavior of laterally loaded concrete piles embedded into cohesive soil. *Earthquake Engineering Structural Dynamics*, 37:43–59.

Vargas, Y. F., Pujades, L. G., González-Drigo, J. R., Alva, R. E., and Pinzón, L. A. (2019). On the Equal Displacement Aproximation for Mid-Rise Reinforced Concrete Buildings. *COMPDYN 2019: 7th International Conference on Computational Methods in Structural Dynamics and Earthquake Engineering*, pages 5490–5502.

Vargas-Alzate, Y. F. (2020). KaIROS Project. Keeping and Increasing Resilience Opportunities and Sustainability of communities against earthquakes. https://cordis.europa.eu/project/rcn/215743/factsheet/en.

Vargas-Alzate, Y. F., Pujades, L. G., Barbat, A. H., Hurtado, J. E., Diaz, S. A., and Hidalgo-Leiva, D. A. (2018). Probabilistic seismic damage assessment of reinforced concrete buildings considering directionality effects. *Structure and Infrastructure Engineering*, 14(6):817–829.

Ventayol, A., Albaiges, J. M., Cortal, J. M., Gallart, F., López, C., López, J., and Santaularia, J. (1978). *Mapa Geotécnico de Barcelona*. LOSAN, Barcelona.

Vigny, C., Socquet, A., Peyrat, S., Ruegg, J.-C., Métois, M., Madariaga, R., Morvan, S., Lancieri, M., Lacassin, R., Campos, J., Carrizo, D., Bejar-Pizarro, M., Barrientos, S., Armijo, R., Aranda, C., Valderas-Bermejo, M.-C., Ortega, I., Bondoux, F., Baize, S., Lyon-Caen, H., Pavez, A., Vilotte, J. P., Bevis, M., Brooks, B., Smalley, R., Parra, H., Baez, J.-C., Blanco, M., Cimbaro, S., and Kendrick, E. (2011). The 2010 Mw 8.8 Maule Megathrust Earthquake of Central Chile, Monitored by GPS. *Science*, 330(6036):1417–1422.

Wald, D. J. and Allen, T. I. (2007). Topographic slope as a proxy for seismic site conditions and amplification. *Bulletin of the Seismological Society of America*, 97(5):1379–1395.

Watson-Lamprey, J. and Boore, D. M. (2007). Beyond SaGMRotI: Conversion to SaArb, SaSN, and SaMaxRot. *Bulletin of the Seismological Society of America*, 107(5):1511–1524.

Wu, Y., Yan, X., and Qi, A. (2017). Deformation, damage, and collapse of phyllite tunnels under strong earthquake dynamic actions. *Ingegneria Sismica*, 34(2):31–48.

Ye, L., Kanamori, H., Avouac, J. P., Li, L., Cheung, K. F., and Lay, T. (2016). The 16 April 2016, MW 7.8 (MS 7.5) Ecuador earthquake: A quasi-repeat of the 1942 MS 7.5 earthquake and partial re-rupture of the 1906 MS 8.6 Colombia–Ecuador earthquake. *Earth and Planetary Science Letters*, 454(April):248–258.

Zhao, J. X., Irikura, K., Zhang, J., Fukushima, Y., Somerville, P. G., Asano, A., Ohno, Y., Oouchi, T., Takahashi, T., and Ogawa, H. (2006). An empirical site-classification method for strong-motion stations in Japan using H/V response spectral ratio. *Bulletin of the Seismological Society of America*, 96(3):914–925.

Zhou, Y. and Li, M. (2015). An area-based intensity measure for incremental dynamic analysis. *Journal of Asian Architecture and Building Engineering*, 14(2):451–457.

Zienkiewicz, O. C., Bicanic, N., and Shen, F. Q. (1988). Earthquake input definition and the transmitting boundary conditions. In Doltsinis, I. S., editor, *Advances in Computational Nonlinear Mechanics.*, chapter 3, pages 109–138. International Centre for Mechanical Sciences (Courses and Lectures), Springer, Vienna.

A Appendix. Chapter 4 tables.

The results obtained for the 20 non-scaled dynamic analyses are shown in tables A1, A2, A3, A4, A5, A6, A7 and A8.

Table A1: Regular building results; roof displacements (δ) in X-Direction summary results for the 20 ground motion pairs selected from the ITACA database.

Roof Displacement (δ) X-Direction [cm]					
#	as-recorded	Median (CRM)	50th Perc. (PPM)	Max. (CRM)	100th Perc. (PPM)
1	11.84	11.47	11.96	15.32	15.66
2	17.37	16.25	16.10	17.40	17.83
3	0.92	0.80	0.84	0.96	1.06
4	3.04	2.92	2.96	3.85	3.95
5	3.53	3.51	3.70	4.16	4.19
6	11.13	8.72	8.91	11.14	11.68
7	15.39	13.51	13.97	15.86	16.38
8	1.13	1.09	0.97	1.31	1.29
9	2.90	2.20	2.42	2.94	2.97
10	2.53	2.01	2.03	2.55	2.61
11	2.94	2.87	3.00	3.49	3.58
12	2.17	1.81	2.04	2.30	2.46
13	0.16	0.16	0.17	0.21	0.22
14	3.17	2.96	2.87	3.53	3.73
15	3.18	3.01	2.95	3.35	3.46
16	0.30	0.28	0.28	0.33	0.34
17	2.90	2.16	2.19	2.99	3.03
18	2.18	1.73	1.72	2.19	2.11
19	2.25	1.94	2.11	2.47	2.78
20	0.44	0.36	0.37	0.47	0.48

Table A2: Regular building results; roof displacements (δ) in Y-Direction summary results for the 20 ground motion pairs selected from the ITACA database.

Roof Displacement (δ) Y-Direction [cm]					
#	as-recorded	Median (CRM)	50th Perc. (PPM)	Max. (CRM)	100th Perc. (PPM)
1	11.64	11.00	12.04	15.48	15.71
2	6.71	5.00	5.15	6.89	7.23
3	1.22	1.14	1.18	1.22	1.34
4	2.27	2.24	2.49	2.97	3.20
5	2.85	2.52	2.57	2.97	2.96
6	13.67	11.65	11.68	13.72	14.24
7	16.77	15.22	15.77	17.23	17.72
8	1.00	0.85	0.82	1.04	1.04
9	2.02	1.60	1.52	2.03	2.11
10	2.17	2.15	2.21	2.37	2.53
11	3.41	3.27	3.25	3.50	3.61
12	3.57	3.19	3.22	3.58	3.61
13	0.29	0.22	0.23	0.29	0.29
14	3.64	3.09	3.23	3.73	3.86
15	5.76	4.49	4.38	5.79	5.90
16	0.35	0.29	0.29	0.39	0.41
17	2.98	2.29	2.40	3.20	3.34
18	2.01	1.54	1.67	2.06	2.42
19	2.04	1.96	2.05	2.37	2.64
20	0.51	0.39	0.41	0.52	0.52

Table A3: Regular building results; base shear (V_B) in X-Direction summary results for the 20 ground motion pairs selected from the ITACA database.

Base Shear (V_B) X-Direction [kN]					
#	as-recorded	Median (CRM)	50th Perc. (PPM)	Max. (CRM)	100th Perc. (PPM)
1	6163	5995	5309	7442	7058
2	7575	7282	7267	7587	7770
3	458	402	396	518	502
4	1639	1639	1690	2104	2267
5	1672	1550	1702	1878	1982
6	5639	4427	4731	5813	5828
7	6840	5825	6101	7142	7077
8	1115	1001	967	1374	1248
9	1743	1348	1482	1746	1984
10	1156	993	957	1256	1296
11	1320	1280	1334	1539	1651
12	999	968	1000	1021	1258
13	106	103	128	118	156
14	1600	1637	1790	1768	2011
15	1716	1523	1641	1719	1780
16	135	127	135	151	155
17	1588	1298	1487	1848	2080
18	1892	1402	1396	1902	1863
19	1337	1070	1210	1373	1601
20	213	185	195	224	252

Table A4: Regular building results; base shear (V_B) in Y-Direction summary results for the 20 ground motion pairs selected from the ITACA database.

Base Shear (V_B) Y-Direction [kN]					
#	as-recorded	Median (CRM)	50th Perc. (PPM)	Max. (CRM)	100th Perc. (PPM)
1	4070	4018	4137	5254	5376
2	2299	1858	1829	2397	2513
3	481	420	477	501	529
4	1093	1075	1061	1379	1390
5	975	813	925	1016	1076
6	4687	4118	4048	4699	4729
7	5865	5105	5321	5905	5903
8	679	534	524	732	737
9	1756	1319	1319	1760	1762
10	875	831	877	929	1028
11	1153	1077	1113	1174	1193
12	1206	1165	1155	1292	1251
13	137	131	130	153	164
14	1495	1368	1330	1713	1597
15	2226	1576	1711	2225	2311
16	135	107	110	150	148
17	988	866	956	1082	1327
18	1325	1074	1046	1315	1441
19	851	789	787	876	1061
20	170	136	145	180	187

Table A5: Irregular building results; roof displacements (δ) in X-Direction summary results for the 20 ground motion pairs selected from the ITACA database.

Roof Displacement (δ) X-Direction [cm]					
#	as-recorded	Median (CRM)	50th Perc. (PPM)	Max. (CRM)	100th Perc. (PPM)
1	11.54	11.59	12.04	15.94	15.50
2	16.88	15.29	15.56	16.89	16.88
3	1.08	0.96	0.94	1.13	1.21
4	2.95	3.01	3.02	4.10	4.59
5	3.48	4.29	4.39	5.72	5.67
6	12.09	9.33	8.63	12.10	12.09
7	14.24	13.76	13.71	14.65	15.87
8	1.16	1.23	1.28	1.46	1.35
9	3.72	3.03	2.82	3.74	3.72
10	2.25	1.89	1.99	2.40	2.54
11	3.65	3.23	3.36	3.90	4.06
12	1.75	1.86	1.87	2.49	2.39
13	0.13	0.20	0.18	0.25	0.21
14	3.36	3.18	3.10	4.02	4.29
15	3.16	3.23	3.15	3.80	3.53
16	0.24	0.33	0.31	0.43	0.42
17	1.44	2.40	2.35	3.06	2.93
18	2.75	1.99	2.03	2.76	2.81
19	2.53	2.30	2.21	2.94	2.85
20	0.45	0.38	0.37	0.49	0.47

Table A6: Irregular building results; roof displacements (δ) in Y-Direction summary results for the 20 ground motion pairs selected from the ITACA database.

Roof Displacement (δ) Y-Direction [cm]					
#	as-recorded	Median (CRM)	50th Perc. (PPM)	Max. (CRM)	100th Perc. (PPM)
1	8.50	8.87	8.74	11.19	11.29
2	4.97	5.04	5.15	6.47	6.76
3	0.86	0.92	0.99	1.29	1.30
4	1.97	2.45	2.59	3.25	3.14
5	2.40	2.12	2.07	2.42	2.77
6	8.92	9.13	8.97	9.75	11.54
7	10.16	11.32	10.54	13.23	13.46
8	0.99	0.88	0.85	1.01	0.99
9	1.13	1.75	1.48	2.19	1.97
10	2.20	1.88	1.88	2.37	2.41
11	2.71	3.07	2.83	3.44	3.59
12	2.57	2.43	2.42	2.62	2.59
13	0.16	0.20	0.23	0.23	0.28
14	2.19	2.55	2.72	3.02	3.04
15	3.36	4.13	4.57	5.87	6.06
16	0.26	0.30	0.32	0.32	0.32
17	2.14	1.78	1.74	2.38	2.41
18	1.55	1.76	1.82	2.13	1.96
19	1.71	1.82	1.77	2.26	2.06
20	0.34	0.36	0.34	0.47	0.44

Table A7: Irregular building results; base shear (V_B) in X-Direction summary results for the 20 ground motion pairs selected from the ITACA database.

Base Shear (V_B) X-Direction [kN]					
#	as-recorded	Median (CRM)	50th Perc. (PPM)	Max. (CRM)	100th Perc. (PPM)
1	7187	7481	7297	10298	9690
2	9882	9443	9317	10260	9882
3	835	711	722	913	895
4	2965	3126	3158	4367	4482
5	2254	2487	2584	3396	3373
6	8575	7410	6854	8934	8575
7	8402	8220	7877	9575	9644
8	2670	2663	2154	2785	2670
9	3830	3190	2887	3832	3830
10	1536	1542	1451	2029	1907
11	2125	1859	2025	2302	2484
12	1186	1191	1235	1476	1443
13	379	309	302	410	395
14	4308	3818	3838	4733	5001
15	2543	2465	2153	2706	2584
16	254	276	280	303	302
17	1994	2216	2147	2582	2996
18	4042	3418	2579	4044	4042
19	2651	2223	1870	2791	2506
20	388	332	344	412	450

Table A8: Irregular building results; base shear (V_B) in Y-Direction summary results for the 20 ground motion pairs selected from the ITACA database.

	Base Shear (V_B) Y-Direction [kN]				
#	as-recorded	Median (CRM)	50th Perc. (PPM)	Max. (CRM)	100th Perc. (PPM)
1	3898	4560	4135	5114	5533
2	2346	2346	2338	3140	3018
3	627	588	568	711	716
4	1952	1936	1646	2127	2113
5	1280	1126	938	1280	1205
6	3538	4111	3967	4540	5087
7	4358	4480	4697	5375	5628
8	1679	1399	1069	1888	1679
9	2639	2834	2316	3627	3072
10	955	964	939	1128	1127
11	853	989	1027	1121	1254
12	1161	1092	1052	1187	1194
13	192	310	293	371	361
14	3124	2675	2857	3143	3492
15	1392	1845	1904	2073	2246
16	190	170	144	197	190
17	997	991	904	1184	1244
18	2290	2638	2467	3576	3219
19	1251	1226	1071	1347	1425
20	194	216	195	265	260

B Appendix. A simplified approach to account for directionality effects on 2D dynamic soil-structure interaction analysis

Based on the published conference article: Pinzón, L. A., Mánica, M. A., Pujades, L. G., & Alva, R. E. (2019). A simplified approach to account for directionality effects on 2D dynamic soil-structure interaction analysis. In *7th International Conference on Earthquake Geotechnical Engineering*, Rome, Italy.

B.1 Abstract

In this study, a simplified approach to account for directionality effects on two-dimensional (2D) dynamic soil-structure interaction analyses (DSSI) is proposed. When an earthquake is recorded, the direction with the maximum intensities rarely corresponds with the orientation of accelerometers and, therefore, the maximum response of a system generally takes place at an intermediate unknown orientation. A straightforward approach is to perform DSSI analyses with a number of linear combinations of the horizontal as-recorded components to obtain the peak response parameters for each orientation. Nevertheless, DSSI analyses are computationally expensive especially when the non-linear behavior of the soil is considered. Here, three hypotheses are evaluated for predicting the angle that generates the maximum response of a building. By determining this angle in advance, only one DSSI analysis would be required to obtain the maximum response of a system for a given earthquake. Here, a particular case is analyzed where a ground motion recorded at a rock outcrop is used to derive the input motion for a finite element model, including a soil deposit and a surface structure. A series of 2D dynamic finite element analyses were performed to assess the proposed approach where input motions were obtained from the linear combination of the horizontal as-recorded components of the 1976 Friuli earthquake. The obtained results show the importance of considering directionality effects in DSSI analyses. The maximum response of the system was reasonably captured with the orientation obtained through the simplified approach.

B.2 Introduction

Existing guidelines consider as-recorded components of an earthquake as input motions for 2D DSSI analyses. Earthquakes' ground-motion are recorded in three orthogonal components: two horizontal (normally N-S and E-W) and one vertical. However, the orientation of recording accelerometers rarely captures the maximum intensities and, therefore, the maximum response of a system generally takes place at an intermediate unknown orientation.

Figure B1 shows (a) the acceleration time histories, (b) the response spectra from the linear combination of the horizontal components (from 0^o to 180^o with increments of 1^o, see Equation 38 below), and (c) the acceleration hodogram from the 1976 Friuli earthquake (Italy). It can be observed that the E-W component shows larger spectral accelerations (for most periods) compared to the N-S, but it lies below the envelope of the spectra from the rotated histories, RotD100 (Boore, 2010). This fact is known as part of the directionality effect of strong motion recordings, and it is nowadays considered in ground-motion prediction equations (GMPEs) (Pinzón et al., 2018b) or in the performance of structures (Vargas-Alzate, 2020; Pinzón et al., 2020a).

An approach to deal with this issue would be to perform DSSI analyses with a number of linear combinations of the two horizontal as-recorded components to obtain the peak response parameters. Nevertheless, DSSI analyses are computationally expensive especially when the nonlinear behavior of the soil is being considered.

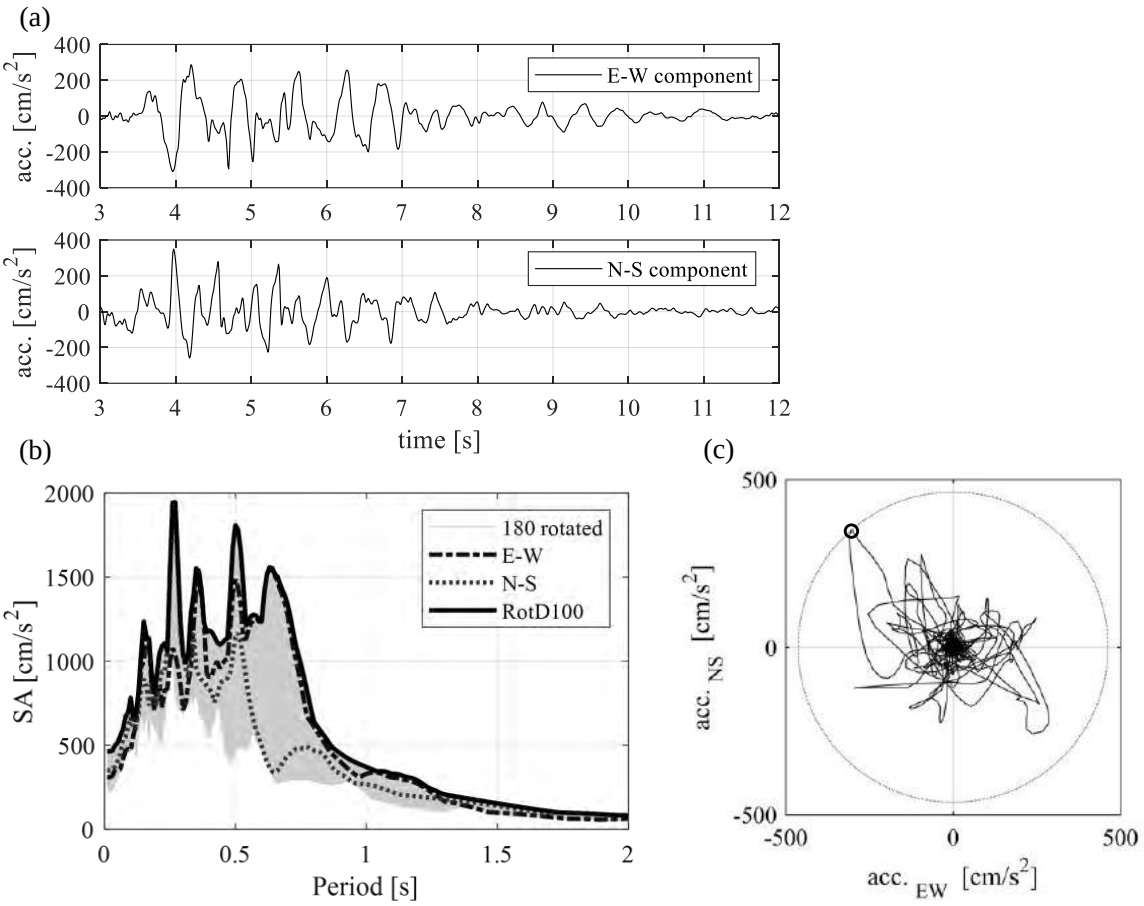

Figure B1: Friuli earthquake with moment magnitude (M_W) = 6.5, recorded at TLM1 station on May 6, 1976. (a) Ground motion horizontal components from Ambraseys *et al.* (2000) database, (b) response spectra from the as-recorded and rotated histories and the RotD100 response spectrum, and (c) acceleration hodogram.

A simplified approach is pursued in this study, where three hypotheses are evaluated to predict the angle that generates the maximum response of a building in a 2D DSSI analysis. These hypotheses are (1) the angle that generates the maximum Arias intensity of the signal (Arias, 1970), (2) the angle where the maximum ground acceleration occurs, and (3) the angle that makes the response spectrum closest to RotD100. The main goal is to identify in advance the incidence angle that produces the maximum response of a system for a given earthquake and, therefore, to perform only one DSSI analysis including directionality effects.

Here, we address the specific problem where accelerograms recorded at a rock outcrop are employed to derive the input motion for a finite element model, including the soil deposit and a surface structure. To assess the proposed hypotheses, a series of 2D dynamic finite element analyses were performed using PLAXIS 2D (Brinkgreve et al., 2017). Input motions were derived from the linear combination of the horizontal as-recorded components of the 1976 Friuli earthquake (from 1° to 180° with increments of 2°). The structure at the surface is a 4-story steel frame building rigidly connected to a concrete raft foundation. The soil deposit corresponds to a 30 m deep medium to dense sandy layer, overlying a bedrock.

B.3 Methodology

B.3.1 Complete rotational approach (CRA)

In this method, a series of DSSI analyses are performed with the rotated horizontal ground motions of an accelerogram (the vertical component is neglected). Increments of 1° are usually employed in the range of 0° and 180°. Thus, 180 dynamic analyses per ground motion pairs need to be performed. In this way, the distribution of any output variable with respect to the incidence angle can be obtained allowing us to estimate the maximum response of a system for a given earthquake. The CRA can be summarized as follow:

STEP 1. Soil-structure interaction (SSI) model
2D modelling of the soil-building system.

STEP 2. Seismic action
Two as recorded orthogonal horizontal acceleration time histories are selected and rotated. The first calculation will be performed for one of the as recorded components, i.e. $\theta = 0$ (see Equation 38 below).

STEP 3. DSSI analysis
Perform the non-linear dynamic analysis for the selected seismic action.

STEP 4. Repeat 2 and 3
Steps 2 and 3 are repeated with increments of 1° in the range of 0° to 180°. Increments can be enlarged to reduce the number of analyses.

The rotated horizontal component accrot (t, θ) is derived through the linear combination of the two as-recorded histories, as a function of the rotational angle θ, using the following equation:

$$acc_{rot}(t,\theta) = acc_1(t) \cdot cos\theta + acc_2(t) \cdot sin\theta \tag{38}$$

where acc_1 and acc_2 are the two as-recorded horizontal components.

As a result, relationships between several output variables (e.g. roof displacement or base shear) can be obtained as functions of the rotation angle θ. However, this method entails high computational costs, and it would be of practical interest to develop a simplified approach allowing the determination of peak parameters with fewer computational resources.

B.3.2 Simplified rotational approach (SRA)

Here, a simplified approach is sought for the prediction of the orientation producing the peak response of the system. By deriving this angle in advance, only one DSSI analysis is required for a given earthquake compared to the 180 analyses needed in the former approach (if increments of 1° are employed). Three different hypotheses are evaluated: (1) the angle that generates the maximum Arias intensity of the signal (Arias, 1970), (2) the angle where the maximum ground acceleration (PGA) occurs, and (3) the angle that makes the response spectrum closest to the RotD100 spectrum.

The Arias Intensity (AI) is a measure of the severity of a ground motion and represents the total energy per unit weight stored by a set of undamped simple oscillators through an earthquake (Arias, 1970). The AI for a given rotated motion is defined in the following way:

$$AI(\theta) = \frac{\pi}{2g} \int_0^{t_f} acc_{rot}^2(t,\theta)dt \tag{39}$$

where g is the acceleration due to gravity and t_f is the total duration of the record.

The AI is estimated for each rotated signal. According to this hypothesis, the rotation angle producing the maximum AI will generate the maximum response of the system.

As seen in the hodogram (Figure B1c), the acceleration direction of a ground motion varies in the horizontal plane. Therefore, for a given time, the maximum acceleration generally occurs at an orientation different from those of the recording accelerometer. By deriving the peak ground acceleration for each of the rotated motions, a PGA as a function of the rotation angle can be defined (PGA_{rot}), computed in the following way:

$$PGA_{rot}(\theta) = max|acc_{rot}(t,\theta)| \quad for \quad \theta = [0 \;\; 180) \tag{40}$$

According to this hypothesis, the rotation angle producing the maximum PGA_{rot} will generate the maximum response of the system.

The third hypothesis is based on the maximum response spectrum. The aim is to find the angle that generates spectral accelerations closest to the RotD100 spectrum within a given range of vibration periods, related with the fundamental period of the system. The two acceleration components are combined using Equation 38 with increments of 1° in the range of 0 and 180°. Because the response spectrum is defined as the maximum absolute amplitude of a single degree of freedom damped oscillator, this measure has a periodicity of 180°. The spectrum for a given rotated motion (SA_{rot}) is estimated as shown in Equation 41. The RotD100 spectrum represents the envelope of the 180 spectra from the rotated motions (Figure B2).

$$SA_{rot}(T,\xi,\theta) = max\,|\ddot{u}_{rot}(t,T,\xi,\theta)|_{for\,t} \tag{41}$$

where $\ddot{u}_{rot}$ is the acceleration response of the oscillator, T is the vibration period, and ξ the damping ratio.

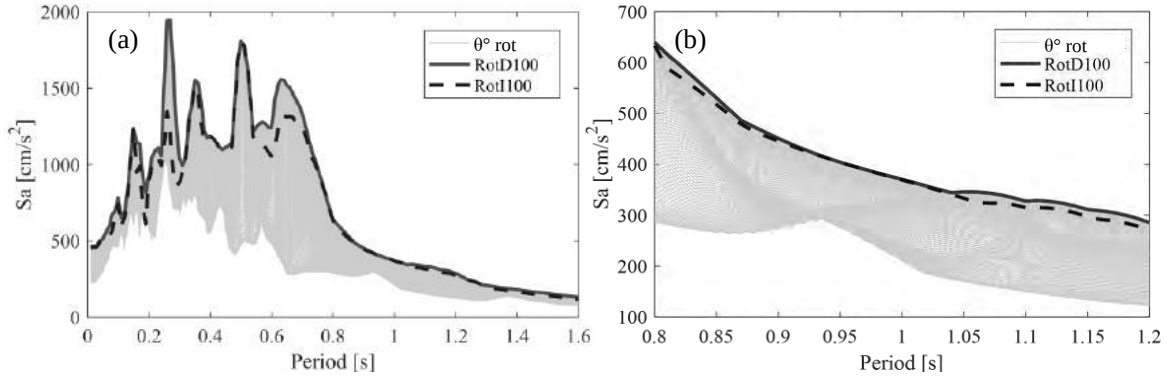

Figure B2: Response spectra from the rotated motions, the RotD100 spectrum, and the RotI100T_1T_2 spectrum [with (a) T_1 = 0.01 s and T_2 = 1.6 s and (b) T_1 = 0.8 s and T_2 = 1.2 s] from 1976 Friuli earthquake.

Then, the angle that generates the RotI100T_1T_2 spectrum is estimated, defined as the response spectrum of an acceleration time series of a given rotation angle θ that minimizes a penalty function, defined in Equation 42, between periods T_1 and T_2. In other words, the RotI100T_1T_2 is the spectrum from a given rotated motion closest to the RotD100 spectrum in the considered range of periods. The present hypothesis assumes that the rotation angle corresponding to the RotI100T_1T_2 spectrum will

produce the maximum response of the system.

$$penalty(\theta) = \frac{1}{N_{per}} \sum_{i=1}^{N_{per}} \left[\frac{SA_{rot}(T_i, \xi, \theta)}{SA_{RotD100}(T_i, \xi)} - 1 \right]^2 \tag{42}$$

where N_{per} is the number of sample periods between T_1 and T_2.

B.4 Finite element model

Two finite element models have been developed to evaluate the directionality effects using the CRA and the SRA. The first one is the 4-story steel building depicted in Figure B3a with W16X89 and W14X68 columns and beam sections respectively. Connections between elements are fully restrained (ANSI/AISC 358-10, 2010). The fundamental period of the building is 1.0 s.

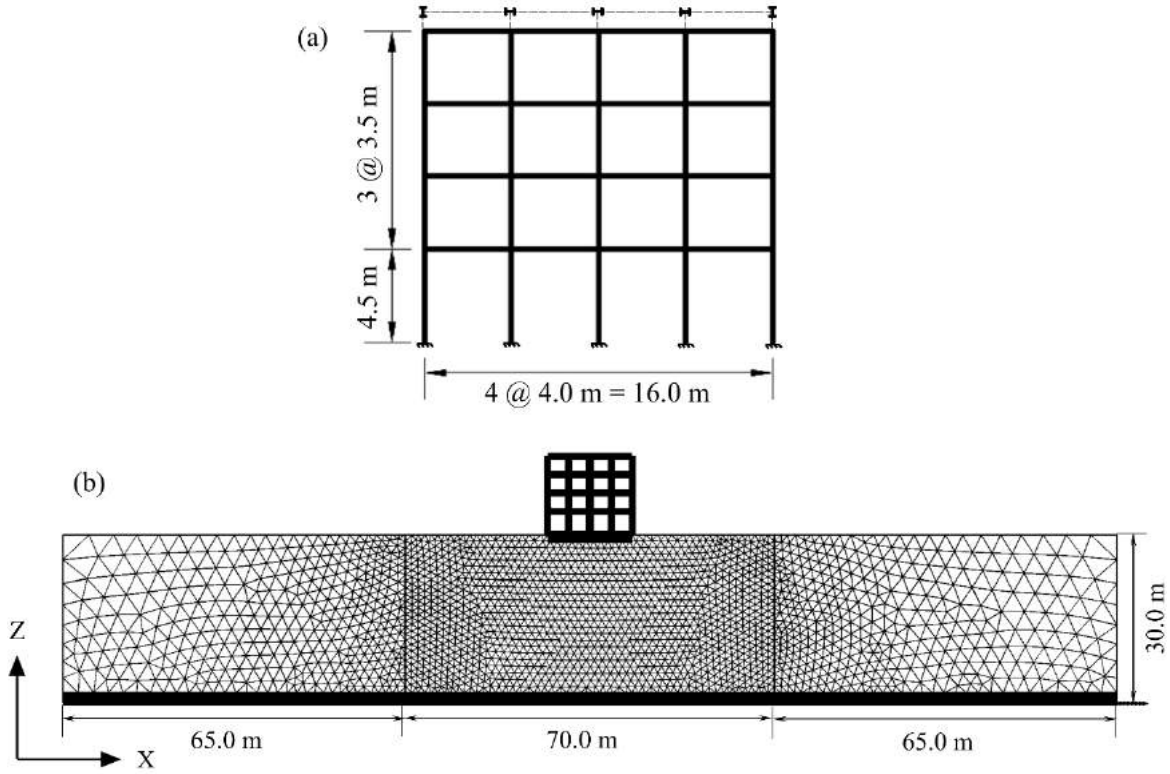

Figure B3: (a) Building and (b) soil-building finite element models.

In the second model, a soil layer is included to assess the influence of the SSI. The surface structure is the same than the first model, but it is founded on a 0.3 m thick concrete raft (Fig. 3b). The soil deposit is characterized as a 30 m deep medium to dense sandy layer, overlying a bedrock. The lateral extension of the model was considered large enough so that any unwanted wave reflections, occurring at the lateral free-field boundary conditions, are damped before reaching the zone were the SSI effects are relevant. The input-motions were applied at the base of the model through a compliant base with minimum flection of the downward propagating waves. An elasto-plastic constitutive model (Brinkgreve et al., 2017) was employed to account for the nonlinear response of the soil. The model includes features like small-strain stiffness degradation, a hyperbolic hardening law, and a Mohr-Coulomb type limit surface. Both finite element models have been developed and analyzed using the PLAXIS 2D software (Brinkgreve et al., 2017).

As mentioned before, input motions were derived from the linear combination of the horizontal as-recorded components of the 1976 Friuli earthquake, recorded at TLM1 station (1° to 180° rotation angles with 2° increments). The station is located at a rock outcrop, which is assumed to correspond to the base rock of the soil's deposit. 90 analyses for each finite element model were performed in the case of the CRA. The main monitored variable was the roof displacement relative to the base of the building.

B.5 Results

Results obtained through the CRA are depicted in Figure B4. Figure B4a shows the AI as a function of the rotation angle, where the maximum value is attained for an incidence angle of 153°. A quite similar result of 154° was obtained for the $SA_{rot}/SA_{RotD100}$ ratio (Figure B4c; gray lines represent the ratio for different periods between T_1 and T_2 and the black line is the average). The period range used was $T_1 = 0.8$ s and $T_2 = 1.2$ s, i.e. ± 0.2 the fundamental period of the building. A somewhat smaller angle of 132° was derived using the PGA_{rot}.

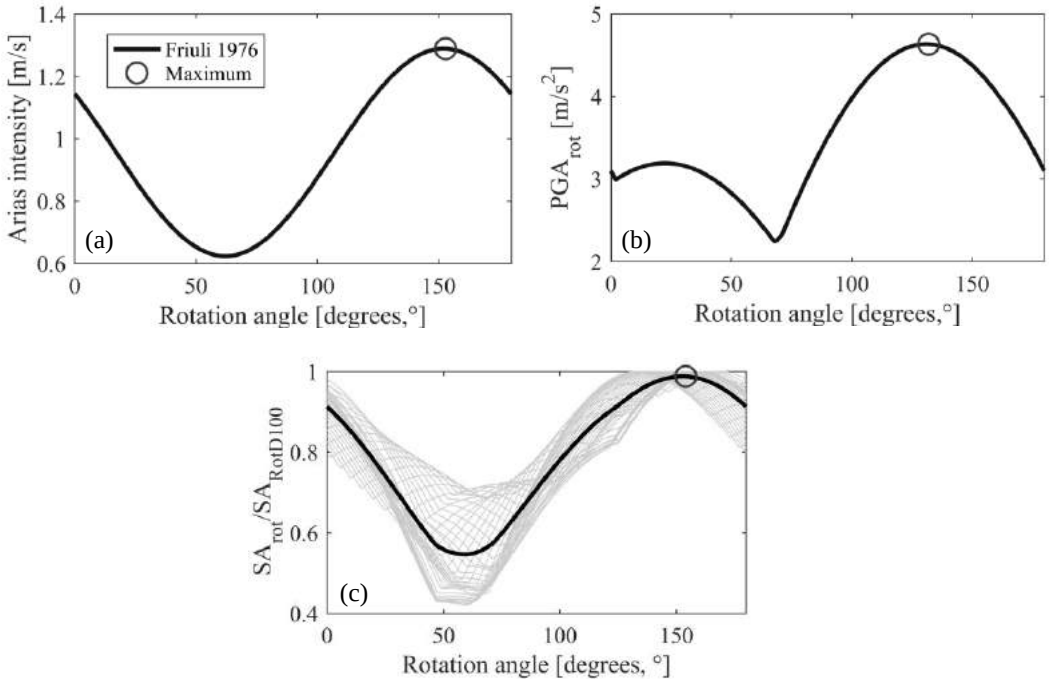

Figure B4: (a) Arias intensity, (b) peak ground acceleration, and (c) $SA_{rot}/SA_{RotD100}$ spectral ratios as a function of the rotation angle for the 1976 Friuli earthquake.

The results obtained with the CRA are compared with those from the SRA. Figure B5 shows the maximum relative roof displacement as a function of the rotation angle, obtained through the CRA, for both models: (a) building and (b) soil-building. The values obtained with the SRA are also depicted in the figure. The SRA using the AI and the $SA_{rot}/SA_{RotD100}$ hypotheses captured adequately the angle where the maximum response of the building occurs (in terms of roof displacements). Values more distant are obtained with the PGA_{rot} hypothesis.

In the case of the soil-building model, none of the three hypotheses of the SRA captured adequately the angle of the maximum response. Since they were derived only from the input time-histories, which are applied at the base of the model, they overlook site effects that might modify the motion when propagating through the soil's deposit. For this reason, free-field calculations were included in the

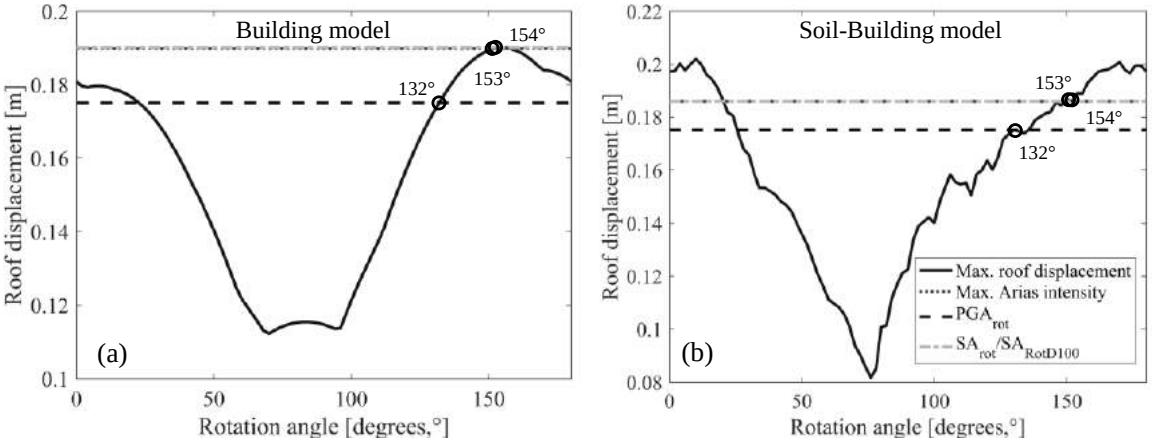

Figure B5: Comparison of the maximum roof displacements obtained for the (a) building and (b) soil-building models using the CRA (continuous line) and the SRA.

SRA. They correspond to finite element models of the soil's deposit, without any surface structure, where the incidence angles of the SRA are computed from the time-histories recorded at the top of the soil layer. Although this entails conducting free-field finite element analyses for each rotation angle, they require significantly less computational resources compared to the full DSSI analysis (Figure B3b) since only a slender column of soil, with special lateral boundary conditions, is required (Mánica et al., 2014). Free-field calculations are generally performed using frequency-domain methodologies to reduce calculation times where non-linearity is introduced through iterative procedures (Schnabel et al., 1972). However, the full elastoplastic model employed prevents the use of frequency-domain methods to assess the free field response.

The obtained results combining the SRA and the free-field calculations are shown in Figure B6. The angles obtained for the AI, PGA_{rot}, and $SA_{rot}/SA_{RotD100}$ hypothesis were 164°, 172°, and 180° respectively; they are all larger than those obtained only from the input time-histories. In Figure B7, they are compared with the results of the full DSSI analysis. In this case, the peak roof displacement was reasonably captured with the three hypotheses of the SRA.

B.6 Conclusions

Obtained results show the importance of considering directionality effects in DSSI analyses. They suggest that peak parameters of a system, including directionality effects, might be obtained from a single DSSI analysis decreasing calculation times considerably. Nevertheless, site effects must be incorporated, at least in this particular case were the input motion was recorded at a rock outcrop which is assumed to correspond to the rock base of the soil's deposit. These site effects might be included through free-field computations. The proposed hypotheses of the SRA must be validated through additional analyses with different characteristics such as diverse ground motion records; building structural typologies, shapes, and heights; and soil's deposits with different properties.

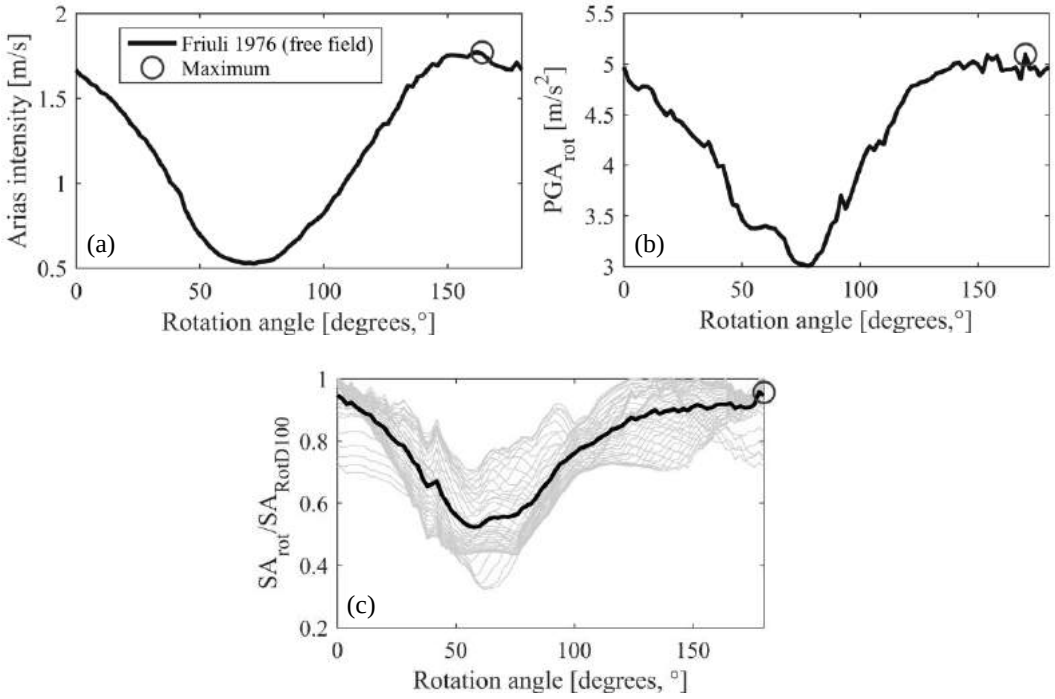

Figure B6: (a) Arias intensity, (b) peak ground acceleration, and (c) $SA_{rot}/SA_{RotD100}$ spectral ratios as a function of the rotation angle for the 1976 Friuli earthquake derived from the time histories computed on the top of the free-field analyses.

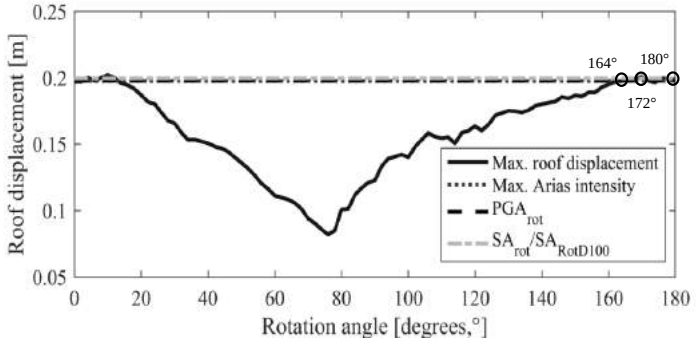

Figure B7: Comparison of the maximum roof displacements obtained for the soil-building model using the CRA (continuous line) and the SRA combined with free-field calculations.

C Appendix. Case study of a heavily-damaged building during the 2016 M_W 7.8 Ecuador earthquake: Directionality effects in seismic actions and damage assessment

Based on a manuscript to be submitted in Ingegneria Sismica journal.

C.1 Abstract

In this work, the directionality effects during the 7.8 M_W earthquake that occurred in Muisne (Ecuador) on April 16, 2016 are analyzed under two perspectives. The first is based on the influence of these effects on seismic intensity measures (IMs). The second one refers to the assessment of the expected damage of a specific building located in Manta, Ecuador as a function of it azimuthal orientation. The records of strong motion in 21 accelerometric stations are used to analyze directionality in seismic actions. At the closest station to epicenter, the peak ground acceleration was 1380 cm/s^2 (1.4 g). A detailed study of the response spectra ratifies the importance of directionality and confirms the need of considering these effects in seismic hazard studies. Differences between the IMs values that consider the directionality and those obtained from the as-recorded accelerograms are significant and they agree with studies carried out in other regions. Concerning to the variation of the expected damage respect to the building orientation, a reinforced concrete building, which was seriously affected by the earthquake is taken as a case study. For this analysis, the accelerograms recorded at a nearby station and detailed structural documentation has been used. The ETABS software was used for the structural analysis. Modal and pushover analyses were performed obtaining capacity curves and capacity spectra in the two main axes of the building. Two advanced methods for damage assessment have been used to obtain fragility and mean damage state curves. The performance points have been obtained through the linear equivalent approximation. This allows estimating and analyzing the expected mean damage state and the probability of complete damage as functions of the building orientation. Results show that the probability of complete damage is close to 60%. This fact is mainly due to the greater severity of the seismic action in one of the two main axes of the building. The results are in accordance with the damage produced by the earthquake in the building and confirm the need to take into account the directionality effects in studies concerning damage and seismic risk assessment.

C.2 Introduction

On April 16, 2016, an earthquake with moment magnitude 7.8, struck the north-western coast of Ecuador at 6:58 pm (UTC-5, local time). The epicenter was located near the town of Muisne, 170 km northwest of Quito. Although the epicenter was located in a remote rural area, several towns in the coastal provinces were affected due to its high intensity. The earthquake occurred at 20 km depth as a result of the relative displacement between the Nazca plate and the South American plate, through a subduction process (Singaucho et al., 2016). This process has generated catastrophic events in South America throughout the contact zone between these two plates, repeatedly affecting Chile, Peru and Ecuador (Bilek, 2010).

During the 2016 Ecuador earthquake, around 700 deceased were reported, and thousands of buildings and structures suffered damage. The most affected areas were the provinces of Manabí, Esmeraldas, Santa Elena, Guayas, Santo Domingo and Los Ríos, which the Government declared state of emergency. The canton of Pedernal in the province of Manabí was declared disaster zone. This confirm

the need of increasing the efforts in the knowledge of this natural phenomenon, providing advanced tools to improve the assessment of the seismic hazard and, particularly, the seismic risk management in urban environments. These facts suggest to be more critic in the design of future structures and focus on a better understanding of the seismic hazard of the region. For this, it will be necessary to develop new seismic hazard studies and update the seismic code of the country.

One interesting topic regarding the seismic hazard and the damage assessment is the one related to the directionality effects. Directionality related issues have been investigated in two areas: i) in seismic hazard and risk studies and ii) in the expected structural performance, as well (Pinzón et al., 2018a, 2019b, 2020a). The first one focuses on the influence of the sensor's orientation on the ground motion records of an earthquake. Whereby, it is possible to estimate intensity measures (IMs) that consider the orientation of the sensor, directly influencing in the development of new ground motion prediction equations (GMPE). These kind of IMs help to reduce the epistemic uncertainty involved in the development of seismic hazard studies. In the second point, the variation of damage of structures is studied according to the angle of incidence of the seismic action to the structure.

In this paper, both aspects are studied based on the Ecuador earthquake of April 16, 2016. Here we analyze the effects of directionality on the seismic action, estimating IMs independent to the orientation of the sensor and defining the variability of the action through these effects. The accelerograms recorded by the National Acelerographic Network of Ecuador (RENAC) were used. A total of 21 ground motions pairs (only horizontal components) were used. Sensor orientation-independent IMs (Boore, 2010; Pinzón et al., 2018b) were estimated for both the peak ground acceleration (PGA) and the spectral response (Sa). These measures were compared with the traditional ones (e.g. the larger of the two as-recorded components (Larger) and the geometric mean of the response spectra of the as-recorded components (GM). Finally, the results are compared with those obtained by other authors, corresponding to others study cases.

In addition, the expected damage of a reinforced concrete building located in the city of Manta (Ecuador) is studied according to its orientation with respect to seismic action. This building suffered complete damage during the 2016 earthquake. The original construction plans were used to model the building in ETABS. The effects of directionality on seismic demand were considered in order to validate the damage suffered during the event. Non-linear static analysis, Pushover, and the parametric model developed by Pujades et al. (2015) were used to obtain the fragility curves of the structure and subsequently estimate the expected damage with the performance point. The results indicate that the probability of complete damage is close to 60%, corresponding with the damage suffered during the event.

C.3 Directionality in ground motions

Normally, the PGA is estimated with the as-recorded acceleration components, acc_{EW} and acc_{NS} (PGA_{EW} and PGA_{NS}, see Equations 43 and 44). Then, the larger value of the PGA of the as-recorded components (PGA_{Larger}, see Equation 45) is commonly used as intensity measure in the development of GMPE.

$$PGA_{EW} = max|acc_{EW}(t)| \tag{43}$$

$$PGA_{NS} = max|acc_{NS}(t)| \tag{44}$$

$$PGA_{Larger} = max[|acc_{EW}(t)|, |acc_{NS}(t)|] \tag{45}$$

The fact is that the peak acceleration is rarely capture with the as-recorded components and therefore it occurs in an unknown intermediate angle. For this reason, the PGA is also estimated for the linear combinations of the as-recorded components for all the non-redundant angles, θ. The ground-motions are rotated using linear combinations of the horizontal as-recorded components for a range [0 180) with increments of $\theta = 1^{o}$ (Equation 46).

$$acc_{Rot}(t,\theta) = acc_1(t) \cdot cos\theta + acc_2(t) \cdot sin\theta \tag{46}$$

where $acc_1(t)$ and $acc_2(t)$ corresponds to the as-recorded acceleration horizontal components, t is the time and θ is the rotation angle. Then, the maximum value of the linear combinations represent the maximum PGA considering all the non-redundant angles (Equation 47). This PGA corresponds to the true maximum acceleration in the ground and is called $PGA_{RotD100}$ in this study. This PGA can also be obtained, in a simplified way, computing the maximum value of the Euclidean norm or the Root-sum-of-squares of the as-recorded acceleration components (Equation 48).

$$PGA_{RotD100} = max|acc_{Rot}(t,\theta)| \quad \theta = [0 \;\; 180) \tag{47}$$

$$PGA_{RotD100} = max\sqrt{[acc_1(t)]^2 + [acc_2(t)]^2} \tag{48}$$

Finally, the orientation where the maximum ground acceleration ($PGA_{RotD100}$) is produced, is estimated following by the following expression:

$$\begin{gathered} PGA_{RotD100} = max\sqrt{[acc_1(t)]^2 + [acc_2(t)]^2} \\ t_i = time\ instant\ where\ the\ PGA_{RotD100}\ is\ generated \end{gathered} \tag{49}$$

To evaluate the directionality effects in ground motions of the April 16, 2016 earthquake, the peak parameters of ground-motion are estimated. The analysis is computed using the ground-motion records from the National Accelerographic Network of Ecuador (RENAC). A total of 21 ground-motion records corresponding to 21 strong-motion stations (Figure C1) are used. The Ecuador shapefile used in this paper was obtained from the Stanford EarthWorks online library.

The PGA_{EW}, PGA_{NS}, PGA_{Larger} and the $PGA_{RotD100}$ are computed for the 21 ground-motion records available. The results are shown in Table C1. These results were georeferenced and interpolated, obtaining accelerations maps for each measure (Figure C2). In Figures C2a and C2b, the maps with the PGA_{NS} and PGA_{EW} are observed. Clearly, the PGA_{EW} present larger values compared to the PGA_{NS}. Figures C2c and C2d, present the PGA_{Larger} and $PGA_{RotD100}$ results respectively. Both present comparable results but the $PGA_{RotD100}$ present greater accelerations, as is seen in Table C1. The maximum as-recorded PGA was produced in the APED station with a value of 1380 cm/s^2. At this station, the true maximum acceleration ($PGA_{RotD100}$) was 1397 cm/s^2. Notice that, the stations ACH1, ACHN, ALIB, AOTA and APO1 have differences between $PGA_{RotD100}$ and PGA_{Larger} higher than 10%. This fact is interesting since we can underestimate the peak acceleration up to 20% (at this event).

In Figure C3, a flow map representing the direction where the maximum acceleration was generated is presented. On average, the maximum accelerations were obtained at a SW direction. Notice that, this flow map shows similar patterns compared to the obtained through coseismic slip measurements during the same event (Ye et al., 2016), and also compared with coseismic slips from other events that occurred in the same subduction zone [e.g., the 2015 M_W 8.3 Illapel, Chile (Shrivastava et al., 2016), 2010 M_W 8.8 Maule, Chile (Vigny et al., 2011)].

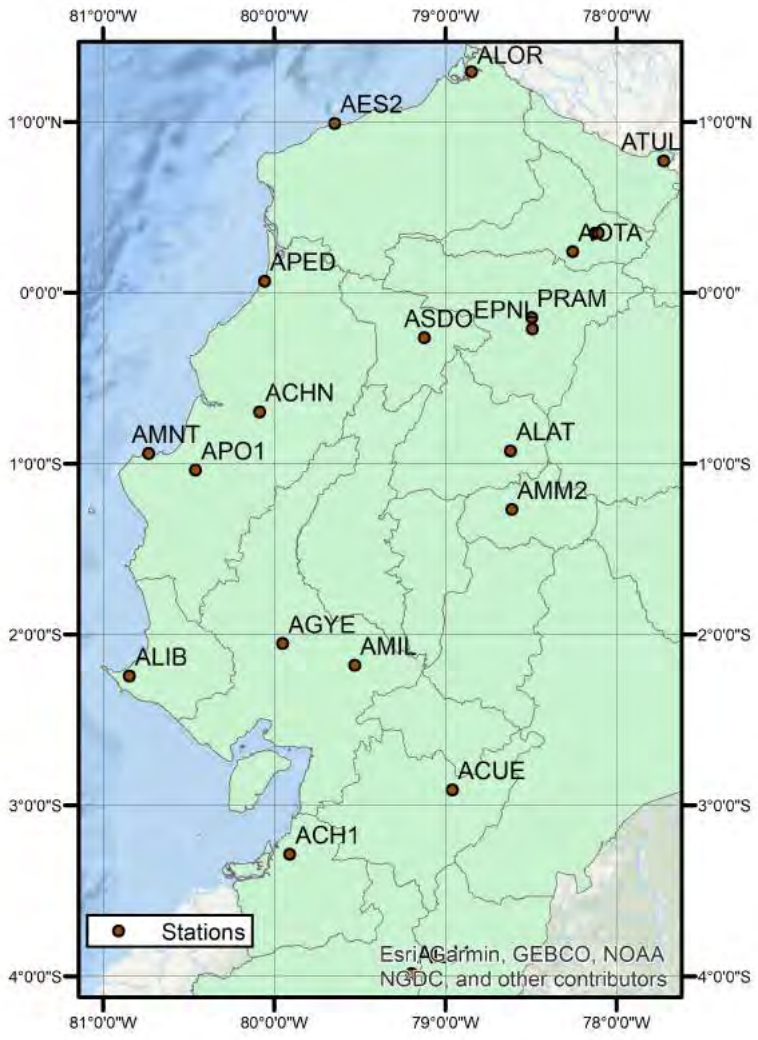

Figure C1: Strong-motion station from the National Accelerographic Network of Ecuador (RENAC).

Table C1: Values of PGA_{EW}, PGA_{NS}, $PGA_{RotD100}$, $PGA_{RotD100}/PGA_{Larger}$ ratio and $\theta_{PGA(RotD100)}$ from the 21 ground motions recorded by the National Accelerographic Network of Ecuador.

Station	$R_{epi.}$ (km)	PGA_{EW} (m/s^2)	PGA_{NS} (m/s^2)	$PGA_{RotD100}$ (m/s^2)	$PGA_{RotD100}/PGA_{Larger}$ (m/s^2)	$\theta_{PGA(RotD100)}$ azimuth north
AMM2	235	0.25	**0.35**	0.35	1.00	354°
ACH1	407	**0.25**	0.24	0.30	1.20	43°
ACHN	120	3.20	**3.64**	4.12	1.13	210°
ACUE	381	**0.35**	0.29	0.35	1.00	271°
AES2	76	**1.51**	1.08	1.52	1.00	96°
AGYE	270	0.18	**0.23**	0.24	1.04	340°
AIB1	202	0.48	**0.57**	0.58	1.02	166°
AIB2	204	0.21	**0.32**	0.32	1.00	357°
ALAT	206	**0.31**	0.27	0.31	1.00	85°
ALIB	308	**0.41**	0.39	0.46	1.12	56°
ALJ1	492	0.15	**0.16**	0.17	1.06	209°
ALOR	159	0.26	**0.26**	0.26	1.00	175°
AMIL	288	**0.51**	0.45	0.53	1.04	244°
AMNT	171	3.97	**5.14**	5.34	1.04	340°
AOTA	188	**0.42**	0.34	0.48	1.14	240°
APED	36	**13.80**	8.13	13.97	1.01	279°
APO1	167	3.11	**3.74**	4.16	1.11	226°
ASDO	115	**2.02**	1.09	2.06	1.02	260°
ATUL	251	0.16	**0.21**	0.21	1.00	0°
EPNL	174	**0.26**	0.20	0.27	1.04	260°
PRAM	171	**0.24**	0.23	0.25	1.04	44°

* In bold the larger value of the two as-recorded orthogonal components (PGA_{Larger}). $R_{epi.}$ is the epicentral distance.

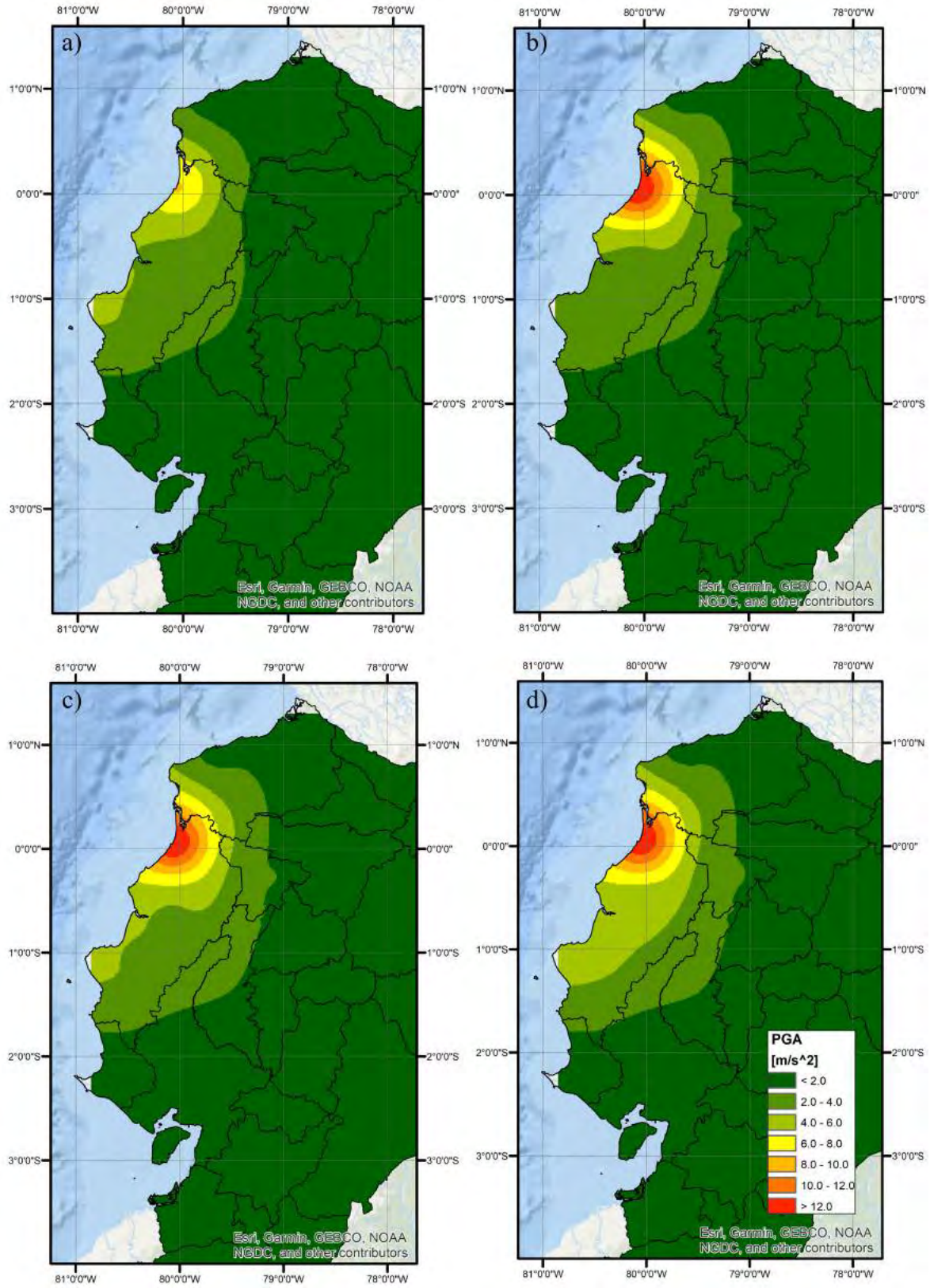

Figure C2: Peak ground acceleration maps from the as-recorded components (a) N-S and (b) E-W, (c) the larger value of the as-recorded components and (d) the true peak acceleration ($PGA_{RotD100}$).

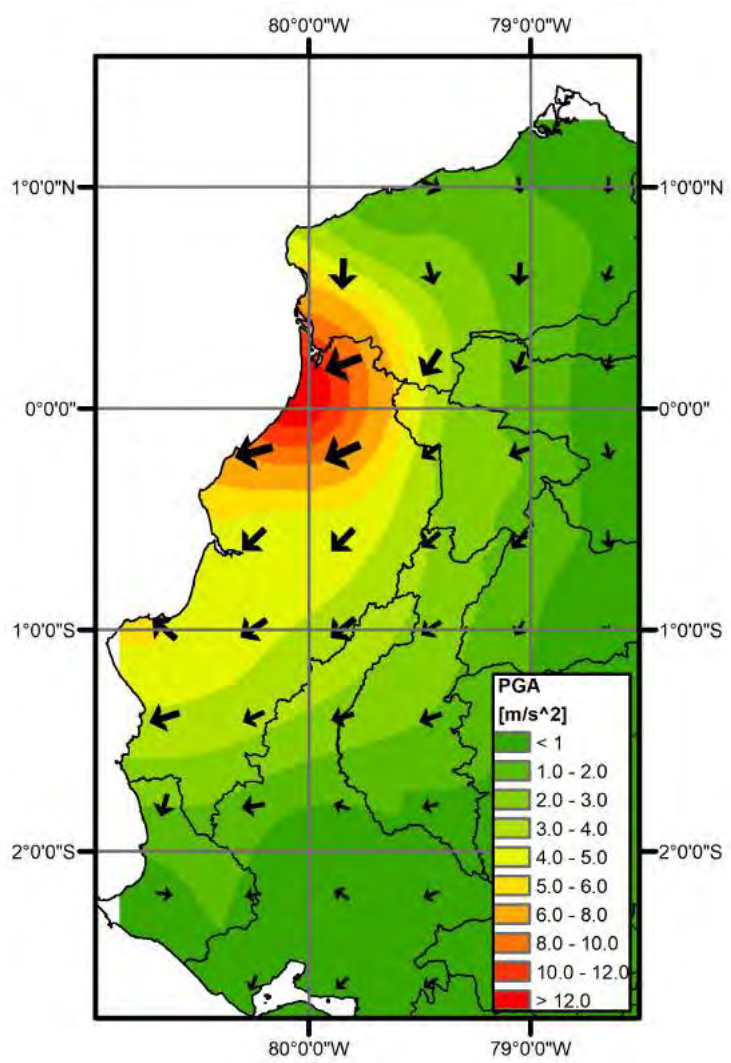

Figure C3: $PGA_{RotD100}$ flow direction in the horizontal plane during the 2016 Ecuador earthquake.

C.4 Directionality in the spectral response

The RotDpp intensity measure has been used in the development of newest GMPE (e.g., NGA-West2 and NGA-East). RotDpp is a sensor orientation independent measure and was introduced by Boore (2010). Is defined as the projection of the response spectra of the two as-recorded components rotated onto all non-redundant azimuths. Once obtained the vector compositions of the acceleration components for each rotation (Equation 46), the acceleration response spectra with 5% of critical damping are computed. A single spectrum for each composition is obtained. Because the response spectrum is defined as the maximum of the absolute amplitude of the response of a single degree of freedom damped oscillator, this measure has a rotation-angle periodicity of 180°. Once the 180 spectra are obtained, the spectral values are ordered for each oscillator period from lowest to highest for all the rotation angles and the ppth centile define the measure of ground motion for that oscillator period. The percentile 100 measure, RotD100, represents the maximum acceleration response for each oscillator period (see Figure C4). This measure will be used to compare the spectral acceleration (Sa) values obtained with the as-recorded components.

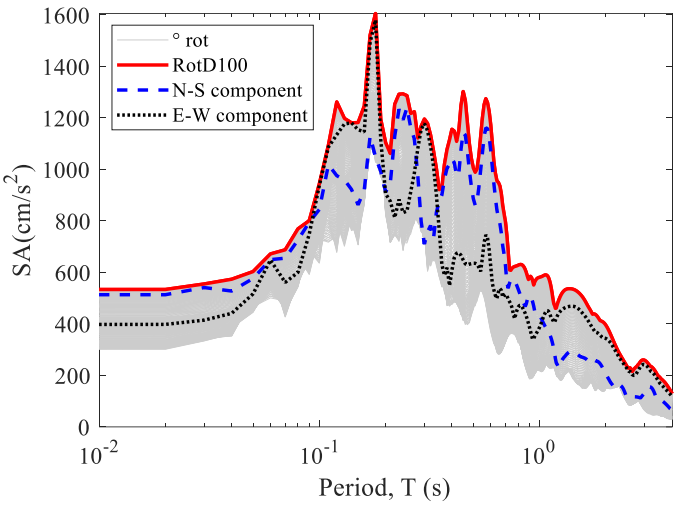

Figure C4: Response spectra from the as-recorded and rotated histories, and the RotD100 response spectrum from the 2016 Ecuador earthquake ground motion recorded in AMNT station.

To compare the Sa intensity measures, the ratios between the as-recorded components (N-S and E-W), the geometric mean of the as-recorded components (GM), the larger of the two as-recorded components (Larger) and the RotD100, are performed using the 21 available records. First, the 5% damped acceleration response spectra are obtained for all the ground-motion pairs and for all the linear combinations considered with the rotation angle variation. Subsequently, the RotD100 measure is calculated, following the methodology described above. For the calculation of the mean ratios, the antilogarithm of the average of the natural logarithms of the ratios was used, which represents the GM of the ratios (Shahi and Baker, 2014). All the ratios are calculated using RotD100 as dividend to compare with the maximum Sa response. Figure C5, displays the results obtained for all the ratios. One commonly comparison used by many authors is RotD100/GM (Haji-Soltani and Pezeshk, 2017; Pinzón et al., 2018b,a). The ratios values are 1.17 for small periods going up to 1.30 for larger periods, very similar to the obtained by other researchers. Another interesting comparison is the one with the Larger measure, where the results for all the periods are very constants and are, in average, around 1.07 (Boore and Kishida, 2016; Pinzón et al., 2018a).

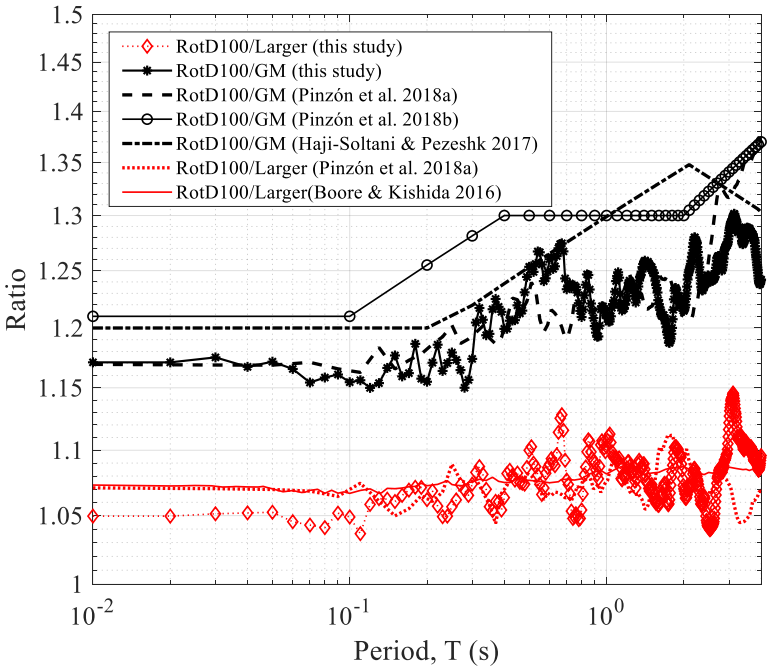

Figure C5: Comparison of the ratios RotD100/GM and RotD100/Larger with ratios proposed by other researchers.

C.5 Damage assessment of a heavily-damage building

In this section, a reinforced concrete building, which was seriously affected by the 2016 Ecuador earthquake is taken as a case study. For this analysis, the accelerograms recorded at a nearby station and detailed structural documentation has been used. An analysis of the capacity, fragility and damage of the studied building is developed. For this, the building is defined by the capacity spectra, in the two main axes of the building. The parametric model proposed by Pujades et al. (2015) was applied to both capacity spectra and then, the damage index is estimated.

Moreover, fragility and expected damage analyses were performed. Four damage states were considered in the analysis in addition to the Null damage state: 0. Null, 1. Slight, 2. Moderate, 3. Severe and 4. Complete. The damage states thresholds were defined by the approximation adopted in the European Risk-UE project and the one based on the damage index of Pujades et al. (2015).

C.5.1 Studied building

The structure under study is a 5-story reinforced concrete building of mixed use (commercial and residential). The building has a main concrete building and in the front part an annex with a steel structure (see Figure C6a). The building is located in Manta city. In this city, multiple buildings collapsed during the 2016 earthquake despite being more than 170 km from the epicenter. The area with the greatest impact was the Tarqui neighborhood, in which the studied building is located, and is where the largest commercial movement of the city occurs.

From a structural evaluation report generated by a professional engineer of Ecuador, determined that the building suffered irreparable damage and should be demolished. In the report he detailed that plastic hinges were formed in the structural system (beam-column), partial collapse of the stairs and collapse of internal walls and façade.

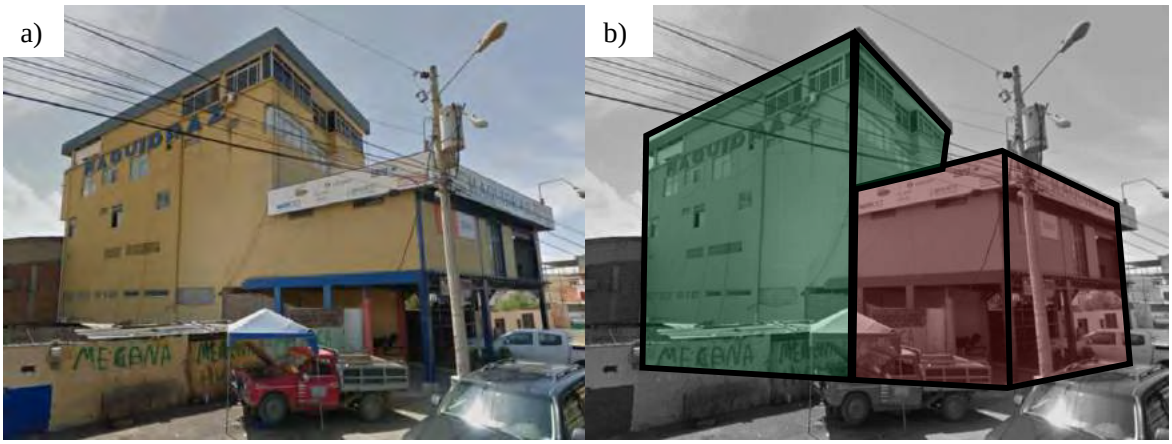

Figure C6: (a) Studied building. (b) In green, the main-building used to generate the structural model and in red, the annex that was not considered in the structural model. Images taken from Google Maps street view.

To perform the damage assessment of the building, a structural model was developed in ETABS software. Only the main building of which we had the original structural plans was considered in the model (Figure C6b). The steel structure attached to the building was not considered in the analysis since it does not appear on the construction plans. The beam-column distribution and geometry are shown in Figure C7. The inter-story high is 2.70 m. The geometry of the structural sections, steel rebar and material specifications are presented in Table C2. The section's geometry and steel rebar specifications were taken from the plans, and the concrete compressive strength from the structural evaluation report.

Table C2: Geometry of the sections and specifications of the materials of the beams and columns of the building studied.

Section code	$f'c$ (kg/cm^2)	Dimensions (mm)	Steel rebar	Rebar specifications
C-4	180	350x350	8 #5	A615 Grade 40
C-5	180	350x350	8 #5	A615 Grade 40
C-6	180	400x400	4 #5 + 4 #6	A615 Grade 40
C-1	180	400x400	8 #5	A615 Grade 40
C-2	180	400x400	8 #5	A615 Grade 40
C-3	180	450x450	4 #5 + 4 #6	A615 Grade 40
C-7	180	300x300	8 #4	A615 Grade 40
C-8	180	300x300	8 #4	A615 Grade 40
C-9	180	350x350	4 #4 + 4 #5	A615 Grade 40
Beam-1	170	200x500	2 #3 + 2 #4	A615 Grade 40
Beam-2	170	200x300	2 #3 + 2 #4	A615 Grade 40
Beam-3	170	200x600	2 #3 + 2 #4	A615 Grade 40

A non-linear static analysis, Pushover, was done in the main axes of the building to obtain the capacity of the building. Figure C8 shows the capacity curves and spectra in the X (transversal) and Y (longitudinal) directions. In this figure, the original points resulting from the pushover analysis, the interpolated capacity spectra at fixed pitch and the bilinear forms are shown in the two main orthogonal directions of the building. The fundamental period of the building is 0.58 s in the X axis and 0.62 s in Y.

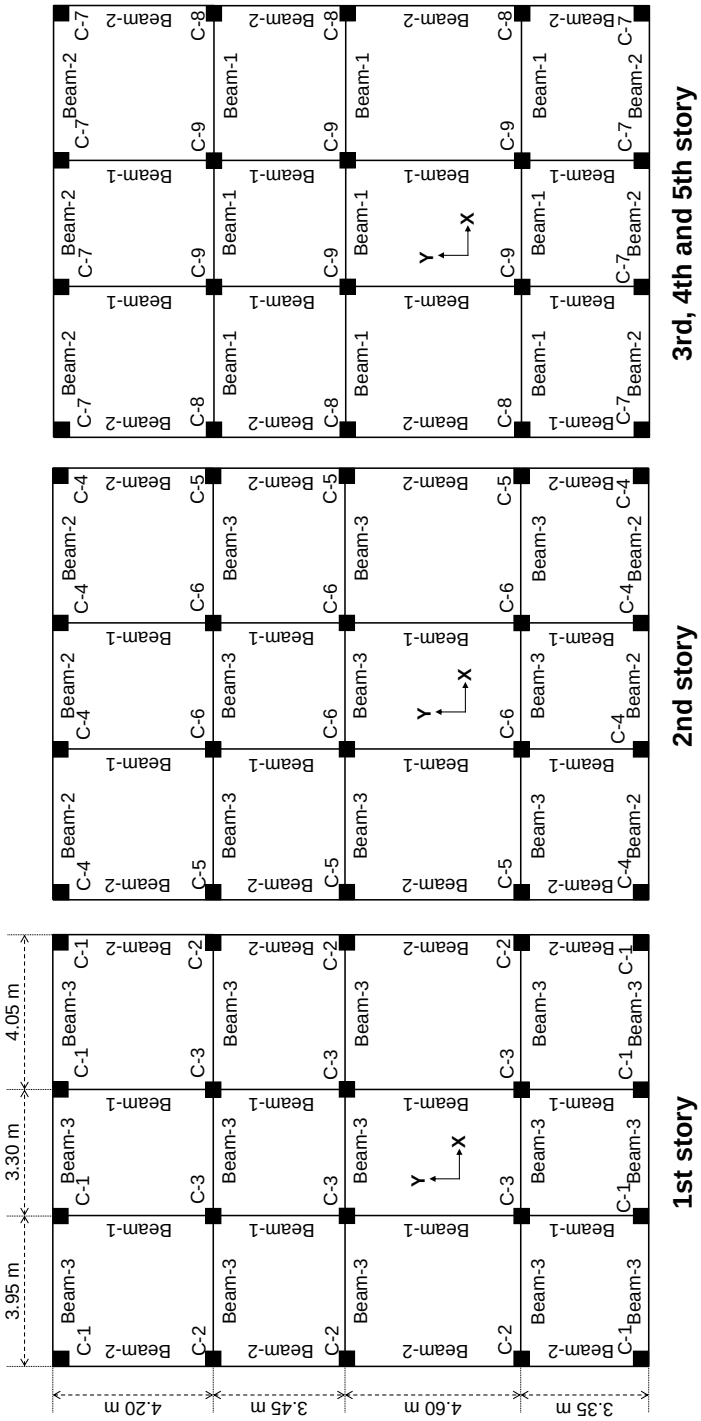

Figure C7: Distribution and geometry of the beams and columns.

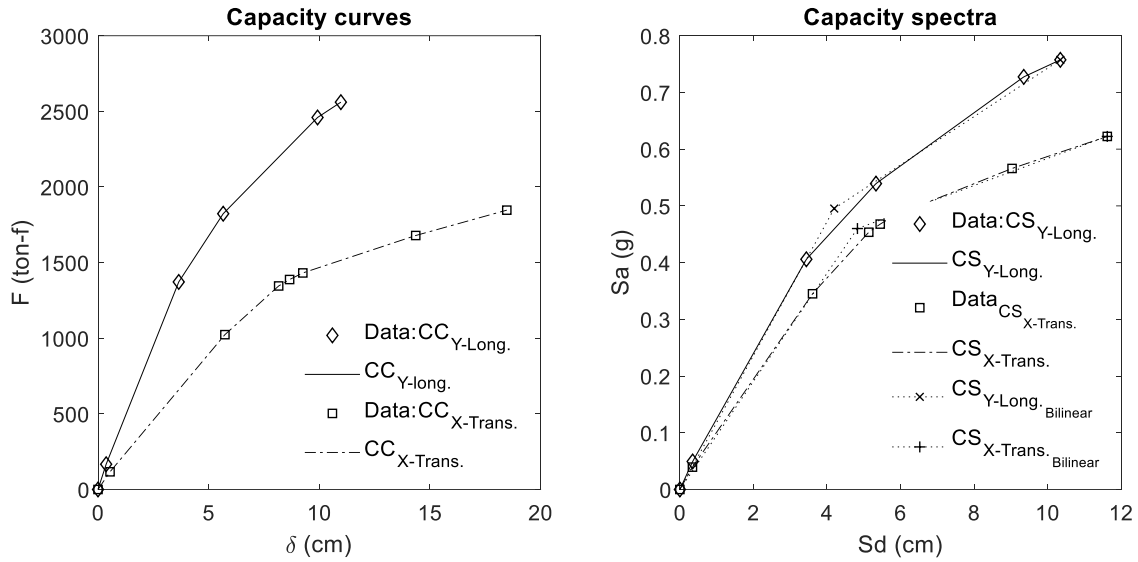

Figure C8: Capacity curve and spectra in the X and Y directions. The points resulting from the pushover analysis, the interpolated curves (int) at a fixed pitch and the bilinear forms (Bilinear) are shown.

C.5.2 Parametric model

Pujades et al. (2015) proposed a relatively simple mathematical model that allows modeling the capacity curves and spectra through five independent parameters. The aim of the model is to separate the linear part and the non-linear part of the capacity curve or spectrum, since the model is valid for both. The non-linear part doubly normalized, in abscissa and in ordinates, is modeled by the cumulative integral of a cumulative lognormal function. The cumulative Beta function can also be used in an equivalent way. Both the lognormal and Beta functions are modeled by two parameters, the mean value, μ, and the standard deviation, σ in the case of the lognormal, and the parameters γ and υ in the case of the Beta function. For more details, the parametric model is well explained and described in Pujades et al. (2015).

The model has been successfully applied to the capacity spectra in both X (transversal) and Y (longitudinal) directions of the studied building. In Figure C9, the adjustment for the capacity spectrum in the X direction is presented. Specifically, the capacity spectrum is shown with the following curves: the original data from the pushover analysis, the interpolated capacity spectrum (CS), the lognormal adjustment, the Beta adjustment and the improved adjustment. For the lognormal and Beta adjustments, all the interpolated points have been used. The improved setting is refined, minimizing the error between the model and the empirical points resulting from the pushover analysis. Also in this figure, the first and second derivative of the capacity spectra and the error function in percentage are shown. The second derivatives have been normalized, so that the minimum value is one. Notice the excellent quality of the adjustment. Figure C10 is analogous to Figure C9 but for the capacity spectrum in the Y direction. Note also the goodness of the adjustment obtained both with the lognormal function and with the Beta function and, above all, for the improved adjustment.

Notice the good fit between the empirical data and the model. In this way, the capacity spectra are fully defined by the following five parameters: the mean value (μ) and the standard deviation (σ) of the lognormal function, the slope (m) at the origin of the capacity spectrum and the point of ultimate capacity (Sdu and Sau). Table C3 shows the parameters of the adjusted models and the errors (ϵ_L).

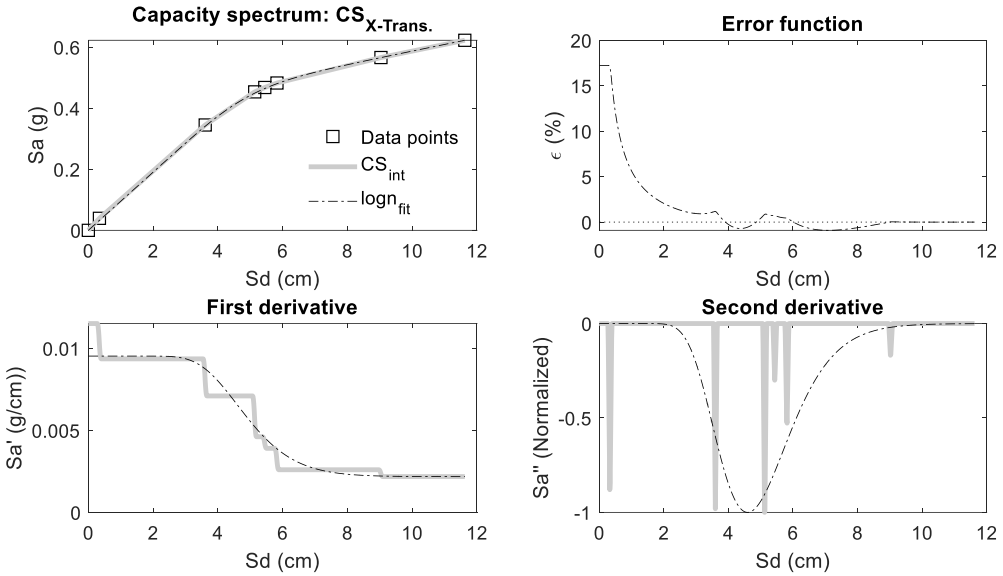

Figure C9: Parametric model adjustment in the X-direction.

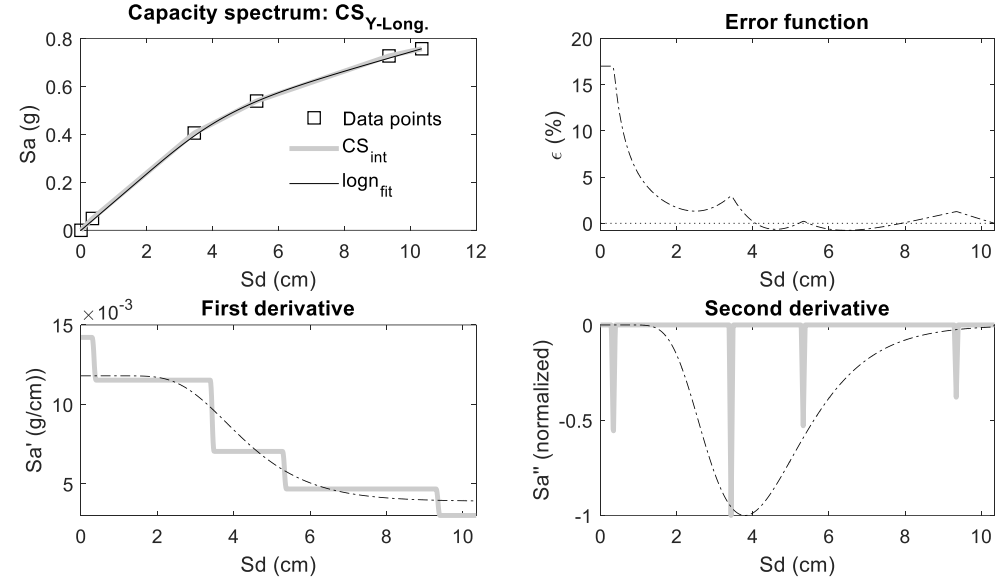

Figure C10: Parametric model adjustment in the Y-direction.

Table C3: Parameters of the parametric model for the capacity spectra (CS) in the X and Y axes.

CS	m (g/cm)	Sdu (cm)	Sau (g)	μ (adim)	σ (adim)	ϵ_L (adim)
X	0.095	11.62	0.622	0.420	0.241	7.35e-03
Y	0.118	10.35	0.757	0.410	0.331	1.28e-02

C.5.3 Park and Ang based damage index

Pujades et al. (2015) defines a new damage index based on capacity curves/spectra. This index is based on the well-known damage index of Park and Ang (1985). The damage contributions are separated in two, one part due to the deformation and another due to the energy dissipation. These two contributions are modeled by two functions that can be obtained simply and quickly from the normalized non-linear part of the capacity curve or spectrum.

In addition, Pujades et al. (2015) performed dynamic analyses with reinforced concrete buildings and typical seismic actions to calibrate the contributions of the deformation and energy dissipation in damage. Thus, the damage index based on the Park and Ang index is defined by the following equation:

$$I_{PA}(\delta_N) = \alpha K_S(\delta_N) + (1-\alpha)E(\delta_N) \tag{50}$$

In this equation, δ_N is the normalized spectral shift, I_{PA} is the new damage index based on the damage index of Park and Ang, K_S is the secant stiffness and E is the energy dissipated; α is the parameter that distributes the contributions of the stiffness degradation and the dissipation of the energy to the damage.

Based on previous studies (Pujades et al., 2015), a mean value of this parameter for typical seismic actions is $\alpha = 0.7$, which may be higher or lower depending on the characteristics of the buildings and the seismic actions. It is expected that for seismic actions of long duration and intensity the contribution of the energy dissipation to the damage may be greater.

Another function that has also proved to be useful (Hidalgo-Leiva et al., 2018) is the tangent stiffness function, K_T, related to the first derivative of the capacity spectrum. The incorporation of this function into the damage index allows incorporating sharp variations in the damage due to sudden drops in stiffness that are not well considered in the secant stiffness function. This improved index is defined by modifying Equation 50 as follows:

$$I_{PA_m}(\delta_N) = \alpha[\beta K_S(\delta_N) + (1-\beta)K_T(\delta_N)] + (1-\alpha)E(\delta_N) \tag{51}$$

In this work, for simplicity, the expression of equation 50 with a value of $\alpha = 0.7$ has been used. In general, this approach is adequate for most capacity curves. The more sophisticated model of equation 51 is useful in special cases, particularly when brittle hinges are incorporated. The estimation of the secant stiffness and energy functions is well explained in Pujades et al. (2015). In a simplified way, the secant stiffness function is obtained through the quotient between the ordinates and the abscissa of the non-linear part of the capacity spectrum. The tangent stiffness is obtained by deriving the non-linear part of the capacity spectrum and the energy function is the cumulative integral of the non-linear part of the capacity spectrum. A normalization of the functions produces that the damage index took values of 1 for the unit abscissa, so the damage index starts with zero in the origin and ends with a unit in the point of ultimate capacity. Figure C11 shows the capacity spectra and the damage curves. Specifically, it shows the normalized non-linear capacity spectrum (CS_{NLN}), and the energy, E, the secant stiffness, K_S, the tangent stiffness, K_T, functions and the damage index, I_{PA}, based on the Park and Ang index. In this same figure, the thresholds of the damage states are also shown. These damage states and thresholds are briefly described below.

C.5.4 Fragility curves and mean damage state

The damage states allow a qualitative evaluation of the expected damage in a structure or infrastructure. Thus, the most frequently used damage states are: 0 or Null damage, 1 or Slight damage, 2 or

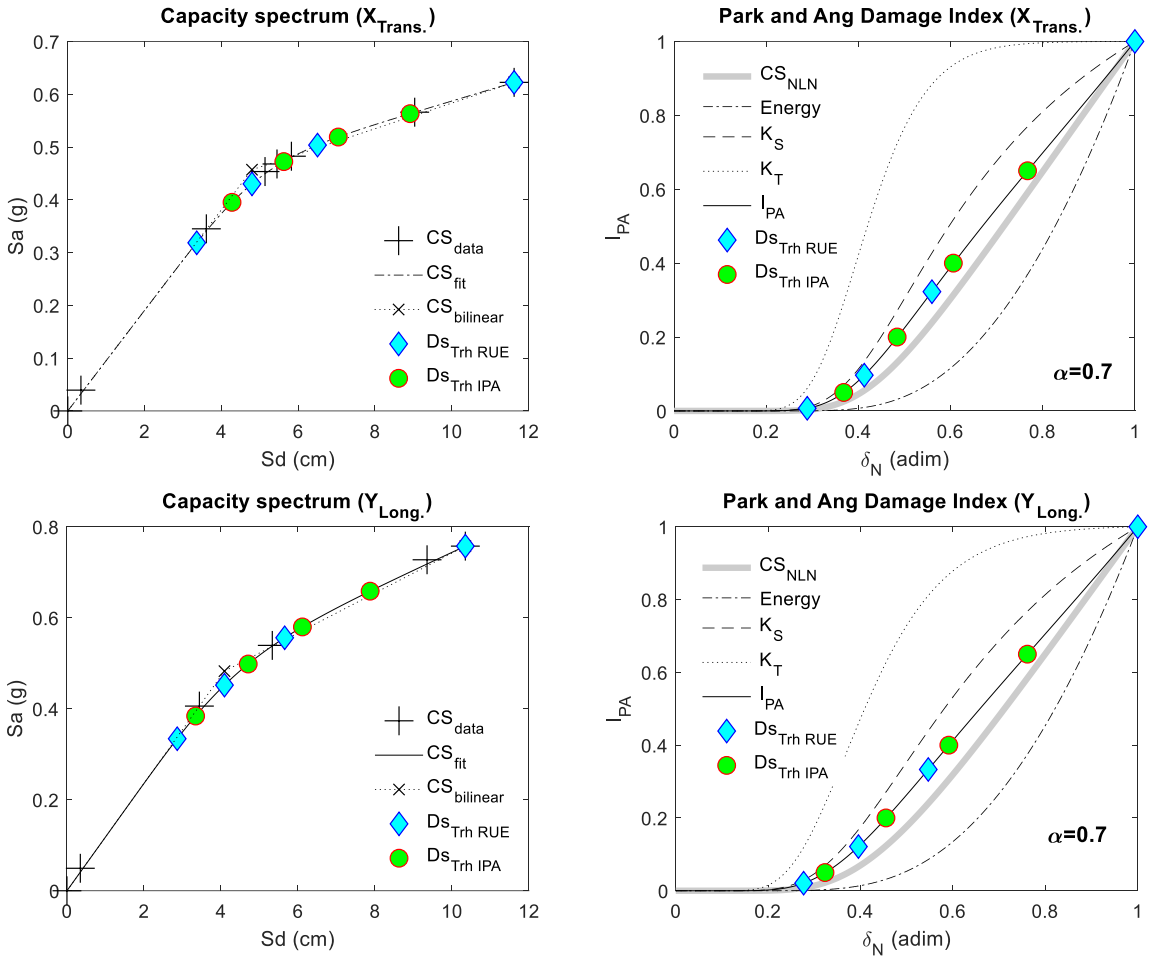

Figure C11: Capacity spectra (left) and damage functions (right) for: a) X direction and b) Y direction. Bilinear forms of capacity spectra and thresholds of damage states based on the Risk-UE project (Ds_{TrhRUE}) and those based on the Park and Ang damage index (Ds_{TrhIPA}) are shown. See also explanations in the text.

Moderate damage, 3 or Severe damage and 4 or Complete damage. In the intensity scale EMS'98, 5 grades or damage states are used, so that the damage state 4 (Complete) is separated into two: 4 or Extensive and 5 or Collapse. The assessment methods used by engineers understand that the repair cost in case of Extensive damage, do not compensate with respect to replacement cost. For this reason, when Generalized damage occurs, it is advisable to demolish, hence, the states of Generalized damage and Collapse are grouped into a single state of damage that we refer as Complete damage.

A delicate and relevant aspect in the evaluation of the expected damage are the damage states thresholds. The probabilities of damage states are usually quantified by damage probability matrices, fragility curves and mean damage states. For a specific damage state, the damage probability matrix defines the probability that a building suffer this damage state and the fragility curve defines the probability that this state is matched or exceeded. The damage state threshold is defined for a probability that the damage state is equal to or exceeded by 50%. This fact added to the hypothesis that the damage is distributed according to a binomial distribution, has been used to construct fragility curves in a simplified way. The hypothesis of the binomial distribution is robust and has been contrasted with the observed damage in seismic catastrophes in Italy (Braga et al., 1982, 1986). As we will see in the following section, the thresholds of damage states and the binomial distribution of

damage allow us to construct directly the fragility curves and, based on them, the damage probability matrices and curves of the mean damage state.

Within the framework of the European project Risk-UE (Milutinovic and Trendafiloski, 2003), different damage states thresholds were proposed based on the bilinear form of the capacity spectrum, taking as reference the spectral shift of the yield point, (Sdy, Say). Based on expert opinion, the following thresholds were chosen:

$$Sd_1 = 0.7Sd_y; \quad Sd_2 = Sd_y; \quad Sd_3 = Sd_y + 0.25(Sd_u - Sd_y); \quad Sd_4 = Sd_u \tag{52}$$

The damage states thresholds have been drawn in Figure 11. Based on damage studies in reinforced concrete buildings (Park and Ang, 1985; Park et al., 1987; Cosenza and Manfredi, 2000), Pujades et al. (2015) established a Park and Ang Damage Index value of 0.05 for the threshold of Slight damage, 0.20 for the threshold of Moderate damage, 0.40 for Severe damage, and 0.65 for the Complete damage state. These thresholds, together with the corresponding spectral displacements, are also shown in Figure C11, both in the bilinear forms of the capacity spectra through the Risk-UE approach, and in the damage rates based on the Park and Ang index, I_{PA}. Significant differences are observed, especially for the states of Severe and Complete damage. Although it depends on the shape of the capacity spectrum, in general, the Risk-UE proposal tends to overestimate minor damage and underestimate serious damage.

For a given damage state, the fragility curve defines the probability that it will equal or exceed. The following hypotheses: i) the fragility curves can be modeled with a cumulative lognormal function, ii) the damage is distributed in a binomial way (Braga et al., 1982, 1986) and iii) in the thresholds of the damage states the fragility curve is worth 0.50, allowing to build fragility curves expeditiously. Figure C12 shows the four fragility curves obtained: a) thresholds based on Risk-UE and X direction, b) thresholds based on the Park and Ang index and X direction, c) thresholds based on Risk-UE and Y direction and d) thresholds based on the Park and Ang index and Y direction. It can be seen how the thresholds based on the Risk-UE proposal lead to underestimate the probabilities of exceeding the states of Severe and Complete damage with respect to the thresholds of the damage states based on the Park and Ang index. Fragility curves are useful for calculating damage probability matrices (DPM). Damage probability matrices define the probability of each of the 5 damage states. The following equation allows this estimation from the fragility curves.

$$\begin{gathered} P_0(Sd) = 1 - F_1(Sd) \\ P_i(Sd) = F_i(Sd) - F_{i+1}(Sd) \quad 1 \leq i < 4 \\ P_4(Sd) = F_4(Sd) \end{gathered} \tag{53}$$

In this equation, $P_i(Sd)$ is the probability of damage state i and $F_i(Sd)$ is the fragility curve of damage state i. It is also useful to have the mean damage state curve (MDS), which is defined by the following equation:

$$Mean\ Damage\ State = MDS(Sd) = \sum_{i=0}^{4} iP_i(Sd) \tag{54}$$

Figure C13 shows the functions of the mean damage state for the X and Y directions and for the fragility curves based on the proposal of the Risk-UE project and the Park and Ang damage index. It can be seen how the Risk-UE proposal tends to overestimate minor damages and underestimate serious damages. On the other hand, this figure also shows the sensitivity of the expected damage to the choice of the thresholds of the damage states and the need to be careful in their definition.

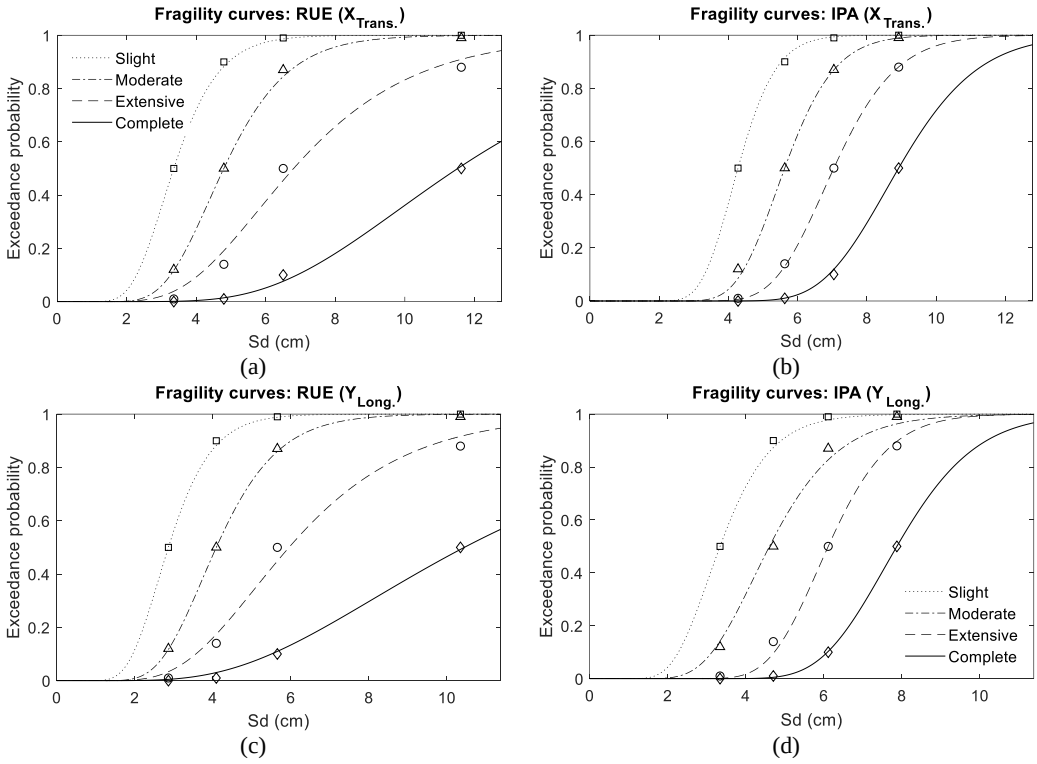

Figure C12: Fragility curves: a) X-direction, Risk-UE thresholds, b) X-direction, Park and Ang index thresholds. c) Y-direction, Risk-UE thresholds, d) Y-direction, Park and Ang index thresholds.

C.5.5 Seismic actions

In this section, the impact of the earthquake on the building is analyzed, assuming that the seismic action that affected the building does not differ much from that recorded near the site. Accelerograms recorded at AMNT station (closest station to the building, see Figure C14 and C15) were used. The X-Trans. axis of the building is oriented 144° from the east (counter-clockwise) and therefor the Y-Long. axis is oriented E54°N (see Figure C14).

Figure C15 shows the horizontal as-recorded acceleration components and the particle motion (hodogram). As seen in this figure, the maximum acceleration ($PGA_{RotD100}$) occurred at a different angle (see pink arrow and Table C1) as the as-recorded ones (0° - EW and 90° - NS). The maximum intensity occurred close to the transversal axis of the building.

For this study, a directionality analysis has been performed. To do this, the as-recorded components EW and NS have been projected on an axis that has been rotated by an angle that has been varied between 0 and 180 degrees, which achieves the record of the accelelerogram assuming that the EW component of the accelerometer was oriented in this direction, using Equation 46.

Figure C16 shows the 5% damped response spectra of the rotated accelerograms. The spectra are shown in $Sa-T$ and in $Sa-Sd$ formats. This figure highlights the response spectra for angle 0° (EW component), angle 90° (NS component), for the transversal direction of the building (X direction, Dir $X_{Trans.}$) and for the longitudinal direction (Y direction, Dir $Y_{Long.}$). The figure also indicates the periods of the building in the X and in the Y axes. Note how the most intense seismic action is given for the $X_{Trans.}$. direction of the building, which most likely meant an increase in the damage caused by the earthquake at this building.

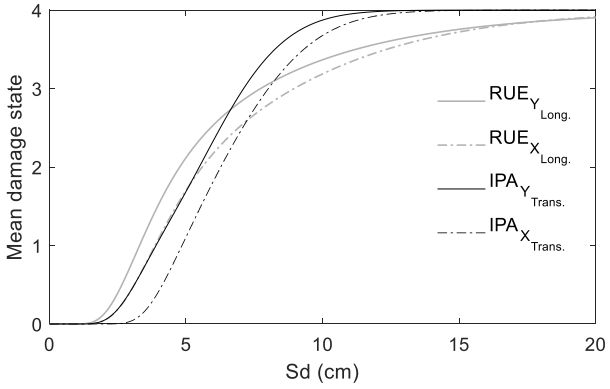

Figure C13: Mean damage state curves based on Risk-UE and Park and Ang damage index.

Table C4: Performance point values from the principal axes of the studied building.

Axis	Angle	Sa_{pp} (cm/s^2)	Sd_{pp} (cm)
X-Trans.	144°	561.8	9.3
Y-Long.	54°	544.2	5.6

C.5.6 Building-seismic action interaction

For a given seismic action, and a specific building, the performance point, PP, specifies the maximum spectral displacement than the earthquake, defined by the 5% damped response spectrum, in spectral acceleration-displacement format ($Sd-Sa$), will cause to the building, defined by its capacity spectrum also in $Sd-Sa$ format. The fragility curves and the functions that define the mean damage state allow to know the level of expected damage that the earthquake will cause in the building. An expedited, although approximate, way of estimating the performance point is the linear equivalent approximation that assumes that the displacement will be the same as if the structure had a linear behavior. Although this approach is conservative, it has been considered sufficient for the purpose of this work which is the study of the influence of the orientation of the building on the expected damage.

Figure C17 illustrates the linear equivalent approximation to cross the 5% damped response spectrum of the rotated accelerograms, in the transversal (X at 144°) and longitudinal (Y at 54°) directions of the building, respectively, to obtain the performance points. As seen in the figure, despite the similarity in the capacity of each of the axes of the building, the expected damage in the $X_{Trans.}$ direction will be larger due to a higher seismic demand. The PP values obtained are shown in Table C4.

The mean damage state curves of Figure C13 have been used to estimate the expected damage and the fragility curves of Figure C12 have been used to estimate the probability of the Complete damage state as a function of the rotation angle of the seismic action. Figure C18 shows the results obtained.

Table C5 summarizes the numerical values for the directions of the main axes of the building, which correspond to the angles of 54° and 144°. The values of the mean damage state and the probability of Complete damage (P4, in percentage) are given for the two hypotheses used to define the thresholds of the damage states, the one based on the Risk-EU project and the one based on the damage index of Park and Ang. It is observed that if we take as reference the thresholds of the damage states based on the Park and Ang damage index, the expected mean damage state is 3.50 and the probability of the complete damage state is 59.2%. This result also agrees with the damage observed in the studied building after the earthquake.

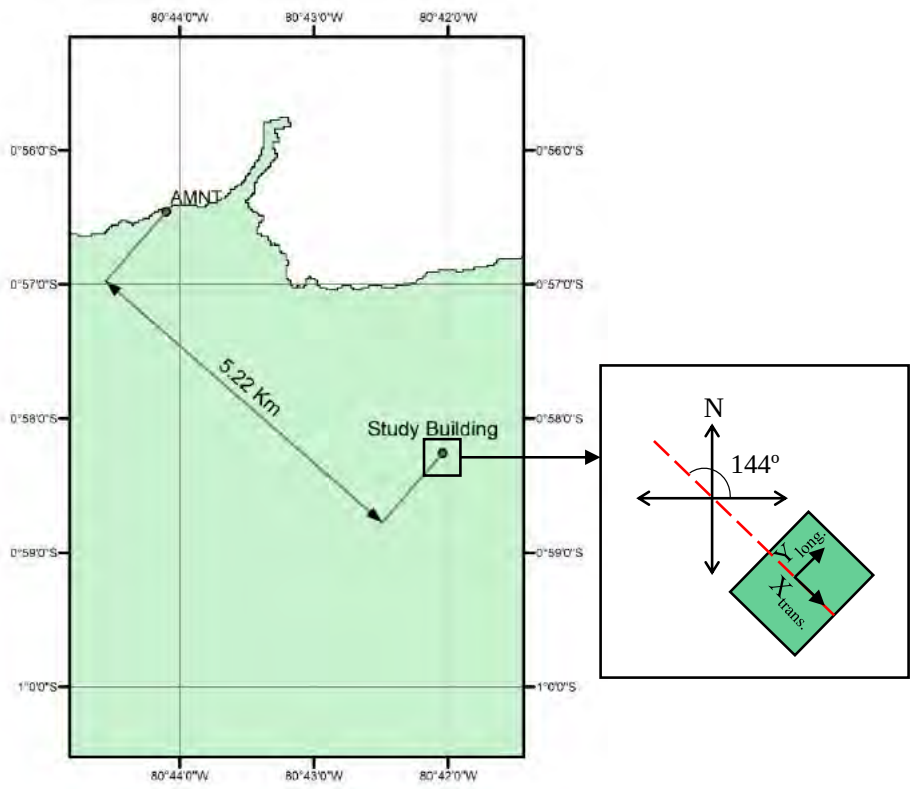

Figure C14: Location and distance between the studied building and the closest accelerometric station, AMNT. The orientation of the building respect to the north is also depicted.

Table C5: Mean damage state and Complete damage probability in the main axes of the building based on the proposal of the Risk- UE project and, the Park and Ang damage index.

Axis	Angle	Mean Damage state		Complete damage probability (%)	
		IPA	RUE	IPA	RUE
X-Trans.	144°	3.50	3.07	59.24	34.85
Y-Long.	54°	2.09	2.40	7.52	12.91

Finally, the damage probability matrices for the orientations of the main axes of the building have been calculated. That is, for the mean damage states of Table C5. Figure C19 shows the results obtained, for these two orientations and for the two hypotheses used to define the thresholds of the damage states.

It is concluded that the lower damage obtained in the direction of the Y axis (approximately 54°) is due more to the lower intensity of the action in this direction than to the greater resistance of the building and the greater damage in the direction of the X axis (approximately 144°) is due more to the greater severity of the action than to the lower resistance of the building, although it is also true that the differences in the resistant properties of the building in its two main directions also influence the expected damage.

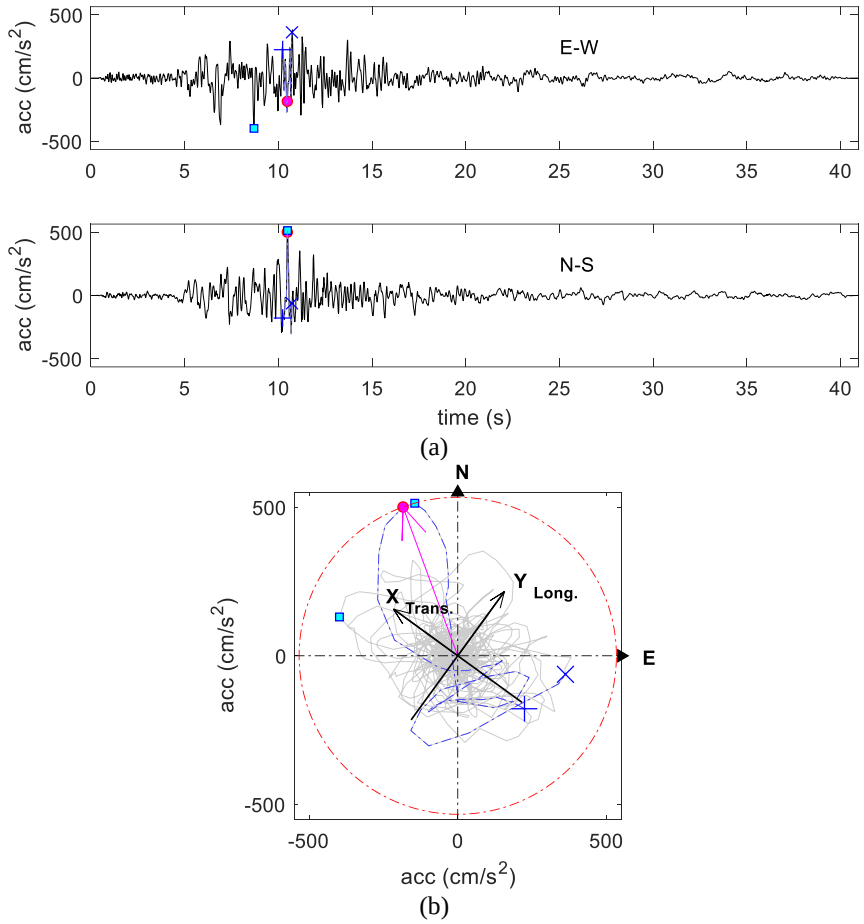

Figure C15: 2016 M_W 7.8 Ecuador earthquake, recorded at AMNT station. (a) As-recorded E-W and N-S accelerograms, and (b) acceleration hodogram.

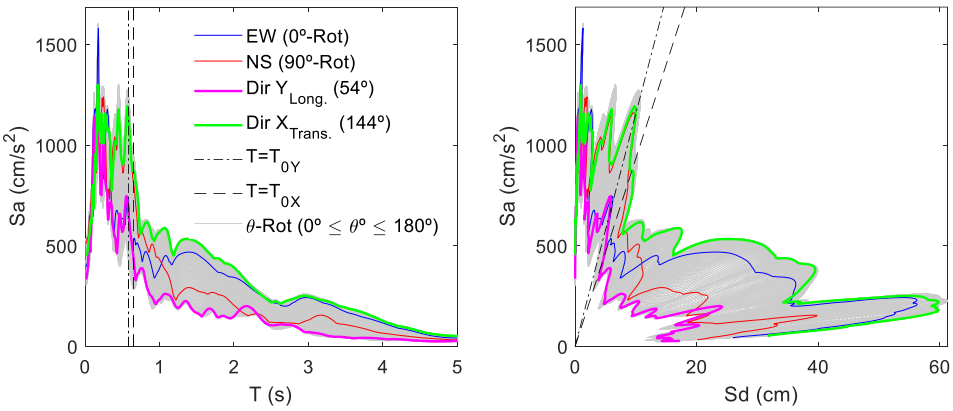

Figure C16: 5% damped response spectra for the accelerograms obtained in the direction defined by the angle θ, from the projection of the as-recorded components EW and NS recorded at AMNT station. Figure is given in spectral acceleration-period ($Sa - T$) and in spectral acceleration-spectral displacement ($Sa - Sd$) formats. The fundamental periods of the principal axes of the building ($X_{Trans.}$ and $Y_{Long.}$) are also indicated.

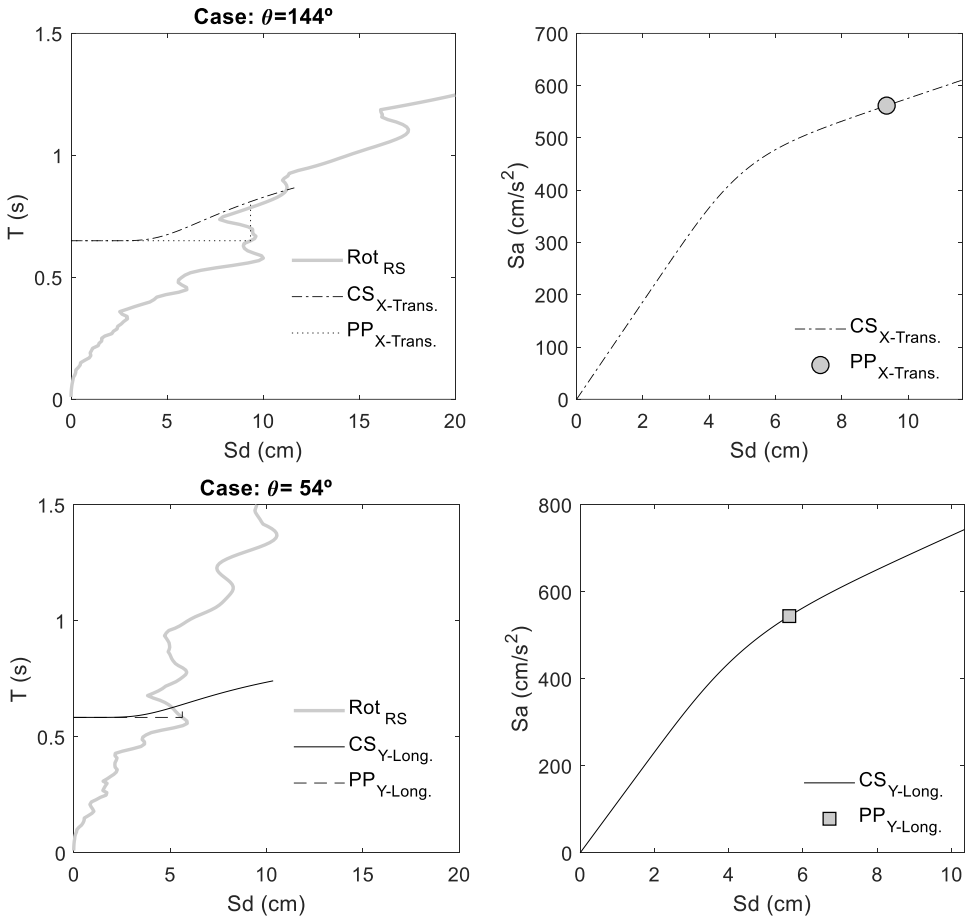

Figure C17: Linear equivalent approximation to estimate the performance point of the $X_{Trans.}$ (144º case) and $Y_{Long.}$ (54º case) axes.

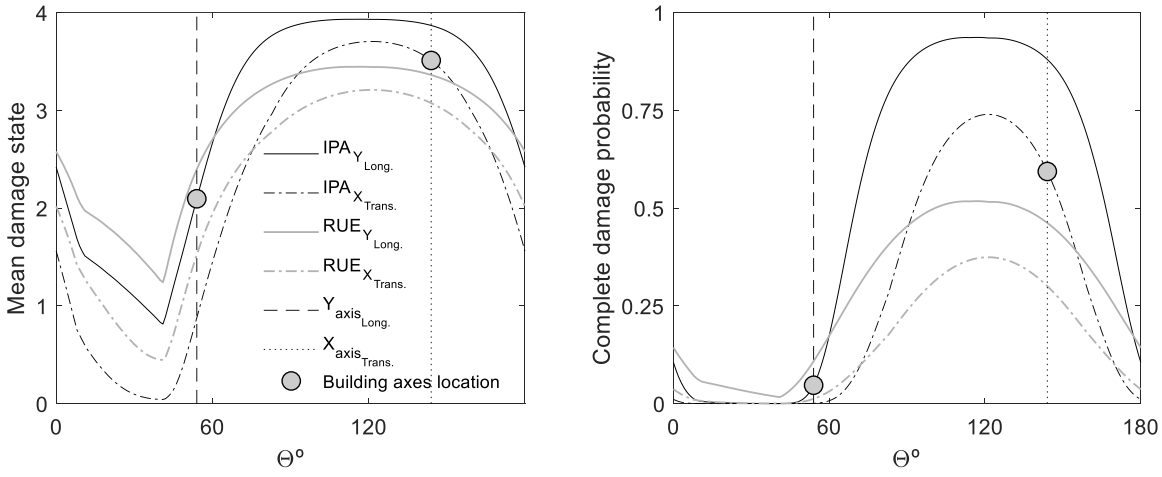

Figure C18: Mean damage state and Complete damage probability as a function of the rotation angle of the seismic action. The orientation of the principal axes of the building (54º and 144º) are shown.

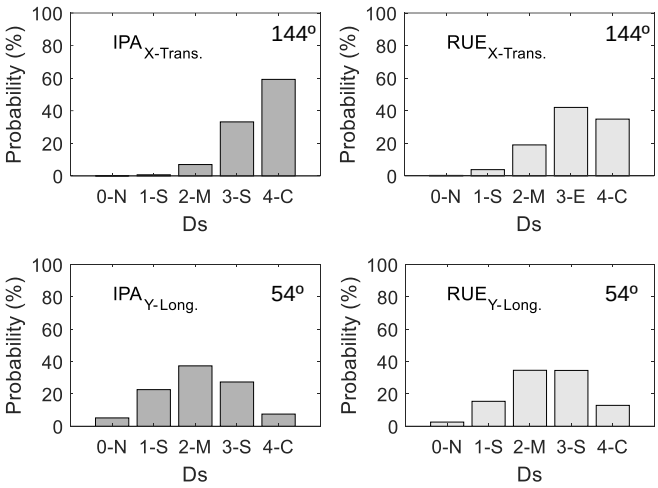

Figure C19: Damage probability matrices for the two main axes of the building (54º and 144º approximately) and for the two hypotheses used to define the damage states thresholds.

C.6 Conclusions

In this study, the peak ground-motion measures of the 2016 Ecuador earthquake were evaluated obtaining interesting results. This event reaffirms the importance of keep developing research to reduce the seismic hazard and risk in Ecuador. Using only the as-recorded components is not entirely correct when the effects of earthquakes are analyzed since the maximum intensity does not occurred necessarily in one of these components. As seen in the results, the PGA is underestimated close to a 10%, on average, when the PGA_{Larger} and the $PGA_{RotD100}$ are compared.

When the acceleration spectra are estimated, the RotD100 is considered as the maximum possible response, corresponding to the most critical case. Thus, these values can be used for the design or risk assessment of structures of special importance. It's possible to estimate the maximum value for an available ground-motion dataset and this envelope can be considered as an earthquake with large return period, representing the 100th percentile of all possible spectra for the available database.

In addition, the directionality effects have been evaluated, through a deterministic analysis, in a building that was seriously damaged by the 7.8 M_W Ecuador earthquake occurred on April 16, 2016. The parametric model has been applied to the capacity curves/spectra of the studied building. This model has been useful and adequate to model the capacity spectra resulting from the pushover analysis in both transversal (X) and longitudinal (Y) directions of the building. The capacity in the X direction is slightly higher than in the Y direction. To obtain the fragility and damage curves, the proposals adopted in the Risk-UE project and those of the damage index proposed by Pujades et al. (2015) based on the Park and Ang index were used. The tendency of the Risk-UE proposal to overestimate the moderate damage and to underestimate the severe and complete damage is confirmed, referring to the method based on the Park and Ang index. However, the sensitivity of the fragility and damage curves to the way of deciding/establishing the ultimate capacity point and the thresholds of the 4 non-null damage states must be taken into account. Thus, studies oriented to increase the reliability and robustness of these limits are recommended. In our opinion, the thresholds based on the Park and Ang index are more versatile and robust than those based on the bilinear form of the capacity spectrum (Risk-UE method).

The ground motion records from AMNT station, located 5 km away from the building, has been used to estimate the expected damages under the hypothesis that this seismic action is what affected

the building. For this purpose, a directionality analysis has been carried out concluding that the acceleration at the direction that coincides with the transversal axis of the building (144°) is close to the greater intensity, and probably be the main cause of the damage caused. The probability of complete damage is close to 60%, which is in accordance with the damage suffered by the building during the earthquake. However, this important damage must be attributed more to the severity of the action than to the uneven resistance of the two directions of the main axes of the building since, although they present differences in resistant properties, these differences are not very significant. This study, has allowed us to test the parametric model, verify the robustness and utility of the Park and Ang damage index and verify the importance of considering the directionality of the seismic actions in damage assessment and seismic risk studies.

D Appendix. Seismic site classification of the Costa Rican Strong-Motion Network based on V_{S30} measurements and site fundamental period

Internal report. Earthquake Engineering Laboratory, University of Costa Rica.

D.1 Abstract

In this paper, a seismic site classification for the Costa Rican Strong-Motion Network (CRSMN) is proposed. The existing classification of the Costa Rican Seismic Code based on the average shear-wave velocity of the top 30 m (V_{S30}) is used as reference. The site fundamental period (T_f) is included as a parameter to complement the existing characterization. For this, the V_{S30} measurements from 35 accelerometric stations are related to the site fundamental period obtained through horizontal-to-vertical spectral ratios (HVSR) using ground motion records from the Costa Rican Strong-Motion Database. The H/V ratios are estimated with 5% damped acceleration response spectra and with traditional Fourier amplitude spectra from the S-wave window. From the relation of V_{S30} and T_f, different ranges of T_f are assigned to existing site classes and a graphic with three-lines and four-areas is proposed to classify new sites. A total of 157 stations of the CRSMN are classified using this proposal.

D.2 Introduction

Costa Rica is considered one of the countries with the greater seismicity of the region. Its complex tectonic framework, subduction zone and active volcanism in the continental zone, has motivated to develop more studies to reduce the seismic risk of the country. In seismic risk studies, three features must be taken into account: the hazard, vulnerability and damage value. A correct definition of the seismic hazard is essential to obtain reliable results. Seismic sources, site characterization and ground motion prediction models must be defined. Let us focus in the site characterization. Several parameters have been used as proxy to define the seismic site conditions based on the topography, geology, site fundamental period (or frequency) and shear-wave velocity of the soil profile. Among these, the most used is the average shear-wave velocity from the top 30 m of the soil profile (V_{S30}). In United States, the NEHRP (BSSC, 2009) and the ASCE7-16 (ASCE, 2017) proposed six site classifications based on V_{S30}, from A (hard rock, $V_{S30} > 1500$ m/s) to F (soil with special condition). The Costa Rican Seismic Code (CRSC) (CFIA, 2016) uses an equivalent classification, based on V_{S30}, varying only nomenclature (S1 to S4). The V_{S30} is estimated using the following expression:

$$V_{S30} = \frac{\sum_{i=1}^{N} d_i}{\sum_{i=1}^{N} \frac{d_i}{V_{Si}}} \tag{55}$$

where d_i is the thickness of each soil layer in the profile until it reaches 30 m deep, V_{Si} is the shear-wave velocity of each layer in m/s and N is the number of layers until it reaches the 30 m.

Recent studies show some limitations and problems of using V_{S30} to classify sites (Steidl, 2000; di Alessandro et al., 2012; Pinzón et al., 2019c). As an alternative, classifications based on the site fundamental period (T_f) have been used (Zhao et al., 2006; Ghasemi et al., 2009; di Alessandro et al., 2012; Pinzón et al., 2019c). The site fundamental period is a parameter that characterizes the dynamics conditions of the soil and has been used as a proxy for soil amplification in ground-motion prediction models (di Alessandro et al., 2012). There are different methods to estimate the

fundamental period, but the most used are those based on the horizontal-to-vertical spectral ratios (HVSR). One is the conventional HVSR with the Fourier amplitude spectra from the S-wave window. This approach has been used to determine different dynamic characteristics of the ground through micrometer measurements (Nakamura, 1989; Alfaro et al., 2001; Caselles et al., 2010) and strong-motions from earthquakes (Nagashima et al., 2014). The ratio is defined by the following expression:

$$HVSR_{Fourier} = \frac{H_F}{V_F} \tag{56}$$

where H_F and V_F are the horizontal and vertical Fourier amplitude spectra of ground-motion determined with the S-wave window, respectively.

Another more recent technique is the one based on the proposal of Zhao et al. (2006). With this approach, a site classification for Japan was determined from all the seismic records available on each station (Zhao et al., 2006). The method is based on the estimation of the spectral ratio H/V from the acceleration response spectra with a 5% of damping for the horizontal components (SA_H) and the vertical (SA_V) (see Equation 57).

$$HVSR_{SA(5\%)} = \frac{SA_H}{SA_V} \tag{57}$$

Zhao et al. (2006) found that the use of averages among all the HVRS obtained at each station eliminates extreme peaks or anomalies. Besides, they observed that these averages are not strongly affected if data is segregated by hypocentral distance, magnitude or depth.

In Costa Rica, the strong-motion network (CRSMN) operates since 1983 and is administrated by the Earthquake Engineering Laboratory at the University of Costa Rica (LIS-UCR for its acronym in Spanish). The LIS-UCR is in charge of recording, processing and storing all acceleration records for academic and research purposes. The network has more than 150 active accelerometric stations around the country. Further details about the network can be found in Moya-Fernández et al. (2020).

To classify the site conditions of this network, based on existing regulations, is essential to have V_{S30} measurements on each station. The main issue is that only the 20% of the accelerometric station has been measured. The lack of data due to the high cost of measurements and other issues, introduces uncertainty in the estimation of the site conditions that directly affect the seismic hazard studies carried out in the country. In recent studies, several relations between the site fundamental period, the topography and the V_{S30} were found (Wald and Allen, 2007; Cadet et al., 2011; Pinzón et al., 2019d). These relations cannot be used to classify Costa Rican stations since they depend on the geomorphology of the region. The objective of this paper is to define a relation between the site fundamental period and the V_{S30}, and thus be able to classify stations that do not have V_{S30} measurements. The fundamental period values are estimated from the recorded ground motions at each station. Finally, a classification based on V_{S30} and T_f is proposed.

D.3 Average shear-wave velocity of the top 30 m (V_{S30})

In the last two years, V_{S30} have been measured in 35 accelerometric stations (22.3% of the network) with the aim of improving the existing classification. To obtain V_{S30} values, the stations of the CRSMN were scanned using the multichannel analysis of surface waves (MASW) geophysical method. The MASW is one of the most used seismic recognition methods where the elastic condition (stiffness) of the soil is evaluated. In this method, the velocity of the surface-waves is measured at different frequencies, obtaining the depth variation of the shear-wave velocity (V_S) from the measured soil profile. The variation of velocity at different frequencies is mainly attributed to the stratification

of the S-waves velocities whose values are obtained with a numerical inversion system. In Figure D1, the shear-wave velocity profile from the accelerometric stations Puntarenas-Cóbano (PCOB) and Puntarenas-Paquera (PPQR) are presented. These stations present V_{S30} values of 407.5 and 241.1 m/s respectively.

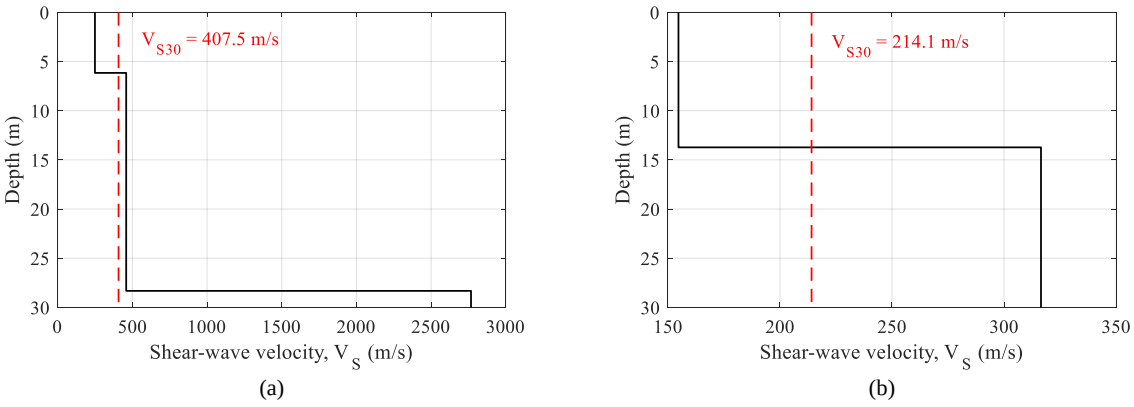

Figure D1: Shear-wave velocity profiles from stations (a) PCOB and (b) PPQR.

D.4 Fundamental period through HVSR

Because almost 80% of the stations do not have measured values of V_{S30}, it was decided to determine the fundamental period of each site (station) through horizontal-to-vertical spectral ratios (HVSR) and fill the gap produced by the lack of information. To estimate site fundamental periods, the average of the HVSR obtained from all the records available at each station is calculated with $\text{HVSR}_{SA(5\%)}$ and $\text{HVSR}_{Fourier}$. Then, the average of both fundamental periods (from both methods) is estimated, obtaining a unique value per station. Records with high acceleration values were discarded (PGA $>$ 0.30 g), preventing fundamental period values from high deformations that could lead to a nonlinear response of the soil (Pinzón et al., 2019c). In Figure D2, the results obtained from the HVSR of the accelerometric stations PCOB and PPQR are exposed. The HVSR are presented normalized by the maximum value. Site fundamental periods of 0.25 and 0.63 s were obtained in PCOB and PPQR stations respectively. $\text{HVSR}_{Fourier}$ presents several peaks while the $\text{HVSR}_{SA(5\%)}$ has a smoother shape. In both cases, the fundamental period was properly captured. This method was applied to the entire network, obtaining the site fundamental period at the 157 stations. A comparison of the results obtained with the $\text{HVSR}_{SA(5\%)}$ and $\text{HVSR}_{Fourier}$ for all the stations is shown in Figure D3.

D.5 V_{S30} and site fundamental period relation

The V_{S30} values measured in the 35 stations were related to their site fundamental period. Results from the relation are observed in Figure D4. As seen in the figure, the relation follows a bilinear trend with a constant value of V_{S30} (260 m/s) in sites with a fundamental period higher than 0.5 s. Similar results were obtained in the United States from Central and Eastern North America (CENA) sites (Hassani and Atkinson, 2016). The bilinear model is defined by the following equations:

$$log_{10}(V_{S30}) = 0.88\, log_{10}(1/T) + 2.15 \qquad T < 0.5\, s \tag{58}$$

$$log_{10}(V_{S30}) = log_{10}(260) \qquad T \geq 0.5\, s \tag{59}$$

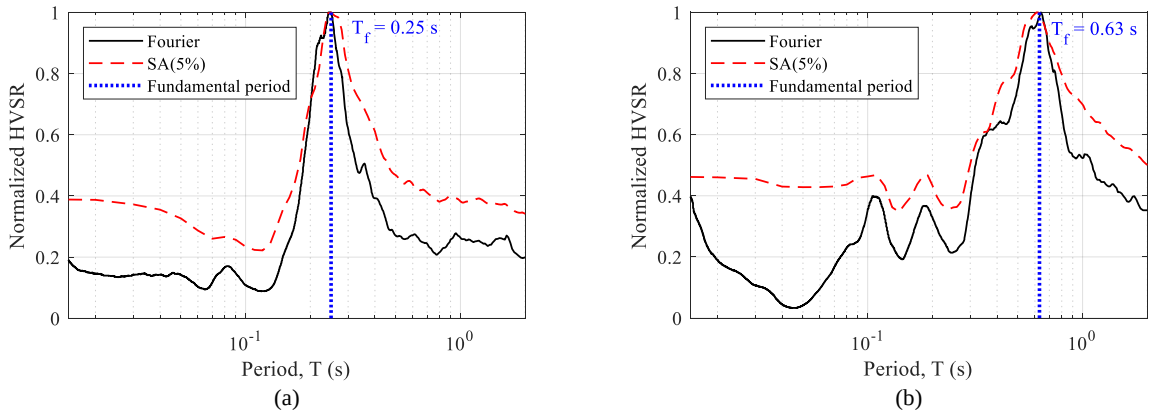

Figure D2: Horizontal-to-vertical spectral ratios normalized by the maximum amplitude value and the site fundamental period from stations (a) PCOB and (b) PPQR.

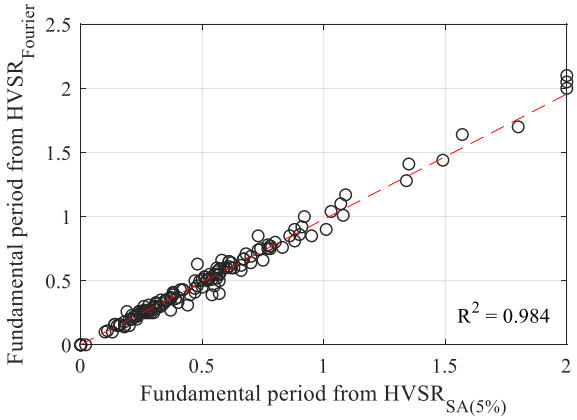

Figure D3: Comparison between the site fundamental periods obtained through $\text{HVSR}_{SA(5\%)}$ and $\text{HVSR}_{Fourier}$.

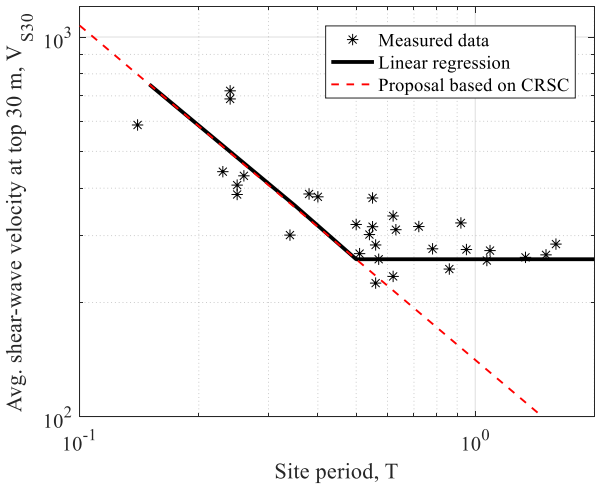

Figure D4: Measured V_{S30} values at the stations of the Costa Rican Strong-Motion Network plotted against the site fundamental period values (T_f) obtained from HVSR. The bilinear model (continuous line) and the proposed model based on the Costa Rican Seismic Code (dashed line) are depicted.

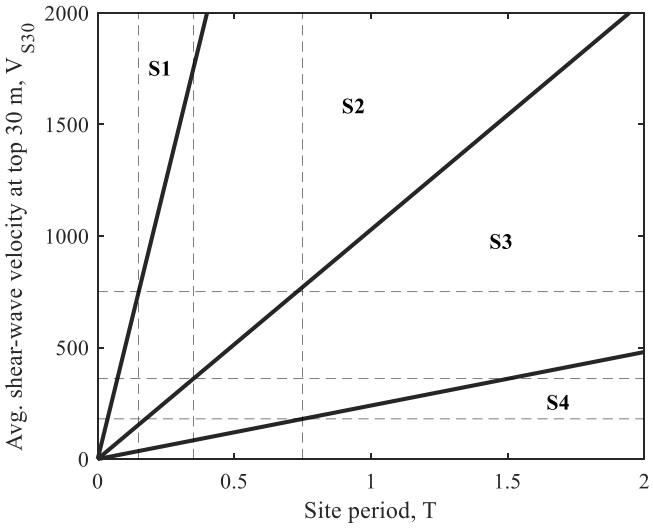

Figure D5: Site classification proposal based on V_{S30} and site fundamental period values.

From these results, different ranges of fundamental periods were assigned to the site classes from the CRSC based on V_{S30} values. The proposed classification is shown in Table D1. Sites with fundamental periods less than 0.15 s are considered rock sites (S1), between 0.15 and 0.35 s hard soils (S2), 0.35 and 0.75 s soft soils (S3) and sites with fundamental period higher than 0.75 s are very soft soils (S4). To assign this classification, only Equation 58 was used (see the dashed line of Figure D4). Equation 59 was neglected since sites with very soft soils (S4) could not be classified.

Table D1: Site classification of the Costa Rican Seismic Code, NEHRP equivalence, V_{S30} ranges and site fundamental periods proposed.

Site class based on Costa Rican Seismic Code (CRSC)	NEHRP equivalence	Shear-wave velocity of top 30 m	Site fundamental period
S1 (rock)	A + B	$V_{S30} > 750$ m/s	$T_f < 0.15$ s
S2 (hard soil)	C	$360 < V_{S30} \leq 750$ m/s	$0.15 \leq T_f < 0.35$ s
S3 (soft soil)	D	$180 < V_{S30} \leq 360$ m/s	$0.35 \leq T_f < 0.75$ s
S4 (very soft soil)	E	$V_{S30} \leq 180$ m/s	$T_f \geq 0.75$ s

In order to classify stations with both V_{S30} and site fundamental period values, a graphic with three-lines and four-areas is proposed (see Figure D5). Each area (triangle) represents a site class based on the CRSC. The lines are plotted from the intersection between values assigned to each site class (see Table D1). The assigned classification at each station will be the one corresponding to the area where the pair of values ($V_{S30} - T_f$) falls. With this proposal, both parameters take relevance and are compensated, reducing the differences due to possible errors in measurements or interpretations. Using this classification, stations PCOB and PPQR are classified as S2 and S3 respectively.

D.6 CRSM site characterization

From the 157 stations of the network, 35 were classified with the proposal described above and the other 122 were categorized only with their site fundamental period using Table D1 ranges. In Figure D6, a map of Costa Rica with the geographic distribution of the accelerometric stations and their assigned site class is shown. A total of 12 stations were classified as rock sites, 51 as hard soils, 67 as soft soils and 27 as very soft soil (see Figure D7). A complete list with the assigned site class of

each station is available at the LIS-UCR website (http://www.crsmd.lis.ucr.ac.cr/?id=Estaciones). In Figure D7b, the mean value of the HVSR per site class, estimated from ratios of all the stations is exposed. The shapes of the mean HVSR values correspond to the expected. The rocky sites have a flat shape with amplification values less than two, while sites S2, S3 and S4 have amplification values around three in the range of periods assigned on each site class (see Table D1).

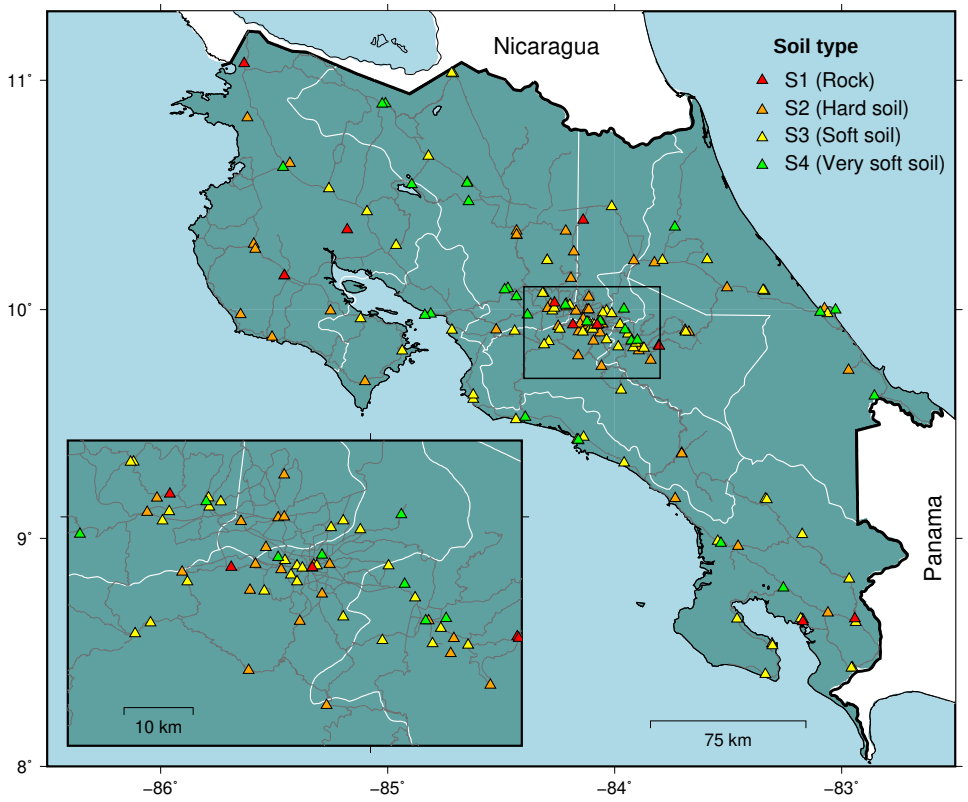

Figure D6: Map with the geographical distribution of the accelerometric stations with the assigned soil class.

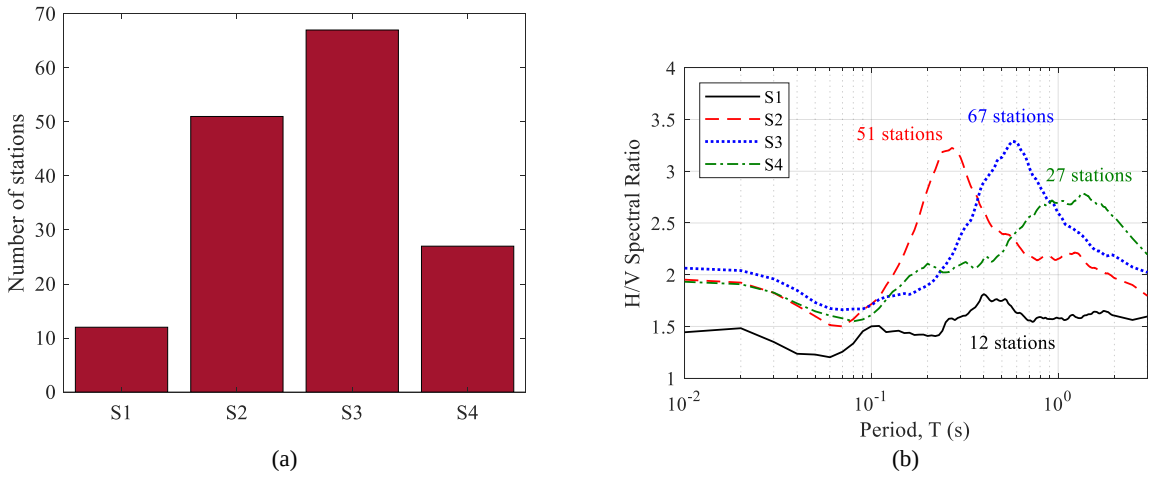

Figure D7: (a) Number of stations per site class and (b) mean HVSR from all the stations per site class.

D.7 Conclusions

In this paper, a site classification has been assigned to the stations of the Costa Rican Strong-Motion Network. A total of 157 stations were classified based on V_{S30} measurements and the site fundamental period values obtained from HVSR of recorded ground-motions. This classification arises from the relationship between the T_f and the V_{S30} values measured in 35 stations. Because the current classification is based on the V_{S30}, the proposal has the advantage that stations that do not have V_{S30} measurements can be classified using the T_f calculated from the earthquake acceleration records. We recommended that stations that do not have V_{S30} measurements should be measured to obtain more accurate results. With this classification, since it considers the fundamental period, we guarantee that sites assigned in the same class have an equivalent dynamic response. This fact plays an important role in the assessment of structures when ground-motion records are used for deterministic and/or probabilistic time-history analyses, decreasing uncertainty and improving the results for a specific region. The influence of this classification on the definition of new ground motion prediction model, compared to the existing/traditional ones remains a significant and interesting issue.

E Appendix. Do Directionality Effects Influence Expected Damage? A Case Study of the 2017 Central Mexico Earthquake

Based on the published article: Pinzón, L. A., Pujades, L. G., Diaz, S. A., & Alva, R. E. (2018). Do Directionality Effects Influence Expected Damage? A Case Study of the 2017 Central Mexico Earthquake. *Bulletin of the Seismological Society of America, 108*(5A), 2543–2555. doi: 10.1785/0120180049
Journal URL: doi.org/10.1785/0120180049
FUTUR UPC URL: futur.upc.edu/23504564

E.1 Abstract

We analyze the case of a building that collapsed in a multifamily complex of Tlalpan borough in Mexico City during the 19 September 2017 Central Mexico earthquake. Despite having similar materials and similar structural and geometric properties, this was the only building that collapsed in the complex. A structural analysis of the building and a study of the soils' predominant periods indicated that resonance effects, if any, would not be significant. However, phenomena related to the anomalous performance of buildings in dense urban areas, such as geological soil, soil-structure interaction, and soil-city interaction effects were also investigated. A detailed analysis of the directionality of seismic actions recorded at nearby accelerometric stations and of the azimuths of sound and damaged buildings pointed to directionality effects as responsible for the collapse of the building.

Subsequently, a set of fifty-eight, two-component acceleration records of the earthquake in the city was used to perform a thorough directionality analysis. The results were then compared with the foreseen uniform hazard response spectra and the design spectra in the city. Seismic actions in the city due to this earthquake were stronger than those corresponding to the uniform hazard response spectra. In addition, although design spectra have been significantly improved in the new 2017 Mexican seismic regulations, they were exceeded in eleven of the fifty-eight analyzed spectra. In four of these eleven cases, the design spectra were exceeded due to directionality effects. These results confirm the necessity of considering directionality effects in damage assessments, in strong motion prediction equations, and in design regulations.

E.2 Introduction

The 19 September 2017 Central Mexico earthquake seriously affected Mexico City. In a multifamily complex belonging to the Civil Service Social Security and Services Institute (ISSSTE) in the Tlalpan borough, interestingly enough, only one building collapsed within a cluster of constructions that had the same structural typology, geometry, and materials. Similar facts were reported by Vargas-Alzate et al. (2018) in the San Fernando neighborhood, during the 2011 Lorca earthquake in Spain. During field work after earthquakes, it is not rare to find collapsed buildings that have the same structural properties as other undamaged, standing buildings nearby. An easy explanation would be that the collapsed building suffered from construction faults, which severely affected its seismic capacity and strength. However, it is well-known that the intensity of ground motion may vary significantly from site-to-close site and is not uniform in all directions, so other effects could significantly increase the seismic actions withstood by specific buildings, thus increasing the damage in comparison with nearby buildings. These effects are analyzed in this paper. First, a structural analysis of the building is performed to determine its modal-eigen properties. Several potential amplification effects due to soil-structure and soil-structure-soil (city-site) interaction are analyzed. Subsequently, attention is paid to directionality as the most likely effect explaining the differences in damage observed. Finally, overall

directionality effects of the strong motion data of the 19 September 2017 earthquake, recorded at the Accelerographic Network of Mexico City (see the Data and Resources Section) are also analyzed.

E.3 Mexico City and the 2017 Central earthquake

E.3.1 Seismic hazard in Mexico City

Mexico City is a zone with high seismic hazard due to the following conditions: i) the city is in a country where tectonic plates and active faults coexist. The Pacific coast is part of the Ring of Fire, which contains the most active seismic zones on Earth. In a seismicity study of the 20th century in Mexico, Kostoglodov and Pacheco (1999) found that, on average, there are five earthquakes of magnitude $M_W \geq 6.5$ every four years. Every year, over a hundred earthquakes with $M_W \geq 4.5$ are registered. In the 21st century, 72 earthquakes with $M_W \geq 6$ have been reported; ii) soft soils therein strongly amplify the seismic waves. These conditions were clearly highlighted during the 1957 ($M_W = 7.7$) and 1985 ($M_W = 8.1$) earthquakes. Since then, the conditions of Mexico City have been the object of study (Singh et al., 1988; Chávez-García and Bard, 1994).

E.3.2 The 2017 Central Mexico earthquake

Like the dates of the 28 July 1957 and 19 September 1985 earthquakes, the 19 September 2017 is a day that no Mexican will forget. An earthquake of magnitude $M_W = 7.1$ on the Richter scale occurred, exactly 32 years after the 1985 Mexico City earthquake. The earthquake was reported as an intraplate event, in the Cocos oceanic plate, at a depth of 57 km and with an epicenter close to 120 km from Mexico City (data from the Mexican Seismological Service, SSN-UNAM).

The Civil Protection in the Mexican Ministry of the Interior (SEGOB) (see Data and Resources) reported 369 fatalities caused by the event (228 in Mexico City, 74 in Morelos, 45 in Puebla, 15 in Mexico State, 6 in Guerrero, and 1 in Oaxaca). Regarding structures, 38 collapsed buildings were reported in Mexico City. Although this earthquake had one degree less magnitude than the 1985 earthquake (in other words, it was 32 times smaller), a high amount of structural damage was reported. This catastrophic situation was attributed to the fact that the earthquake hypocenter was much closer than that of the 1985 earthquake (400 km approx.). Moreover, a different frequency band was excited. The 1985 event had the greatest effect on zones with soft soils (with longer resonant periods), whereas this event generated greater acceleration in the transition zones where the predominant periods of the soils are shorter. These effects can be seen in Figures E1 and E2, in which the response spectra of the horizontal components of both earthquakes are shown and compared. The response spectra correspond to very close stations that have the same type of soil. In Figure E1, the values for short periods of approximately 0.5 seconds show an amplification in the spectral response for the 2017 earthquake.

Both stations are in the transition zones, so it can be observed clearly that the 2017 event had a greater effect in this area than that of the 1985 event. In Figure E2, the response spectra for the horizontal components of two stations with very soft soil (seismic zone III C, according to the Mexico City seismic codes) are presented, showing that the 1985 earthquake generated higher spectral accelerations than the 2017 earthquake.

E.4 The case of the Tlalpan 1C building

The building identified as 1C is part of the ISSSTE multifamily complex development consisting of 11 masonry mid-rise buildings (Figure E3). The 1C building has the same structural typology, geometry,

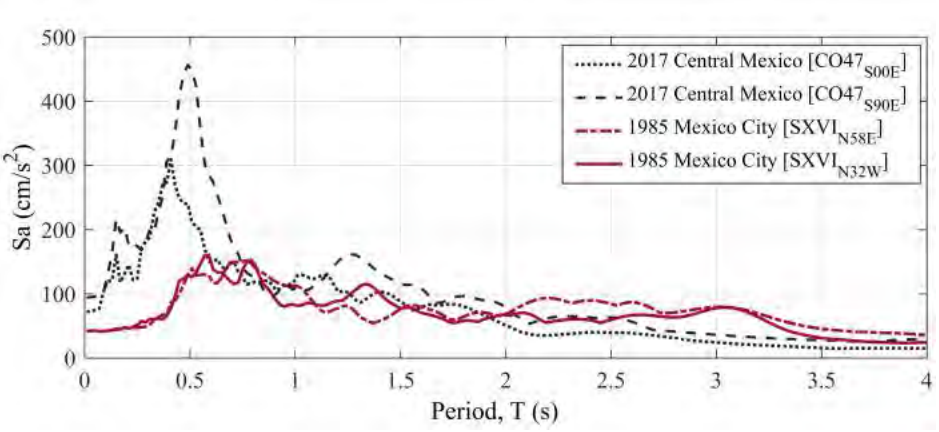

Figure E1: Comparison between the response spectra (5% damped) of the horizontal as-recorded components from the 1985 Mexico City earthquake (SXVI station – seismic zone II) and the 2017 Central Mexico earthquake (CO47 station – seismic zone II).

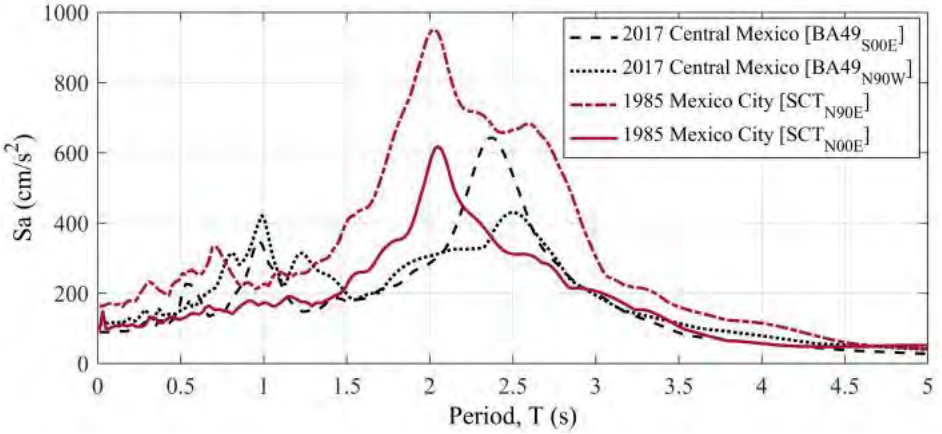

Figure E2: Comparison between the response spectra (5% damped) of the horizontal as-recorded components from the 1985 Mexico City earthquake (SCT station – seismic zone III C) and the 2017 Central Mexico earthquake (BA49 station – seismic zone III C).

and materials as another six buildings in the complex (2A, 2B, 2C, 4A, 4B and 4C). However, this building was the only one that collapsed on the site (see Figure E3b). According to official reports, buildings 2A, 3A and 3C did not suffer significant damage, buildings 2B, 2C, 3B, 1A, 1B, 4A, 4B and 4C suffered repairable damage, and building 1C collapsed at higher levels.

The studied building had six stories and contained 30 apartments. The first level was dedicated to offices and commerce. The shape of the building was rectangular (7.7 x 56.4 m) and 12.8 m high. The structure used orthogonal confined hollow brick masonry walls as seismic resistant elements and reinforced concrete slabs as horizontal diaphragms.

The complex is located within transition seismic zone II in the south of Mexico City; 113.5 km from the epicenter. Buildings in the complex were designed and constructed according to the Mexican State Construction Code of 1942 with a seismic coefficient of 0.025 (see the MSCC 1942 for details on this coefficient). The construction was completed in 1957 after the earthquake of the same year (7.7 M_W) and no major damage due to that earthquake or the earthquake of 19 September 1985 were documented.

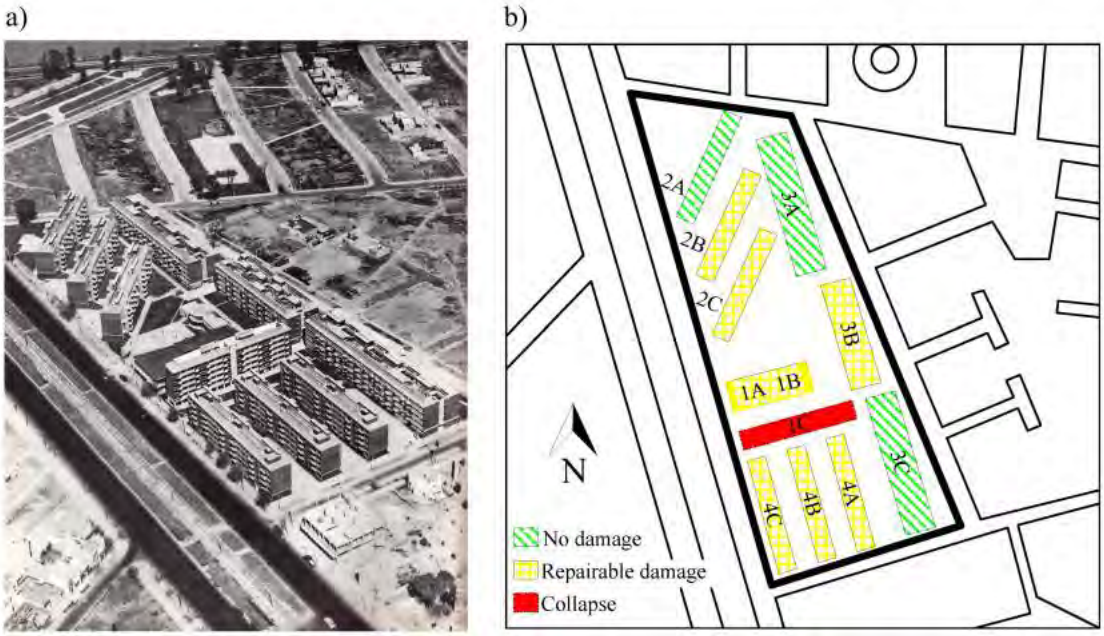

Figure E3: (a) ISSSTE multifamily complex development, Tlalpan, Mexico City, 1957 (see Data and Resources). (b) Plan view of the complex. Damage levels in the complex are shown.

Table E1: Modal properties, period (T), and mass participation factors (W) of the studied building.

Mode	Weak axis		Strong axis	
	T (s)	W (%)	T (s)	W (%)
1	**0.30**	0.68	**0.25**	0.71
2	0.21	0.18	0.08	0.15
3	0.10	0.12	0.03	0.09

E.4.1 Structural analysis

To evaluate the amplification and other effects that could affect the structural behavior of the Tlalpan complex, a 3D model was developed. The plans of the 1C building and SAP2000 software (see Data and Resources) were used. Figure E4 shows a sketch of the building.

The weak and strong axes are depicted. First, a modal analysis was performed to obtain the modal properties of the building. The period and mass participation factors for each mode are shown in Table E1. The predominant periods obtained in the weak and strong axes were 0.30 and 0.25 s respectively. A dynamic analysis (time history) was also performed, using the ground motions from stations DX37 and AO24. The records from these stations were used due to their proximity to the building complex. The analysis was performed taking into account the orientation of the buildings (see Figure E3) assigning their corresponding rotated ground-motion pairs according to the following azimuths: 344° (1C), 294° (2A, 2B and 2C), and 254° (4A, 4B and 4C).

The peak parameters, base shear (F), and roof displacement (δ) obtained in the dynamic analysis are shown in Table E2. The results show maximum values in the weak axis of the 1C building in both analyses. The overall maximum was obtained through the analysis performed with the closer station DX37. This gave values of 8249 kN of base shear and 0.87 cm of roof displacement for the weak axis of the collapsed building (1C).

Inter-story drifts and shears in each story were estimated for the buildings 1C and 4 (A, B and C) (see Figure E5).

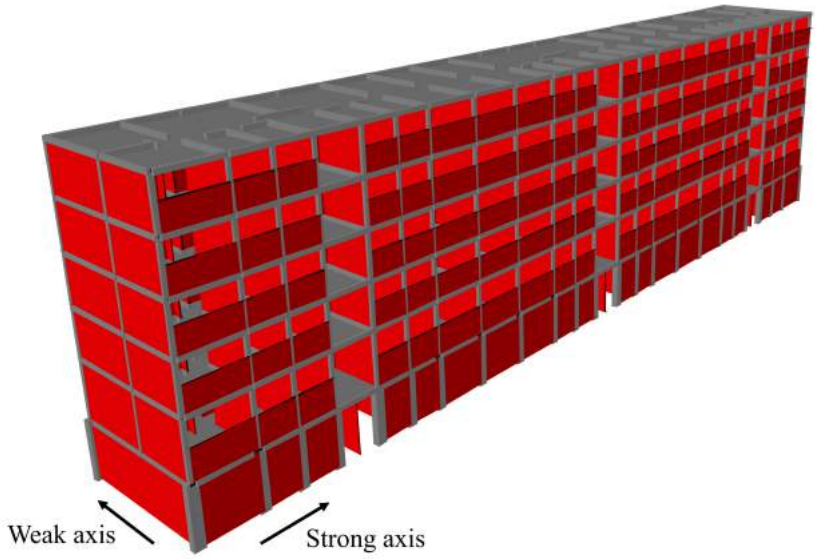

Figure E4: 3D building model.

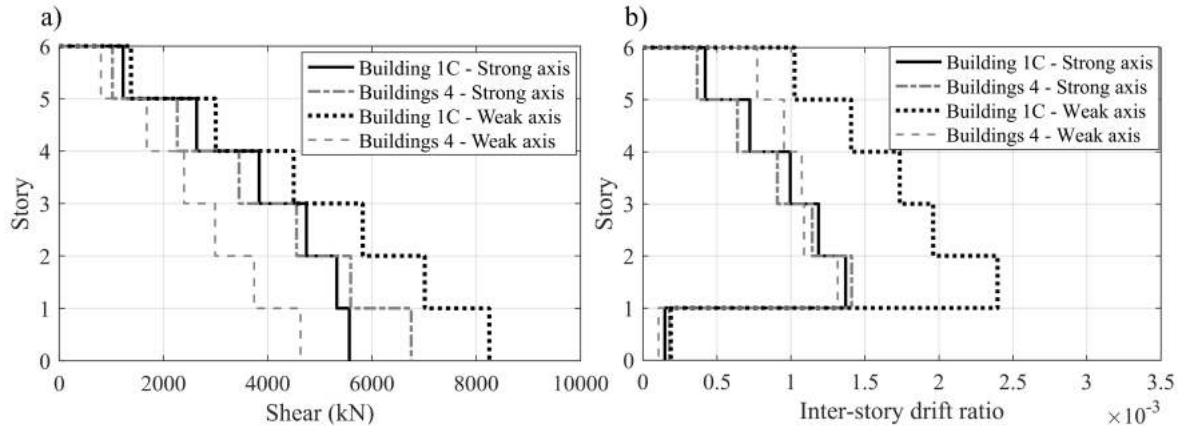

Figure E5: (a) Shear and (b) inter-story drift comparison between the 1C and 4A, B and C buildings obtained through the time-history analysis with the ground motion of the DX37 station.

Table E2: Maximum base shear (F in kN) and maximum roof displacements (δ in cm) generated in each building through the time-history analysis.

Station	1C building				2 (A, B, and C) buildings				4 (A, B and C) buildings			
	Weak axis		Strong axis		Weak axis		Strong axis		Weak axis		Strong axis	
	F	δ	F	δ	F	δ	F	δ	F	δ	F	δ
DX37	8249	0.87	5567	0.48	6339	0.74	5392	0.41	4629	0.50	6752	0.46
AO24	4953	0.61	3679	0.28	4891	0.59	3603	0.28	3406	0.41	4230	0.47

The weak axis of the 1C building had the maximum inter-story drifts and shears in each story. Moreover, the inter-story drifts indicated that the base plant was less deformed, due to its higher rigidity, and show why the upper stories collapsed while the first floor remained intact (pictures of the damage reported in the buildings of the complex after the earthquake can be seen in the reports; see Data and Resources). The structural analysis allowed us to identify a brittle type failure observed in the stories above the first floor due to the mechanical properties of the structural typology, that is, a low-ductility masonry building. Thus, the building would collapse with relatively small displacements (Sucuoglu and Erberik, 1997; Bothara et al., 2010). Effects of stiffness irregularity and strength discontinuity in elevation were also seen. These effects were due to the abrupt change in column size in the first floor and above, increasing the inter-story drift in the first story (the soft story effect). In addition, a short-column effect, due to the window openings was observed; this effect amplifies the moment demand in the first story. All these effects become relevant when seismic action is applied to the building, altering the structural behavior and increasing the risk of collapse.

E.5 Phenomena related to anomalous performance of buildings

Several site effects, concerning both the soil geology and the structure itself, may influence the seismic actions beneath buildings (Menglin et al., 2011) and, therefore, might be responsible for anomalous seismic responses and performance. Relevant, well-known effects that alter input ground motions are: i) geological/geotechnical soft soil (GSS), ii) soil-structure interaction (SSI) (Guéguen et al., 2000; Laurenzano et al., 2010), iii) site-city interaction (SCI) (Guéguen et al., 2002; Kham et al., 2006; Semblat et al., 2008), and iv) directionality effects. In this section, these effects are described and discussed to determine which of them could be responsible for the response of the 1C building.

E.5.1 Geological soft soil (GSS) effects

The geological characteristics of the site affect the frequency content and duration of ground motions. This is a well-known effect, and seismic codes allow for it by means of soil classes. Depending on the thickness, geometry, and geotechnical properties of the soil deposits, soft-soils amplify free-field motions in the long-period range (Elnashai and Di Sarno, 2008). Then, the closeness between amplified periods of soils and fundamental periods of buildings would cause the effect known as site resonance. Thus, from information on the soil's amplification frequencies and on fundamental periods of vibration of the buildings, likely resonant effects can be detected. There are many techniques and procedures to deal with soft soil transfer functions. Several methods are based on spectral ratios, using both microtremor and earthquakes. Below, the predominant periods of the soils in the site are estimated, to investigate whether soil effects could be responsible for the anomalous response of the 1C building. The available historic strong-motion data recorded at the three closest stations (DX37, CH84 and AO24) were collected and analyzed. The H/V spectral ratio method proposed by Zhao et al. (2006) was then used to estimate the predominant site periods. Figure E6 shows the results obtained at each station. For the DX37 and AO24 stations, a predominant period of T = 1.0 s was obtained, and a value of 1.3 s was obtained for the CH84 station.

Moreover, a Mexico City structural code application SASID (NTCDS-RCDF, 2017) enabled us to obtain the predominant periods of soils in these sites. The values obtained with SASID are in good agreement with those obtained with H/V ratios (Table E3). The site fundamental period of the Tlalpan complex was also estimated. We obtained a value of T = 0.95 s, which is close to that corresponding to strong-motion stations DX37 and CH84. Notably, the geotechnical report after the September 2017 earthquake (see Data and Resources), declared uniformity in the soil underneath the

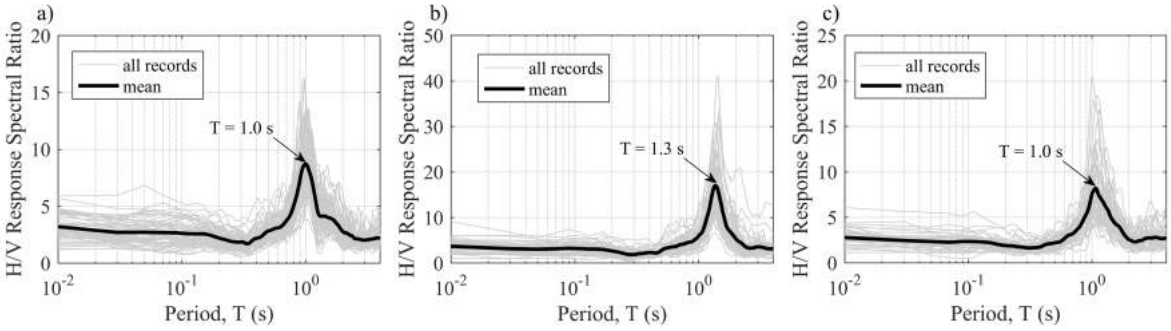

Figure E6: H/V response spectral ratios for the strong-motion stations (a) DX37, (b) CH84, and (c) AO24.

Table E3: Site fundamental periods obtained through SASID Software and Horizontal-to-Vertical (H/V) Response Spectral Ratio.

Site	Site period, T (s)	
	SASID	H/V ratio
DX37	0.8	1.0
CH84	1.3	1.3
AO24	1.0	1.0
Tlalpan complex	0.95	-

buildings. Therefore, the same site predominant period (T = 0.95 s) was considered for the entire complex. The periods of the buildings in the area (see Table E1) are far from these amplifying periods, thus making it unlikely that soil effects could be responsible for the bad response of the 1C building.

E.5.2 Soil-structure interaction (SSI)

Soil structure interaction (SSI) can be defined as the coupling between a structure and its supporting medium during earthquakes (Thusoo et al., 2015). Often, this effect can be seen in structures built on soft-soils (Bard et al., 2005) and it was responsible for a dramatic increase in the damage on the Hanshin expressway in the Kobe earthquake (Mylonakis et al., 2000). However, until a few years ago, seismic codes ignored the SSI effect on the seismic demand on buildings, based on the consideration that SSI effects reduce demands on structures, so that it is more conservative to apply conventional structural regulations. However, recent work has shown that it is not always conservative to ignore SSI (Givens, 2013). SSI modifies the free-field ground motions due to inertial and kinematic interaction effects. The SSI effect concerns the joint response of three connected systems: the structure, the foundations, and the soil underlying and surrounding the foundations. These three connected systems modify the building and foundation responses and the free-field seismic actions (Tuladhar et al., 2008).

The National Institute of Standards and Technology Grant Contract Report [NIST GCR] 12-917-21 (NIST-GCR-12-917-21, 2012) synthesizes the state-of-the-art of SSI and provides guidelines and techniques for simulating and modeling SSI effects in engineering practice. In this report, the structure-to-soil stiffness ratio, $r = h/(V_s T)$, is suggested as a relative measure for determining when SSI effects may become significant. h is the effective height to the center of mass for the first mode shape, V_s is the effective shear wave velocity, and T is the period of the fundamental mode of vibration. Values of r above 0.1 would indicate that SSI effects should be considered. From the available information (see the Data and Resources section), h = 8.6 m and Vs = 475 m/s, and soil class C [according to FEMA (2004)] have been obtained for the 1C building, so that the values for periods 0.30 and 0.25

(see Table E1) are 0.06 and 0.07 respectively. Because these ratios are less than 0.10, strong inertial SSI effects are not expected. In any case, due to the similarity of the structural and soil properties of the buildings in the complex, SSI effects would not explain the singularly bad performance of the 1C building.

E.5.3 Site-city interaction (SCI)

In dense urban areas subjected to strong seismic actions, the multiple interactions between soil, layers, and buildings is known as the site-city interaction (SCI) effect. SCI effects appear when there is resonance between buildings and soils. Building density and regular or irregular city configurations play a crucial role in energy distribution inside the city (Guéguen et al., 2002, 2012; Semblat et al., 2002, 2004, 2008; Kham et al., 2006; Bard et al., 2005). SCI in cities with a regular configuration reduces the top motion of buildings with respect to the single-building case and significantly reduces the ground motion inside the city. In several cases, the energy of the ground motion may be reduced by 50%. On the contrary, ground motion may increase outside the city; the energy radiated outside the city may involve about 10% of the free-field motion (Kham et al., 2006). In the case of irregular dense distributions of buildings, the coherency among the building responses diminishes resulting in a stronger decrease in the spatial correlation of the ground motion. This loss of coherency may result in constructive interference that could produce local peaks, in which the site-to-site energy variability may reach 50% (Kham et al., 2006). Therefore, despite there being no resonance conditions in the Tlalpan residential complex, SSI effects could not be fully discarded. A more detailed analysis would require more high-quality data and information, and is beyond the scope of this study.

Because directionality effects emerged as the factor that was probably responsible for the anomalous performance of the 1C building, these effects were analyzed in more detail. The influence of the azimuth of the buildings on the expected damage and the directionality effects in the response spectra are analyzed below.

E.6 Directionality effects

Directionality effects in seismic actions are evaluated by rotating the two horizontal orthogonal as-recorded ground motions, usually acc_{E-W} and acc_{N-S}, according to the following equations:

$$acc_x(\theta) = acc_{E-W} \cdot cos(\theta) + acc_{N-S} \cdot sin(\theta) \tag{60}$$

$$acc_y(\theta) = -acc_{E-W} \cdot sin(\theta) + acc_{N-S} \cdot cos(\theta) \tag{61}$$

in which θ is the rotation angle. Equations 60 and 61 allows us to obtain new acceleration time histories, $\mathrm{acc}_x(\theta)$ and $\mathrm{acc}_y(\theta)$, in a θ-rotated reference system. Peak ground accelerations (PGA) and acceleration response spectra, Sa (T), for any given period, T, are strongly influenced by the orientation of the recording sensors. The influence of this on the ground-motion prediction equations (GMPE) and on the expected damage of a structure is well-known. A number of studies have analyzed these effects on seismic hazard (Watson-Lamprey and Boore, 2007; Boore and Kishida, 2016; Haji-Soltani and Pezeshk, 2017), on how the angle of incidence of the seismic action influences the performance of a structure (Lagaros, 2010; Torbol and Shinozuka, 2014; Vargas-Alzate et al., 2018) and on the horizontal-to-vertical spectral ratios of micrometers (Matsushima et al., 2017).

E.6.1 Effects on the 1C building

Ground motions may be polarized so that the intensity in a specific direction may be significantly greater. Moreover, as pointed out above (see Figure E4), most of the buildings have strong and weak axes, which depend on the rigidity or flexibility of the building in the directions defined by its principal axes (see Figure E7a). Therefore, a specific ground motion can have a greater effect on the performance of a building, depending on the orientation of these axes with respect to the action. Thus, the demand on the structure may strongly depend on the orientation of the building with respect to the direction in which the maximum intensity of the seismic action occurs, that is, depending on the azimuth of the building [see for instance Huang et al. (2008) and Vargas-Alzate et al. (2018)]. Figure E7b illustrates how the impact of a unitary force varies depending on the orientation of the building. Therefore, the expected damage would depend on the combined effects of the directionality of the seismic actions and the azimuthal orientation of the building. Accordingly, the expected damage will be greater when the strongest seismic forces hit the building in the weak axis direction.

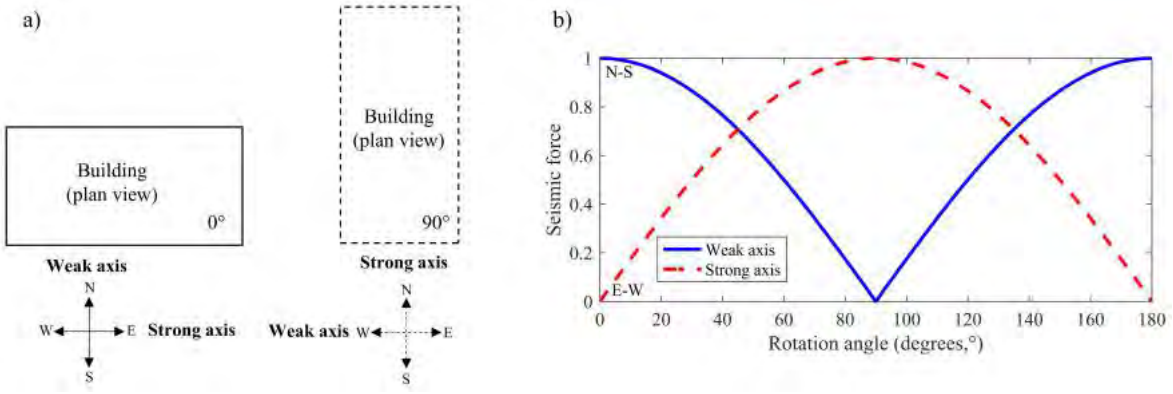

Figure E7: (a) Strong and weak axes of a building and (b) effective seismic forces affecting the strong and weak axes, as a function of the rotation angle.

Noticeably, the 1C building was the only one that collapsed in the Complex (Figure E3b), and, among the buildings with the same geometrical and structural properties it was the only one whose weak axis had an azimuth of 164°, measured from the south (Figure E8). To try to find an explanation for this fact, a thorough analysis of the seismic actions that could likely hit the building was made. For this purpose, the accelerograms recorded at the three closest stations were analyzed (see Figure E9); namely AO24 (2.52 km), DX37 (0.70 km), and CH84 (1.98 km). As a first step, the particle motion during the earthquake in these three stations was displayed (Figure E10). For the closest station, DX37, a maximum acceleration of 196 cm/s^2 was found at an azimuth of 165° measured from the south. This angle is very close to the orientation of the weak axis of the 1C building. This suggests that the building was probably more affected by the earthquake due the combined effects of the directionality of the seismic action and the orientation of its weak axis. The other buildings in the complex were clearly subjected to similar accelerations, but the strongest acceleration did not directly affect their weak axes. Similar results were obtained from strong motion data from the other two stations, CH84 and AO24 (Figure E10). A similar phenomenon was also observed and studied in Lorca, Spain, after the 5.1 M_W magnitude earthquake of 11 May 2011 (Vargas-Alzate et al., 2018).

The PGA and the maximum responses of a single degree of freedom 5% damped oscillator with a period of 0.30 s were also analyzed as functions of the rotation angle. Figure E11 shows the results. The orientations of the weak axis of each building are also shown. Azimuths of 74° and 114°, measured from the south, correspond to the directions of the weak axes of buildings 4 (A, B and C) and 2 (A,

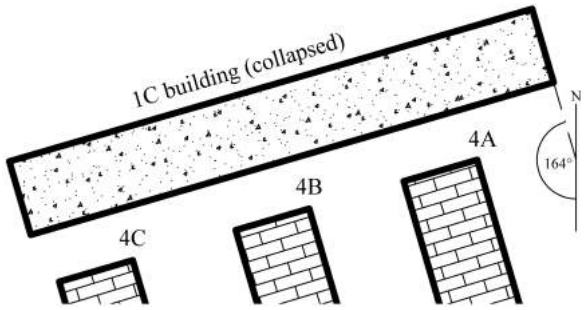

Figure E8: The azimuth of the 1C building measured from the south.

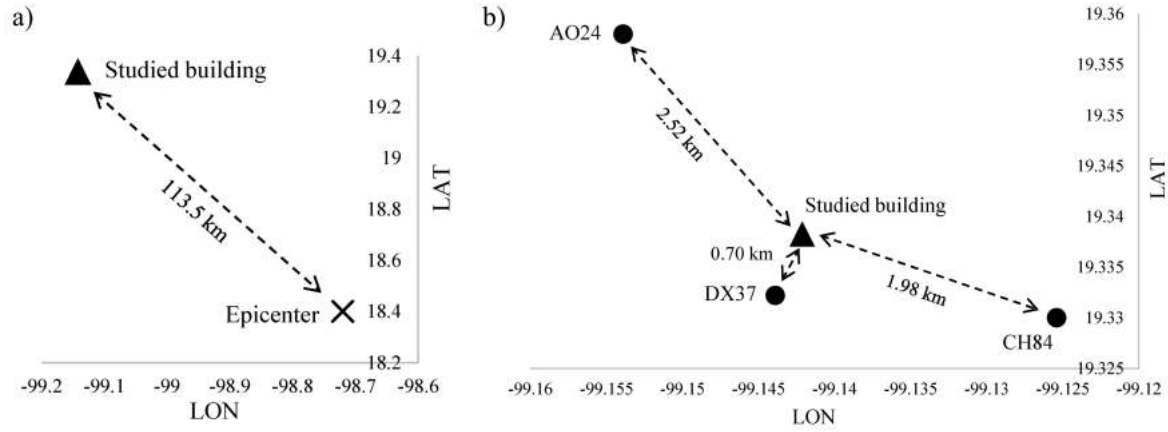

Figure E9: (a) Epicentral distance from the 2017 Central Mexico earthquake to the 1C building. (b) The three accelerographic stations closest to the 1C building site.

B and C) respectively. It can be seen how maximum values of PGA and of the acceleration response of a 5% damped system with a period of 0.3 s were obtained very close to the 164° orientation of the weak axis of the 1C building (see Figure E8), which, accordingly, bore the most unfavorable seismic action. The other buildings in the complex clearly received smaller accelerations in their weak axis.

E.6.2 Ground motions and design spectra

Conscientiousness and awareness of the influence of directionality effects on ground motions and ground motion prediction equations (GMPE) have increased in recent decades [see for instance Boore et al. (2006); Abrahamson et al. (2008); Boore (2010); Shahi and Baker (2014); Bradley and Baker (2015); Boore and Kishida (2016)]. The GMRotI50 Sensor-orientation-independent measure, as proposed by Boore et al. (2006), was considered for the Next Generation Attenuation-West project (NGA-West, Abrahamson et al. (2008)); In the GMRotIpp intensity measure, GM stands for geometric mean, Rot for rotation, I for period-independent, and pp corresponds to the pp-percentile. Later, in 2012, the projects NGA-West2 (Bozorgnia et al., 2012; Shahi and Baker, 2014) and NGA-East (PEER, 2015) used the 50th percentile (pp=50) of the Rotation Dependent measure (RotDpp), proposed by Boore (2010), to update these GMPEs. For existing GMPE worldwide see Douglas (2017). Regarding structural regulations, the ASCE/SEI 7-10 (ASCE, 2010) adopted the measure RotD100 in the ground-motion design maps. These types of updates are of fundamental importance and they must be considered for a proper definition of the seismic hazard.

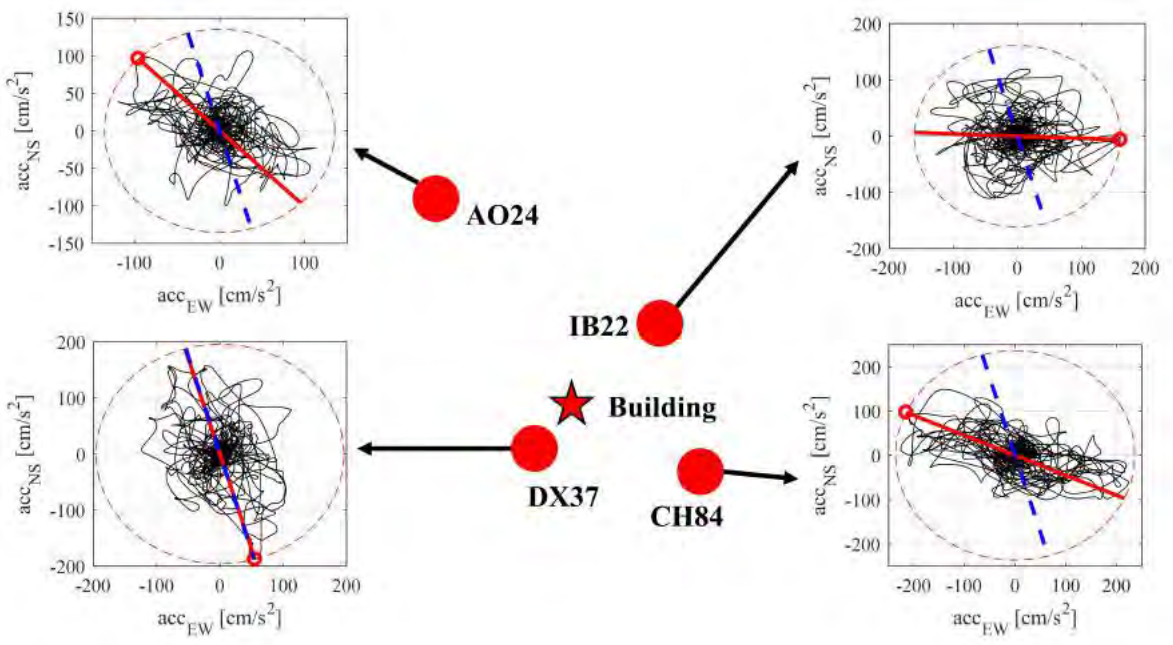

Figure E10: Particle acceleration motions at the four accelerometric stations closest to the 1C building site: DX37 station, CH84 station, IB22 station and AO24 station. The weak direction of the building (dashed blue line) is depicted.

Table E4: Summary of ground motion IMs considered in this study.

IM symbol	Definition*
N-S, E-W	As-recorded horizontal orthogonal components.
GM	Geometric mean.
RotD100	Maximum (100th percentile) values of response spectra of the two as-recorded horizontal components rotated onto all non-redundant azimuths (Boore, 2010).
Larger	The larger of the two horizontal components (Beyer and Bommer, 2006).

* Definitions apply for peak ground acceleration (PGA) and for response spectral accelerations, Sa (T), which are functions of the period, T, of vibration.

In this section, the directionality effects of the 2017 earthquake in Mexico City are analyzed. The results are then compared with the design spectra. In addition to the as-recorded accelerograms, the intensity measures (IM) described in Table E4 are used.

Fifty-eight ground motion (N-S and E-W) pairs, which were supplied by the Accelerographic Network of Mexico City, were selected for the directionality analysis. For comparison purposes, we used the design spectra of the structural design codes for Mexico City, published in 2004 (NTCDS-RCDF, 2004) and more recently in 2017 (NTCDS-RCDF, 2017). With respect to the 2004 regulations, the elastic design spectra without reduction factors were used, both those published in the main section and the alternative method proposed in Appendix A. In addition, the uniform hazard spectrum for each station was added to the comparison. To this end, the SASID A v4.0.2.0 application that proposes the new structural regulation was used (NTCDS-RCDF, 2017).

To assess the directionality effects, the 58 ground motion pairs were rotated (Equations 60 and 61) and their respective 5% damped response spectra were obtained. The rotation was made for the range between 0° and 180°, with increments of $\theta = 1°$. Finally, the RotD100 spectrum was estimated. This spectrum represents the maximum spectral acceleration generated for each 5% damped single-degree-of-freedom oscillator system.

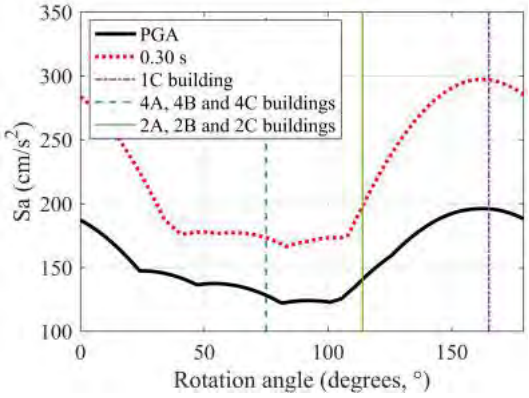

Figure E11: Variation of PGA and spectral acceleration, Sa, of a single-degree-of-freedom 5% damped oscillator with T=0.3 s as a function of the orientation angle, at DX37 accelerographic station. Vertical lines indicate the azimuths, measured from the south, to the weak axis of the 1 (C), 2 (A, B and C), and 4 (A, B and C) buildings.

From the comparison of the spectra, it was found that the elastic design spectrum of the 2004 regulation was not exceeded in only 9 of the 58 stations. However, when the obtained spectra were compared with those provided in Appendix A of the same code, using an alternative method, the design spectrum was exceeded in 15 of the 58 acceleration time histories tested. Concerning the new structural regulations published in December 2017, in 11 of the 58 stations, the proposed elastic design spectrum was exceeded. This represents an improvement with respect to Appendix A of 2004, but several of the new design spectra were still surpassed. Another important point is that, in four of the 11 stations where the new regulation was exceeded, the excess was due to directionality effects (these results are summarized in the Appendix A. The 11 stations where the newer design spectra were exceeded are in areas of stiff to soft soil, 4 in seismic zone I, 3 in zone II (transition), and 4 in zone IIIA. In the zones with softer soils (IIIB, IIIC and IIID), the design spectra were not exceeded at all. This fact agrees with the structural damage reported since most of the buildings that collapsed were in zones I, II and IIIA (see Data and Resources). Figure E12 shows the comparisons of the response spectra for 6 stations: 2 in zone I, 2 in zone II, and 2 in zone IIIA.

In the stations of zone I of stiff soil (Figure E12 a and b), the maximum spectral accelerations occurred for low periods, in the range from 0.3 to 0.6 s, and have a value that exceeds 500 cm/s^2 at the station CP28 and, approximately, 340 cm/s^2 at the station PA34. These spectral accelerations would affect relatively low buildings, those with roughly 3 to 6 stories. In zone II (Figure E12 c and d), spectral accelerations greater than 1 g were estimated at the DX37 station (Figure E12 c), for periods slightly greater than 1 second. Amplification in this period would affect buildings of approximately 10 floors. Finally, the highest spectral accelerations were obtained in the stations of the IIIA zone (Figure E12 e and f). A maximum spectral acceleration of 1600 cm/s^2 was obtained at Station CH84 for a period of approximately 1.4 seconds, and the maximum spectral acceleration at station JC54 was 1200 cm/s^2 for the same period.

E.6.3 Overall directionality effects

Finally, to evaluate IMs with respect to the maximum spectral acceleration (RotD100), ratios were estimated using N-S, E-W, Larger and GM measures (see definitions in Table E4). The E-W component had, on average, values closer to RotD100 than the N-S (see Figure E13). The ratio RotD100/GM had values between 1.20 and 1.30.

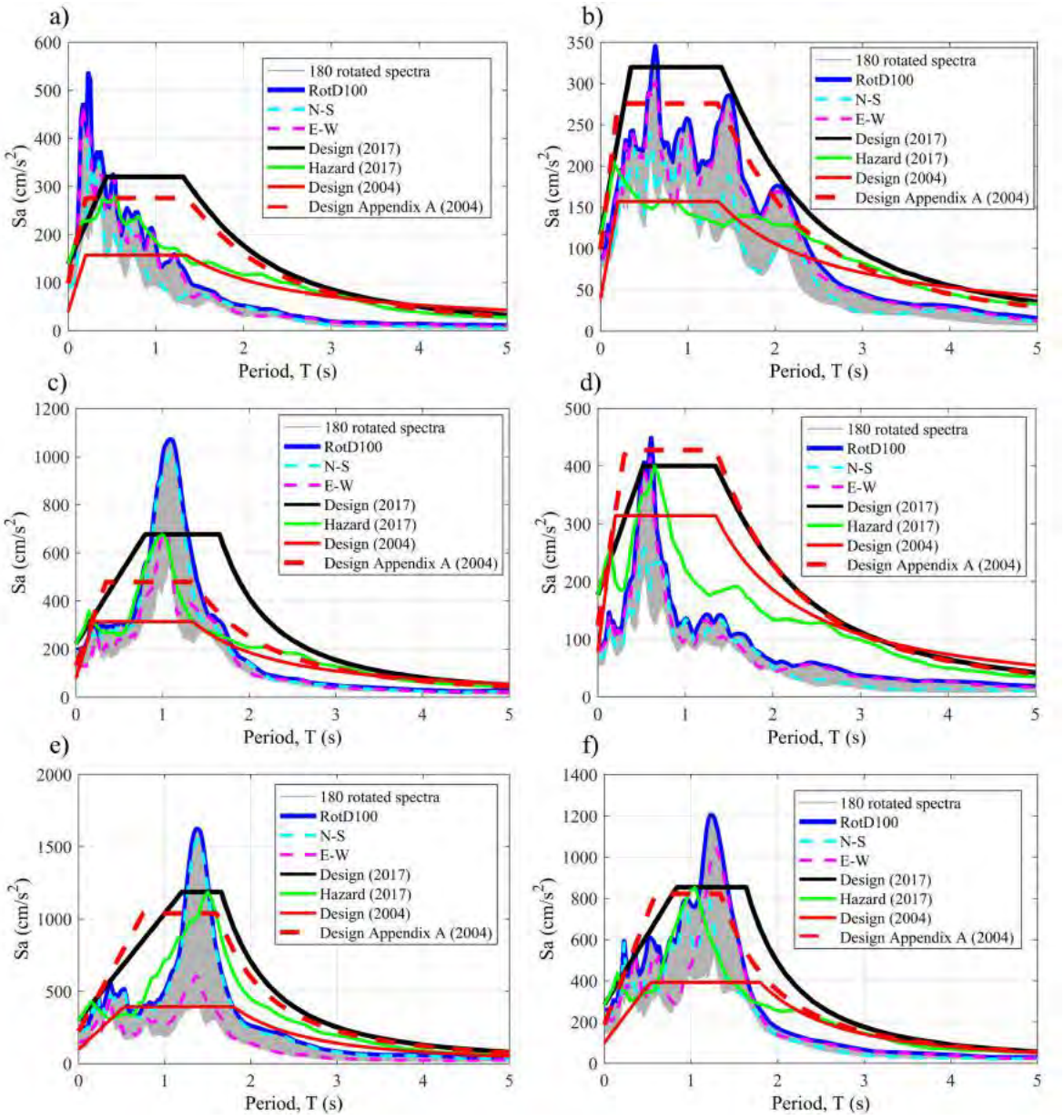

Figure E12: Comparison of response spectra of records at different accelerometric stations in Mexico City, during the 2017 Central Mexico earthquake: (a) CP28 station [zone I], (b) PA34 station [zone I], (c) DX37 station [zone II], (d) EO30 station [zone II], (e) CH84 station [zone IIIA], and (f) JC54 station [zone IIIA].

When we evaluated the ratio of RotD100 with respect to the Larger measure, we observed differences of 10%, on average. These trends in the ratios were compared with the ratio RotD100/Larger (for earthquakes with 0 km $< R_{RUP} \leq$ 200 km and $7.0 \leq M < 8.0$) obtained by Boore and Kishida (2016) and the ratio RotD100/GM model proposed by Haji-Soltani and Pezeshk (2017). Very similar results were obtained for the ratio RotD100/Larger, while the ratios obtained herein for the RotD100/GM were slightly lower than that proposed by Haji-Soltani and Pezeshk.

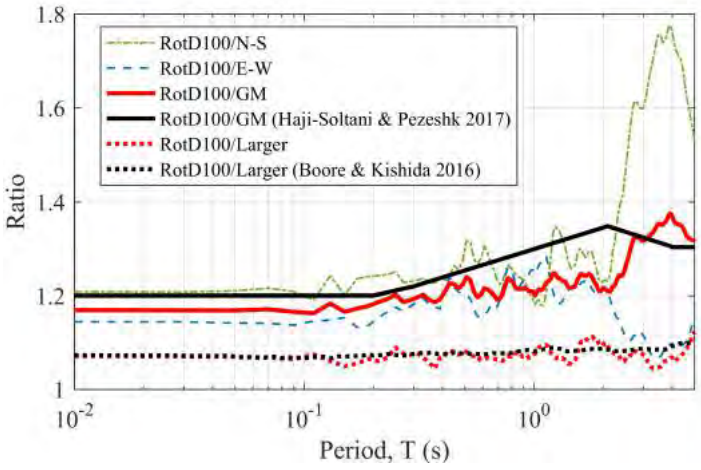

Figure E13: Comparison of the ratios RotD100/N-S, RotD100/E-W, RotD100/GM, and RotD100/Larger with ratios proposed by other researchers.

E.7 Conclusions

We analyzed the anomalous seismic performance of a specific building in a multifamily residential complex in Tlalpan borough in Mexico City, during the 19 September 2017 earthquake of M_W=7.1. Soil, SSI, SCI, and directionality effects were investigated to find a reasonable explanation for such an inconsistent seismic response. The homogeneity of the soils and the similarity of the geometrical and structural properties of the buildings in the complex allowed us to discard soil, SSI, and SCI effects as causative of significant differences in the seismic actions suffered by the buildings. Thus, directionality effects emerge as the main cause. The concurrence of the orientation of the weak axis of the building and the direction at which the maximum demand of the seismic actions is attained would be responsible for the collapse of the building. Thus, in damage and risk assessments, the direction in which the strongest seismic actions hit the buildings, directionality, should be considered, as similar buildings, located in the same place, may suffer different damage grades.

Concerning seismic hazard, Figure E12 shows how the response spectra predicted by the SASID A v4.0.2.0 application (NTCDS-RCDF, 2017) are lower than those corresponding to the seismic actions produced by the 2017 earthquake. This fact confirms that it is important to incorporate the results of directionality studies into the GMPEs by means of sensor orientation-independent measures. Thus, epistemic uncertainties in GMPE would be significantly reduced, and the foreseen seismic actions would be more realistic. However, the consideration of maximum seismic actions could lead to excessively conservative GMPE. Therefore, the median values or specific percentiles should be considered. The use of acceleration time-histories that are compatible with the RotD100 measure in dynamic analysis of structures would allow the most unfavorable case to be analyzed. These extreme values could be adopted for the design and/or rehabilitation of special structures such as historical-cultural heritage buildings or other essential and special high-risk structures.

Regarding design spectra, seismic regulations in Mexico City have been improved in recent years. However, later design spectra were still surpassed by several accelerograms recorded during the September 2017 earthquake. Noticeable, these excesses were due to directionality effects. Thus, an important conclusion of this study is that directionality effects must be considered in Probabilistic Seismic Hazard Analyses (PSHA), in damage assessments, and in design regulations. Specific studies on directionality effects should be performed in urban areas located in high seismic hazard zones. However, studies undertaken in other countries may be useful as the ratios RotD100/GM and RotD100/Larger, found in other studies, are comparable to those found in this study, in a wide range of periods.

E.8 Data and Resources

The ground-motion records used for this study were provided by the Centro de Instrumentación y Registro Sísmico (Instrumentation and Seismic Recording Center), Mexico, through the Red Acelerográfica de la Ciudad de México (Accelerographic Network of Mexico City) at http://www.cires.org.mx/ (last accessed on 19 May 2018). The reports and plans from the ISSSTE multifamily complex were obtained from the Secretaría de Obras y Servicios at http://www.obras.cdmx.gob.mx/uh-tlalpan (last accessed on 19 May 2018). A map with a summary of the damages due to the Central Mexico Earthquake is available at http://learningfromearthquakes.org/2017-09-19-puebla-mexico/data-map (last accessed on 19 May 2018). Figure E3a was obtained at http://unavidamoderna.tumblr.com/image/86044704110 (last accessed on 19 May 2018). The building structural model was numerically simulated using SAP2000 software (http://www.csiamerica.com/products/sap2000; last accessed 18 April 2018).

F Appendix. Reply to "Comment on 'Do Directionality Effects Influence Expected Damage? A Case Study of the 2017 Central Mexico Earthquake' by Luis A. Pinzón, Luis G. Pujades, Sergio A. Diaz, and Rodrigo E. Alva" by Eduardo Reinoso, Pablo Quinde, Danny Arroyo, Mario Ordaz, and Amador Terán-Gilmore

Based on the published article: Pinzón, L. A., Pujades, L. G., Diaz, S. A., & Alva, R. E. (2018). Reply to "Comment on 'Do Directionality Effects Influence Expected Damage? A Case Study of the 2017 Central Mexico Earthquake' by Luis A. Pinzón, Luis G. Pujades, Sergio A. Diaz, and Rodrigo E. Alva" by Eduardo Reinoso, Pablo Quinde, Danny Arroyo, Mario Ordaz, and Amador Terán-Gilmore. *Bulletin of the Seismological Society of America, 110*(1), 393–396. doi: 10.1785/0120190168
Journal URL: doi.org/10.1785/0120190168

F.1 Introduction

In a comment on the paper of Pinzón et al. (2018a), Reinoso et al. (2020) discuss two important issues. The first one points towards directionality effects, which Pinzón et al. (2018a) indicated as the most likely cause of the collapse of a single building in a multifamily complex belonging to the Civil Service Social Security and Services Institute (ISSSTE) in the Tlalpan borough in Mexico City. Reinoso et al. (2020) dispute this conclusion and claim that the main causes for the collapse were structural changes (structural walls were removed) that weakened the strength of the building in comparison to other undamaged or slightly damaged buildings in the same complex. The second relevant discord concerns the fact that the design spectra for Mexico City, including those provided in the new structural regulations published in December 2017, were exceeded by a number of strong ground motions. These two issues are further discussed in the following sections.

F.2 Collapse of a building in the ISSSTE multifamily complex

When directionality effects are considered for damage assessment of a specific building subjected to an actual seismic action it is crucial to have accurate and reliable information about the seismic action and about the building itself. Pinzón et al. (2018a) performed damage analysis assuming that the available strong motion data recorded close to the building would be similar to the actual seismic action that affected the building, and performed the structural calculations by using the most accurate information available at that time. No detailed information about important structural alterations was known publicly at the time the paper of Pinzón et al. (2018a) was written. A principal conclusion of this work was that, under the assumed seismic action and the available structural information, directionality effects would have increased the expected damage in comparison to the damage suffered by similar buildings in the ISSSTE multifamily complex with different orientations of their two main structural axes. However, there are large uncertainties in the strong seismic actions, even at distances as short as 700 m. Therefore, we agree that, to establish the right reason for the anomalous behavior of this building during the M_W=7.1 2017 central Mexico earthquake, would require: i) to have accurate accelerograms recorded in the building during the earthquake and ii) accurate blueprints of the building at this time instant including the structural modifications with respect to other buildings in the complex. Besides, to have direct measurements of the resonant frequencies of the buildings by placing

instruments on them and recording ambient vibrations before, during and after the earthquake would also have been of great help for an accurate characterization of the structural response of buildings. Also, inspections before the earthquake would help to establish the initial conditions of the building immediately before the earthquake hit.

Even if the seismic actions are accurately known, the orientation of the recording instruments is also crucial. In this respect, the information used in Pinzón et al. (2018a) was taken from the data provided by the Center of Instrumentation and Seismic Recording of Mexico [see Data and Resources section of Pinzón et al. (2018a)]. In those records, there are three components, corresponding to the two orthogonal horizontal directions and to the vertical accelerograms. The information on the orientation of the recording instruments can be found in two lines of the header of the files. Namely in line 37 and also, below, in line 108. In our case, the information in line 37 was: /N00E/+V/N90W, /N00E/+V/N90W, /S00E/+V/N90W respectively for AO24, CH84 and DX37 strong motion stations. However, in line 108 of the DX37, station this information was N00E/+V/N90W. Due to the fact that the last orientation agreed with the orientations of stations AO24 and CH84, this last information was used in our analyses (Pinzón et al., 2018a). The other concern refers to the way particle motion diagrams, also known as hodograms, are set up. The important issue is how the as-recorded accelerograms are translated into a homogeneous standard reference system, which usually is abscissa x positive to the east, called East axis and equivalent to N90E orientation, and ordinate y, positive to the north, which is named North axis and that would be equivalent to N00E. The procedure used in Pinzón et al. (2018a), is briefly described in the following. The acceleration in a rotated -axis can be computed in the following way:

$$A(t,\theta) = A_E(t) \cdot cos\theta + A_N(t) \cdot sin(\theta) \tag{62}$$

In this equation, θ is the angle between the positive directions of the x (EW) axis and the new axis. Thus, values of θ equal to 0°, 90°, 180° and 270° correspond to axes' orientations of N90E, N00E, N90W and S00E respectively. Or equivalently,

$$A_E(t) = A_{N90E}(t) = -A_{N90W}(t) \quad and \quad A_N(t) = A_{N00E}(t) = -A_{S00E}(t) \tag{63}$$

With these criteria, the hodograms for CH84 and AO24 stations are those of Figure 4f) and Figure 4i) of Reinoso et al. (2020). Figure 4c corresponds to the orientation N00E-N90W as defined in the line 108 of the data corresponding to the DX37 accelerometric station. However, the important point in this specific case is the difficulty to clearly establish the actual cause for the collapse of the building and in general, the need of accurate information when such studies are tackled and, more especially, if legal issues are involved. However, hodograms at close stations have been carefully recalculated by using the information provided in the acceleration records. Equations 62 and 62 have been used to obtain the standard orientations N90E and N00E. Figure F1 displays the obtained particle motion diagrams, which agree with the ones of Figure 4 of Reinoso et al. (2020) (middle column) that we acknowledge are right. We thank Reinoso et al. (2020), and we appreciate this correction.

Although Reinoso et al. (2020) focus on station CH84, the most relevant ground motions are those at station DX37, as that station is only 0.7 km from the building site whereas station CH84 is more than twice that distance. Figure 1 in this reply, and figure 4b in Reinoso et al. (2020), show that the strongest ground motion at station DX37 is nearly perfectly aligned with the collapsed building's weak axis. The other basin edge station (AO24) is also only about 20 degrees different from the orientation of the building's weak axis. Thus, it seems quite likely that the strongest ground motions were within 10 or 20 degrees of the optimum direction for damaging the building, and given the uncertain variation

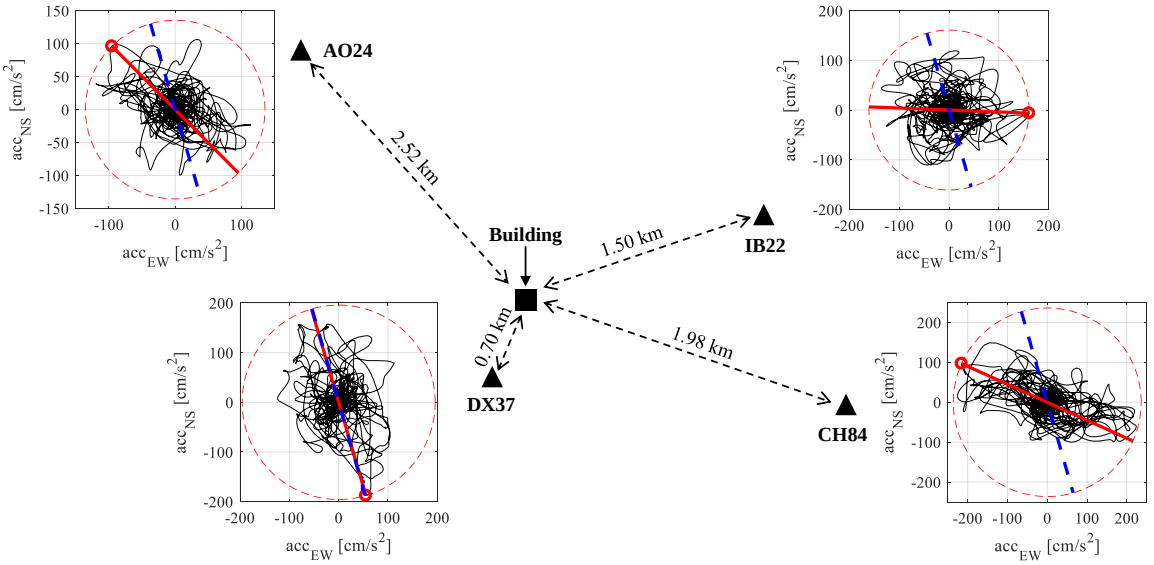

Figure F1: Hodograms at stations AO24, IB22, DX37 and CH84 close to the building site. The weak direction of the building (dashed blue line) is depicted.

with distance, the direction might indeed have been nearly perfectly aligned.

Reinoso et al. (2020) also claim that for the period range between 0.25 and 0.35 s, according to Figure 12 of Pinzón et al. (2018a), directionality effects are small. But, fundamental periods of buildings may be lengthened due to soil-structure-interaction (SSI) effects, structural changes and strong dynamic loads. Çelebi (2008) discusses SSI effects on performance of buildings during earthquakes, stating that they can be beneficial or adverse; adverse effects during the 1985 Michoacan (Mexico) earthquake were pointed out by Tarquis and Roesset (1988) who showed that fundamental periods of mid-rise buildings (5-15 stories) lengthened due to SSI, placing them in a resonant environment. A similar effect would lengthen the periods of the buildings in the ISSSTE multifamily complex during the 2017 central Mexico earthquake.

Concerning structural and architectonic modifications, removing walls and other elements can increase the fundamental period of the building substantially. Several studies show the converse: decreasing building period as walls and elements are added. Espinoza (1999) by using ambient noise accelerometric measurements, followed the changes in the dynamic response of an administrative reinforced concrete building in the period between when the main structural elements (columns and slabs) were finished and the end of the construction, including enclosures, partitions in the floors and other finishes. The building has 8 floors, four of which are underground floors. He found that the period of the building decreased by 40% and 33% in longitudinal and transversal directions respectively, from when the columns and slabs were constructed until the final serviceable building was delivered. Also, for reinforced concrete buildings with waffle slabs, Kobayashi et al. (1996) reported that fundamental periods of finished buildings could be as much as 33% smaller than the one of the nude structures. Torkamani and Ahmadi (1988) found period decreases of about 15% during the construction of a tall building in Pennsylvania and Kose (2009) found that RC frames with infill walls had a shorter period, about 5%-10%, compared with RC frames without infill walls regardless of whether they had shear walls or not. Thus, the removal of structural walls in the damaged building, as stated by Reinoso et al. (2020), could have significantly increased the period of the collapsed building.

Finally, concerning fundamental periods of buildings subjected to strong shaking, Meli and Faccioli

(1996) studied the dynamic response of a 14-story reinforced concrete building which was founded in soft soils in the lake-bed area of Mexico City. An important conclusion was that the dynamic response of the structure is very sensitive to the ground motion and that early non-linear behavior produced a continuous reduction of the lateral stiffness, thus significantly increasing the fundamental period of vibration. Besides, Calvi et al. (2006), in a thorough analysis of the elongation of periods of RC buildings during earthquakes, concluded that strong ground shaking can lead to periods of vibration of up to 1.8 to 2.5 times the initial period, which correspond to a stiffness degradation in the range 70-85 %.

The combined effects of soil interaction, removal of structural walls, and the dynamic response during strong motion thus may have increased the fundamental period of the building, moving it towards periods where the directionality effects in the seismic actions could have been more important. Thus, in our view and based on the new information presented in Reinoso et al. (2020), this singular collapse is likely due to a combination of two factors: the directionality effects that we describe in our paper, combined with the inadequate structural modifications described in Reinoso et al. (2020) that may have increased the building's period.

The analysis of the relationship between the expected damage and the direction of the seismic action is also well explained in Vargas-Alzate et al. (2018).

F.3 Directionality effects and earthquake-resistant design

Reinoso et al. (2020) claim that the design spectra were only exceeded in two of the recording stations, though they do not specify if directionality effects were considered. Again, in our opinion, the interesting lessons of this and other recent well-documented earthquakes are summarized in two relevant conclusions of Pinzón et al. (2018a); namely: 1) concerning the hazard analysis and ground motion predictive equations (GMPE) *"it is important to incorporate the results of directionality studies into the GMPEs by means of sensor orientation-independent measures"* and 2) concerning earthquake resistant design regulations, *"directionality effects must be considered in probabilistic seismic hazard analyses, damage assessments, and design regulations"*. But special care must be taken to not overestimate or underestimate the likely seismic actions. Thus, the use of adequate simplified approaches as the one shown in equation (1) of Reinoso et al. (2020), and many others, are welcome but, in our opinion, further options based on adequate percentiles of rotated response spectra would improve and would enrich the design options of civil engineers. Further details on directionality effects in probabilistic seismic hazard assessments can be found in Pinzón et al. (2018b).

F.4 Closure

With the aim of contributing to a better knowledge of directionality effects in the damage expected in buildings, Pinzón et al. (2018a) carefully analyzed the information available, concluding that directionality effects would have strongly contributed to the anomalous damage observed in the 1C building in the Tlalpan complex. Other case studies of buildings damaged during strong earthquakes and additional computations done by the authors confirm the relevance of directionality effects. We are confident that the scientific and technical expertise of BSSA readers, will allow them to be the ultimate referees of this debate. Finally, we are extremely grateful to the editor-in-chief, Thomas Pratt, who mediated this discussion perfectly with his knowledge, mastery and kindness.